BONNER METEOROLOGISCHE ABHANDLUNGEN

Heft 94 (2022) (ISSN 0006-7156)
Herausgeber: Andreas Hense

Michael Langguth

REPRESENTATION OF DEEP CONVECTION AT GRAY-ZONE RESOLUTIONS - IMPLEMENTING AND TESTING THE HYBRID MASS FLUX CONVECTION SCHEME (HYMACS) IN THE ICON MODEL

BONNER METEOROLOGISCHE ABHANDLUNGEN

Heft 94 (2022) (ISSN 0006-7156)
Herausgeber: Andreas Hense

Michael Langguth

REPRESENTATION OF DEEP CONVECTION AT GRAY-ZONE RESOLUTIONS - IMPLEMENTING AND TESTING THE HYBRID MASS FLUX CONVECTION SCHEME (HYMACS) IN THE ICON MODEL

Representation of deep convection at gray-zone resolutions - Implementing and testing the HYbrid MAss flux Convection Scheme (HYMACS) in the ICON model

Dissertation
zur
Erlangung des Doktorgrades (Dr. rer. nat.)
der
Mathematisch-Naturwissenschaftlichen Fakultät
der
Rheinischen Friedrich-Wilhelms-Universität Bonn

vorgelegt von
M.Sc.
Michael Langguth
aus
Köln

Bonn, September, 2021

Diese Arbeit ist die ungekürzte Fassung einer der Mathematisch-Naturwissenschaftlichen Fakultät der Rheinischen Friedrich-Wilhelms-Universität Bonn im Jahr 2021 vorgelegten Dissertation von Michael Langguth aus Köln.

This paper is the unabridged version of a dissertation thesis submitted by Michael Langguth born in Köln to the Faculty of Mathematical and Natural Sciences of the Rheinische Friedrich-Wilhelms-Universität Bonn in 2021.

Anschrift des Verfassers: Address of the author:

Michael Langguth
Institut für Geowissenschaften, Abt. Meteorologie
Universität Bonn
Auf dem Hügel 20
D-53121 Bonn

1. Gutachter: Prof. Dr. Andreas Bott,
Rheinische Friedrich-Wilhelms-Universität Bonn
2. Gutachter: PD Dr. Martin Georg Schultz,
Research Center Juelich

Tag der Promotion: 22. Februar 2022

Veröffentlichte Teile der Dissertation

Bei der vorliegenden Dissertation handelt es sich um eine Monographie. Einzelne Abschnitte sowie ein Kapitel der Dissertation wurden jedoch bereits im Vorfeld veröffentlicht.
Der bereits publizierte Inhalt ist wie folgt in dieser Dissertation wiederzufinden:

1. Kapitel 1: geringe Übereinstimmung
2. Kapitel 2: nur in Dissertation
3. Kapitel 3: weitgehende Übereinstimmung nur in Unterkapitel 3.1
4. Kapitel 4: weitgehende Übereinstimmung (besonders Unterkapitel 4.1, 4.3., 4.5 und 4.6)
5. Kapitel 5: nur in Dissertation
6. Kapitel 6: geringe Übereinstimmung

Die entsprechende Publikation ist zu finden als:

M. Langguth, V. Kuell, and A. Bott (2020). "Implementing the HYbrid MAss flux Convection Scheme (HYMACS) in ICON-First idealized tests and adaptions to the dynamical core for local mass sources". In: *Quarterly Journal of the Royal Meteorological Society* 146.731, pp. 2689–2716. DOI: 10.1002/qj.3812

Zusammenfassung

Trotz steigender Rechenleistung sind die Gitter heutiger Atmosphärenmodelle oft noch zu grob, um konvektive Prozesse explizit zu repräsentieren. Da diese einen wichtigen Antrieb der atmosphärischen Dynamik darstellen, werden Konvektionsparametrisierungen eingesetzt, die bereits seit mehreren Jahrzehnten entwickelt werden. Aktuelle Anwendungen regionaler Klima- und operationeller Wettervorhersage-Modelle erreichen jedoch eine räumliche Auflösung, die die Umwälzzirkulation hochreichender Konvektion teilweise auf der Gitterskala abbilden können. Diese so genannte Grauzone hochreichender Konvektion stellt den konventionellen Parametrisierungsansatz vor Herausforderungen, die in den letzten beiden Jahrzehnten zunehmende wissenschaftliche Beachtung erlangt haben.

In der vorliegenden Arbeit wird das hybride Massenfluss Konvektionsschema HYMACS in das ICOsahedral Non-hydrostatic (ICON) Modell implementiert und ausgiebig getestet. Anders als gängige Konvektionsparametrisierung-Schemata überlässt HYMACS das kompensatorische Absinken der gitterskaligen Dynamik und ermöglicht auf diese Weise einen Nettomassentransport. Obwohl das Schema bereits seit der wegweisenden Arbeit von Kuell et al. (2007) entwickelt wird, wurde es bisher nur in einigen Fallstudien mit dem COSMO (COnsortium for Small-scale Modeling) Modell getestet. Das hybride Schema verbesserte in diesen Studien zwar die Darstellung hochreichender Konvektion in der Grauzone, eine statistisch fundierte Auswertung der Vorzüge von HYMACS wurde jedoch noch nicht durchgeführt. Zudem erscheint eine Implementierung in ICON attraktiv, da dieses Modell für ein breites Spektrum räumlicher Auflösungen entwickelt wurde.

Diese Arbeit beginnt mit einer ausführlichen Einführung in die Grundlagen von HYMACS und dokumentiert die jüngsten Weiterentwicklungen des Schemas. Zusätzlich zu den notwendigen Anpassungen der Physik-Dynamik-Kopplung mit ICON aufgrund des alternativen Parametrisierungsansatzes, ergeben sich Probleme in Verbindung mit dem numerischen Filter des Modells. Die operative anisotrope Divergenzdämpfung verzerrt die dynamische Antwort auf einen parametrisierten Nettomassentransport, so dass diese angepasst werden muss. Verschiedene numerische Filteroperatoren werden sowohl in Tests des dynamischen Kerns auf der Kugel als auch in in Massenauftriebsexperimenten untersucht. Auf Grundlage dieser Tests wird eine revidierte Filterkonfiguration vorgeschlagen, die mit HYMACS kompatibel ist und die numerisches Rauschen effizient entfernt.

Mit der überarbeiteten numerischen Filterkonfiguration wird eine Testreihe von Vorhersagen über drei Sommermonate im mitteleuropäischen Raum durchgeführt, um die Leistung von HYMACS in ICON zu analysieren. Es wird gezeigt, dass das hybride Schema den konvektiv bestimmten Tagesgang des Niederschlags besser erfasst, als das operationelle Schema zur Parametrisierung von Konvektion. Die modellierte Randverteilung der Niederschlagsmengen und die räumlichen Muster des Niederschlags werden ebenfalls besser repräsentiert. Während die statistische Analyse damit die Ergebnisse früherer Fallstudien bestätigt, werden auch Probleme aufgrund des Nettomassentransports der flachen Konvektion identifiziert. Gleichwohl sind die Ergebnisse vielversprechend, so dass diese Arbeit als Ausgangspunkt für skalenadaptive Weiterentwicklungen von HYMACS in ICON dient.

Abstract

Despite the increasing computing resources, the grids of contemporary atmospheric models are often still too coarse to explicitly represent convective processes. Since these processes are known to be an important driver of atmospheric dynamics, convection parametrization schemes must be deployed which have been developed over several decades. However, recent applications of regional climate and operational numerical weather prediction models have reached spatial resolutions where the overturning circulation of deep convection becomes partly resolved onto grid-scale. The so-called gray-zone of deep convection imposes challenges to the conventional parametrization approach which have attained increasing scientific attention in the last two decades.

The present work implements and tests extensively the HYbrid MAss flux Convection Scheme (HYMACS) in the ICOsahedral Non-hydrostatic (ICON) model. In contrast to other convection parametrization schemes, HYMACS passes the compensational subsidence to the grid-scale dynamics, thereby allowing for a net mass transport. While the scheme has been developed since the pioneering work of Kuell et al. (2007), it has only been tested in a couple of case studies with the COSMO (COnsortium for Small-scale Modeling) model. Although the hybrid scheme improved the representation of convection at gray-zone resolutions in these studies, a statistically well founded assessment of the merits of HYMACS is still outstanding. Besides, its implementation into ICON is appealing since the new hosting model is designed to operate over a broad range of spatial resolutions.

This thesis starts with a in-depth introduction of the theoretical framework of HYMACS and documents recent developments of the scheme. Apart from some required adaptions of the physics-dynamics coupling with ICON, problems in conjunction with the numerical filter in the model's dynamical core are identified. The operational anisotropic divergence damping operator distorts the dynamical flow response to a parametrized net mass transport and therefore has to be revised. Different numerical filter operators are investigated in dynamical core tests on the sphere and in mass lifting experiments. Based on these tests, a revised filter configuration is proposed which is compatible with HYMACS and which efficiently removes computational noise.

With the revised numerical filter configuration, a series of re-forecasts over Central Europe spanning a summery three-monthly period is conducted to analyze the performance of HYMACS in ICON. It is demonstrated that the hybrid scheme captures the convectively driven diurnal cycle of precipitation better than the operational convection parametrization scheme. The modelled marginal distribution of precipitation amounts and the spatial patterns of precipitation also get improved. Albeit the statistical analysis confirms the results of former case studies, issues to the net mass transport of shallow convection are identified as well. Nonetheless, the merits are encouraging and this work is considered to serve as the basis for further developments focusing on the scale adaptivity of HYMACS in the modeling framework of ICON.

Contents

1 Introduction

1.1 Motivation

The beauty and complexity of the Earth's atmosphere can be illustrated impressively from satellite images taken from space. Figure 1.1 shows exemplary a snapshot from the Moderate Resolution Imaging Spectroradiometer (MODIS), a sensor aboard the Terra satellite launched by the National Aeronautics and Space Administration (NASA), on July 11, 2005. Cloud systems on several spatial scales as a visible manifestation of atmospheric dynamics and processes are visible all over the globe. Cloud bands spanning more than 1000 km can be attributed to travelling cyclones in the midlatitudes while cloud clusters with a diameter of a few 10-100 km due to organized thunderstorms dominate the tropical belt. Besides, patchy cloud patterns are identified, for instance, over the subtropical ocean where shallow (strato-)cumulus clouds persist. The horizontal size of these cellular cloud patterns can be smaller than one kilometer so that individual clouds are barely identifiable from global satellite images such as Figure 1.1.

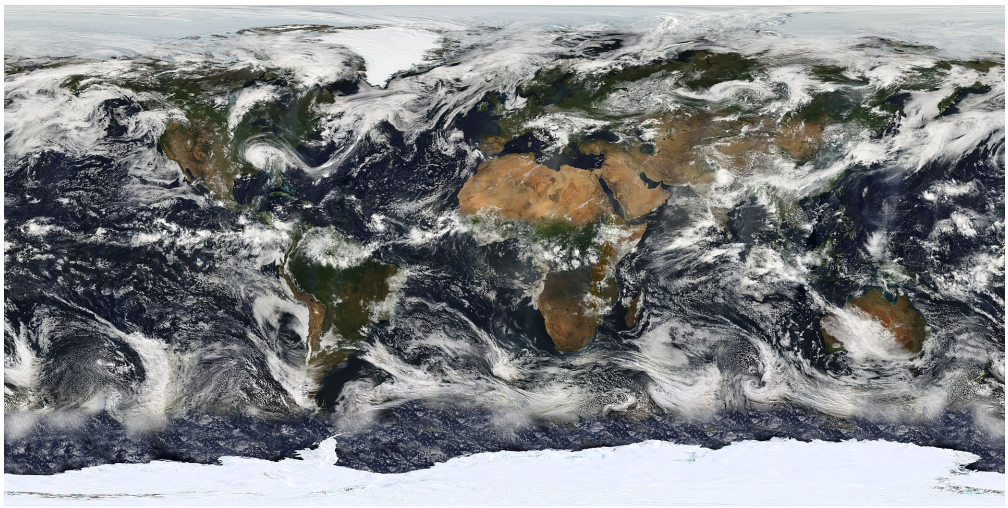

Figure 1.1: Satellite image of the Earth on July 11, 2005 in the visible wavelength spectrum synthesized from the MODIS. Data gaps have been filled by observations from the GOES weather satellites and the latest version of the NASA Blue Marble. Source: NASA.

In fact, the horizontal length scale L of atmospheric processes ranges over more than 10 orders of magnitude from the smallest Kolmogorov microscale ($L \lesssim \mathcal{O}(10^{-3}\,\mathrm{m})$) to the planetary scale ($L \gtrsim \mathcal{O}(10^{7}\,\mathrm{m})$). Since the temporal scale of these processes is correlated with the spatial scale, different phenomena are commonly classified into spatio-temporal scale regimes (Fig. 1.2). The above mentioned cyclones have a characteristic time scale of several days and are therefore part of

the macro-β scale following Orlanski (1975). By contrast, the smallest convective clouds in Figure 1.1 belong to the micro-α scale with a lifetime of one hour or less.

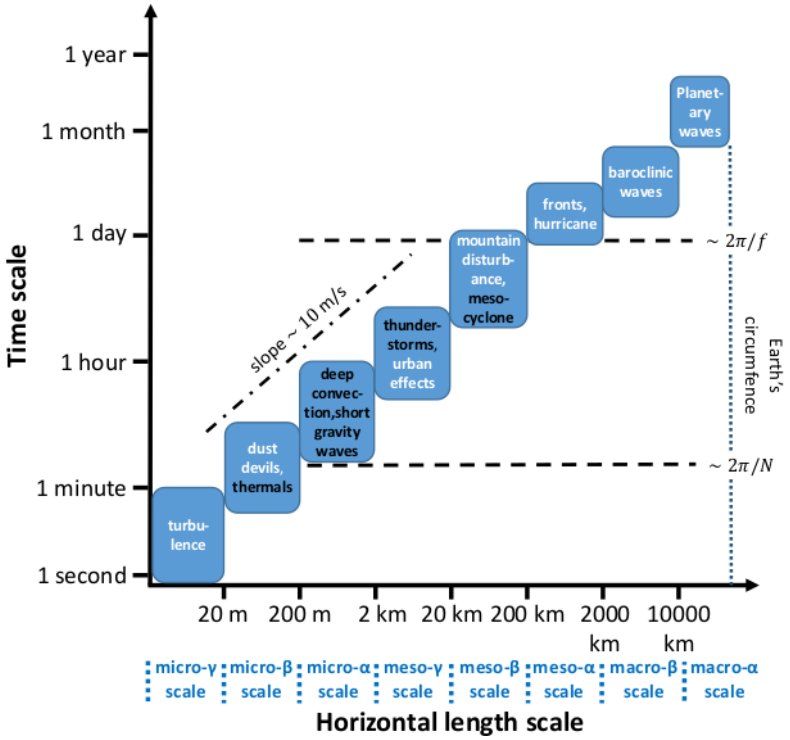

Figure 1.2: Spatio-temporal scale definitions for atmospheric processes based on Orlanski (1975). For each class, exemplary processes are depicted where moist convective ones are highlighted in black. The dashed horizontal lines bound the mesoscale with a time scale between pure buoyancy oscillations and a pendulum day. The former is related to the Brunt-Väisälä frequency N characterizing the atmospheric stratification while the latter depends on the Coriolis frequency f. Adopted from Markowski and Richardson (2011).

The complexity of atmospheric processes does not only arise from the variety of spatio-temporal scales, but also from pronounced interactions among all scales. The interactions thereby lead to an energy transfer which can be directed down-scale, i.e. from large to smaller scales, or vice versa, from small to larger scales (upward energy propagation). Thus, understanding atmospheric processes and dynamics not only comprises understanding distinct processes, but also the way they interact with each other.

An illustrating example for the complexity of atmospheric processes constitutes moist convection which is of central interest in this study. In general, convection is linked to Archimedes' principle stating that a body within a fluid experiences an upward force equal to the weight of the fluid that the body displaces. The term moist convection then deals with upward and downward motions of humid air accompanied by water phase changes. As depicted in Figure 1.2, these motions may occur over a wide range of spatial scales. Narrow thermals of a few hundred meters, commonly referred as updrafts, transport air upwards which become visible as individual convective clouds (cells). Occasionally, such individual cells get organized on larger scales so that the horizontal length scale may occupy several kilometers. The upward mass transport induces a overturning circulation whose

horizontal extent also varies. While narrow downwards motions (downdrafts) may partly compensate the updraft mass flux, the overturning circulation commonly gets closed via subsidence on larger horizontal length scales with $L \sim \mathcal{O}(10^4\text{-}10^5\,\mathrm{m})$ (Bretherton and Smolarkiewicz, 1989).

The multi-scale nature of moist convection is highly relevant for numerical models of the atmosphere. These models aim to depict the current atmospheric state and its evolution with the help of physical laws for fluid motion, mass and enthalpy encoded in a set of partial differential equations, the Navier-Stokes equations. However, these equations cannot be solved analytically so that they must be discretized and filtered in space and time to allow for numerical integration. The basic characteristics of the spatio-temporal filter are defined by the time step and the grid onto which the state of the atmosphere gets represented. Consequently, depending on the corresponding spatio-temporal filter scale, the spectrum of atmospheric dynamics gets separated into resolved and unresolved processes.

Due to the above mentioned multi-scale nature of atmospheric processes including scale interactions, unresolved processes are by no means irrelevant. Since their neglection may induce excessive error growth on all scales, parametrization schemes are applied in numerical models of the atmosphere (see, e.g., Gross et al., 2016, for a review). In general, these schemes rely on the concept that the effect of *unresolved* processes can be approximated with a function of some *resolved* variables once averaging over the truncated scales is performed.

Nowdays, several modern model applications such as operational numerical weather prediction (NWP) make use of grid spacings $\Delta x \sim$ 1-10 km (Bauer et al., 2015). Bearing in mind that the *effective* spatial model resolution typically ranges between 5-8 Δx due to the need for numerical filters (Skamarock, 2004), the (artificial) truncation scale gets placed within the meso-β or meso-γ scale. For the representation of mesoscale processes such as moist convection, this imposes a couple of numerical challenges since their characteristic length scales approach the size of individual grid boxes (Gross et al., 2018). While, for instance, the overturning circulation of deep convective clouds in thunderstorms becomes partly represented onto grid-scale (Arakawa and Jung, 2011), substantial parts of the dynamics are still unresolved as long as $\Delta x > \mathcal{O}(10^2\,\mathrm{m})$ holds (Bryan et al., 2003). This is commonly referred as the *gray-zone for deep convection* whose presence has led to contradictory opinions regarding the grid spacing that allows for an explicit representation of deep convection in real modelling applications[1].

Several studies point out that switching off the parametrization at grid spacings of $\Delta x \sim 4$ km adds a substantial degree of realism to numerical simulations (see, e.g., Kain et al., 2008; Weisman et al., 2008; Prein et al., 2013). In addition to a more realistic organization of convective systems, an improved capturing of the diurnal cycle of precipitation is highlighted. However, other studies also point out that a grid spacing of $\Delta x = 4$ km is too coarse to yield a proper representation of deep convection. Malardel and Wedi (2016) argue that a hasty deactivation of deep convection parametrization at gray-zone resolutions may result in unrealistic kinetic energy spectra. Their finding is further confirmed by studies noting the occurrence of excessive updrafts on grid-scale, so-called grid storms, in simulations

[1] A concise distinction between shallow and deep convection is presented in Section 2.1.

with $\Delta x = 4\,\text{km}$ (Deng and Stauffer, 2006; Lean et al., 2008).

Contrarily, some studies even report on benefits of so-called *convection-permitting* simulations at much coarser spatial resolutions with $\Delta x \geq 10\,\text{km}$ (e.g. Marsham et al., 2013; Miyakawa et al., 2014; Pearson et al., 2014; Birch et al., 2015; Ou et al., 2020). Albeit noticing that their deployed grids are too coarse to represent properly deep convection, they favor such an approach due to severe deficiencies of convection parametrization schemes (CPS) in regions where convection acts as the dominant driver for atmospheric motions such as the tropics. Examples in this context are an improved simulation of the West African monsoon and the Madden-Julian Oscillation.

Indeed, theoretical studies indicate that a misrepresentation of convection can yield to an upscale error propagation process that contaminates the modelled atmospheric state on meso-α or macro-β scale in midlatitudes (Zhang et al., 2007; Bierdel et al., 2017). As illustrated in Figure 1.3, small-scale unbalanced errors related to convective instability induce an upscale error transition to the balanced large scales within one day. Subsequently, these errors may further grow to modulate baroclinic waves in the midlatitudes so that the simulated and observed atmospheric state start to diverge on all spatial scales.

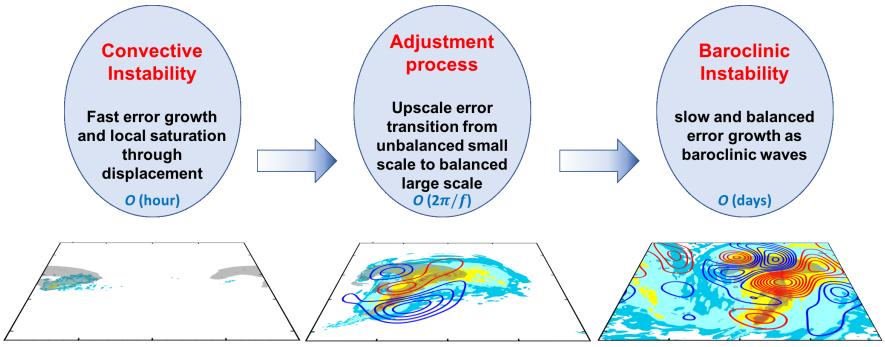

Figure 1.3: Schematic visualization of the three-staged error growth mechanism in the midlatitudes as proposed by Zhang et al. (2007). The colored contours denote the total differences in total energy between simulation and analysis which propagate upscale from 3h (left), over 18h (center) until 36h (right) after initialization. The shaded contours highlight precipitation patterns. From Sun (2017).

Hence, there is theoretical and experimental evidence that the representation of (deep) moist convection at gray-zone resolution is of great relevance for the performance of atmospheric models. While it cannot be expected that a universal threshold for switching to convection-permitting simulations exists at all, addressing the physical parametrization of deep convection is argued to be more urgent than seeking for ad-hoc grid spacing rules (Prein et al., 2015).

1.2 Research questions

The proper representation of moist convection together with a smooth transition from fully parametrized to explicit, grid-scale convection has attained increasing research interest over the last years (Arakawa et al., 2016). While there has been undoubtedly success in improving the scale-adaptivity of CPS (see, e.g., Kwon and

Hong, 2017; Jeworrek et al., 2019), a couple of questionable assumption still reside in contemporary schemes. As will be seen in the next chapter, these questionable assumptions can be traced back to ages where the whole spectrum of convection could be safely treated as unresolved processes, i.e. at times when the grid spacing in numerical models of the atmosphere ranged at $\Delta x \sim \mathcal{O}(10^2\,\mathrm{km})$.

Among other approaches to relax some fundamental assumptions which will be briefly outlined later, the so-called hybrid approach was proposed by the study of Kuell et al. (2007). While classical CPS take the complete overturning circulation consisting of up- and downdrafts and environmental subsidence into account, the hybrid approach aims to parametrize the convective draughts only. The rationale behind the hybrid approach can be given by the typical horizontal length scales of the respective components of the overturning circulation (cf. Fig. 1.2). While the narrow up- and downdrafts are still too small to be explicitly represented at kilometer-scale, the environmental subsidence can spread over the meso-β and meso-α scale which are considered to be explicitly resolved. Although the basic idea of this approach appears trivial at first sight, it constitutes a notable change in the conceptual design of a CPS. Related to the split of the convective circulation pattern is also a (so far) unique feature of the associated parametrization scheme, that is the admission of a *net* mass transport.

The coupling of the HYbrid MAss flux Convection Scheme (HYMACS) into the regional, non-hydrostatic COSMO (Consortium for Small-Scale Modeling) model (Baldauf et al., 2011; Doms et al., 2011; Doms and Baldauf, 2015) constitutes the first practical realization of this approach. Following several idealized studies to ensure the integrity of the scheme into the modeling framework (Kuell et al., 2007), HYMACS was tested successfully in several real applications under various synoptic situations over Europe with the COSMO model using $\Delta x \simeq 7\,\mathrm{km}$ (Kuell and Bott, 2008, 2009, 2011, 2014, 2019).

While the COSMO model is nowadays still used for scientific purposes, it has been replaced by the ICOsahedral Non-hydrostatic (ICON) model in the operational forecasting chain at the German Weather Service (Deutscher Wetterdienst, DWD) over the last years. The ICON model was jointly developed by the Max Planck Institute for Meteorology (MPI-M) and DWD and went operational on 20^{th} January 2015. Its development targets an unified modeling system being appropriate for a broad range of applications ranging from large-eddy simulations (LES) studies (Dipankar et al., 2015) over regional and global NWP applications to climate studies (Giorgetta et al., 2018). Thus, it is considered to be an excellent modeling framework for HYMACS whose integration is the central aim of this thesis.

This target thereby comes along with further research questions onto which this thesis elaborates in the following:

- What are the basic differences between the hybrid and the classical convection parametrization approach apart from the conceptual idea mentioned above?

- How can HYMACS be integrated into the ICON model and which challenges must be tackled due to a net, subgrid-scale mass transport?

- How does HYMACS perform in ICON in a quasi-operational series of simulations with focus on the representation of convective precipitation compared to the operational CPS at gray-zone resolutions?

Apart from the technical integration of HYMACS into the new modeling system, the latter research question is of particular interest. The systematic application in a quasi-operational set-up allows to reveal strengths and potential weaknesses of HYMACS and therefore enables us to pinpoint features of the scheme which can be further improved in the future. Thus, a necessary prerequisite of this thesis is also to provide a brief summary of other existing approaches which aim to enhance the scale-adaptivity of convection parametrization schemes with a focus on deep convection.

1.3 Outline of the thesis

In order to advance on the aims listed above, this thesis is organized as follows:

Chapter 2 starts with a brief survey on the phenomenology of moist convection in the Earth's atmosphere and introduces fundamental physical quantities and relationships which help to understand its nature. With this background information, the fundamentals of classical CPS in numerical models of the atmosphere are sketched followed by a summary on the challenges of representing deep convection at gray-zone resolutions. The chapter is then closed by a more in detail description of a particular classical CPS that is used operationally in the ICON model, the Bechtold-Tiedtke scheme.

The classical parametrization approach and the Bechtold-Tiedtke scheme are then opposed to HYMACS in Chapter 3. After an introduction of the theoretical basis of the hybrid approach, a comprehensive overview on HYMACS is provided. While parts of this overview are taken from the existing literature, undocumented changes and further developments as part of this study are reported.

Chapter 4 then deals with the implementation of HYMACS into the modeling framework of ICON. After a general model description, the chapter is dedicated to the physics-dynamics coupling and the usage of numerical filters in ICON. Revised filter configurations, which turn out to be necessary with HYMACS, are presented, and their performance is compared with the help of dynamical core tests. The best numerical filter is finally used to conduct idealized mass lifting tests demonstrating the integrity of the hybrid CPS into ICON.

A series of real case simulations with HYMACS in ICON is documented in Chapter 5. After a description of the experimental design and the model configuration, the observational dataset for verification purposes and a climatological classification of the test series period are presented. Guided by a discussion of precipitation forecast verification, ICON simulations with HYMACS and the operational Bechtold-Tiedtke scheme are evaluated and compared in detail with each other. The evaluation is complemented by a in-depth analysis of the obtained results.

Chapter 6 finally provides a summary of this thesis and picks up the results from the test series to sketch future development perspectives of HYMACS.

2 The nature of moist convection and its parametrization in numerical atmospheric models

In this chapter, a brief overview on the nature of moist convection in the atmosphere and its parametrization in numerical atmospheric models is provided. After summarizing the phenomenology in Section 2.1, the description becomes more quantitative in Section 2.2 where special attention is also devoted to the effects of moist convection on its environment. Understanding these effects is also key for convection parametrization schemes which are nowadays still applied in atmospheric models. While the concept of such parametrization schemes is outlined in Section 2.3, the challenges of parametrizing deep convection at gray-zone resolutions are outlined complemented by recent methods to tackle these challenges (Sec. 2.4). Finally, the operational Bechtold-Tiedtke scheme used in ICON is presented as a specific example of a classical parametrization scheme for convection in numerical weather prediction (NWP) models (Sec. 2.5).

2.1 Phenomenology of moist convection

Although atmospheric moist convection appears over a broad range of different sizes and shapes, it is common to distinguish so-called *deep* convection and *shallow* convection (see, e.g., Stensrud, 2009). As suggested by the name, deep convection typically penetrates large parts of the troposphere, thus constituting thermals of moist air with a depth of several kilometers (4-15 km). The growth of convective cells occasionally reaches the tropopause and can even penetrate the lower stratosphere (see, e.g., Liu and Liu, 2016; Rysman et al., 2016). The horizontal scale ranges from a few 100 m up to a couple of 10 km with the latter being reached by intensive thunderstorms (see Fig. 1.2).

By contrast, shallow convection is typically bounded by the inversion separating the planetary boundary layer (PBL) from the free troposphere. Thus, its vertical depth ranges from a few 100 m up to 2-3 km. Their horizontal scale is also somehow smaller with typical sizes in the order of 100 m (see Fig. 1.2).

With *congestus* clouds topping near the melting level in the tropics, convective clouds show up with a tri-modal character (Johnson et al., 1999). However, since congestus clouds usually reach up to height of 5-6 km, they can also be categorized as deep convective clouds (e.g. Bechtold et al., 2014a).

In addition to the typical depth of moist convection types, it is also convenient to assume that only deep convective clouds produce precipitation while shallow convection is non-precipitating (Betts, 1973). As a result, deep convection leads to net

heating and drying of the atmosphere, whereas shallow convective clouds only redistribute enthalpy, moisture and momentum (Stensrud, 2009). As seen below, this implies that the effect of both convection types on the ambient (non-convective) atmosphere and likewise their role in the climate system differ substantially.

Figure 2.1 shows the annual occurrence frequency of deep and shallow convection on the globe. Even though their occurrence frequency is inferred from parametrized convection in the Integrated Forecasting System (IFS) of the European Centre for Medium-Range Forecasts (ECMWF), the spatial distribution compares well to satellite observations and can therefore be used for a qualitative assessment on the occurrence of moist convection in the atmosphere (Bechtold et al., 2014a; ECMWF, 2017). While deep convection frequently develops in the tropical belt, shallow convective clouds dominate large parts of the subtropical oceans. In midlatitudes, both types of convection are less dominant, but by no means negligible. Especially during the summer season, deep and shallow convection are typical processes over the continent in the presence of strong surface heating.

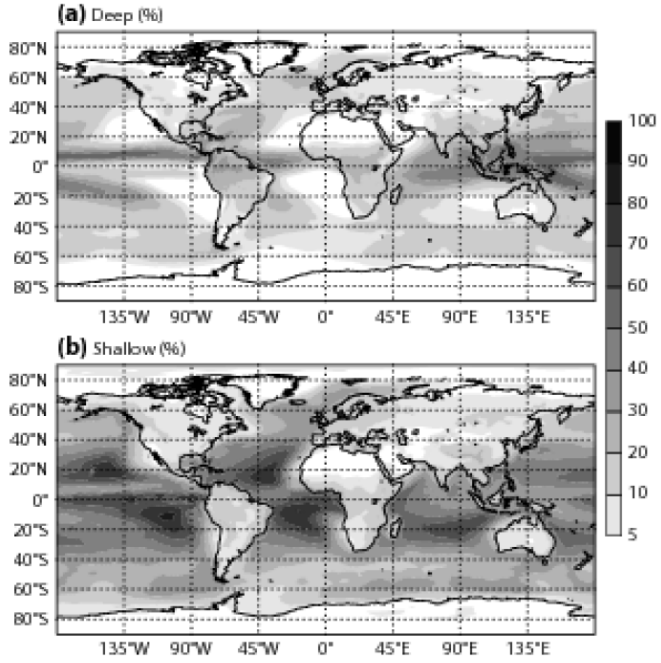

Figure 2.1: Mean annual occurrence frequency of deep (top) and shallow (bottom) convective clouds on the globe from the IFS model (model version: Cy40r1, one-year integration at T159 spectral resolution). Both types of convection are parametrized with the Bechtold-Tiedtke scheme which will be presented in Section 2.5. From Bechtold et al. (2014a).

The ubiquity of moist convection manifests itself in the relevance for the energy and water budget of the Earth. For instance, shallow convection balances the surface fluxes of enthalpy and moisture in the subcloud layer and thereby creates a diabatic dipole in the cloud layer (e.g. Salzen et al., 2005; Bellenger et al., 2015). While the transported (detrained) condensate near the cloud top cools and moistens the capping PBL inversion layer, the lower part becomes warmer and drier due to compensating subsidence. Shallow convection is thereby common in the descending part of the Hadley circulation in the subtropics and under anticyclonic

circulation pattern in the midlatitudes (Houze Jr, 2014). Besides, extensive stratocumulus clouds, a variant of shallow convection in oceanic regions with relatively low sea surface temperatures due to upwelling of deep water, are known to enhance noticeably the planetary albedo in the subtropics (Stevens, 2005).

Due to its penetrative nature, the relevance of deep convection in the atmospheric system is even larger. In the absence of baroclinity, it is the main driver of dynamical processes in the tropics, where the net convective heating largely balances the radiative cooling of the atmosphere (e.g. Emanuel et al., 1994; Raymond et al., 2015). In midlatitudes, deep convection is on the one hand often driven by synoptic forcing (e.g Maddox, 1983; Doswell III et al., 1996), but is on the other hand also capable to modulate the large-scale flow (Stensrud and Anderson, 2001). The latter is especially true when deep convection becomes organized as briefly outlined below. Deep convection is therefore known to be the main physical process generating kinetic energy in the atmosphere (Steinheimer et al., 2008).

The reason for this strong dynamical relevance is related to the adjustment process following the vertically extended net heating and drying of the atmosphere. The feedback to deep convection is accompanied by the emission of gravity waves which also stabilize the atmosphere in the vicinity of the deep convective cloud (Bretherton and Smolarkiewicz, 1989). Thus, deep convective clouds have nonlocal effects with the radius of influence being bounded by the so-called (first) baroclinic Rossby radius of deformation L_R (Bretherton et al., 2005). In midlatitudes, the L_R is of $\mathcal{O}(100 - 1000\,\mathrm{km})$ showing that the effect of deep convection can spread over the whole mesoscale, even though being a process on the meso-γ scale. Since L_R depends inversely on the Coriolis parameter f, the horizontal scale of the effects due to deep convection even becomes larger with decreasing latitude until it affects potentially the whole tropical belt.

While isolated convective drafts are a phenomenon on the meso-γ scale, deep convection may also get organized in clusters under favorable conditions (see Houze Jr, 2004, for a comprehensive review). In the tropics, these so called mesoscale convective systems (MCS) are favored during active phases of the Madden-Julian oscillation (MJO), while they may form in front of synoptic-scale troughs during the warm season in the midlatitudes. Vertical wind shear is a prerequisite for MCS which helps to separate the cold downdraft air from the moist and warm air feeding the convective updrafts (Rotunno et al., 1988). Thus, those systems usually constitute of a leading edge with intense updrafts and a large trailing region with weaker, rather stratiform ascent (see Figure 11 in Houze Jr, 2004). Owing to the large amounts of lifted moist air and the accompanied strong midtropospheric heating, these systems also give rise to a pronounced geostrophic adjustment (Paegle, 1978; Chagnon and Bannon, 2005b) in addition to the aforementioned gravity-wave response. The resulting mid-level vortices may then impact on synoptic-scale disturbances of the midlatitudes or tropical wave modes as part of the MJO (e.g. Tromeur and Rossow, 2010; Ahn et al., 2020), while also influencing the development of convection (deep and shallow) on large scales (e.g. Schlemmer and Hohenegger, 2014; Torri et al., 2015).

Thence, moist convection plays a key role in shaping the local and large-scale circulation suggesting that a proper representation in atmospheric models is of

high relevance. Due to the transport of large amounts of moisture with convective clouds and due precipitation, convection is additionally of major relevance for the hydrological cycle (e.g. Hagemann et al., 2006) which also feedbacks strongly on the atmospheric dynamics.

Before passing over to a more quantitative view on moist convection in the next section, the diurnal cycle of convection is presented as another important feature. In the absence of strong synoptic forcing, precipitation typically peaks in the late afternoon or evening over continental areas of the tropics and the summery midlatitudes (Bechtold et al., 2004; Dai et al., 2007). At first glance, the notable time shift with respect to the diurnal cycle of surface fluxes appears to be surprising. Due to the strong latent and sensible heat fluxes destabilizing the atmosphere from the surface, one might expect that convective precipitation is in phase with the sinusoidal course of solar altitude. However, as outlined by Chaboureau et al. (2004), most of the added moisture and heat in the PBL is first balanced by shallow convection which usually already develops in the late morning. Over noon, the shallow convective clouds start to penetrate the capping inversion layer, but dry air aloft still inhibits the development of deep convective clouds. Nonetheless, moistening and heating in the lower part of the free atmosphere helps to reduce the convective inhibition above the PBL. Since this process takes a few hours of time, the instability induced by surface fluxes gets not released completely before the late afternoon/early evening. Indeed, instability of the residual layer keeps on fueling convection over the first half of the night.

Figure 2.2 exemplary shows the diurnal cycle of precipitation for the summer months over Germany derived from the RADKLIM dataset (Winterrath et al., 2017), a rain gauge-adjusted radar product for quantitative precipitation observation by the Deutscher Wetterdienst (engl.: German Weather Service) (DWD) (see Sec. 5.2). Although no separation between convective and stratiform precipitation is made, the diurnal cycle as described above with a maximum in the early evening is visible. This indicates that summery precipitation over Central Europe is largely convectively driven.

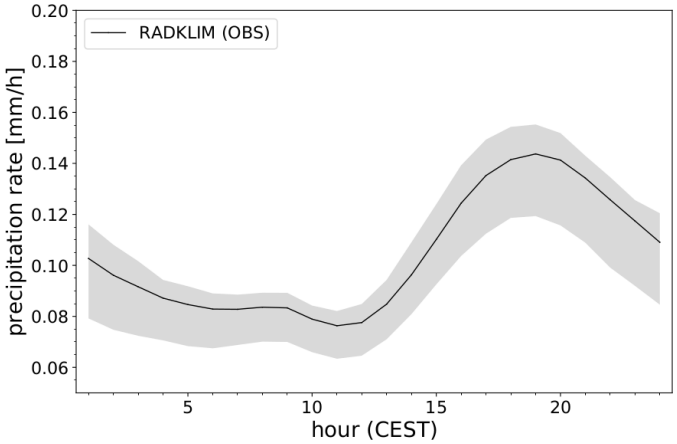

Figure 2.2: Diurnal cycle of domain-averaged hourly precipitation in the summer months June-August over Germany based on 19 years (2001-2019) of RADKLIM data (YW-product). The shaded area indicates the interquartile range of spatial variability. More details on the RADKLIM dataset are provided in Section 5.2.

2.2 A quantitative view on moist convection

Basic dynamics of convective air parcels

In the introduction, atmospheric moist convection has been introduced as buoyant motion of air parcels which are associated with moist air and water phase changes. A convenient way to access the buoyancy of an air parcel is to consider its vertical momentum equation

$$\frac{dw}{dt} = -\frac{1}{\rho}\frac{\partial p}{\partial z} - g, \tag{2.1}$$

where the acceleration of the vertical motion w is determined by the vertical gradient in pressure p and the gravitational force g.

By splitting up the thermodynamic variables on the right hand side (RHS) into a hydrostatic basic state and its perturbation denoted by an overbar and a prime

$$\rho = \overline{\rho} + \rho', \quad p = \overline{p} + p' \quad \text{with} \quad \frac{\partial \overline{p}}{\partial z} = -\overline{\rho} g,$$

one obtains

$$\frac{dw}{dt} \approx \frac{1}{\overline{\rho}}\frac{\partial p'}{\partial z} - \frac{\rho'}{\overline{\rho}} g. \tag{2.2}$$

Note that double products of perturbations are neglected in the given equation for the vertical acceleration of the fluid parcel.

The second term on the RHS constitutes the buoyancy acceleration B. This term can be rewritten by linearizing the ideal gas law

$$\rho = \frac{p}{R_d T_v} \tag{2.3}$$

to get an expression in terms of the virtual temperature T_v:

$$B = -g\frac{\rho'}{\overline{\rho}} = -g\frac{T_v'}{\overline{T_v}}. \tag{2.4}$$

Here, the contribution of the pressure perturbation to the buoyancy has been neglected since it is commonly much smaller than the contribution due to variations in the virtual temperature (Stevens, 2005). The virtual temperature

$$T_v = T(1+\alpha) = T\big(1 + (R_v/R_d - 1)q^v - \sum_{k \neq v,d} q^k\big) \tag{2.5}$$

thereby accounts for the effect of moisture onto density. It is the temperature that dry air would attain if its pressure and density were equal to that of moist air and can be conveniently written with the help of the virtual moisture increment α. The remaining terms constitute the gas constant R_d and R_v for dry air and water vapor, respectively, where the presence of the latter is expressed in terms of the specific water vapor content q^v. Other specific moisture species also contribute to the density effect, that are the liquid and frozen cloud condensate (q^l and q^i) as well as precipitable hydrometeors in form of rain and snow (q^r and q^s).

The most notable effect of moisture on the buoyancy of an air parcel however comes into play when the air parcel becomes subject to phase changes. This happens, for instance, when a near surface air parcel experiences forced lifting when advected over a mountain. While a dry adiabatic displacement may be reversible (stable case), the situation potentially changes when the air gets saturated and condensation results into latent heat release. Depending on the atmospheric stratification of the environment, the air parcel may then become positively buoyant leading to the initiation of a convective updraft. Particularly, it can be shown from Equation 2.2 that the stability property of a vertically displaced air parcel depends on the so-called (moist) Brunt-Väisälä frequency N (N_m) whose sign is given by the vertical change of the ambient (equivalent) potential temperature θ (θ_e) profile (see, e.g., Durran and Klemp, 1982):

$$\text{dry: } N^2 = \frac{1}{\theta}\frac{\partial\theta}{\partial z}\begin{cases} > 0: \text{ stable} \\ = 0: \text{ neutral} \\ < 0: \text{ unstable,} \end{cases} \qquad \text{saturated: } N_m^2 = \frac{1}{\theta_e}\frac{\partial\theta_e}{\partial z}\begin{cases} > 0: \text{ stable} \\ = 0: \text{ neutral} \\ < 0: \text{ unstable.} \end{cases} \tag{2.6}$$

Thus, a negative vertical change in θ_e is a prerequisite for moist convection. It is noted that θ and θ_e given by

$$\theta = T\left(\frac{p_{00}}{p}\right)^{\frac{R_d}{c_p}}, \qquad \theta_e \approx \theta \exp\left(\frac{L_v r_s^v}{c_p T}\right) \tag{2.7}$$

are conserved for dry and moist adiabatic motions, respectively. Thereby, r_s^v denotes the saturation mixing ratio of water for given temperature, while L_v is the latent heat of evaporation and c_p is the specific heat capacity at constant pressure. For the reference pressure, $p_{00} = 1000\,\text{hPa}$ is typically chosen.

Strongly related to the buoyancy and the concept of convection is the so-called Convective Available Potential Energy ($CAPE$). This quantity constitutes the vertical integral of the buoyancy over the layer where a hypothetical air parcel is warmer than the environment, that is $T_v' = T_v^{prcl} > T_v^{env} = \overline{T_v}$. The upper bound of this layer is called the level of neutral buoyancy (LNB).

Conversely, the Convective Inhibition (CIN) denotes the energy which is required to lift the air parcel from the bottom of the unstable layer which is commonly referred as the level of free convection (LFC). Due to the crucial role of moist processes, this level is typically located above the lifting condensation level (LCL).

Formally, $CAPE$ and CIN are given by

$$CAPE = \int_{z(LFC)}^{z(LNB)} B\,\mathrm{d}z = g\int_{z(LFC)}^{z(LNB)} \frac{T_v^{prcl} - T_v^{env}}{T_v^{env}}\,\mathrm{d}z = \int_{p(LNB)}^{p(LFC)} R_d(T_v^{prcl} - T_v^{env})\,\mathrm{d}\ln p, \tag{2.8}$$

$$CIN = -\int_{z_0}^{z(LFC)} B\,\mathrm{d}z = g\int_{z_0}^{z(LFC)} \frac{T_v^{env} - T_v^{prcl}}{T_v^{env}}\,\mathrm{d}z = \int_{p(LFC)}^{p_0} R_d(T_v^{env} - T_v^{prcl})\,\mathrm{d}\ln p, \tag{2.9}$$

where z_0 and p_0 denote the height and pressure of the departure level, respectively.

However, the pure concept of $CAPE$ and CIN is too simplistic in reality since it assumes adiabatic ascent of the convective air parcel without any mixing (see Zhang, 2009, for an analysis on $CAPE$ in the convection framework). This can be readily seen from the following consideration: Let the averaged excess of the air parcel's virtual temperature with respect to the environment be 3 K across a cloud layer of 10 km depth. With $w_c = \sqrt{2CAPE}$, one would attain a value of $w_c = 50\,\mathrm{m/s}$ which is unrealistic large even for strong deep convection[1].

Indeed, the engulfment of environmental air is an important process during convective motions. Turbulent mixing across the lateral boundaries, i.e. entrainment of environmental air and detrainment of cloudy air, dilute the parcel properties. Especially when dry air gets involved, convection can be effectively suppressed due to evaporative cooling (see Fig. 3 and 4 in Zhang, 2009). Thus, turbulent entrainment and detrainment as well as organized entrainment occurring preferably near the cloud base and top (Heus et al., 2008; De Rooy et al., 2013) are considered to be crucial for the development of convection.

Large-scale effects of moist convection

With the basic dynamics of convection in mind, we now turn our attention to the effects of convection. While it is difficult to observe individual convective clouds since they are highly variable in space and time, the effects of a convective clouds collectives on large-scale, the ensemble effect, can be observed with a network of radiosonde stations. A couple of field campaigns have been undertaken in the past to quantify these effects. Among others, the GARP Atlantic Tropical Experiment (GATE) (Polavarapu and Austin, 1979) and the Barbados Oceano-graphic and Meteorological Experiment (BOMEX) (Holland, 1970) constitute prominent field campaigns that have been frequently used for convection monitoring.

The framework for describing the effect of convection on large-scale can be traced back to the study by Yanai et al. (1973) which is revisited in the following. The starting point constitutes the thermodynamic equations of dry static energy $s = c_pT + gz$ and water vapor expressed in terms of the specific humidity q^v. For dry, hydrostatic motions, s is approximately conserved. Adding L_vq^v, the resulting moist static energy h_m is nearly conserved for moist adiabatic motions.

Assuming a region of horizontal area A that is large enough to contain an ensemble of cumulus clouds, the terms in the budget equations undergo a Reynolds averaging procedure in space which is defined by

$$\psi = \overline{\psi} + \psi' \quad \text{with} \quad \overline{\psi} = \frac{1}{A}\int_A \psi \,\mathrm{d}A. \tag{2.10}$$

[1]The mentioned relationship can be derived from Equation 2.2, 2.4 and 2.8.

After applying the Reynolds averaging rules and some rearrangement, one obtains

$$\begin{aligned} \frac{\partial \overline{s}}{\partial t} + \overline{\mathbf{v}_h} \cdot \nabla_h \overline{s} + \overline{\omega} \frac{\partial \overline{s}}{\partial p} &= \overline{Q}_R + L_v(\overline{c^v} - \overline{e^v}) - \frac{\partial \overline{\omega' s'}}{\partial p}, \\ \frac{\partial \overline{q^v}}{\partial t} + \overline{\mathbf{v}_h} \cdot \nabla_h \overline{q^v} + \overline{\omega} \frac{\partial \overline{q^v}}{\partial p} &= -(\overline{c}^v - \overline{e}^v) - \frac{\partial \overline{\omega' q^{v\prime}}}{\partial p}, \end{aligned} \tag{2.11}$$

where $\omega = dp/dt$ is the generalized vertical velocity in pressure coordinates, Q_R denotes the radiative heating rate and c_v and e_v represent the condensation and evaporation rate, respectively. Note that contributions to horizontal eddy fluxes have been omitted[2].

The terms on the left hand side (LHS) of Equation 2.11 are denoted as large-scale terms which can be observed with the help of a radiosonde network. The terms on the RHS are considered to be dominated by convective processes in the area of interest in addition to net radiative fluxes. Yanai et al. (1973) used these terms to define the *apparent heat source* Q_1 and the *apparent moisture sink* Q_2 to describe the large-scale effect of convection:

$$\begin{aligned} Q_1 &= L_v(\overline{c^v} - \overline{e^v}) - \frac{\partial \overline{\omega' s'}}{\partial p} + Q_R, \\ Q_2 &= L_v(\overline{c^v} - \overline{e^v}) + L_v \frac{\partial \overline{\omega' q^{v\prime}}}{\partial p}. \end{aligned} \tag{2.12}$$

Figure 2.3 shows typical profiles of Q_1 and Q_2 together with Q_R for tropical deep convection and shallow convection in the trade wind region. In addition to the vertical extension of the apparent sources, the large-scale effect of both convection types differs substantially from each other.

Apart from the near-surface layer, deep convection is associated with strong drying and warming throughout the troposphere. While the heating attains its maximum in the middle troposphere, the strongest drying effect is located at around 800 hPa. The shift between both is related to the quick reduction in saturation water vapor content with decreasing temperature at higher altitudes. While this places the maximum of condensation near cloud base, the maximum of Q_1 indicates that the convective transport is strongest at mid-tropospheric levels.

By contrast, the apparent heat source in case of shallow convection is weaker in amplitude and constitutes a dipole-structure. While there is heating in the subcloud-layer due to surface fluxes and upward turbulent transports, the upper cloud layer at about 800 hPa is marked by cooling. This cooling is induced by strong moistening due to detrained cloud condensate accompanied by evaporation.

While it has become more common over the last two decades to obtain similar profiles with the help of cloud resolving models or large-eddy simulations (LES), especially for quantifying the large-scale effect of MCS (e.g. Xu et al., 2002; Lang et al., 2003; Liu and Moncrieff, 2007), these profiles have been widely used to tune and adjust convection parametrization schemes in NWP and climate models (e.g.

[2] As noted in ECMWF (2017), Equation 2.11 for the dry static energy is not exact since the production of kinetic energy is excluded. While a better approximation is available in terms of θ from the first law of thermodynamics, this equation is used for convenience.

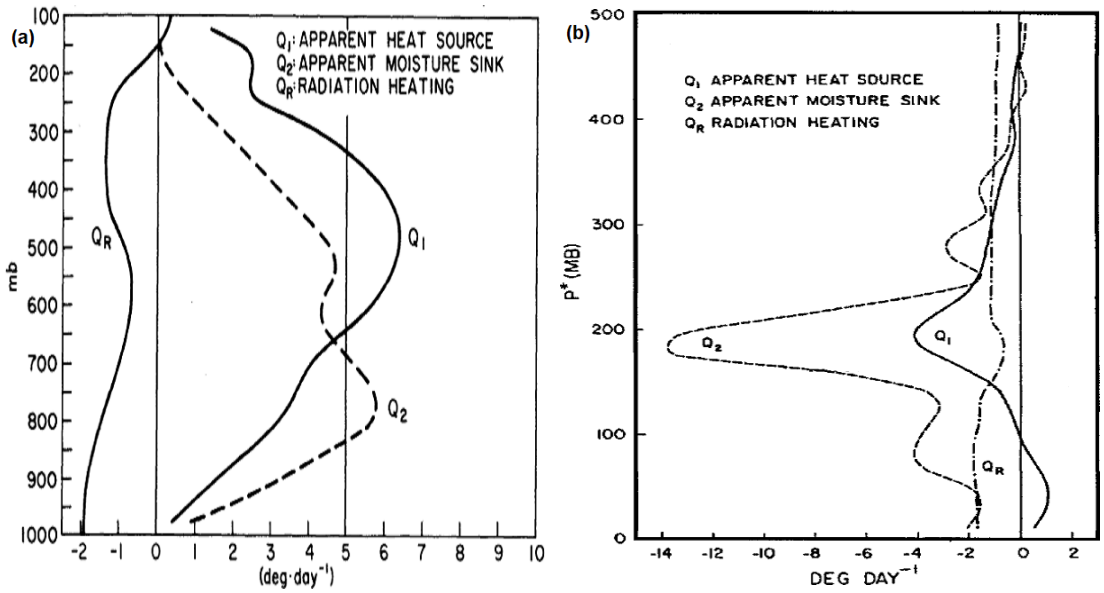

Figure 2.3: Vertical profiles of observed apparent sources for deep (a) and shallow (b) convection during GATE phase III and during BOMEX, respectively. The plots are adopted from (a) Yanai et al. (1973) and (b) Ciesielski et al. (1999), where the latter makes use of data from Nitta and Esbensen (1974). Note that the values of the y-axis in (b) displays the pressure difference with respect to the surface pressure, whereas (a) makes use of pressure levels.

Tiedtke, 1989; Kain and Fritsch, 1990; Bechtold et al., 2001). The principles in the design of such parametrization schemes are reviewed subsequently.

2.3 Parametrization of moist convection in atmospheric models

In general, the task of a convection parametrization schemes in numerical atmospheric models is to estimate the effect of convective clouds that are too small to be resolved explicitly on the model's grid-scale quantities. Given a set of simplifying assumption in order to make the problem traceable, the convective effect is calculated as a function of grid-scale variables provided by the hosting model.

With the general task of a CPS in mind, the parametrization approach can be further decomposed into three steps (e.g ECMWF, 2017):

i) Initiate convection at the correct position in space and time, commonly described by certain trigger conditions/functions.

ii) Compute a vertical profile of the convective transport which redistributes air mass accompanied by (latent) heating/cooling and moistening. This is performed with the help of a cloud model which may also involve convective momentum transport.

iii) Estimate the strength of the convective overturning circulation in order to obtain a closed set of parametrization equations. Commonly, this closure prob-

lem constitutes a link function relating the cloud-base mass flux to available grid-scale quantities which are considered to drive the convective intensity.

In light of the complex dynamical and thermodynamic processes associated with moist convection, it is not surprising that a vast number of different CPS have been developed over the last decades (e.g Arakawa and Schubert, 1974; Betts, 1986; Tiedtke, 1989; Kain and Fritsch, 1990; Bechtold et al., 2001, and many others). The differences pertain all above mentioned sub-steps of the parametrization procedure.

For instance, the cloud model may involve different assumptions on the important mixing of the draughts with the environment. Likewise, the complexity of the incorporated microphysical processes, especially concerning the ice phase, varies remarkably between individual schemes. The specific formulations of the trigger function and the closure usually reflects the modeler's understanding on the processes dominating the initiation of convection and its strength. Thus, various conceptual approaches exist for the trigger functions and the closure assumption, both further reasoning the diversity of existing CPS.

While even a review on the most common approaches is beyond the scope of this work, see e.g. Suhas and Zhang (2014) and Yano et al. (2013) for a comprehensive overview on trigger functions and closure assumptions, respectively, we proceed with the basic framework to determine the effect of convection on the grid-scale quantities of an arbitrary hosting NWP or climate model. This framework already involves a couple of simplifications in order to make the approach computationally feasible. The majority of these simplifications have been well justified in former days when the horizontal grid spacing of numerical atmospheric models was in the order of $\mathcal{O}(100\,\mathrm{km})$ in the late 70s and 80s. However, with the ever increasing computational power and the associated decreasing grid spacing in the models, some of them have become more and more questionable. These simplifications are briefly reviewed and highlighted subsequently and may be seen as a complement to review studies such as Arakawa (2004) and Gross et al. (2018).

A fundamental assumption in practically all (deterministic) CPS is that the collective effects of an ensemble of convective clouds on the grid-scale quantities is targeted. In light of this, it is common practise to tackle the parametrization problem with the help of the mass flux approach together with the Reynolds averaging procedure (see Eq. 2.10). With the assumption that the horizontal area covered by a grid box A_g is large enough to contain an ensemble of convective clouds, the area-averaged quantity of interest $\overline{\psi}$ is assigned to the grid-scale quantity of the model. Although this becomes evidently questionable with increasing resolution of numerical models, this procedure as described, for instance, in Arakawa and Schubert (1974), Anthes (1977) or Tiedtke (1989) still serves as the basis for contemporary CPS.

The starting point of the mass flux approach constitutes the quasi- Boussinesq form of the continuity equation, where the density ρ is assumed to vary in vertical direction only. After Reynolds averaging, this equation reads

$$\nabla \cdot (\rho \overline{\mathbf{v}_h}) + \frac{\partial}{\partial z} (\rho \overline{w}) = 0. \tag{2.13}$$

The net vertical mass flux $\rho\overline{w}$ can be splitted into a convective part, the convective mass flux per unit area m_c, and an environmental part m_e:

$$\rho\overline{w} = m_c + m_e. \tag{2.14}$$

The sign of these three terms does not necessarily be equal. Indeed, m_c is positive and typically exceeds the net vertical mass flux in a convective regime, while environmental subsidence $m_e < 0$ occurs.

With the application of the Reynolds averaging procedure, the convective flux of the dry static energy can also be related to its net vertical flux:

$$\begin{aligned} \rho\overline{w's'} &= \rho\overline{ws} - \rho\overline{w}\,\overline{s} \\ &= m_c s_c + m_e s_e - \rho\overline{w}\,\overline{s}. \end{aligned} \tag{2.15}$$

Here, s_c and s_e correspond to the (averaged) dry static energy of all convective clouds and of the environment, respectively.

This equation can then be further decomposed to contributions of individual convective clouds in the ensemble (see Fig. 2.4 for an illustration). Assigning individual clouds with a subscript i, Equation 2.15 can be written as

$$\begin{aligned} \rho\overline{w's'} &= \sum_i \rho\sigma_i \left[w_i(s_i - \overline{s}) - w_e(s_i - s_e) \right] \\ \text{with} \quad m_c &= \sum_i \rho\sigma_i w_i \\ \text{and} \quad \overline{s} &= (1-\sigma_c)s_e + \sum_i \sigma_i s_i \quad \text{where} \ \sum_i \sigma_i = \sigma_c. \end{aligned} \tag{2.16}$$

Here, σ_i (σ_c) corresponds to the fractional area of individual (all) convective clouds. Apart from the Reynolds averaging procedure in a quasi-Boussinesq flow, no further approximation is involved so far.

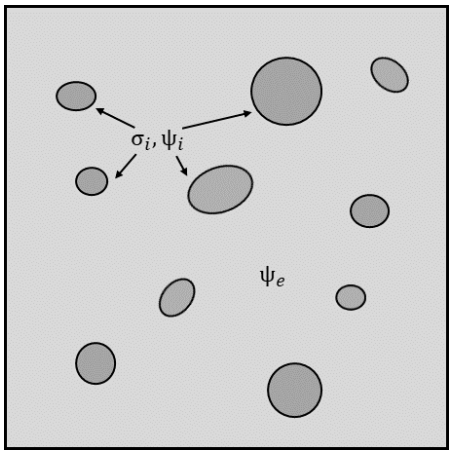

Figure 2.4: Ensemble of cumulus clouds in a grid box with area A_g. The individual clouds with fractional coverage σ_i are highlighted in dark gray. While these clouds carry the generic property ψ_i (e.g. w_i), the environmental, non-convective air is characterized by ψ_e.

However, in order to arrive at the conventional mass flux formulation, the following simplifications are made on top:

i) It is assumed that the fractional area covered by cumulus clouds is small, that is:

$$\sum_i \sigma_i = \sigma_c << 1 \quad \Rightarrow \quad (1 - \sigma_c) \approx 1. \tag{2.17}$$

As result of the *small-area approximation*, environmental and grid-scale quantities are set equal to each other. However, the vertical wind in the convective drafts w_i is assumed to be much larger than its environmental complement w_e.

ii) The individual clouds are assumed to be in steady-state. Thus, no (at least) explicit temporal dependencies are taken into account and the CPS becomes diagnostic.

iii) The bulk mass flux approach is used. This means that the individual convective clouds are collocated together and represented by a representative plume with only one value for each relevant thermodynamic quantity.

iv) Internal variability of the clouds is neglected which is commonly called the *top hat*-approximation. Note that this assumption is also related to the preceding bulk approach.

With these approximations, Equation 2.16 reduces to

$$\rho\overline{w's'} \approx \rho\sigma_c w_c(s_c - \overline{s}) = m_c(s_c - \overline{s}) \tag{2.18}$$

where the convective quantities have to be parametrized by the CPS while $\overline{s}$ is obtained from the model. Note that it is straightforward to derive analogous equations for other quantities of interest, such as q^v for the apparent moisture sink, but also for the horizontal momentum $\rho\mathbf{v}_h$.

The large-scale effect of cumulus convection on the dry static energy s is then obtained by inserting Equation 2.18 in the formula for Q_1 (see Eq. 2.12). After subtracting the radiative contribution, one obtains[3]

$$\left.\frac{\partial s}{\partial t}\right|_{conv} \equiv Q_1 - \overline{Q}_R = -\frac{1}{\rho}\frac{\partial}{\partial z}\left(m_c[s_c - \overline{s}]\right) + L_v(\overline{c^v} - \overline{e^v}), \tag{2.19}$$

$$\frac{\partial m_c}{\partial z} = \epsilon - \delta, \tag{2.20}$$

$$\frac{\partial}{\partial z}(m_c s_c) = \epsilon\overline{s} - \delta s_c + L_v(\overline{c^v} - \overline{e^v}), \tag{2.21}$$

where the two latter equations complement the equation system for the dry static energy. Here, ϵ and δ denote the fractional entrainment and detrainment rates per unit length (in m^{-1}), respectively. Note that both equations are subject to the cloud model of the CPS, while the first equation is used to couple the CPS with a hosting model.

[3]The transformation of the vertical coordinate from the p into the z-system is straightforward and therefore omitted here.

For interpretation purposes, the Eqs. 2.19–2.21 can be combined to yield

$$\left.\frac{\partial s}{\partial t}\right|_{conv} = m_c \frac{\partial \overline{s}}{\partial z} + \delta(s_c - \overline{s}). \tag{2.22}$$

Thus, convection affects the static energy on grid-scale by compensating subsidence (first term) and detrainment of convective air mass (second term). The latent heating terms are not explicitly part of Equation 2.22, but they crucially modulate the dry static energy within the convective drafts.

A conceptual illustration of the conventional convection parametrization approach is depicted in Figure 2.5. The representative plume consists of a parametrized up- and downdraft which interact with the grid-scale environment by turbulent mixing and organized inflow/outflow. The parametrized dynamics of the convective plume that are represented by gray arrows also involve environmental subsidence.

It is noted that the conventional mass flux approach constitutes a locally closed mass system which can be considered as a direct consequence of the quasi-Boussinesq approximation used in Arakawa and Schubert (1974). In case that the mass flux approach is derived in the p-coordinates involving the hydrostatic approximation (see, e.g., Betts, 1986), Reynolds averaging directly yields a closed equation system with respect to mass. Thus, this property is considered to be inherent for the conventional cumulus parametrization approach.

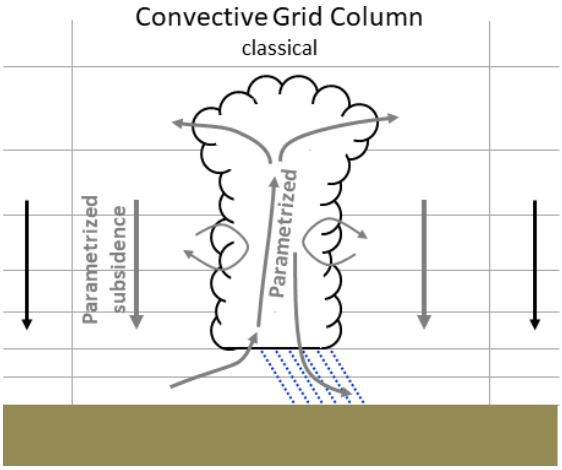

Figure 2.5: Illustration of a representative convective plume and handling of the related dynamics with the conventional mass flux approach. Parametrized (grid-scale) dynamics are indicated by gray (black) arrows, while microphysical processes are symbolically sketched by the cloud and the falling precipitation below cloud base. Note that ambient grid-scale subsidence is common, but not necessary.

2.4 Parametrization challenges of the convective gray-zone

As already mentioned in the preceding text, fundamental assumptions in the conventional convection parametrization approach become questionable with increasing spatio-temporal resolution of atmospheric models.

Nowadays, the spatial resolution of many operational NWP and regional climate models have entered the so-called gray-zone of deep convection (e.g. Prein et al., 2015). With grid spacings in the order of $\Delta x \sim 2-10\,\mathrm{km}$, deep convection is neither a completely subgrid-scale nor a grid-scale process. This results into a potential competition between explicitly and parametrized moist convection which imposes a couple of challenges in contemporary CPS in light of the basic simplifications mentioned above (Gross et al., 2018). In analogy, there also exists a gray-zone of shallow convection. However, due to its smaller vertical and horizontal extent, it still constitutes a subgrid-scale process with $\Delta x \sim 2-10\,\mathrm{km}$ to a good approximation[4]. Thus, the parametrization of deep convection attains considerable attention for applications in operational NWP and climate models at present.

Instead of rebuilding parametrization schemes, existing CPS have commonly been modified and tuned steadily to relax questionable simplifications. While most of the relaxation techniques can be traced back to the approximations listed in the previous section, even more subtle conceptual problems arise at gray-zone resolutions. Some of the tackled challenges are outlined briefly in the following.

It is well known that the grid boxes in many atmospheric models are too small to occupy a sufficiently large ensemble of convective clouds (Arakawa and Jung, 2011). As a consequence, the modeled variability in convective precipitation is typically too small at higher resolutions compared to observations (Stephens et al., 2010). As argued by Plant and Craig (2008), a possible way to mitigate this deficiency is to introduce a stochastic closure assumption in place of a deterministic one. By varying randomly the strength of the parametrized convection, consistent variability can be achieved across a broad range of grid spacings (Keane et al., 2014) which is also considered to beneficial for representing low-frequency features in the tropics (e.g. Horinouchi et al., 2003).

Other approaches to mitigate the subsampling problem are more heuristic and may include tuning the entrainment and detrainment rates. While mixing with the environment crucially affects the updraft air, empirical approaches exist to imitate this process for an ensemble of convective plumes (see, e.g, Bechtold et al., 2008 and the appendix of Bechtold et al., 2014b). In order to hamper the parametrized convective activity at resolutions where the separation between grid- and subgrid-scale convective dynamics becomes blurry, larger values of the tuneable mixing parameters are typically chosen.

The steady-state assumption is also apparently questionable at higher spatio-temporal resolutions. In general, a diagnostic scheme is barely able to represent the evolution of convective clouds such as the transition of shallow convection to deep cumulus clouds (see, e.g., Gerard and Geleyn, 2005; Rio et al., 2019). When a convective grid column is triggered, the convection and its effects are instantaneously established without any explicit evolution of the characteristic life cycle. Likewise, the advection of convective cells with the mean flow as well as propa-

[4]It is noted that some modern limited area models are already operating with grid spacings smaller than 2 km. So these models have crossed the gray-zone of deep convection, but entered the gray-zone of shallow convection and PBL turbulence. Even though there are shared problems, they are not targeted in this thesis. An overview can however be obtained from Wyngaard (2004) and Boutle et al. (2014)

gating cold pools which favor the triggering of secondary cells are hardly captured with such approaches. However, these processes are crucial for representing the diurnal cycle of convection (see, e.g., Rio et al., 2009; Grandpeix and Lafore, 2010; Rio et al., 2013) and its mesoscale organization (e.g. Torri et al., 2015). Especially the latter process is of particular importance since modelling errors can upscale onto synoptic scales (see Sec. 1.1).

In light of this, so-called prognostic CPS have been developed in the last two decades which introduce explicit temporal dependencies commonly referred as *convective memory* in the parametrization schemes (see, e.g., Gerard and Geleyn, 2005; Park, 2014). Although being appealing, this approach come at the price of high computational costs of a prognostic scheme which currently often thwarts their application in operational NWP models.

Over the recent years, an approach by Arakawa and Wu (2013) tackling explicitly the small-area approximation has attained a lot of attention. Their *unified parametrization* framework eliminates this assumption from the beginning and turns the convective area fraction σ_c to a key parameter ensuring a smooth transition to explicit representation of deep convection with increasing resolution. With the help of idealized cloud-resolving model simulations, they demonstrate that the σ_c-dependency of the convective transport is given by a quadratic function and also suggest a flexible closure for σ_c which does not explicitly depend on the grid spacing. However, in practical applications the closure for the convective area fraction often comprises at least a partial explicit dependency on the grid spacing (e.g. Grell, Freitas, et al., 2014; Han et al., 2017; Kwon and Hong, 2017). Regardless of the specific approach to determine σ_c, the unified parametrization framework inhabits an important property by definition, that is a full representation of convective processes on grid-scale in the cloud-resolving limit.

The desired smooth transition towards an explicit representation of convection at high resolutions does not only affect the convective transport, but also the handling of the microphysical effects in convective clouds. Over the recent years and decades, the complexity of microphysical schemes computing the formation and evolution of condensed water species on grid-scale has been drastically expanded (see, e.g., Morrison and Gettelman, 2008; Seifert, 2008). These schemes are nowadays capable to simulate complex interactions between different water species such as accretion, aggregation and riming. By contrast, the microphysical processes in CPS are rather crudely handled although some effort has been made to refine cloud microphysical processes in parametrized convective clouds (e.g. Fowler and Randall, 2002; Del Genio et al., 2005; Song and Zhang, 2011). In order to avoid spurious competition between grid-scale and convective precipitation/ cloud formation, Wu and Arakawa (2014) suggest a unified microphysical scheme.

Another questionable assumption with decreasing grid spacing in atmospheric models pertains the locally closed mass system of the classical parametrization framework. Tackling this conceptual limitation is of central interest in this thesis and will be discussed extensively in the first part of the next chapter. However, before passing over to the so-called hybrid parametrization approach, the Bechtold-Tiedtke scheme will be introduced in the final section of this chapter.

2.5 Description of the Bechtold-Tiedtke scheme

The CPS used operationally in the ICOsahedral Non-hydrostatic (ICON) model was adopted from the Integrated Forecasting System of the European Centre for Medium-Range Forecasts. The scheme is based on the work by Tiedtke (1989) and has been continuously developed in the IFS model over the last three decades. After first updates by Gregory et al. (2000) and Jakob and Siebesma (2003), further substantial changes by Peter Bechtold and his colleagues (Bechtold et al., 2004; Bechtold et al., 2008, 2014b) were integrated in order to make the scheme applicable in the IFS model with a grid spacing of $\Delta x \sim 10\,\mathrm{km}$. The basic features of the resulting Bechtold-Tiedtke scheme are rendered in the following. While a detailed description of the scheme in the IFS model can be obtained from Bechtold (2017), some ICON-specific details will be given in Section 5.1.

2.5.1 The cloud model of the Bechtold-Tiedtke scheme

The Bechtold-Tiedtke scheme makes use of the bulk mass flux approach and comprises a diagnostic entraining/detraining plume cloud model. The two basic types of moist convection, that are shallow and deep convection, are subject to the parametrization scheme which computes the effect of convection on the grid-scale variables of the hosting atmospheric model with the help of the conventional Reynolds averaging procedure presented in Section 2.3. In addition to the convective forcing on the dry static energy s and the specific water vapor content q^v, convective momentum transport as well as detrainment of liquid and frozen condensate in terms of $q^{l,r}$ and $q^{i,s}$ are computed. Apart from a decomposition into up- and downdrafts, the associated equations are formulated in analogy to Equation 2.19.

As a first step in the parametrization algorithm, each grid column is checked for the occurrence of shallow convection. A test parcel is formed in the surface layer and receives a temperature and moisture perturbation which depends on the underlying surface fluxes. This test parcel is then lifted under strong entrainment (further details on volume mixing are given below) up to the LCL. During its subcloud ascent, the vertical updraft wind w_u is calculated from the updraft kinetic energy K_u which is computed by

$$\frac{\partial K_u}{\partial z} = -\frac{e_u}{m_u}(1+\beta c_d)2K_u - \frac{g}{f_t(1+\gamma)}B; \quad w_u = \sqrt{2K_u}. \tag{2.23}$$

Here, the entrainment rate of the updraft $e_u = m_u/\rho\epsilon_u$ is now given in s^{-1}. The first term involving $\beta = 1.875$ and the drag coefficient $c_d = 0.506$ accounts for the dilution due to entrained air, while $f_t = 2$ is set to reduce the buoyancy effect in highly turbulent flow. A further correction to the buoyant acceleration is included with the virtual mass coefficient $\gamma = 0.5$ to mimic non-hydrostatic pressure perturbations (Kuo and Raymond, 1980).

In case that $w_u(z(LCL))$ is positive, the ascent is continued until the kinetic updraft energy is exhausted at the cloud top level (CTL). If the (hydrostatic) pressure difference between CTL and LCL Δp_{cl} is smaller than 200 hPa, shallow convection is allowed to occur.

Afterwards, the conditions for penetrative convection are checked, where two different subtypes of deep convection are possible. The first subtype is called *surface-based* deep convection which roots in the first 60 hPa above surface and involves a 30 hPa mixed layer. Fixed temperature and moisture perturbations are added to the weakly entraining plume and again a check on w_u at LCL decides if convection is allowed to occur. Furthermore, the cloud depth Δp_{cl} now has to exceed the threshold of 200 hPa. If the minimum cloud depth for penetrative convection is not attained, the test is repeated from elevated departure levels.

When the departure level is placed above the first 60 hPa of the model atmosphere, the occurrence of *midlevel* convection is tested. This second subtype of penetrative convection is initiated with air from individual model layers instead of being formed from mixed layers. Additionally, the closure assumption for midlevel convection differs from surface-based deep convection as outlined below. In case that a penetrative convective test parcel is found in the first 300 hPa of the atmosphere, this solution replaces the shallow convection profile from the first step.

Parametrization of the convective updraft

During ascent, the thermodynamic properties and the mass flux of the updraft (denoted with the subscript u) are computed with the help of the following equation system of the cloud model. The updraft mass flux per unit area m_u and the dry static energy of updraft air s_u are given by

$$-g\frac{\partial m_u}{\partial p} = e_u - d_u, \tag{2.24}$$

$$-g\frac{\partial}{\partial p}(m_u s_u) = e_u s_u - d_u \overline{s} + L_v c_u + L_f G_u^{l\to i}, \tag{2.25}$$

where c_u^v denotes the updraft condensation rate, d_u the updraft detrainment rate and L_f stands for the latent heat of fusion.

The specific moisture species which coexist in all phases (q^v, q^l and q^i) including precipitable hydrometeors (q^r and q^s) are computed with the help of

$$-g\frac{\partial}{\partial p}(m_u q_u^v) = e_u \overline{q^v} - d_u q_u^v - c_u^v, \tag{2.26}$$

$$-g\frac{\partial}{\partial p}(m_u q_u^{l,i}) = -d_u q_u^{l,i} + c_u^v - G_u^{(l,i)\to(r,s)} \mp G_u^{l\to i}, \tag{2.27}$$

$$-g\frac{\partial}{\partial p}(m_u q_u^{r,s}) = -d_u q_u^{r,s} + G_u^{(l,i)\to(r,s)} - F_{u\to d}. \tag{2.28}$$

In the cloud model equations, the overbar indicates grid-scale quantities. Additionally, $G_u^{(l,i)\to(r,s)}$ denotes the conversion of cloud condensate to precipitation, while $G_u^{l\to i}$ denotes the freezing rate. The term $F_{u\to d}$ represents the fallout of precipitable hydrometeors from the updraft.

The involved microphysical processes (condensation, freezing, precipitation formation) are thereby parametrized in a strongly simplified way: The condensation rate c_u^v is obtained from a saturation adjustment procedure which removes supersaturation of the updraft air during its ascent. The glaciation of cloud water

depends on the updraft temperature, where the fraction of the frozen phase is assumed to increase quadratically between the freezing point and −38°C. The conversion of cloud condensate to precipitation is parametrized following Sundqvist (1978):

$$G_u^{(l,i)\to(r,s)} = \frac{m_u}{\overline{\rho}} \frac{c_{pr}}{0.75 w_u} q_u^{l,i} \left[1 - \exp\left\{ - \left(\frac{q_u^{l,i}}{q_{crit}^{l}} \right)^2 \right\} \right]. \tag{2.29}$$

Here, $c_{pr} = 1.5 \times 10^{-3}\,\mathrm{s}^{-1}$ denotes the auto-conversion coefficient, while $q_{crit}^{l} = 5 \times 10^{-4}\,\mathrm{kg\,kg}^{-1}$ is the critical cloud water content. The effect that less coalescence-collision and aggregation takes place with decreasing residence time of the updraft air in a specific model layer is imitated by setting the conversion process inversely proportional on w_u. The related maximum value of w_u is set to $10\,\mathrm{m\,s}^{-1}$.

The updraft velocity also affects the fallout of precipitable hydrometeors which transfers rain and snow from the up- to the downdraft. As can be seen from

$$F_{u\to d} = \frac{g}{\Delta p} m_u \frac{V_t}{w_u} q_u^{r,s} \quad \text{with } V_t = 21.18 \left(q_u^{r,s} \right)^{0.2}, \tag{2.30}$$

the transfer again decreases with increasing w_u since more hydrometeors can then be carried with the updraft air. The terminal velocity V_t is depending on the specific precipitation content in order to mimic the effect of larger hydrometeors that attain higher falling speed.

In addition to the convective transport of dry static energy and moisture, horizontal momentum transport is part of the CPS. The cloud model equation is formulated in analogy to the other relevant quantities, but without the occurrence of internal source terms:

$$-g \frac{\partial}{\partial p} (m_u \mathbf{v}_{h,u}) = e_u^{\star} \mathbf{v}_{h,u} - d_u^{\star} \overline{\mathbf{v}_h}. \tag{2.31}$$

However, the horizontal momentum is known to be affected by horizontal pressure gradient forces across the draughts which acts to push the in-cloud profile towards the ambient horizontal wind shear (Gregory et al., 1997). This effect is implicitly considered by increasing the entrainment and detrainment rate which are therefore denoted with a star in Equation 2.31.

Apart from the artificially increased mixing rates for the horizontal momentum in the updraft, the updraft entrainment and detrainment rates depend on the ambient relative humidity $\overline{RH}$ and on the type of convection. The entrainment rate which is applied for positively buoyant updraft air is given by

$$e_u = \epsilon_1 \frac{m_u}{\rho} (1.3 - \overline{RH}) \left(\frac{q_{sat}^{v}(\overline{T})}{q_{sat}^{v}(\overline{T}(z(LCL)))} \right)^3, \tag{2.32}$$

where the saturation specific water vapor content q_{sat}^{v} is a function of the ambient temperature. By taking the ratio against the saturation water vapor content at the LCL, the entrainment rate typically decreases with height. This effect is further enforced due to the exponent so that convective clouds entrain preferably near cloud base. The second term on the RHS thereby favors dilution in dry environmental situations. With the two scaling terms on the RHS exhibiting a strong

height and ambient moisture dependence, the effects of a cumulus cloud ensemble is mimicked (Bechtold et al., 2014b). The resulting entrainment profiles are considered to resemble the entrainment rate profiles obtained by the LES study by Derbyshire et al. (2011). While the base fractional entrainment rate ϵ_1 attains a value in the order of $1 \times 10^{-3}\,\mathrm{m}^{-1}$ for penetrative convection (with higher values for increasing horizontal resolution, cf. Bechtold et al. (2008) and Bechtold et al. (2014b)), its value is doubled for shallow convective clouds, i.e $\epsilon_1^{shal} = 2\epsilon_1^{deep}$.

The detrainment rate in the Bechtold-Tiedtke scheme also depends on the environmental moisture profile and can be written for shallow and penetrative convective clouds as

$$d_u = \delta_1 \frac{m_u}{\rho}(1.6 - \overline{RH}). \tag{2.33}$$

For penetrative convection, a constant base fractional detrainment rate $\delta_1^{deep} = 0.75 \times 10^{-4}\,\mathrm{m}^{-1}$ is set. Due to the absent decreasing scaling factor with height (cf. Eq. 2.32), detrainment may become dominant in the upper parts of penetrative convective clouds. However for shallow convection, the detrainment rate is directly proportional to the entrainment rate such that $d_u^{shal} = e_u^{shal}$ is imposed.

Above the LNB, entrainment is assumed to be zero, while organized detrainment occurs to dissolve the updraft plume. In order to do so, the decrease in updraft mass flux is set proportional to the change in kinetic updraft energy with height. Together with Equation 2.23, the organized detrainment rate $d_{u,org}$ reads

$$d_{u,org} = \frac{g}{\Delta p} m_u \frac{1}{\sqrt{\frac{K_u(z)}{K_u(z+\Delta z)}}} \left(1 - \frac{K_u(z)}{K_u(z+\Delta z)}\right), \tag{2.34}$$

where Δp and Δz denote the layer depth in pressure and height coordinates, respectively. Thus, overshooting tops aloft the equilibrium level are enabled, where the depth of organized updraft detrainment layer crucially depends on the ambient atmospheric stratification.

Parametrization of the convective downdraft

Convective downdrafts are associated with negatively buoyant air masses that are fueled with precipitation provided by the updraft. In the Bechtold-Tiedtke scheme, no explicit distinction between shallow and penetrative convection is made in with respect to precipitation formation. This means, that even shallow convective clouds form precipitation, albeit its formation is limited due to the small vertical extent and the stronger mixing with the environment which effectively dries the updraft air. The rationale for this is supported by observations of slightly precipitating shallow convection over the subtropical ocean (e.g Rauber et al., 2007). Thence, every type of convection is assumed to form a convective downdraft originating at the so-called level of free sinking (LFS). This level constitutes the highest model layer where a mixture of updraft and environmental air becomes negatively buoyant due to evaporation and melting of cloud condensate and precipitation particles. The downdraft mass flux m_d is then set proportional to the updraft mass flux at the cloud base $m_u(z(LCL))$ which is given by the closure assumption

(see below):

$$|m_d(z(LFS))| = \lambda_u m_u(z(LCL)) \quad \text{with } \lambda_u = 0.3; \quad m_d(z(LFS)) < 0. \tag{2.35}$$

The thermodynamical properties and the dynamics of the downdraft air are computed in analogy to updraft except that evaporation and melting instead of condensation and freezing drive the downdraft. For instance, the equation for the specific humidity is given by

$$-g\frac{\partial}{\partial p}(m_d q_d^v) = e_d\overline{q^v} - d_d q_d^v + e_d^v, \tag{2.36}$$

where e_d^v denotes the downdraft evaporation rate. Within the convective cloud, i.e. above the LCL, e_d^v is specified with the help of saturation adjustment which retains saturation during descent.

Below the cloud base, an empirical evaporation profile is imposed where evaporation increases with decreasing height as well as drier environment. Besides, it is generally stronger over land compared to water surfaces. Simultaneously, linear organized detrainment is enforced over the lowest 50 hPa of the subcloud layer.

2.5.2 Closure assumptions

In order to determine the convective mass flux, different closure assumptions are applied for the three types of convection in the Bechtold-Tiedtke scheme.

For near-surface rooted deep convection, the closure follows the concept of quasi-equilibrium that has been introduced by Arakawa and Schubert (1974) and which is widely used in contemporary CPS (see, e.g., Yano et al., 2013, for a review). In short, this concept states that the stabilizing effect of convection on the atmospheric stratification is in quasi-equilibrium with the forcing due to mean advection and other processes than convection. In the Bechtold-Tiedtke scheme, a density-weighted form of convective available potential energy $PCAPE$ is used to quantify stabilization and destabilization. Based on the definition of $CAPE$ in Equation 2.8 and using the hydrostatic approximation, $PCAPE$ is given by

$$PCAPE = \int_{p(CTL)}^{p(LCL)} \frac{T_{v,u} - \overline{T_v}}{\overline{T_v}}\,\mathrm{d}p, \tag{2.37}$$

where $T_{v,u}$ now corresponds to the virtual temperature in an entraining updraft plume. It is also noted that the integral of the (density-weighted) buoyancy over the whole convective cloud is considered.

An explicit relation to the mass flux at cloud base is then obtained by taking the local time derivative of $PCAPE$ and splitting up the resulting tendency into a forcing and convective term:

$$\frac{\partial}{\partial t}PCAPE = \frac{\partial}{\partial t}PCAPE\Big|_{frc} + \frac{\partial}{\partial t}PCAPE\Big|_{conv}. \tag{2.38}$$

The (net) forcing on $PCAPE$ constitutes advective processes, radiative cooling of the atmosphere and production of $PCAPE$ due to PBL processes other than convection such as surface enthalpy fluxes directed into the atmosphere.

The convective $PCAPE$-tendency can be expressed in two ways, that is with the help of a relaxation term and with the help of the assumption that convection balances the forcing predominately through environmental subsidence. While the former leads to the introduction of a convective time-scale τ_c over which $PCAPE$ is relaxed towards a reference value $PCAPE_{ref}$, the latter involves the net convective mass flux $m_c = m_u + m_d$ as shown in Gregory et al. (2000):

$$\frac{\partial}{\partial t} PCAPE\big|_{cu,1} = -\frac{PCAPE - PCAPE_{ref}}{\tau_c}, \tag{2.39}$$

$$-\frac{\partial}{\partial t} PCAPE\big|_{frc} \approx \frac{\partial}{\partial t} PCAPE\big|_{cu,2} = -g \int_{z(LCL)}^{z(CTL)} \frac{m_c}{\overline{T_v}} \left(\frac{\partial \overline{T_v}}{\partial z} + \frac{g}{c_{pd}} \right) \mathrm{d}z. \tag{2.40}$$

Equating out both expressions for the convective tendency, the final cloud base mass flux is obtained by

$$m_u\left(z(LCL)\right) = m_u^\star(z(LCL)) \frac{PCAPE - PCAPE_{ref}}{\tau_c} \left\{ g \int_{z(LCL)}^{z(CTL)} \frac{m^\star}{\overline{T_v}} \left(\frac{\partial \overline{T_v}}{\partial z} + \frac{g}{c_{pd}} \right) \mathrm{d}z \right\}^{-1}. \tag{2.41}$$

Here, $m^\star(z)$ denotes the normalized mass flux profile which is obtained by probing the computations in the cloud model with an initial value of the mass flux at cloud base $m_c^\star(z(LCL))$. It is related to the total convective mass flux m_c by the closure factor which reads

$$m(z) = \frac{m_c(z(LCL))}{m_c^\star(z(LCL))} m^\star(z).$$

Albeit being widely used in contemporary CPS, the original quasi-equilibrium assumption with $PCAPE_{ref} = const.$ is known to be improper over the continental tropics and midlatitudes. As argued in Zhang (2002) and Donner and Phillips (2003), the reason for this can be attributed to the strong boundary-layer control on $CAPE$ over land where destabilization is largely driven by surface fluxes. As a result, CPS schemes using quasi-equilibrium in their closure assumption typically produce a daily cycle in precipitation that follows the daily cycle of solar irradiation, even when the observed diurnal cycle shows a maximum in the later afternoon or evening (e.g. Bechtold et al., 2004; Dai, 2006; Brockhaus et al., 2008).

In the Bechtold-Tiedtke scheme, the rapidly varying boundary-layer forcing is explicitly taken into account by adapting $PCAPE_{ref}$ in a dynamical manner. Using

$$PCAPE_{ref} = PCAPE_{PBL} = \frac{\tau_{PBL}}{T^\star} \int_{p(LCL)}^{p(z_{sfc})} \left. \frac{\partial \overline{T_v}}{\partial t} \right|_{PBL} \mathrm{d}p, \tag{2.42}$$

where $\partial \overline{T_v}/\partial t\big|_{PBL}$ comprises the virtual temperature tendency due to PBL processes other than convection (i.e. mean advection, turbulence and radiation), only the free-tropospheric part of $PCAPE$ is used in Equation 2.39 as long as the subcloud layer in the PBL is heated. Thus, the classical quasi-equilibrium assumption is effectively relaxed until the PBL reaches an equilibrium. As demonstrated in

Bechtold et al. (2014b), this approach improves remarkably the representation of the diurnal cycle in the global IFS model (see their Fig. 5).

The remaining quantities in Equation 2.42 constitute the temperature scale $T^\star$ and the characteristic PBL time scale τ_{PBL}. With $T^\star = 1\,K$, the overall scaling is performed via τ_{PBL} for which different time scales are chosen over continental and maritime regions:

$$\tau_{PBL} = \begin{cases} \tau_c & \text{land} \\ \frac{z(LCL)-z_{sfc}}{\overline{u}_{PBL}} & \text{water.} \end{cases}$$

From similarity theory, this means that the τ_{PBL} over water is set to the horizontal advective time scale depending on the average wind speed in the PBL $\overline{u}_{PBL}$. Over land, it is assumed that the PBL gets adjusted through the heat transports of the convective draughts. The associated turnover time scale τ_c is thereby chosen to be dependant on the model's grid spacing via $f(\Delta x)$ in order to enhance the scale adaptivity of the scheme:

$$\tau_c = \tau_{c,0}\,\frac{D_{cl}}{\overline{w}_u^D} f(\Delta x).$$

Here, D_{cl} denotes the depth of the convective cloud over which the updraft velocity is averaged to yield $\overline{w}_u^D$.

For penetrative convection rooted aloft the 50 hPa surface layer, the convective mass flux is set proportional to the grid-scale vertical velocity $\overline{w}$ at cloud base

$$m_u\left(z(LCL)\right) = \overline{\rho}\,\overline{w}\Big|_{z=z(LCL)}. \tag{2.43}$$

Thus, it is assumed that midlevel convection is accompanied by grid-scale horizontal convergence below the convective cloud-base. Additionally, the atmosphere must be sufficiently moist with $\overline{RH} > 80\,\%$ at the cloud base.

For shallow convective clouds ($\Delta p_{cl} < 200\,\text{hPa}$), a balance between PBL forcing due to non-convective and convective processes in the subcloud layer is assumed. However, instead of using $PCAPE$ as a diagnostic quantity for convective intensity, the moist static energy $h_m = s + L_v q^v$ is chosen. Assuming that shallow convection vents the subcloud layer while being fueled by processes other than convection, one arrives at

$$\int_{p(z(LCL))}^{p(z_{sfc})} \left.\frac{\partial \overline{h_m}}{\partial t}\right|_{conv} \mathrm{d}p = -\int_{p(z(LCL))}^{p(z_{sfc})} \left.\frac{\partial \overline{h_m}}{\partial t}\right|_{noconv} \mathrm{d}p. \tag{2.44}$$

With vanishing convective mass fluxes at the surface, the cloud base mass flux is then given by

$$m_u(z(LCL)) = \frac{1}{g\left(h_{m,u}(z(LCL)) - \overline{h_m}(z(LCL))\right)} \int_{p(z(LCL))}^{p(z_{sfc})} \left.\frac{\partial \overline{h_m}}{\partial t}\right|_{noconv} \mathrm{d}p. \tag{2.45}$$

The term $\partial\overline{h_m}/\partial t\big|_{noconv}$ comprises tendencies of grid-scale moist static energy due to mean advection, radiation, turbulence and surface fluxes.

All together, the different closure assumptions used in the Bechtold-Tiedtke scheme are designed to provide convective fluxes that adapt flexibly to different synoptic and boundary conditions.

3 The HYbrid MAss flux Convection Scheme (HYMACS)

In the previous chapter, the conventional convection parametrization approach in atmospheric models has been outlined. It has been seen that this framework assumes a locally closed mass budget by definition (Arakawa and Jung, 2011). Thus, the mass transport due to convective up- and downdrafts is always balanced by subsidence in the convective grid column.

As already mentioned, HYMACS deviates from the classical approach by allowing for a net mass transfer due to convective motions. The qualitative motivation for this has already been formulated in Kain and Fritsch (1993) in the context of mesoscale modeling. With the ever decreasing grid spacing in numerical weather prediction (NWP) and climate models, they noted that the assumption of compensating subsidence confined to the single grid column becomes more and more questionable. Whilst the small convective drafts can still be safely considered to constitute a subgrid-scale dynamical process, its counterpart, the compensational subsidence, typically occupies a wide range of spatial scales up to the Rossby deformation radius. The latter is in the order of a few 100 km in the midlatitudes (Bretherton et al., 2005).

This point of view is also supported by Gross et al. (2018). In their review, they coarsened mass fluxes from a convection-permitting model (with $\Delta x = 2.2\,\mathrm{km}$) onto a 24-km grid and noted that the compensational (dry) mass flux is uncorrelated with updraft mass flux (see their Fig. 3). Hence, the basic assumption of a locally closed system with respect to mass in a convective column is already violated with this rather coarse grid spacing.

Treating the environmental subsidence in an improper manner may result in unrealistic effects which have the potential to degrade noticeably the model performance. As argued by Ong et al. (2017), the forced local compensation of the convective mass flux concentrates artificially the apparent heat source and moisture sink in the vertical grid column (cf. Secs. 2.2 and 2.3). With decreasing size of the horizontal grid box area, this may result in an unrealistic strong secondary circulation which is known be crucial for the development of tropical cyclones (Rotunno and Emanuel, 1987; Houze Jr, 2010) and mesoscale convective systems (MCS) in midlatitudes (Houze Jr, 2004).

To break up the conceptual limitations of the classical convection parametrization framework, an alternative view on the problem of representing convection becomes necessary. Picking up the ideas presented in the pioneering work by Kuell et al. (2007), the hybrid approach was elucidated with some detail in Langguth et al. (2020). The following section recapitulates its conceptual idea while focusing on a comparison with the classical approach. Afterwards, details on HYMACS as

a specific convection parametrization schemes (CPS) realizing the hybrid approach are presented. This overview sums up the descriptions given in Kuell and Bott (2008, 2009, 2011) and is complemented by undocumented changes to HYMACS as well as new developments that have been introduced in the scope of this thesis.

3.1 The hybrid approach

We start by considering an arbitrary fluid volume (see, e.g., Zdunkowski and Bott, 2003, for a comprehensive overview on fluid volumes) which consists of a an environmental (non-convective) part and an ensemble of convective clouds such as illustrated in Figure 3.1. This fluid volume moves with its barycentric velocity $\mathbf{v}_b$ through space and time, whereas $\tilde{\mathbf{v}}_c$ and $\mathbf{v}_e$ are designated to the convective and non-convective part, respectively. Supposing that $\tilde{\mathbf{v}}_c$ constitutes a superposition of the relative velocity $\mathbf{v}_c$ with the environmental velocity $\mathbf{v}_e$, i.e. $\tilde{\mathbf{v}}_c = \mathbf{v}_e + \mathbf{v}_c$, the barycentric velocity is given by

$$\begin{aligned} \rho\mathbf{v}_b &= \rho_e\mathbf{v}_e + \rho_c\big(\mathbf{v}_e + \mathbf{v}_c\big) \\ &= \rho\mathbf{v}_e + \mathbf{J}_c. \end{aligned} \tag{3.1}$$

Here, ρ_e and ρ_c denote the partial densities of both volume parts under consideration which sum up to the total density ρ. For the subsequent discussion, it is postulated that only the environmental velocity $\mathbf{v}_e$ is explicitly resolved by an atmospheric model. While its product with ρ is then the resolvable environmental mass flux, the convective mass flux per unit area $\mathbf{J}_c = \rho_c\mathbf{v}_c$ is of particular interest in our case[1].

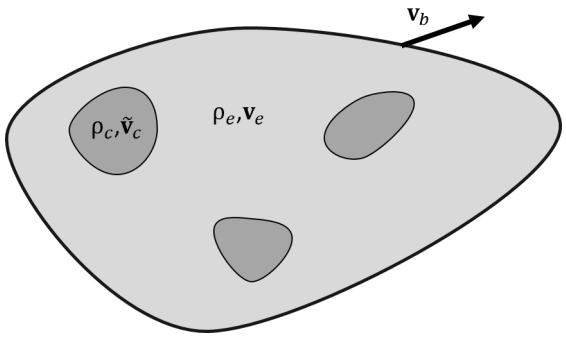

Figure 3.1: Fluid volume which consists of an environmental part (light gray area) and a convective part. The convective part may consist of an ensemble of individual clouds (dark gray areas). The fluid volume moves with its barycentric velocity $\mathbf{v}_b$ through space and time, while the environmental part (with partial density ρ_e) and the convective part (with partial density ρ_c) move with $\mathbf{v}_e$ and $\mathbf{v}_c$, respectively.

The significance of $\mathbf{J}_c$ can be readily deduced from the continuity equation which can be decomposed with Equation 3.1 as follows

$$0 = \frac{\partial\rho}{\partial t} + \nabla\cdot\big(\rho\mathbf{v}_b\big) = \frac{\partial\rho}{\partial t} + \nabla\cdot\big(\rho\mathbf{v}_e\big) + \nabla\cdot\mathbf{J}_c. \tag{3.2}$$

[1]Note that $\mathbf{J}_c$ must be distinguished from the convective mass flux m_c introduced in Equation 2.14 since it involves the partial density ρ_c instead of the the full density ρ.

It is seen that a local change in density can be realized by both, mass flux divergence of the environmental flow (second term on the right hand side (RHS)) and divergence of the convective mass flux (third term). Since the latter is not part of the explicit model dynamics, this term has to be parametrized.

Equation 3.2 constitutes the most general form of the hybrid approach. The subsequent consideration further particularizes this form with focus on the application in a modeling framework. Therein, it is commonly assumed that the convective transport is dominated by motions in the vertical direction, i.e. $w_c >> u_c$. As pointed out by Wu and Arakawa (2014), this assumption is well justified even at gray-zone resolutions. Consequently, the convective fluxes are confined to the grid column and can be related to the area-integrated mass fluxes of the up- and downdraft regions $M_{u,d}$ (in kg/s):

$$\left.\frac{\partial \rho}{\partial t}\right|_{conv} = -\nabla \cdot \mathbf{J}_c = -\frac{1}{A_g}\left(\frac{\partial M_u}{\partial z} + \frac{\partial M_d}{\partial z}\right). \tag{3.3}$$

In the absence of mass loss due to precipitation, the total mass within the grid column covering a horizontal area A_g is conserved. However, mass can be redistributed which results in a local convective density tendency.

Lateral mixing, which can be either turbulent or organized, guides the mass fluxes of the convective drafts. Letting $E_{u,d}$ and $D_{u,d}$ (in kg/s) denote the area-integrated entrainment and detrainment rates over a layer with depth Δz, Equation 3.3 can be discretized as

$$\left.\frac{\partial \rho}{\partial t}\right|_{conv} = -\frac{1}{A_g \Delta z}(E_{u,d} - D_{u,d}). \tag{3.4}$$

Here, it is again emphasized that *only* the motions of the small-scale up- and downdrafts are parametrized with the hybrid approach. The compensating subsidence is passed completely to the grid-scale dynamics as illustrated in Figure 3.2.

Formally, this means that the hybrid approach cannot be derived in analogy to the classical approach. With the quasi-Boussinesq form of the continuity equation as proposed by Arakawa and Schubert (1974), where ρ only varies with the height z, this difference is obvious.

However, the uniqueness of the net mass transfer can be further highlighted with the help of the *Hesselberg averaging* procedure which is a common approach to separate turbulent fluxes in modern nonhydrostatic models (Gassmann and Herzog, 2008; Thuburn et al., 2018).

The Hesselberg averaged form of the continuity equation is given by

$$\frac{\partial \overline{\rho}}{\partial t} + \nabla \cdot (\widehat{\mathbf{v}}_b \overline{\rho}) = 0, \tag{3.5}$$

where the symbol $\widehat{\ }$ denotes a density weighted-averaging operator

$$\widehat{\psi} = \frac{\overline{\rho\psi}}{\overline{\rho}} \quad \text{with} \quad \psi = \widehat{\psi} + \psi''. \tag{3.6}$$

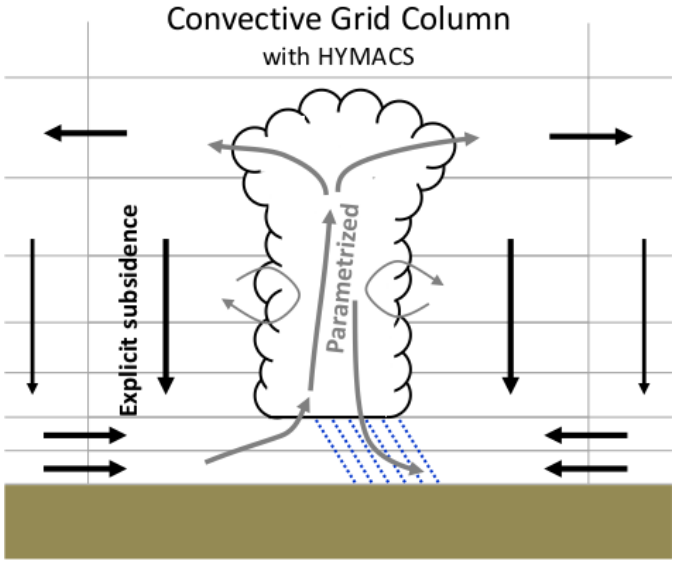

Figure 3.2: Illustration of a representative convective plume and the handling of the related dynamics with the hybrid mass flux approach. In contrast to Figure 2.5, the compensational subsidence is completely part of the grid-scale dynamics (black arrows). The only parametrized dynamics (gray arrows) are the convective fluxes of the drafts which undergo organized and turbulent mixing.

With the Hesselberg averaging framework, $\widehat{\psi}$ and ρ constitute the grid-scale quantities. While the turbulent mass-flux term $\overline{\rho \mathbf{v}''}$ vanishes per definition with Equation 3.6, convective motions can be separated from the resolved dynamics by applying the postulated decomposition of the barycentric velocity $\widehat{\mathbf{v}}_b$ in Equation 3.1:

$$\frac{\partial \overline{\rho}}{\partial t} + \nabla \cdot \left(\overline{\rho \mathbf{v}_e + \rho_c \mathbf{v}_c}\right) = \frac{\partial \overline{\rho}}{\partial t} + \nabla \cdot \left(\overline{\rho} \widehat{\mathbf{v}}_e\right) + \nabla \cdot \mathbf{J}_c = 0. \tag{3.7}$$

Here, the divergence term $\nabla \cdot \left(\overline{\rho} \widehat{\mathbf{v}}_e\right)$ is part of the grid-scale dynamics, whereas a subgrid-scale, convective term enters the continuity equation. By establishing this term, turbulent and convective fluxes are formally distinguished with the hybrid approach which allows us to attach an explicit three dimensional character to the convective overturning circulation. The formal separation can thereby be reasoned with the inherently anisotropic and penetrative nature of cumulus convection as also noted in Arakawa (2004).

Besides, the effect of net lateral mixing as seen from Equation 3.4 resembles the multifluid framework suggested by Thuburn et al. (2018) (see their Eq. 44). However, as pointed out by Weller and McIntyre (2019), a strict realization of the multifluid approach based on conditional averaging the Euler equations would not result in a parametrization scheme, but a complete new model. The hybrid approach can therefore be seen as a pragmatic extension of the classical CPS framework allowing the resolved dynamics to control the environmental subsidence.

For convenience, the Hesselberg and Reynolds averaging operators as seen in Equation 3.7 are omitted in the remainder of this section and we proceed with the formalism introduced in the Equations 3.2–3.4[2]:

[2]This implies that ρ, ψ and $\mathbf{v}_e$ denote grid-scale variables corresponding to $\overline{\rho}$, $\widehat{\psi}$ and $\widehat{\mathbf{v}}_e$, respectively.

Just like classical CPS, the convective effect on the atmospheric state in terms of the generic specific quantity ψ is also subject to the hybrid scheme. Thus, an expression of the respective convective tendency $\frac{\partial \psi}{\partial t}|_{conv}$ must be derived.

In analogy to the proceedings above, the balance equation of any conserved quantity Ψ in the fluid volume

$$\frac{\partial}{\partial t}(\rho\psi) + \nabla \cdot (\rho \mathbf{v}\psi) = -\nabla \cdot \mathbf{F}_\psi + Q_\psi \tag{3.8}$$

is the starting point, where $\rho\psi$ stands for the density of Ψ.

Here, the terms on the RHS denote changes due to the convergence of non-convective fluxes $-\nabla \cdot \mathbf{F}_\psi$ (e.g. radiation or diffusion fluxes) or internal sources Q_ψ (e.g. condensation or latent heat release). Although these terms are of great interest for moist convection as well, we first focus on the effects of the subgrid-scale transport and abbreviate both terms with S_ψ subsequently.

In analogy to the steps described above for deriving the convective density tendency (Eqs. 3.2– 3.4), the balance equation of Ψ can be decomposed to assess the effect of convective transports:

$$\begin{aligned} &\frac{\partial}{\partial t}(\rho\psi) + \nabla \cdot (\rho \mathbf{v}_e\psi) + \nabla \cdot \mathbf{J}_c^\psi = S_\psi \\ \text{with} \qquad &\frac{\partial}{\partial t}(\rho\psi)\big|_{conv} = -\nabla \cdot \mathbf{J}_c^\psi = -\frac{1}{A_g \Delta z}\left(E_{u,d}\psi - D_{u,d}\psi_{u,d}\right). \end{aligned} \tag{3.9}$$

Thus, the divergence of the convective flux $\mathbf{J}_c^\psi$ is again guided by entrainment and detrainment which are now weighted with ψ and $\psi_{u,d}$, respectively. Here, $\psi_{u,d}$ denotes the specific content of Ψ within the parametrized up- and downdrafts.

A careful remark should be left at this stage on the entrainment term in the second line of Equation 3.9: Instead of using its environmental value ψ_e, the grid-scale value $\psi \triangleq \widehat{\psi}$ is used here. The significance of this approximation can be deduced by rewriting the density of Ψ of the fluid volume:

$$\rho\psi = \rho_e\psi_e + \rho_c\psi_c. \tag{3.10}$$

After using $\rho_e = \rho - \rho_c$ and rearranging the terms on the RHS of Equation 3.10, one obtains

$$\psi = \psi_e + \frac{\rho_c}{\rho}(\psi_c - \psi_e). \tag{3.11}$$

Given that the difference between the convective and environmental values of ψ cannot be neglected, the approximation $\psi \approx \psi_e$ only holds if the partial density ρ_c is much smaller than ρ. In the modeling framework where the specific value of Ψ of the fluid volume is assigned to the grid-scale value $\overline{\psi}$, this is equivalent to the *small-area approximation* which is also applied in the conventional mass flux approach. Thus, its validity can be questioned analogously when representing convection at gray-zone resolutions (Arakawa and Wu, 2013).

Converting the flux form given in Equation 3.9 to the convective ψ tendency sheds further light on the effect of a net mass transfer with the hybrid approach.

Expansion of the first divergence term in Equation 3.9 to include the continuity equation results after some algebraic steps in

$$\begin{aligned}\rho\frac{\partial\psi}{\partial t} &= -\rho\mathbf{v}_e\cdot\nabla\psi - \nabla\cdot\mathbf{J}_c^{\psi} + \psi\nabla\cdot\mathbf{J}_c + S_\psi \\ &= -\rho\mathbf{v}_e\cdot\nabla\psi + \frac{\partial}{\partial t}(\rho\psi)\Big|_{conv} - \psi\frac{\partial\rho}{\partial t}\Big|_{conv} + S_\psi.\end{aligned} \tag{3.12}$$

This shows that in addition to non-convective fluxes and internal sources aggregated in S_ψ, a local change in ψ can be realized by

i) advection of ψ with the environmental flow, i.e. grid-scale advection,

ii) divergence of the convective flux of ψ and

iii) convective mass flux divergence.

Thus, the net mass transfer also affects explicitly the convective ψ-tendency with the hybrid approach.

Following Kuell et al. (2007), the final discretized form of the convective ψ-tendency reads

$$\frac{\partial\psi}{\partial t}\Big|_{conv} = -\frac{1}{A_g\Delta z\rho^{\tilde{n}^\star}}(E_{u,d}\psi - D_{u,d}\psi_{u,d}) + \left[\frac{\rho^n}{\rho^{\tilde{n}^\star}} - 1\right]\frac{\psi^n}{\Delta t}, \tag{3.13}$$

where $\rho^{\tilde{n}^\star}$ denotes the updated density due to the parametrized net mass transfer from time-level n with

$$\rho^{\tilde{n}^\star} = \rho^n + \Delta t\frac{\partial\rho}{\partial t}\Big|_{conv}. \tag{3.14}$$

As demonstrated in the appendix of Langguth et al. (2020), the discretized convective ψ-tendency is conservative so that the vertical integral within the convective grid column does not change when $S_\psi = 0$. The convective contributions S_ψ (e.g. latent heat release) are subject to the cloud model of the hybrid CPS.

Finally, it is worth mentioning that the presented hybrid approach constitutes a general framework. Its basic concept, the parametrized net mass transfer, can be applied to existing classical CPS. The studies by Ong et al. (2017) and Malardel and Bechtold (2019) are two specific examples where the Kain-Fritsch scheme in the Weather Research and Forecasting (WRF) model and the Bechtold-Tiedtke scheme in the Integrated Forecasting System (IFS) model have been adopted to allow for a net mass transfer.

However, due to the convective density tendencies, the coupling of an hybrid CPS to a hosting model is by no means trivial. Indeed, subtle challenges arise since the model-specific physics-dynamics interface is usually not designed to take local mass sources and sinks into account. Details on the physics-dynamics coupling in the particular case of the ICON model are given in Chapter 4 after providing an in-depth description of HYMACS in the subsequent sections.

3.2 Overview on HYMACS

Apart from the unconventional handling of the environmental subsidence, the formulation of HYMACS has taken up several ideas from other CPS which are well-established in the modeling community. Namely, this includes the Tiedtke scheme (Tiedtke, 1989), the Kain-Fritsch scheme (Kain and Fritsch, 1993) and the Bechtold scheme (Bechtold et al., 2001).

Thus, just like a classical CPS, HYMACS consists of three parts which are designed to fulfill the parametrization targets listed in Section 2.3, that are a cloud model, a set of trigger functions and a closure assumption. All three components are described in the following, while also some explicit comparisons to the Bechtold-Tiedtke scheme, presented in Section 2.5, are drawn.

3.2.1 The cloud model of HYMACS

Analogously to the Bechtold-Tiedtke scheme, HYMACS is based on the bulk mass flux approach and makes use of a diagnostic entraining/detraining plume cloud model. However, in addition to the purely diagnostic nature of such a scheme, a simplified approach to involve *convective memory* is available on a quadrilateral grid that is briefly sketched at end of the cloud model description.

In order to describe the thermodynamic properties of the parametrized drafts, the liquid water static energy h_{il} given by

$$h_{il} = s - L_v q^l - L_f q^i \quad \text{with } s = h + gz = c_p T + gz \tag{3.15}$$

is used in HYMACS. The merit of h_{il} is that it is conserved in the presence of phase changes. It is therefore a convenient quantity for parametrizing moist convection and is also chosen, for example, in Bechtold et al. (2001).

However, the scheme provides convective tendencies of enthalpy h to the hosting model which can be computed from Equation 3.15 given that the liquid and frozen cloud condensate content are known. The other thermodynamic variables in HYMACS, that are the specific moisture quantities q^v, q^l, q^i, q^r and q^s as well as momentum in terms of $\mathbf{v}_h$, are also used in the Bechtold-Tiedtke scheme.

The parametrization procedure in the hybrid CPS again starts with a check of each grid column for the occurrence of shallow convection. Starting from the surface layer, a test parcel is lifted up to the lifting condensation level (LCL) provided that the ambient flow is convergent. During its dry ascent, organized entrainment in accordance with the closure assumption (see Sec. 3.2.3) takes place which dilutes the updraft air. In contrast to the Bechtold-Tiedtke scheme, no kinetic energy computation of the updraft plume is performed in the subcloud layer. Instead, the kinematic computation is initialized at the LCL with an updraft velocity of $w_u(z(LCL)) = w_{u,0} = 1\text{m/s}$. The kinetic energy of the layers above is then computed iteratively with the help of

$$\Delta K_u = -K_u \left[\left(\frac{M_u}{M_u + E_u} \right)^2 - 1 \right] + \frac{g}{1+\gamma} B \Delta z, \tag{3.16}$$

where $\gamma = 0.5$ accounts for non-hydrostatic pressure perturbations in the buoyancy term (second term on the RHS). The dilution due to entrained air (first term on

the RHS) is formulated in a simpler way than in the Bechtold-Tiedtke scheme (compare Eq. 2.23) and assumes that the entrained air has zero momentum.

At the LCL, the updraft air does not have to be positively buoyant with respect to the grid-scale environment. The sufficient condition for further convective ascent is that the plume's air becomes warmer than the ambient air before the initial updraft energy gets exhausted. A trigger contribution (see Sec. 3.2.2) is added to boost the potential candidate for a convective updraft.

Given that the level of free convection (LFC) is reached with $K_u > 0$, the ascent is continued until the kinetic energy becomes negative at the cloud top level (CTL). When the cloud depth is smaller than the minimum cloud depth for deep convection $D_{cl,min}^{deep}$, which will be defined in Section 3.3, shallow convection is assumed to take place. In case that the threshold is exceeded, the updraft procedure is repeated which now incorporates precipitation processes and the formation of a convective downdraft. While further details on the microphysics of the cloud model will be outlined shortly, this constitutes a remarkable difference to the Bechtold-Tiedtke scheme: Shallow convection is assumed to be non-precipitating without the formation downdrafts in HYMACS in analogy to many other classical CPS (Tiedtke, 1989; Kain and Fritsch, 1990; Bechtold et al., 2001; Kain, 2004).

When the first test parcel rooting in the surface layer does not yield a successfully triggered updraft plume, the check is repeated for subsequent model layers. For computational efficiency, the source layer is shifted upwards by the half-value thickness of a characteristic source layer Δp_{src} until the source layer would be placed above the 700 hPa-level. Following Bechtold et al. (2001), a value of $\Delta p_{src} = 60$ hPa is chosen in HYMACS.

Parametrization of the convective updraft

The equation system for the thermodynamic properties of the updraft air in HYMACS is in general similar to the cloud model equations used in the Bechtold-Tiedtke scheme. However, in addition to the formulation in z- instead of p-coordinates, the parametrization of the microphysical processes and the mixing differ in some details that are outlined subsequently.

The interaction of the updraft fluxes with the environment in terms of the intensive quantities $\psi \in (h, q^v, q^l, q^i)$ is given in analogy to Equation 3.9 by

$$\frac{\partial}{\partial z}(M_u \psi_u) = \frac{1}{\Delta z}(E_u \overline{\psi} - D_u \psi_u), \tag{3.17}$$

where the area-integrated updraft mass flux M_u is guided by the layer-integrated entrainment and detrainment rates E_u and D_u, respectively (see Eq. 3.9). Note that the overbar is used again to denote grid-scale variables following the notation established in Section 2.3.

While entrainment and detrainment in the Bechtold-Tiedtke scheme crucially depend on the ambient moisture profile and also differ for shallow and penetrative convection, HYMACS applies a formulation in analogy to Tiedtke (1989):

$$E_u = E_u^{turb} + E_u^{org} = \mu_u^{turb} M_u \Delta z - \nabla_h \cdot (\overline{\rho}\,\overline{\mathbf{v}_h}) A_g \Delta z, \tag{3.18}$$

$$D_u = D_u^{turb} = \mu_u^{turb} M_u \Delta z. \tag{3.19}$$

The turbulent mixing parameter μ_u^{turb} is held constant with a value of $1 \times 10^{-3}\,\mathrm{m}^{-1}$ between the LCL and the level of neutral buoyancy (LNB). Thus, no distinction between the different types of convection is made. In addition to turbulent mixing, organized entrainment takes place when grid-scale convergence is present.

Within the convective cloud, the kinematics of the updraft air are driven by condensation and freezing. In analogy to the Bechtold-Tiedtke scheme, supersaturation is removed with a saturation adjustment that follows the mixing process. Gradual glaciation is assumed to depend linearly on the updraft temperature $-5°\mathrm{C} \leq T_u \leq -35°\mathrm{C}$. This is in contrast to the quadratic dependence in the Bechtold-Tiedtke scheme and also differs from Kuell et al. (2007) where a sinusoidal temperature dependency of the ice phase was chosen. Several sensitivity tests with the simplified temperature dependency however showed only minor effects on the performance of HYMACS (Kuell, personal communication).

For penetrative convective clouds, the microphysical computation becomes extended. The conversion of cloud condensate to precipitable hydrometeors in the updraft follows the simple parametrization approach given by Ogura and Cho (1973) which also involves a dependency on the inverse of the updraft velocity w_u such as the formulation by Sundqvist (1978):

$$\Delta(M_u q_u^{(r,s)}) = M_u q_u^{(l,i)} (1 - \exp(-c_{pr} \Delta z / w_u). \tag{3.20}$$

In HYMACS, a value of $c_{pr} = 0.04\,\mathrm{s}^{-1}$ for the autoconversion factor is chosen which is similar to the value used by Bechtold et al. (2001).

The formed precipitation is thereby directly removed from the updraft air and transferred to the convective downdraft (see below). Additionally, some further updraft air is split off to supply the downdraft where the transferred fraction $\mu_{u\to d}$ is set proportional to the formed precipitation amount Δq_u^{pr}

$$\mu_{u\to d} = \frac{\Delta q_u^{pr}}{\Delta q_u^{pr} + q_u^v + q_u^l + q_u^i} \qquad \text{with } \Delta q_u^{pr} = \Delta q_u^r + \Delta q_u^s. \tag{3.21}$$

Thus, for precipitating penetrative convection, the detrainment rate for the updraft (cf. Eq. 3.18) is extended due to a mass transfer to the downdraft

$$D_u = D_u^{turb} + D_{u\to d} = \mu_u^{turb} M_u \Delta z + \mu_{u\to d} M_u \Delta z + M_u \Delta q_u^{pr}, \tag{3.22}$$

where the latter term accounts for the instantaneous fallout of precipitating hydrometeors. It is noted that the intensive variables of the updraft remain unchanged when mass is solely transferred to the downdraft.

The transport of convective momentum using Equation 3.9 is also subject to HYMACS. Unlike in the Bechtold-Tiedtke scheme, an explicit (net) source term is involved accounting for the horizontal pressure force that acts across the draughts. Following Gregory et al. (1997), the source term can be approximated by

$$\frac{\partial}{\partial z}\left(M_u \mathbf{v}_{h,(u)}\right)\Big|_{source} = c_m M_u \frac{\partial \overline{\mathbf{v}_h}}{\partial z} \tag{3.23}$$

with a parameter value of $c_m = 0.7$. The convective momentum source is also part of the parametrized downdraft which will be described below.

Above the LNB, organized entrainment as well as turbulent mixing are turned off, while organized detrainment dissolves the updraft plume up to the cloud top. In former versions of HYMACS, the organized detrainment took place at the CTL only. In this study, this approach has been revised to yield a more physically based detrainment profile. Further details will be given in Section 3.3.

Parametrization of the convective downdraft

In case that a deep convective cell is detected, HYMACS parametrizes a convective downdraft fueled by evaporative cooling and melting of precipitation. While the Bechtold-Tiedtke scheme explicitly relates the downdraft mass flux to the updraft mass flux at LCL (see Eq. 2.35), the downwards directed, buoyancy-driven density flow is solely controlled by the precipitation formation in the updraft with HYMACS. Starting from the LNB, equal amounts of updraft and environmental air supply the downdraft according to the generated precipitation fraction given by Equation 3.21. The latter increases the net convective mass flux and thus, can be regarded as an organized entrainment process. When the (generally) subsaturated mixture becomes negatively buoyant, the air enters the model layer underneath where further organized entrainment is then accompanied by turbulent mixing. Thus, the total area-integrated entrainment and detrainment rates of the downdraft read

$$E_d = E_d^{turb} + E_{u\to d} + E_d^{org} = \mu_d^{turb} M_d \Delta z + M_u \Delta q_u^{pr} + 2\mu_{u\to d} M_u \Delta z, \tag{3.24}$$

$$D_d = D_d^{turb} = \mu_d^{turb} M_d \Delta z, \tag{3.25}$$

where $\mu_d^{turb} = 2 \times 10^{-4}\,\mathrm{m}^{-1}$ is set.

In analogy to the updraft, the kinematics of the downdraft are computed with the help of Equation 3.16, where the kinetic energy of the downdraft K_d is initialized with $w_{d,0} = -1\mathrm{m/s}$. When the initial air mixture of the downdraft does not become negatively buoyant or when its kinetic energy gets exhausted at intermediate levels, the downdraft is dissolved via organized detrainment. The involved precipitating hyrdometeors are converted back to cloud condensate and a new downdraft is initiated in the model layer below.

The important cooling by evaporation and sublimation is thereby achieved by imposing a simple linear profile of the relative humidity RH_d between the CTL and the LCL:

$$RH_d(z) = 1 - 0.05\frac{z(CTL) - z}{z(CTL) - z(LCL)}. \tag{3.26}$$

Thus, in contrast to the Bechtold-Tiedtke scheme, downdraft air becomes already subsaturated above the cloud base of the convective updraft. Below the LCL, a stronger linear decrease with $0.05\,\mathrm{km}^{-1}$ is set in HYMACS which enhances evaporative cooling in the subcloud layer.

Additionally, melting of frozen precipitation and condensate occurs when the temperature in the downdraft air exceeds the freezing point $T_f = 273.16\,\mathrm{K}$. The proportion of the ice phase is assumed to decrease linearly up to $T_{f\to l} = 274.16\,\mathrm{K}$.

Similarly to the Bechtold-Tiedtke scheme, organized detrainment is enforced in the subcloud layer for which a maximum detrainment layer depth of 60 hPa

is chosen in HYMACS. In the downdraft detrainment layer, turbulent mixing is switched off and the downdraft mass flux decreases linearly towards the surface where the sedimentation mass flux constitutes a Dirichlet boundary condition.

Non-local effects with HYMACS

As already mentioned in Section 2.4, the interaction of convective cells in different grid columns of the model is limited in classical CPS since it can only be realized via grid-scale variables. Subgrid-scale effects such as the propagation of cold-pools due to convective downdrafts are largely averaged out onto grid-scale variables and thus, triggering of secondary cells are hardly represented with parametrized convection. Likewise, the evolution of the convective cells cannot be captured with a purely diagnostic scheme.

While different sophisticated approaches for involving both processes in CPS have been undertaken, a simplified and efficient approach was implemented in HYMACS with the study of Kuell and Bott (2011). Therein, a cell aging effect and a gust front parametrization are proposed allowing for horizontal communication over neighbouring grid boxes and for the incorporation of *convective memory*.

The cell aging effect adds a temporal property to the state of a convective grid column which affects the turbulent mixing of the updraft (see Eq. 3.17) and the precipitation formation in case of penetrative convection (see Eq. 3.20). Both processes are assumed to favor precipitating convection with on-going duration of convective activity, that is a temporal decrease in turbulent mixing and a temporal increase in the efficiency of cloud condensate to precipitation conversion (see Eqs. 2.12–2.14 in Kuell and Bott, 2011). By parametrizing a propagation vector, the cell age is allowed to be inherited to neighbouring convective grid columns.

The gust front parametrization adds a trigger contribution (see Sec. 3.2.2) to neighbouring grid cells in order to mimic the effect of downdraft induced cold pool propagation. By doing so, it can be interpreted as a cellular automaton which may enhance advective effects as well as convective organization along mesoscale squall-lines (Bengtsson et al., 2013).

Albeit being appealing especially for representing convection at gray-zone resolutions, the parametrization of the non-local effects as developed in Kuell and Bott (2011) is limited to quadrilateral grids. In case that the hosting model makes use of a irregular grid structure, the propagation and decision rules associated with the non-local effects have to be revised. Depending on the underlying grid geometry, non-trivial neighbouring relations have to be considered whose implementation may not be straightforward[3].

Staggering and discretization in HYMACS

For convenience, details on the spatial discretization and the staggering of the variables used in HYMACS have been omitted or just stated implicitly so far. In the following paragraph, this is made more explicit:

[3]This is especially true for highly scalable modeling frameworks where the computations are distributed over a large number of processing units.

Modern atmospheric models often make use of a so-called the *Arakawa C-grid staggering* which places scalar quantities at the center of a grid box and vector quantities such as the normal wind vector components or fluxes on the corresponding grid box faces. Thus, in a vertical grid column, there exist ke full levels denoted by k lying between $ke+1$ half-levels which can be denoted by $k+1/2$ and $k-1/2$, respectively. Besides, some models (such as the COSMO and the ICON model) number the model levels in a top-down manner, meaning that the first (last) half-level coincides with the model top (the Earth's surface).

The spatial discretization of HYMACS is aligned with such a staggering approach. Thus, the convective fluxes are staggered on the half-levels while the mixing with the environment takes place at full levels. By doing so, vertical interpolation of the grid-scale quantities and the convective tendencies, which are given on full levels with a finite difference method as well, is avoided. Since the thermodynamic quantities of HYMACS are formulated in terms of conservative quantities (e.g. the liquid water static energy h_{il}), the convective tendencies on the full levels (e.g. in terms of the enthalpy h) can be computed in a straightforward manner.

An exception holds for the buoyancy calculation which has to be done on the half-levels. For this purpose, the grid-scale virtual temperature $\overline{T_v}$ has to be interpolated from full to half levels. Note that the virtual temperature of the drafts' air mass $T_{v,(u,d)}$ can be conveniently computed from the liquid water static energy h_{il} (see Eq. 3.15). For consistency, the interpolation procedure should be adopted, if possible, from the hosting model. It is furthermore noted that the characteristic cloud levels such as the LCL, LFC, and CTL are also defined on the half-levels since they are derived from buoyancy checks or flux characteristics.

Similar consistency arguments hold for the grid-scale horizontal wind vector. HYMACS requires the horizontal wind vector centered in the grid box and provides a convective tendency at the same position. Thus, an interpolation step is required for the input of HYMACS, while a back interpolation needs to be performed for the respective convective tendencies. For this, it is also advised to follow the approach used in the hosting model for consistency.

An illustration of the staggering together with the sequential order of the (diabatic) processes is depicted in Figure 3.3. In the updraft, the algorithm applies a bottom-to-top procedure which starts with precipitation formation and the up-to-downdraft mass transfer in case of penetrative convection. Afterwards, the mixing with the environment is computed which is followed by the saturation adjustment and the parametrization of the momentum source. The buoyancy check which is used to identify key levels of the convective cell such as the LFC is performed at the upper interface level of the layer at hand.

Conversely, the downdraft follows a top-to-bottom procedure which starts with the environmental mixing and the subsequent saturation adjustment. For consistency with the sequential order in the updraft, the up-to-downdraft as well as the precipitation mass transfer are performed afterwards. Finally, the convective momentum source is computed and the buoyancy check is performed to decide if the downdraft mass flux is propagated to the model layer below or if it is dissolved.

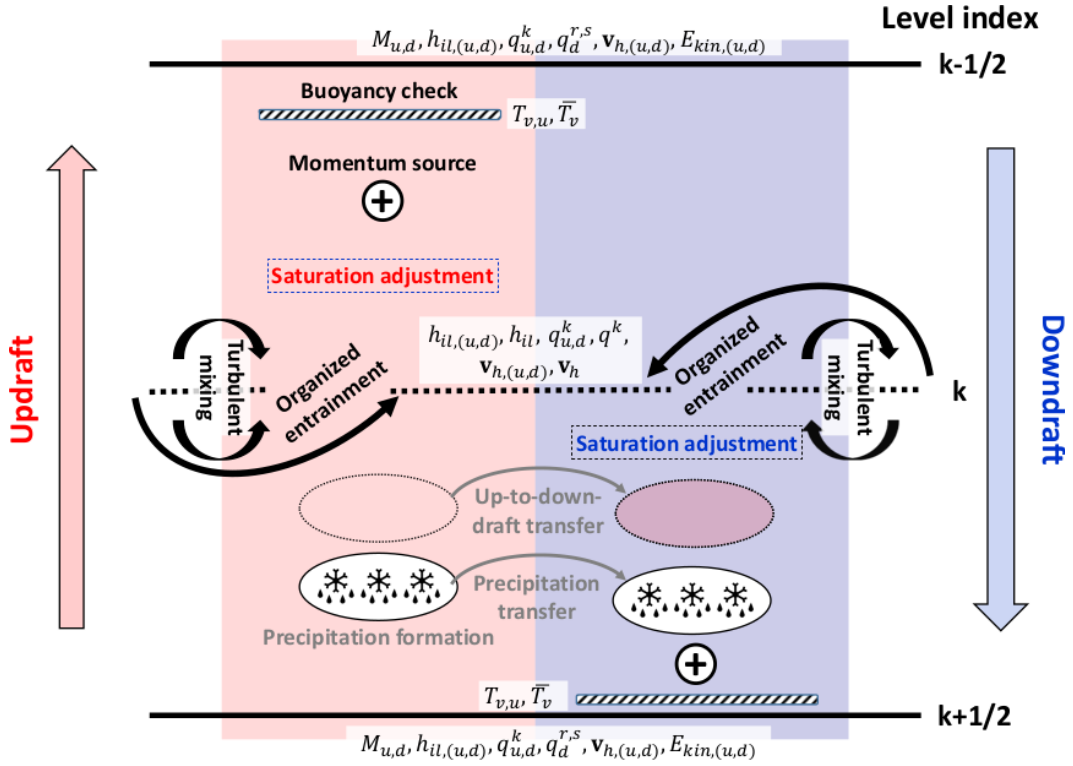

Figure 3.3: Illustration of the computational order of parametrized processes and variable staggering in HYMACS. The updraft procedure runs in down-top direction as indicated by the left arrow, while the downdraft procedure is organized in top-down direction as indicated by the right arrow. The precipitation formation as well the related up-to-downdraft transfer only occur for deep convection and are therefore gray-shaded. The specific moisture quantity q^k symbolizes water vapor q^v as well as cloud water q^c and ice q^i. Further details are given in the text.

3.2.2 Trigger functions

For the buoyancy check in the updraft procedure trigger contributions are of particular interest. The aim of these trigger contributions is to approximate processes that lead to convection in the nature even though these processes are either poorly represented or completely unresolved on grid-scale.

The first contribution to the virtual temperature increment added at the LCL is adopted from Fritsch and Chappell (1980). The Fritsch-Chappell trigger accounts for the observation that convection is favored under the presence of background low-level convergence. For continuity reasons, this is related to grid-scale lifting whose favoring effect is considered to be strongest near surface. The corresponding virtual temperature increment $\Delta T^{FC}_{v,u}$ is obtained by scaling the difference between the grid-scale vertical wind at LCL $\overline{w}(z(LCL))$ and a reference vertical velocity w_0 following

$$\begin{aligned} \Delta T^{FC}_{v,u} &= \sqrt[3]{k_{FC}(\overline{w}(z(LCL)) - c(z))} \\ \text{with} \qquad c(z) &= \begin{cases} w_0(z(LCL)/2000\,\text{m}), & \text{for } z(LCL) \le 2000\,\text{m} \\ w_0, & \text{for } z(LCL) > 2000\,\text{m}, \end{cases} \end{aligned} \tag{3.27}$$

where the disposal parameters $w_0 = 0.02\,\text{m/s}$ and $k_{FC} = 100\,\text{K}^3\text{s/m}$ are chosen.

Note, that the sign of $\Delta T_{v,u}^{FC}$ is solely determined by $\overline{w}(z(LCL))$. Thus, convection gets suppressed in the presence of grid-scale subsidence or neutral vertical velocity.

In order to account for the subgrid-scale dynamics of the planetary boundary layer (PBL), Kuell and Bott (2008) added a trigger contribution dependant on the TKE. Based on the idea that strong turbulence occurring at daytime in the presence of strong surface enthalpy fluxes favors convection, they formulated the related virtual temperature increment $\Delta T_{v,u}^{TKE}$ as

$$\Delta T_{v,u}^{TKE} = T^{\star\star} \sqrt[3]{v_{TKE}} - T_0 \qquad \text{with} \quad v_{TKE} = \sqrt{2\overline{TKE}}. \tag{3.28}$$

Here, $\overline{TKE}$ denotes the mean TKE in a surface-based layer with a depth of $\Delta p_{src} = 60\,\mathrm{hPa}$. For the parameters, $T^{\star\star} = 3\,\mathrm{K(m/s)}^{-1/3}$ and $T_0 = 2\,\mathrm{K}$ are chosen. These values differ from the original values proposed in Kuell and Bott (2008) and have been chosen to enhance the sensitivity to the subcloud turbulence.

Additionally, HYMACS involves a gust front trigger contribution resulting from parametrized convective downdrafts in the neighbouring grid columns. The trigger bonus depends on the shear of the horizontal wind over the downdraft detrainment layer and on the cold pool velocity contributions from neighboring grid columns $\mathbf{c} = \sum_i \mathbf{c}_i$. While further details on the compuatation of $\mathbf{c}$ can be found in Kuell and Bott (2011), the resulting virtual temperature increment $\Delta T_{v,u}^{GF}$ is given by

$$\Delta T_{v,u}^{GF} = \eta \sqrt[3]{\gamma_{GF} |\mathbf{c}|}, \tag{3.29}$$

where $\gamma_{GF} = 200\,\mathrm{K^3 s/m}$ constitutes an empirical scaling factor. Again, it is worth mentioning that the original gust front proposed in Kuell and Bott (2011) is limited to hosting models using a quadrilateral grid structure.

3.2.3 Closure assumption

While the Bechtold-Tiedtke scheme makes use of different closure assumptions for surface-based deep convection, midlevel and shallow convection, HYMACS applies a *single* closure assumption for all types of parametrized moist convection. Besides, HYMACS can be classified as a pure *low-level control scheme* where the strength of convection is determined by the process controlling convective activation (Mapes, 1997). Thus, rather the process leading to the release of $CAPE$ is taken into account than constraining the amount of convection to the changes in $CAPE$. The latter approach which is pursued for surface-based deep convection in the Bechtold-Tiedtke scheme is referred to the class of *deep-layer control schemes*.

Aligned with the Fritsch-Chappell trigger contribution (see Eq. 3.27) and the in-cloud organized entrainment (see Eq. 3.19), the updraft mass flux at LCL is determined by the subcloud grid-scale mass convergence

$$M_u(z(LCL)) = -A_g \int_{z(DEP)}^{z(LCL)} \nabla_h \cdot (\overline{\rho}\,\overline{\mathbf{v}_h})\,\mathrm{d}z \quad \text{with} \;\; M_u(z(LCL)) \overset{!}{>} 0, \tag{3.30}$$

where $z(DEP)$ denotes the height of the departure layer. Since grid-scale lifting is linked to horizontal mass flux convergence by continuity, the initiated convection is scaled to absorb its causing process. For the same reason, the closure assumption of HYMACS is similar to the closure assumption for midlevel convection in the Bechtold-Tiedtke scheme (cf. Eq. 2.43).

It is also noted that the organized entrainment rate of the updraft (see Eq. 3.17) is consistent with the closure assumption which allows the cloudy plume to increase the mass flux in analogy to the subcloud part.

The chosen closure assumption thereby also eases the numerical procedure since an interactive computation of the mass flux is possible. The mass flux is solely determined by grid-scale mass convergence up to the LNB so that no closure factor for the convective fluxes is required.

3.3 Updates on HYMACS

Within the scope of this work, some updates in the cloud model of HYMACS have been undertaken. The updates constitute the introduction of a *pre-trigger criterion*, a variable minimum cloud depth for penetrative convective clouds and the revision of the organized detrainment near the CTL. In the following, these modifications are documented and reasoned with physical intuition while also references to similar approaches in other CPS are included.

Pre-trigger criterion

As described above, the cloud model of HYMACS performs a buoyancy check and solves a simplified equation for the vertical velocity of the drafts' air masses in order to parametrize their kinematics. However, no explicit buoyancy check was present in the source layer of the updraft underneath the LCL in previous HYMACS versions. Irrespective of the subcloud stratification, the homogeneous mixture of entrained air from several layers received the trigger contributions which then might become positively buoyant even in the presence of strongly stable layers below cloud base.

Further investigation on the origin of the updraft air reveals that the required lifting energy for air from the lowest source layer occasionally attained unrealistic high values. Especially at night when the near-surface atmosphere is typically stable, high CIN values exceeding 100 J/kg are not uncommon as demonstrated exemplary from a COSMO simulation (see Fig. 3.4).

Although convection is likely to occur in these situations (note that the buoyancy check above the LCL is accomplished), the source layer is expected to be placed at higher levels. Thus, a pre-trigger criterion is introduced which re-initiates the updraft procedure with the next source layer candidate if convective inhibition

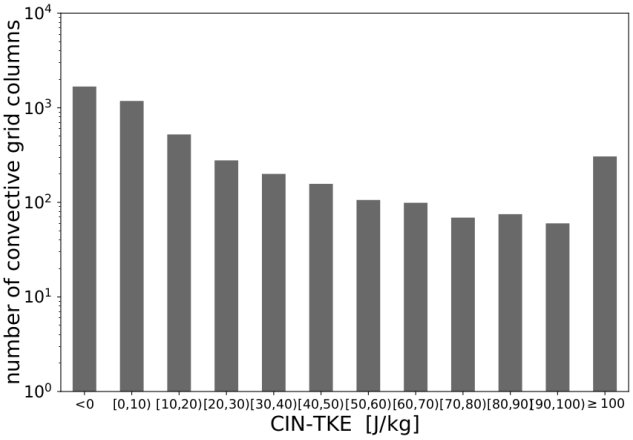

Figure 3.4: Histogram of subcloud $CIN - TKE$ from an exemplary COSMO simulation with HYMACS (initialization: 2018-05-27, 00 UTC (02 CEST)). At 2018-05-27, 03 UTC (05 CEST), 4734 convective grid columns in a domain with 350x230 grid points in zonal and meridional direction are parametrized. 306 (6.5 %) of these show up with $CIN - TKE \geq 100\,\mathrm{J/kg}$ (last bar).

relaxed by the subcloud averaged TKE is too large:

$$\begin{aligned} CIN_{u,subcl} - \overline{TKE}_{subcl} &\overset{!}{\leq} CIN_{crit} \\ \text{with} \qquad CIN_{u,subcl} &= -\int_{z(DEP)}^{z(LCL)} B\,\mathrm{d}z. \end{aligned} \tag{3.31}$$

The physical reasoning for involving the subcloud turbulence is thereby similar to the TKE-trigger (see Eq. 3.28). The critical CIN threshold CIN_{crit} is set to 10 J/kg to lessen the dominance of the lowest cloud layer which determines the subcloud convective inhibition $CIN_{u,subcl}$ in Equation 3.31. Donner et al. (2001) use the same threshold for a similar requirement on convective initiation.

Variable minimum cloud depth for deep convection

In HYMACS, the cloud depth of the parametrized updraft Δz_{cl} determines if deep convection with surface precipitation or shallow convection occurs. In previous version of HYMACS, a fixed threshold for the cloud depth to distinguish between both types of convection has been used with $D_{cl,min}^{deep} = 3000\,\mathrm{m}$. However, as stated by Kain (2004), this threshold appears to be inadequate for convective clouds where the ice phase plays a dominant role. A notable example constitutes the lake-effect snow during cold air outbreaks. Although the vertical growth of convective clouds is usually bounded by a boundary layer inversion, the rather shallow convective clouds may produce large amounts of snow and graupel (see, e.g., Niziol et al., 1995; Barthold and Kristovich, 2011). In order to account for the favor of precipitation formation under active ice phase processes, Kain (2004) suggest to let the minimum cloud depth for precipitating vary depending on the grid-scale temperature at the

parametrized LCL. Their empirical formula

$$D_{cl,min}^{deep} = \begin{cases} 2000\,\mathrm{m} & \text{for } T(z(LCL)) < 0°\mathrm{C} \\ 2000\,\mathrm{m} + k_D T(z(LCL)) & \text{for } 0°\mathrm{C} \le T(z(LCL)) \le 20°\mathrm{C} \\ 4000\,\mathrm{m} & \text{else} \end{cases} \tag{3.32}$$

with $k_D = 100\,\mathrm{m}/°\mathrm{C}$ is also applied with HYMACS in this thesis.

Organized detrainment near cloud top

The organized detrainment near the convective cloud top is considered to constitute an important process with HYMACS since its associated positive mass forcing induces compensational subsidence as well as grid-scale divergence (see Ch. 4 and Kuell et al. (2007)).

In former HYMACS versions, the dissolution of the updraft mass flux was assumed to occur exclusively in the model layer right below the CTL. Even though upper tropospheric layers in atmospheric models are typically much deeper than the layers near the cloud base, the overshooting beyond LNB may comprise more than one layer. Thus, in light of the *top-hat approximation*, the physical realism of organized detrainment confined to a single layer is questionable. Likewise, strong density tendencies in the presence of strong updrafts may jeopardize numerical stability, especially with increasing vertical resolution of the underlying model grid.

Inspired by the approach used in the Bechtold-Tiedtke scheme for organized detrainment (cf. Eq. 2.34), a revised procedure is pursued in this study. The analytical derivation is based on the conservation law of an arbitrary quantity ψ in a Boussinesq flow ($\rho = const.$) and follows De Rooy et al. (2013):

$$\frac{\partial \psi}{\partial t} + \nabla \cdot (\mathbf{v}\psi) = \frac{S_\psi}{\rho}. \tag{3.33}$$

Similarly to the hybrid approach[4], we consider a horizontal area of interest A which consists of a cloudy and an environmental area A_c and A_e (cf. Fig. 3.1) After integrating Equation 3.33 horizontally over the time and height varying convective area A_c and dividing by A to yield the fractional cloud cover σ_c, we arrive at

$$\frac{\partial}{\partial t}(\sigma_c \psi_c) + \frac{1}{A}\oint_\Gamma (\mathbf{v}_b - \mathbf{v}_{h,\Gamma}) \cdot d\mathbf{r} + \frac{\partial}{\partial z}(\sigma_c w_c) = \sigma_c \frac{S_{\psi,c}}{\rho}. \tag{3.34}$$

Here, the Leibniz rule and the Gauss theorem have been applied to derive Equation 3.34, where $S_{\psi,c}$ denotes the source term of the convective part only.

The second term denotes the flux of ψ over the interface Γ between the cloudy and cloud-free area resulting from the difference between the barycentric velocity and the velocity vector at the interface $\mathbf{v}_{h,\Gamma}$. Its horizontal component can therefore be interpreted as the net effect of entrainment and detrainment on the cloudy air

[4]Note that the density ρ is allowed to vary in the hybrid approach.

properties. With $\psi = 1$ and the assumption of steady-state conditions, one obtains after multiplying with ρ:

$$m_u(\epsilon_u - \delta_u) = -\frac{\partial}{\partial z}(\rho \sigma_c w_c), \tag{3.35}$$

where ϵ and δ denote the fractional entrainment and detrainment rates, respectively, and m_u constitutes the updraft mass flux per unit area.

In case that only organized detrainment occurs above the LNB , i.e. $\epsilon_u = 0$ and $\delta_u = \delta_u^{org}$, Equation 3.35 reduces to

$$\delta_u^{org} = -\frac{1}{w_c}\frac{\partial w_c}{\partial z}. \tag{3.36}$$

Thus, the organized detrainment profile can be determined by the buoyancy-driven deceleration above the LNB scaled by the inverse of w_c.

To come up with a formulation of the layer-integrated detrainment rate at full levels $D_u^{org}(k)$, the computation is related to the mass flux at the LNB $M_u(z(LNB))$. Since $M_u(z(LNB))$ enters a region where organized detrainment leads to the dissolution of the convective updraft, the detrained updraft fraction $r_u^{org}(k)$ can be obtained which yields

$$D_u^{org}(k) = r_u^{org}(k) M_u(z(LNB)) \quad \text{with } r_u^{org}(k) = \frac{\delta_u^{org}(k)}{\sum_{k=k_{LNB,fl}}^{k_{CTL,fl}} \delta_u^{org}(k)}. \tag{3.37}$$

Here, $k_{LNB,fl}$ and $k_{CTL,fl}$ denote the full-levels right above the LNB and right below the CTL, respectively. Since the detrained fraction $r_u^{org}(k)$ is computed from Equation 3.36, a flexible scheme for the dissolution of the updraft plume near the clout top is established.

4 Coupling HYMACS into the ICON model

The following chapter deals with the coupling HYMACS into ICON, the operational numerical weather prediction (NWP) model used at DWD since January 2015. While Kuell et al. (2007) have already implemented the scheme into the regional COSMO model, its implementation into ICON (model version 2.3.0 is used throughout this study) requires adaptions due to the different set of model equations and the associated implications on the physics-dynamics coupling. Furthermore, new challenges related to the grid geometry of the hosting model entail a careful reconfiguration of ICON's numerical filter for horizontal momentum.

Subsequently, a compact description of the ICON model is provided in Section 4.1 before details on the physics-dynamics coupling of HYMACS are outlined in Section 4.2. Section 4.3 demonstrates that the numerical filter used in the model's equation of horizontal motion leads to a distorted grid-scale dynamical response to subgrid-scale mass sources and sinks. Approaches to adopt the numerical filter while retaining an effective suppression of numerical modes inherent from the model's grid geometry are discussed in Section 4.4. Different alternative filter configurations are tested and compared in Section 4.5 in the scope of benchmark tests for dynamical cores. The best suited numerical filter is then applied in various mass lifting experiments to ensure the compatibility of a subgrid net mass transport with ICON's dynamical core (Sec. 4.6). Finally, a discussion wraps up the implementation of HYMACS into the new hosting model.

It is noted that this chapter largely reproduces work that was previously published in Langguth et al. (2020).

4.1 Model description of ICON

The ICON grid

As suggested by the acronym of the modeling framework ICON, the horizontal model grid is based on a spherical icosahedron which constitutes of 20 triangles with equilateral edges. Finer grids are then generated by refining these native triangle faces in a two-step subdivison procedure.

In the first step, each edge of the native triangles is divided into n_r equal arcs. The root division is then completed by connecting pairs of section endpoints with great circle arcs so that new n_r^2 triangles are formed. It's worth to note that the newly formed triangles are not equilateral anymore which is also related to the observation that their vertices are now shared by six triangles. By contrast, the vertices of the native triangles are shared by five cells only.

The application of successive k_b bisections on the triangle edges finalizes the mesh refinement procedure. Thereby, each bisection step forms four new triangles from each parent grid cell. The resulting so-called Rn_rBk_b grid can then be characterized by

$$n_c = 20n_r^2 4^{k_b}; \quad n_e = 30n_r^2 4^{k_b}; \quad n_v = 10n_r^2 4^{k_b} + 2 \tag{4.1}$$

cells, edges and vertices, respectively.

The spherical grid creation process finally undergoes a so-called *spring dynamics optimization* following Tomita et al. (2002). The spring dynamics minimize the distortion of the triangles which was introduced during the root division step.

In addition to the relatively homogeneous grid structure, the triangular grid based on a spherical icosahedron also allows for straightforward nesting. By performing a further bisection step, a regionally refined grid can be constructed as illustrated exemplary in Figure 4.1. Since the bisected parent cell results into four new quasi equilateral child cells, the child-to-parent feedback (upscaling from higher to lower resolution grid) becomes relatively straightforward. Due to this, ICON's grid structure eases the possibilities for efficient *two-way nesting* applications (see Prill et al., 2020, for more details).

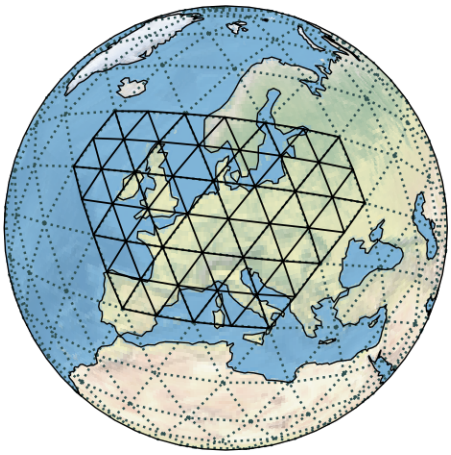

Figure 4.1: Exemplary illustration of a global triangular grid on the sphere with a regional nest centered over Western Germany. With a global R02B02-grid ($\Delta x_{ICON} \approx 631\,\text{km}$), the regional nest is a R02B03-grid ($\Delta x_{ICON} \approx 316.5\,\text{km}$) whose cell vertices coincide with the cell vertices and the cell edge midpoints of the parent grid cells.

In particular, this option is exploited operationally at DWD. While a R03B07-grid is used for global modeling of the atmosphere (ICON-global), a R03B08-nest is placed over Europe (ICON-EUnest). Expressing the grid spacing Δx_{ICON} by the square root of the averaged triangular cell area $\overline{A_c}$ on the sphere with radius $r_E = 6371\,\text{km}$ and using the relations from Equation 4.1, one obtains

$$\Delta x_{ICON} = \sqrt{\overline{A_c}} = \sqrt{4\pi r_E^2 / n_c} = \sqrt{\frac{\pi}{5}} \frac{r_E}{n_r 2^{k_b}}. \tag{4.2}$$

The above mentioned ICON grids have therefore a grid spacing of approximately 13 km and 6.5 km, respectively.

However, the triangular grid structure also comes along with some subtle downsides. The first systematic difficulty is related to the above mentioned grid distortion which cannot be completely removed on a spherical grid. As pointed out by Wan (2009) and Wan et al. (2013), the triangle distortion is most noticeable near the vertices of the native icosahedron which is prone to induce truncation errors and undesired numerical modes. Another weakness of the triangular grid is related to the representation of the horizontal wind vector. As discussed in detail by Gassmann (2013), alternating divergence patterns are favored on ICON's grid. Thus, as further elaborated in Section 4.4, a careful selection of efficient numerical filters is required.

In vertical direction, terrain-following height based coordinates are chosen which gradually change into levels of constant height with increasing altitude. More specifically, a variation of the hybrid Gal-Chen coordinate is used, where the signature of small-scale topographic features decays quicker than the signature of larger-scale features. The resulting Smooth LEvel VErtical (SLEVE) coordinate was developed by Schaeer et al. (2002) and Leuenberger et al. (2010) and is used operationally in ICON.

The model equations, the dynamical core and tracer advection

To predict the development of the atmosphere, the equation system for the prognostic variables suggested by Gassmann and Herzog (2008) is solved numerically in ICON. For this, it is assumed that atmospheric air constitutes a two-component system of dry air and water, where the latter can coexist in its three different phases, that are vapor (v), liquid and ice. Furthermore, a distinction between cloud and precipitable hydrometeors, i.e. cloud water/ice (l,i) and rain/snow/graupel (r,s,g), is made.

Using C-staggering on the above mentioned triangular grid (see Fig. 4.2a), the prognostic variables in ICON are the horizontal wind vector component normal to the triangle edges v_n, the vertical velocity w, the total density ρ, the Exner pressure π and the specific masses of the moisture tracers q^k with $k \in \{v, l, i, r, s, g\}$. After applying a density-weighted averaging procedure following Hesselberg (1926) together with the shallow atmosphere approximation, the model equation system reads as

$$\frac{\partial v_n}{\partial t} + \frac{\partial K_h}{\partial n} + (\zeta + f)v_t + w\frac{\partial v_n}{\partial z} = -c_{pd}\theta_v \frac{\partial \pi}{\partial n} - F_s(v_n) + F_d(\mathbf{v}), \tag{4.3}$$

$$\frac{\partial w}{\partial t} + \mathbf{v}_h \cdot \nabla w + w\frac{\partial w}{\partial z} = -c_{pd}\theta_v \frac{\partial \pi}{\partial z} - g + F_d(w), \tag{4.4}$$

$$\frac{\partial \rho}{\partial t} + \nabla \cdot (\rho \mathbf{v}) = \sum_{k \in \{r,s,g\}} \sigma_k^{conv}, \tag{4.5}$$

$$\frac{\partial \pi}{\partial t} + \frac{R_d}{c_{vd}} \frac{\pi}{\rho\theta_v} \nabla \cdot (\rho \mathbf{v} \theta_v) = Q_{\pi,dia} + F_d(\theta_v), \tag{4.6}$$

$$\frac{\partial (\rho q^k)}{\partial t} + \nabla \cdot (\rho \mathbf{v} q^k) = F_s(q^k) + I^k, \tag{4.7}$$

where the Hesselberg averaging operators are omitted for convenience[1]. Thus, the dynamical core of ICON solves the hydro-thermodynamical equations of a compressible, non-hydrostatic flow.

The following description focuses on the aspects that are most relevant for the coupling of HYMACS in ICON. If not stated differently, this description largely draws on literature that is dedicated to document the development of the ICON model, that are namely Wan et al. (2013), Zaengl et al. (2015), and Prill et al. (2020). Likewise, not all terms appearing in ICON's equation system (cf. Eqs. 4.3–4.7) are mentioned explicitly in the text. However, remaining symbols are listed in Table 4.1 along with a short description for the sake of completeness.

Of particular interest for this study are the forcing terms due to subgrid-scale transport processes on the right hand side of the Equations 4.3–4.7. These are the tendencies due to turbulent and convective fluxes of momentum and moisture tracers $F_s(v_n)$ and $F_s(q^k)$, respectively, the mass sink due to parametrized convective precipitation σ_k^{conv} with $k \in \{r, s, g\}$ and the diabatic heating effect on the Exner pressure $Q_{dia,\pi}$.

The latter term is part of Equation 4.6 which is based on the first law of thermodynamics expressed as a function of the virtual potential temperature θ_v. The formulation in terms of the Exner pressure π in ICON is achieved by exploiting various expressions for the relation between θ_v and π:

$$\begin{aligned} \pi &= \left(\frac{p}{p_{00}}\right)^{\frac{R_d}{c_{pd}}} = \left(\frac{R_d}{p_{00}}\rho\theta_v\right)^{R_d/c_{vd}} = \frac{T_v}{\theta_v} \\ \text{with} \quad \theta_v &= T_v\left(\frac{p_{00}}{p}\right)^{\frac{R_d}{c_{pd}}} \end{aligned} \tag{4.8}$$

In ICON, $p_{00} = 1000\,\text{hPa}$ is chosen while the specific heat capacities are set to $c_{pd} = 1004.64\,\text{J/(kg K)}$ and $c_{vd} = 716.6\,\text{J/(kg K)}$, respectively. The relations in Equation 4.8 are not only used to reformulate the first law of thermodynamics, but are also helpful when converting the tendencies from different physical processes to the diabatic term $Q_{dia,\pi}$. While more details on this term are provided

[1] Furthermore, forcing terms on v_n, ρ, θ_v and q^v due to the incremental analysis update method are omitted from the set of equations. These terms are only applied over a limited time window at the beginning of a model run when the model is started from an uninitialized analysis product. However, some details on these terms are provided in Appendix A.2.

Table 4.1: Description for the remaining symbols which occur in the prognostic system (Eqs. 4.3–4.7).

Symbol	Description
$\frac{\partial}{\partial n}$	horizontal derivative in edge-normal direction
v_t	tangential wind component; (v_n, v_t, w) form a right-handed system
$K_h = \frac{1}{2}\left(v_n^2 + v_t^2\right)$	horizontal kinetic energy
$\zeta = \mathbf{k} \cdot \nabla \times \mathbf{v}$	relative vorticity
f	Coriolis parameter
I^k	source/sinks due to phase changes

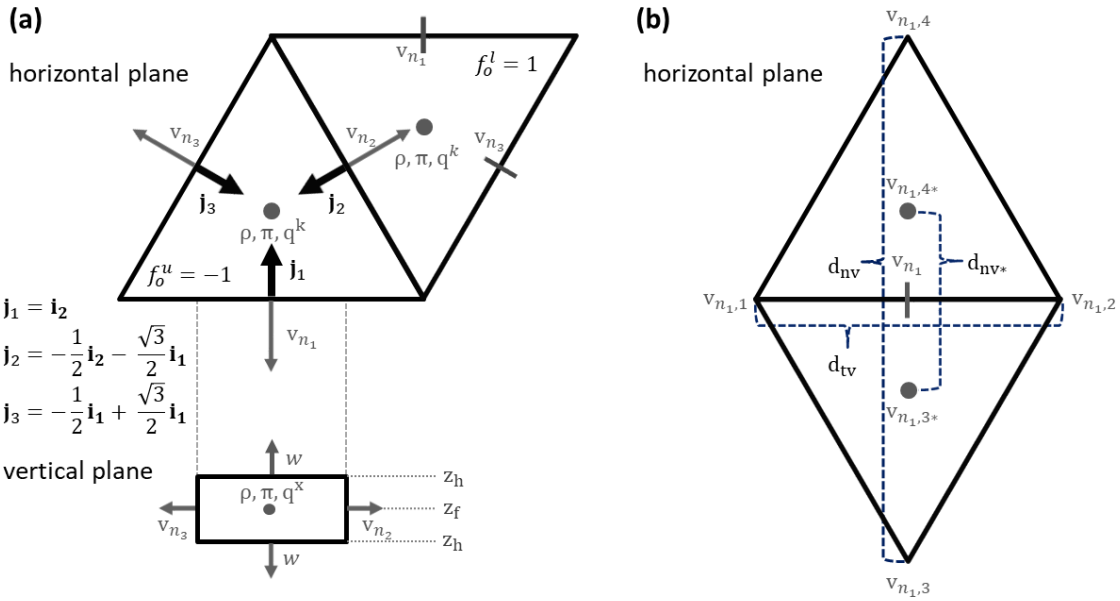

Figure 4.2: (a) Position of ICON's prognostic variables on a triangular C-grid in horizontal and vertical plane. In the horizontal plane, an upper-tip and a lower-tip triangle are illustrated with their corresponding orientation factor $f_o^{u,l}$. The basis vectors of the trivariate coordinate system $\mathbf{j}_i$ including their representation in Cartesian coordinates $\mathbf{i}_i$ are given as well. (b) Exemplary stencil used for discretizing the Laplacian operator (see Eq. 4.11 and 4.32) acting on v_{n_1}. The $v_{n_1,i(\star)}$ wind vector components on the vertices and cell centers are obtained with a radial basic function (RBF) vector reconstruction (Rípodas et al., 2009).

in Section 4.2, it is worth noting that $Q_{dia,\pi}$ also involves processes other than unresolved transports such as phase changes due to microphysical processes.

The numerous numerical filter terms $F_d(\psi)$ with $\psi \in \{\mathbf{v}, w, \theta\}$ in ICON's equation system ensure a high level of numerical stability in the dynamical core and yield a good performance in various benchmark tests for dynamical cores.

The numerical filter in the vertical wind equation (Eq. 4.4) and in the first law of thermodynamics (Eq. 4.6) comprises a Smagorinsky and a purely numerical fourth-order background diffusion, respectively. Details on their role and discretization are presented in Zaengl et al. (2015) and are therefore skipped here.

However, the numerical filter $F_d(\mathbf{v})$ employed in the prognostic equation of the edge-normal wind velocity v_n is of special interest in this study. While a more detailed discussion on its necessity follows in Section 4.4, the involved terms are briefly introduced here.

In ICON, $F_d(\mathbf{v})$ comprises two filter methods, that are horizontal diffusion and a quasi 3D divergence damping term

$$F_d(\mathbf{v}) = F_{d1}(\mathbf{v}_h) + F_{d2}(\mathbf{v}). \tag{4.9}$$

The horizontal diffusion operator is thereby twofold and constitutes a combination of a Smagorinsky and a fourth-order background (purely numerical) diffusion so that $F_{d1}(\mathbf{v}_h)$ can be further decomposed to:

$$F_{d1}(\mathbf{v}_h) = F_{smag}(\mathbf{v}_h) + F_{diff}(\mathbf{v}_h) = 4K_h(\mathbf{v}_h)\tilde{\nabla}^2(v_n) - k_4\tilde{\nabla}^2\left\{\tilde{\nabla}^2(v_n)\right\}. \tag{4.10}$$

The discrete Laplace operator acting on v_n in both filters is designed to match the edge point of operation with a conventional centered difference approach:

$$\tilde{\nabla}^2(v_n) = \frac{v_{n,2} - v_{n,1} - 2v_n}{d_{tv}^2} + \frac{v_{n,4} - v_{n,3} - 2v_n}{d_{nv}^2}. \tag{4.11}$$

This discretization is second-order accurate on equilateral triangles and requires a horizontal wind vector reconstruction by means of radial basis functions (RBF) to obtain $v_{n,i}$ at the neighbouring triangle vertices (Rípodas et al., 2009). An illustration of the stencil used for computing the Laplacian is given in Figure 4.2b.

The vector reconstruction on the vertices is also used to calculate the deformation of the horizontal flow that drives the Smagorinsky diffusion via K_h in Equation 4.10. While further details on F_{smag} can be found in Zaengl et al. (2015), it is worth mentioning that the fourth-order background diffusion F_{diff} is not applied to ensure numerical stability in ICON. Although acting as a scale-selective damping mechanism on kinetic energy near the smallest resolvable scale, it is rather tuned to yield a beneficial impact on the model dynamics over orography. Thus, the associated damping coefficient k_4, defined in terms of an „e-folding time to time step ratio“ τ_{v_n}, is typically chosen to be small. Besides, the both diffusion types are applied with a reduced calling frequency with respect to the temporal integration in the dynamical core (see below).

The fourth-order anisotropic divergence damping given by

$$\begin{aligned} F_{d2}(\mathbf{v}) = F_{div,4o}(\mathbf{v}) = -f_{d,4o}\overline{A_c}^2 \nabla_n \left[div \left\{ \nabla_n \left(D_h + \frac{\partial w}{\partial z} \right) \right\} \right] \\ \text{with} \qquad D_h = div(\mathbf{v}_h), \end{aligned} \tag{4.12}$$

is crucial for stabilizing the ICON's dynamical core and constitutes the second filter method in Equation 4.9. It acts on the three-dimensional divergence field and is called *anisotropic* since it is applied for horizontal momentum only. With a typical value range between 0.001 and 0.004 for the divergence damping coefficient $f_{d,4o}$, numerical stability was found to be warranted with ICON. In operational mode, the upper bound of this value range is chosen to optimize the simulation results.

The spatial discretization of the divergence operator div makes use of the Gauss theorem and reads as

$$div(\mathbf{F}) = \frac{1}{A_c} \sum_{i=1}^{3} \left(F_n l_e f_o^{l,u} \right). \tag{4.13}$$

Here, F_n denotes the normal component of the generic flux vector $\mathbf{F}$ over the triangle edges of length l_e. In order to distinguish between inward and outward directed fluxes of upper and lower triangles (see Fig. 4.2a), an orientation factor $f_o^{l,u}$ is introduced. The gradient in normal direction ∇_n is computed with a finite difference approach between two cell center values adjacent to the edge of operation.

Equation 4.13 is conceptually applied to any divergence term in ICON. However, in order to ensure efficient reduction of small-scale noise in v_n, no velocity averaging is performed in scope of the divergence damping (see Eq. 4.12). Such an averaging

procedure is otherwise involved to obtain a higher discretization accuracy of the flux vector **F** as described in the appendix of Zaengl et al. (2015).

A final remark on ICON's model equations pertains the mass conservation: By solving the continuity equation explicitly, mass conversation is ensured provided that the mass flux divergence term is properly handled in Equation 4.5. However, due to a simplified boundary condition at the surface neglecting sedimentation and evaporative fluxes, total instead of dry air is conserved in ICON. In other words, mass loss (gain) due to precipitation (evaporation) is not taken into account and it is assumed that a fictitious flux of dry air compensates sedimentation (evaporation). In agreement with the simplified boundary condition at the surface, the mass sink term due to parametrized convective precipitation σ_k^{conv} in the continuity equation of moist air (cf. Eq. 4.5) is set to zero.

The temporal integration of the model equation system except from the moisture tracers (cf. Eqs. 4.3–4.6) is performed with a predictor-corrector scheme in the dynamical core. Apart from the terms related to the propagation of sound waves in vertical direction, i.e. terms involving the vertical derivative of w and the Exner pressure π, such an integration procedure is still explicit in time while retaining a higher accuracy than a simple Euler forward scheme. However, the time step of the dynamical core is limited by the fastest modes in the system. In a fully compressible atmosphere, sound waves constitute the fastest mode which leads to the maximum recommended time step Δt_{dyn} given by

$$\Delta t_{dyn} = 1.8 \times 10^{-3} \frac{\mathrm{s}}{\mathrm{m}} \Delta x_{ICON}. \tag{4.14}$$

Based on the average distance between two cell centers[2] and using the speed of sound $c_{s,0} = 330\,\mathrm{m/s}$, this corresponds to a Courant number of about 0.68. Using Equation 4.14 also ensures numerical stability in the presence of high wind speeds exceeding 250 m/s at spatial resolutions resolving breaking gravity waves in the stratosphere. More details on the predictor-corrector scheme including a description of the implicit vertical wind solver are given in Appendix A.3.

The continuity equation of the moisture tracers (cf. Eq. 4.7) can be integrated with a less restrictive constraint on the time step. This is related to the fact that fast sound or gravity wave modes are not relevant for the tracer transport. Given that the wind and density field are prescribed, a reduced calling frequency of the tracer transport scheme with Δt_{tr} can be chosen. In ICON, a multiple of the dynamics time step is chosen, that is, $\Delta t_{tr} = n \Delta t_{dyn}$ with a default value of $n = 5$.

A Flux Form Semi-Lagrangian scheme with directional splitting is used for the tracer transport. While a detailed description is provided in Prill et al. (2020), tracer-mass consistency has to be ensured when a reduced calling frequency of the transport scheme is exploited to save computational costs. In addition to the basic physics-dynamics coupling in ICON, this aspect requires special attention with HYMACS as outlined in the upcoming section.

[2]The distance between two cell centers equals to $\frac{\sqrt[4]{3}\sqrt{3}}{2} \Delta x_{ICON} \approx 1.14 \Delta x_{ICON}$ on a plane.

4.2 Physics-dynamics coupling of HYMACS

4.2.1 Overview on the basic physics-dynamics coupling in ICON

In analogy to the tracer transport, fast modes such as sound and gravity waves are of minor relevance for the processes which are subject to physical parametrizations. Thus, the parametrization schemes are not called at every dynamical time step, but at maximum with a frequency of $\Delta t_{phy} = \Delta t_{tr}$. Likewise, although their effect on the atmospheric states excites fast modes such as the generation of gravity waves due to diabatic heating, they are fed with a filtered atmospheric state. Particularly, the above mentioned diffusion filters, the Smagorinsky and the background diffusion $F_{d1}(\mathbf{v}_h), F_d(w)$ and $F_d(\theta_v)$, are applied to the atmospheric state before it enters the computation of the physical processes.

For efficiency reasons, a further distinction between *slow* and *fast* physical processes is made in ICON. While the former constitutes processes whose time scale is longer than the physical time step Δt_{phy}, the latter are considered to have a shorter time scale. Saturation adjustment and microphysical processes are examples for fast-physics processes, whereas, for instance, radiation interaction and convection belong to the group of slow physics.

The numerical treatment of the two different groups differs substantially from each other: Parametrizations of fast-physics processes are called sequentially at every physical time step $\Delta t_{phy} = \Delta t_{i,fast}$ and directly act on the atmospheric state. This so-called sequential-update split means that each process passes a new state to the subsequent parametrization since its effect is taken into account instantaneously. While this implies that the sequence order matters, saturation adjustment is applied twice at the beginning and at the end of the chained of fast-physics processes to ensure an adjusted final state with respect to moisture. In between, the surface transfer, the land-surface, the turbulent vertical diffusion and the microphysics scheme are called.

The slow processes do not update the atmospheric state in place, but provide tendencies to the dynamical core. Besides, they are not explicitly depending on each other since they are fed with the atmospheric state from the dynamical core which has already been updated by the (moisture) tracer advection, the numerical diffusion and the fast-physics processes. Such a method is also known as the *parallel split* approach. Due to the rather long characteristic time scales, the respective parametrization schemes are called with a (further) reduced frequency $\Delta t_{i,slow} = n_i \Delta t_{phy}$. The calculated tendencies are then held constant over this time period. Since different integer prefactors n_i can be chosen, indirect dependencies may occur. In ICON, the radiation scheme is always called together with the convection scheme (Prill et al., 2020), although n_{rad} is typically greater than n_{conv}. Thus, n_{rad} has to be a multipler of n_{conv}, where the latter is usually chosen to yield $\Delta t_{conv,slow} \approx 1 - 10\,\text{minutes}$. In addition to convection and radiation, the subgrid-scale cloud cover scheme as well as the non-orographic and orographic gravity wave drag are treated as slow-physics processes.

A schematic overview on the time-stepping in ICON is given in Figure 4.3. Note

that the numerical diffusion applied at each physical time step Δt_{phy} is included in the overview, while the divergence damping acting at every dynamical time step Δt_{dyn} is omitted for convenience.

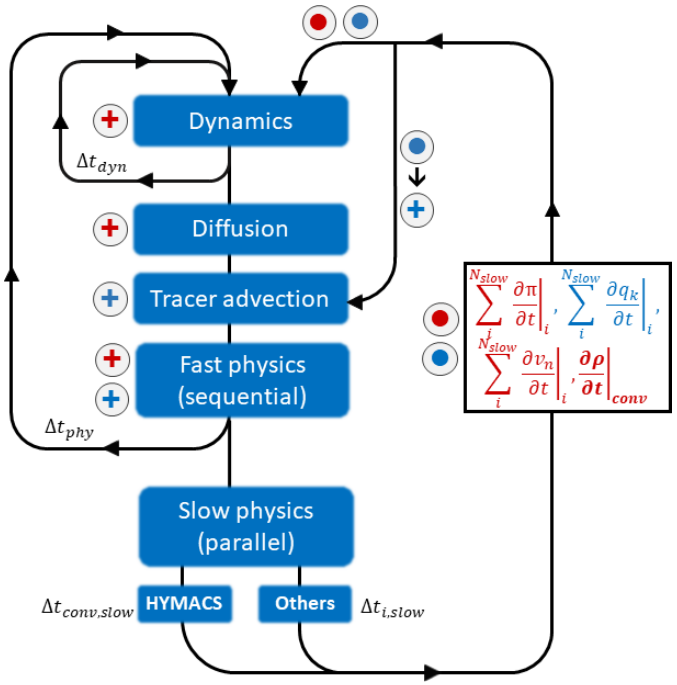

Figure 4.3: Illustration of ICON's time-stepping approach. The +-symbols denote operators which update the atmospheric state in place, while the •-symbols represent forcing terms that are integrated into the dynamical core (see tendencies in the box). Updates and forcing of the moisture species are highlighted in blue. The moisture tendencies from the slow physics update the tracer field in place after the advection, whereas they are also part of the forcing on the Exner pressure π. The convective density tendency highlighted in bold is exclusively provided by HYMACS.

As pointed out in Zaengl et al. (2015), a remarkable difference in ICON compared to many other NWP models pertains its isochoric coupling strategy. Due to the explicit usage of the continuity equation in the model equation set (see Eq. 4.5), the density ρ is kept constant in the physics-dynamics interface. By contrast, physical parametrizations inherited from other models usually assume an isobaric ($p = const.$) coupling. As a consequence, the tendencies from slow-physics processes, e.g. from parametrized radiative flux divergences, are adopted by re-scaling them with c_{vd}/c_{pd}. After re-scaling, the final transformation to the Exner pressure tendency reads

$$\left.\frac{\partial \pi}{\partial t}\right|_{i,slow} = \frac{R_d}{c_{pd}} \frac{1}{\theta_v} \left((1+\alpha) \left.\frac{\partial T}{\partial t}\right|_{i,slow} + T \left.\frac{\partial \alpha}{\partial t}\right|_{i,slow} \right) \tag{4.15}$$

where also changes to the virtual moisture increment α must be taken into account. Since several slow physics processes are part of the total forcing $Q_{dia,\pi}$ in Equation 4.6, summation of individual Exner pressure tendencies is performed with

$$Q_{dia,\pi} = \sum_i^{N_{slow}} \left.\frac{\partial \pi}{\partial t}\right|_{i,slow}, \tag{4.16}$$

where N_{slow} is the number of all slow-physics processes parametrized.

Also related to the usage of the full air density ρ as one of the prognostic equations is that a hydrostatically integrated pressure instead of the non-hydrostatic pressure enters some parametrization schemes. In these schemes, the air pressure is used to calculate the air mass of a model layer (e.g. in the operational Bechtold-Tiedtke convection scheme). However, with a non-hydrostatic dynamical core the pressure is not a proxy for the air mass since the hydrostatic relation $-\Delta p = g\rho\Delta z$ is not valid anymore. Notably, the pressure may even decrease in the presence of strong diabatic heating near the surface as pointed out in Prill et al. (2020).

Furthermore, the physical parametrization schemes usually work on mass points. Thus, when providing a horizontal momentum tendency, the interpolation to the edge midpoints followed by a projection of $\mathbf{v}_h$ onto v_n, the respective prognostic variable in ICON, may be inaccurate. A pragmatic way to reduce the interpolation errors was found by interpolating the velocity increments rather than the full velocities (Zaengl et al., 2015).

4.2.2 Coupling details of HYMACS

In terms of the time-split approach, the coupling of HYMACS does not differ from the coupling of the operationally used Bechtold-Tiedtke scheme. Thus, convection with HYMACS is a slow-physics process which effects the grid-scale atmospheric state by providing tendencies to the dynamical core.

As stated in Section 3.2, HYMACS computes convective tendencies of density, enthalpy, momentum and of the specific moisture quantities. The latter does not comprise precipitating hydrometeors which are formed only in case of parametrized deep convection. Since no detrainment of precipitation particles from the downdraft takes place, they are treated in an isolated manner in HYMACS.

The inclusion of the convective momentum and moisture tendencies is straightforward. The pre-existing interface routines of the ICON model[3] can be used, given that the net mass transfer effect is already considered by using Equation 3.13.

As the total density ρ is one of the model's prognostic variables, the implementation of the convective density tendency is also fairly uncomplicated, albeit a corresponding term is not involved in ICON's original interface routine due to the isochoric coupling approach. The net mass transfer effect is directly passed to the dynamical core and added as a forcing term in the continuity equation by employing

$$\frac{\partial \rho}{\partial t} + \nabla \cdot (\rho \mathbf{v}) = \left.\frac{\partial \rho}{\partial t}\right|_{conv}, \tag{4.17}$$

where the term on the right hand side (RHS) is given by Equation 3.4. Here, it is worth noting that $\mathbf{v}$ denotes the (Hesselberg averaged) *grid-scale* wind-vector only. Following the notation used in Section 3.1, this corresponds to the environmental velocity vector $\mathbf{v}_e$.

Furthermore, it is noted that the mass loss due to precipitation is naturally taken into account with HYMACS. However, since moist air is conserved with

[3]The physics-dynamics interface module is part of the `mo_nh_interface_nwp.f90`-routine in ICON's model source code.

ICON (see Sec. 4.1), this mass loss has to be compensated for consistency. Thus, a fictitious flux of dry air is added to the mass flux divergence of the downdraft in the lowest model layer which counteracts the convective sedimentation.

For the convective forcing in the prognostic equation of the Exner pressure π (see Eq. 4.6), the transformation equation for the isochoric physics-dynamics coupling as stated in Equation 4.15 does not apply anymore. Instead, a re-derivation based on the first law of thermodynamics expressed in terms of the enthalpy is required to account for the net mass fluxes with the hybrid scheme:

$$\begin{aligned} c_p \frac{d}{dt}(\rho T) - c_p T \frac{d\rho}{dt} - \frac{dp}{dt} &= Q_{dia,h} \\ &= Q_{dia,h}\big|_{noconv} + \rho \frac{\partial h}{\partial t}\bigg|_{conv} . \end{aligned} \tag{4.18}$$

Here, the diabatic forcing $Q_{dia,h}$ is splitted into a non-convective (due to phase changes, radiation etc.) and a convective part that is provided by HYMACS.

While a step-by-step derivation is presented in Appendix B of Langguth et al. (2020), Equation 4.18 can be rewritten to yield a formula for the local tendency of the Exner pressure π:

$$\begin{aligned} \frac{\partial \pi}{\partial t} = -c_{pd}\pi \nabla \cdot (\rho \mathbf{v} \theta) + \frac{R_d}{c_{vd}} \pi \Bigg(& \frac{1}{1+\alpha} S(\alpha)\big|_{noconv} + \frac{1}{1+\alpha} \frac{\partial \alpha}{\partial t}\bigg|_{conv} \\ & + \frac{1}{\rho c_{pd} T} Q_{dia,h}\big|_{noconv} + \frac{1}{h} \frac{\partial h}{\partial t}\bigg|_{conv} + \frac{1}{\rho} \frac{\partial \rho}{\partial t}\bigg|_{conv} \Bigg). \end{aligned} \tag{4.19}$$

In this equation, the convective tendencies of the moisture species q^k are gathered in a convective tendency of the virtual moisture increment α which reads

$$\frac{\partial \alpha}{\partial t}\bigg|_{conv} = \left(\frac{R_v}{R_d} - 1 \right) \frac{\partial q^v}{\partial t}\bigg|_{conv} - \sum_{k \neq \{v,d\}} \frac{\partial q^k}{\partial t}\bigg|_{conv} . \tag{4.20}$$

Changes in the α due to non-convective transports and phase changes are part of the short cut term $S(\alpha)\big|_{noconv}$.

By collecting the convective tendencies in Equation 4.19, the Exner pressure tendency $Q_{dia,\pi}\big|_{conv}$ is given by

$$Q_{dia,\pi}\big|_{conv} \equiv \frac{\partial \pi}{\partial t}\bigg|_{conv} = \frac{R_d}{c_{vd}} \pi \left(\frac{1}{1+\alpha} \frac{\partial \alpha}{\partial t}\bigg|_{conv} + \frac{1}{\rho} \frac{\partial \rho}{\partial t}\bigg|_{conv} + \frac{1}{h} \frac{\partial h}{\partial t}\bigg|_{conv} \right), \tag{4.21}$$

where all terms are provided by the hybrid scheme (see Sec. 3.2).

This expression is thereby easily transferred to Equation 4.15 describing the diabatic forcing of other parametrization schemes in ICON. Setting the density tendency to zero and replacing $h = c_{pd}T$, the same transformation relation is recovered, given that the above mentioned rescaling with c_{vd}/c_{pd} is performed.

It is also noteworthy that each summand of the convective Exner pressure tendency has a prefactor of grid-scale variables. As shown and discussed in Appendix A.1, this enables a partly implicit formulation of the diabatic forcing which

was found to enhance the numerical stability. By evaluating the grid-scale variables in Equation 4.21 *after* the update due to convection at the intermediate time level $\tilde{n}^\star$, the forcing on the Exner pressure π can be written as

$$\begin{aligned} \left.\frac{\partial \pi}{\partial t}\right|_{conv} &= \frac{A_\pi^\star}{A_\pi}\pi^n \\ \text{with} \quad A_\pi &= c_{vd} - R_d \Delta t_{dyn}\left(\frac{1}{h^{\tilde{n}^\star}}\left.\frac{\partial h}{\partial t}\right|_{conv} + \frac{1}{1+\alpha^{\tilde{n}^\star}}\left.\frac{\partial \alpha}{\partial t}\right|_{conv} + \frac{1}{\rho^{\tilde{n}^\star}}\left.\frac{\partial \rho}{\partial t}\right|_{conv}\right) \\ \text{and} \quad A_\pi^\star &= \frac{c_{vd} - A_\pi}{\Delta t_{dyn}}. \end{aligned} \tag{4.22}$$

A final remark on the coupling of HYMACS pertains the moisture transport scheme. In agreement with the basic isochoric physics-dynamics coupling approach, it is assumed that mass fluxes occur on grid-scale only. However, not accounting for the net mass transfer with HYMACS in the coupling of the Semi-Lagrangian transport scheme breaks up the so-called *consistency with continuity* which in turn then induces inconsistencies in the temporal integration of the LHS of Equation 4.7. As a result, strong buoyancy effects may occur which result in intense grid-scale lifting ($w >> 10\,\mathrm{m/s}$) and excessive grid-scale precipitation. However, for the sake of brevity, details on handling the net mass transport consistently with the moisture tracer transport scheme is put to the Appendix A.2 and we proceed with stating that a proper adaption was performed in this study.

4.3 Dynamical flow distortion in the mass lifting experiment

With the adopted physics-dynamics coupling of HYMACS in ICON, it becomes necessary to check that the expected response due to a net mass transport is reproduced in the new hosting model.

From the literature, it is well known that the effect of a local mass source and sink on the atmospheric state is manifold and therefore was addressed in idealized frameworks in some studies. Oftentimes, the geostrophic adjustment due to a subgrid-scale net mass transport was of particular interest (e.g. Gill, 1981; Shutts, 1994, 1995) and was identified as playing an important role in shaping the dynamics of mesoscale convective systems (e.g. Gray et al., 1998; Gray, 1999). Excited inertia-gravity waves as a response to local mass sources are also known to be crucial for stabilizing the environment of convective cells up to the Rossby deformation radius (Bretherton and Smolarkiewicz, 1989; Chagnon and Bannon, 2005a). Finally, a distinct flow response with forced divergence (convergence) around a local mass source (sink) is expected due to continuity.

In order to ensure compatibility with the hosting model, Kuell et al. (2007) performed idealized dry mass lifting experiments with HYMACS in COSMO and investigated the simulated dynamical flow response in detail. This approach is taken up here by employing an analogous set-up of the ICON model while the

experiments are also repeated with the COSMO model (version 5.1) for comparison purposes. As it turns out subsequently, this sanity check is mandatory since an adopted physics-dynamics coupling is not necessarily sufficient to ensure the compatibility of HYMACS in a new hosting model.

4.3.1 The set-up of the mass lifting experiment

For the mass lifting experiment proposed by Kuell et al. (2007), a dry, polytropic atmosphere at rest is set up. A constant lapse rate $\Gamma = -\partial T/\partial z$ is chosen which can be varied to analyze the dynamical flow response under differing atmospheric stratification. For the *standard* case, $\Gamma = 6\,\mathrm{K/km}$ is chosen. Thus, the background atmosphere is stably stratified.

In the central grid column of the model domain, the net mass transfer due to a convective cell is imitated. Using an equidistant vertical grid with a layer depth of $\Delta z = 300\,m$, a mass sink is placed at the lowest model layer. The counterpart of the organized entrainment layer is placed at higher altitudes with a top height of 9 km. According to the typical life cycle of a deep convective cell, mass is convected for one hour at a mass flux rate which overturns a 60 hPa deep layer over this period. In order to isolate the effect of the subgrid-scale mass transfer, the entrained air at high altitudes gets the same temperature as the environment. Thus, the enthalpy tendency vanishes and potential energy is added to the system.

A planar model grid neglecting the curvature of the Earth with double-periodic boundary conditions, i.e. a so-called Torus grid, is applied. The Coriolis force is set to zero so that no geostrophic adjustment accompanies the forcing.

Following Kuell et al. (2007), a horizontal grid spacing of $\Delta x_{cos} = 0.0625 \approx 6.95\,\mathrm{km}$ is used in the reference COSMO simulation. Hence, a grid spacing at convective gray-zone resolution is chosen at which the application of HYMACS is considered to be beneficial[4]. Due to the triangular grid, an equivalent set-up is not possible in ICON. However, in order to ensure reasonable comparability, the grid cell area is equalized between the two models translating to an edge length $l_E = 10.5\,\mathrm{km}$ of the triangular cells in ICON. The total domain size is about 375 km in both horizontal directions which allows us to neglect inference effects of emitted fast waves on the Torus grid. The Rayleigh sponge between 14 km altitude and the model top at 20.7 km damps reflection of vertically propagating gravity waves.

4.3.2 Results from the COSMO reference simulation

To get an overview of the expected dynamical flow response, Figure 4.4 displays the results of the COSMO simulation. Despite a revised dynamical core and some changes in the configuration of the numerical filter, they are in good agreement with Kuell et al. (2007) which confirm their usability as a reference simulation.

As seen from Figure 4.4(a,b), the initiation of the mass transfer results in the emission of grid-scale gravity waves which become visible as oscillations in the

[4]The specific value of Δx_{cos} corresponds to the grid spacing used by the COSMO-EU configuration/ LM model which was operational at DWD until end of November 2016.

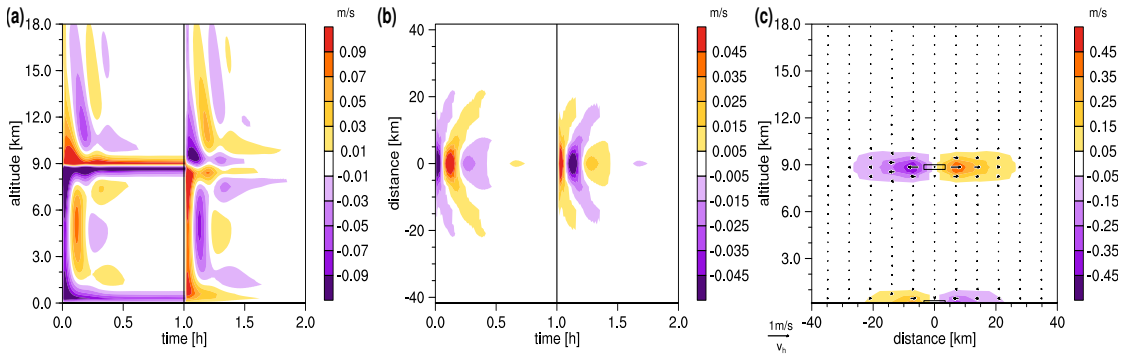

Figure 4.4: Dynamical flow response in the mass lifting experiment with COSMO. (a) Time series of the *grid-scale* vertical wind $\overline{w}$ in the convective grid column. (b) Time series of $\overline{w}$ on a horizontal plane in x-direction at z = 4500 m. (c) Vertical cross-section through the convective cell in x-direction after 30 min. of mass transfer. The color shading shows the amplitude of the radial component of the plotted wind vectors. The vertical lines in (a, b) highlight the end of the mass transfer. The results may be compared with Figure 2a in Kuell et al. (2007). From Langguth et al. (2020).

vertical wind field. The gravity waves are radiated from the mass source and sink in horizontal and vertical direction interfering at a height of 5 km as seen from the local amplitude maximum of the vertical wind (Fig. 4.4a). In horizontal direction, a vertical wind signal with an amplitude of at least 0.01 m/s is invoked up to a distance of 20 km.

Following the initial gravity wave period, the flow pattern becomes rather stationary. After about 20-30 minutes, the flow pattern is characterized by continuous, three dimensional grid-scale mass-flux divergence (convergence) which counteracts the local mass source and sinks (see Fig. 4.4c). Thus, in addition to the horizontal outflow (inflow) extending vertically over several grid levels, a strong dipole in the vertical wind field is established. The absolute value of w at the edges of the entrainment/detrainment layer attain values of approximately 0.1m/s.

After switching off the subgrid mass transfer, the imposed perturbation again leads to the emission of gravity waves with opposing sign in the vertical wind field compared to onset of the mass transport. However, due to the missing forcing, not only the gravity wave activity starts to fade away, but also the continuous inflow (outflow) around the former mass source (sink) decays. Thence, the system is restored to a new equilibrium with vanishing horizontal pressure gradients and a hydrostatic stratification. Note that the center of mass is placed higher due to the supply of potential energy during the forcing period.

4.3.3 Results from the ICON simulation with the operational numerical filter

When the mass lifting experiment is performed with the operational filter configuration in the horizontal momentum equation in ICON, the dynamical flow response severely differs from the aforementioned reference simulation with COSMO. As seen in Figure 4.5a, the grid-scale flow response is clearly distorted with a sharp gradient of the horizontal wind in vertical direction around the forcing layers.

While outflow (inflow) still counteracts the subgrid-scale mass source (sink), the horizontal flow pattern becomes even convergent (divergent) in the mass source (sink) layer (see Fig. 4.5b).

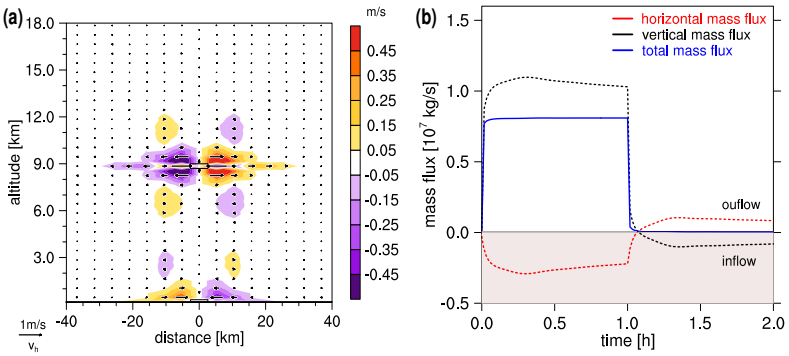

Figure 4.5: Distorted dynamical flow response with the operational numerical filter configuration in ICON. (a) Vertical cross-section through the convective cell in x-direction after 30 min. of mass transfer as Figure 4.4c. Every second wind vector results from an interpolation due to ICON's triangular grid. (b) Time series of the mass flux through the lateral boundaries of the organized detrainment box. Here, outflow (inflow), that is mass flux divergence (convergence), takes place for positive (negative) values. Redrawn from Langguth et al. (2020).

The reason for the unphysical evolution of the grid-scale fluxes can be attributed to the anisotropic fourth-order divergence damping term appearing in Equation 4.12. As mentioned above, the local mass source and sink induce a dipole in the vertical wind field which leads to a strong contribution of the $\partial w/\partial z$ term in Equation 4.12. Although an analogous contribution is expected from the horizontal divergence, it is only the horizontal flow which gets affected by the divergence damping. Interpreting the divergence damping term as a hyper-viscosity for the horizontal wind, the horizontal outflow (inflow) in the vicinity of the mass source (sink) gets hampered. In turn, the compensating mass fluxes in vertical direction are favored which further fosters the effect on v_n. Thence, the flow response to a net mass transfer becomes crucially dependant on the damping coefficient $f_{d4,o}$ as verified by sensitivity experiments (not shown).

It is worth noting that the same flow distortion can be reproduced with COSMO when the operational second-order divergence damping is applied. While the experiments in Kuell et al. (2007) have been performed with deactivated divergence damping so that numerical diffusion becomes the only filter acting on the horizontal wind, *isotropic* divergence damping is applied in the COSMO reference simulation presented in this study. The term *isotropic* thereby means that the vertical wind also gets explicitly affected by the divergence damping. As discussed in Gassmann and Herzog (2007), this approach is appealing since the gravity wave modes remain unaffected in this case. In conjunction with HYMACS, one may even claim that this is the *only* way to achieve a proper representation of the dynamical flow response to local mass sources and sinks, at least when the full three-dimensional divergence is used for damping (see below).

The option for applying an isotropic divergence damping was made available with the new fast wave solver in COSMO version 4.24. Details on its implemen-

tation and a discussion on its high stability properties in the dynamical core of COSMO can be found in Baldauf (2013).

While Skamarock and Klemp (1992) and Baldauf (2010) highlight the role of the divergence damping in warranting numerical stability in dynamical cores exploiting a time-split approach, the application of the (anisotropic) divergence damping in ICON is strongly related to the triangular grid geometry. Before seeking for a revised numerical filter configuration, further clarification on this topic is provided in the following section.

4.4 On the role of numerical filters in ICON

Despite the appealing option for straightforward nesting, the triangular grid comes along with a subtle, but systematic problem in properly representing horizontal vector quantities such as $\mathbf{v}_h$. As already noted during the development of the hydrostatic dynamical ICON core, this issue translates into a checkerboard pattern of the divergence field, that is an alternating sign of the divergence between two adjacent grid cells (Wan, 2009). Such noise pattern at lowest grid-scale can potentially conceal *real* physical processes and may also jeopardize numerical stability. Thus, it is mandatory to minimize their excitement or, if possible, to avoid them completely.

Special attention to the checkerboard pattern on triangular grids has been dedicated in several studies over the last decade (Danilov, 2010; Gassmann, 2011; Wolfram and Fringer, 2013). As commonly argued, the issue stems from the impossibility of properly handling the additional degree of freedom of the mass field with respect to the velocity field on a triangular C-grid. To seek for an alternative approach to mitigate the checkerboard problem while also avoiding the severe flow distortion due to a net subgrid mass transfer, an overview on this issue is given. The description largely draws on the comprehensive analysis provided in Gassmann (2011).

Using a triangular C-grid staggering as shown in Figure 4.2a, it is convenient to investigate the vector representation of the horizontal wind $\mathbf{v}_h$ and all involving differentiation operators (i.e. divergence, gradient and Laplace operator) in terms of a trivariate coordinate system with coordinate lines x_1, x_2 and x_3. Hence, $\mathbf{v}_h$ can be represented either by using common Cartesian basis vectors $\mathbf{i}_i$ or by using the basis vectors $\mathbf{j}_i$ of the planar trivariate coordinate system

$$\mathbf{v}_h = u\mathbf{i}_1 + v\mathbf{i}_2 = v_{n_1}\mathbf{j}_1 + v_{n_2}\mathbf{j}_2 + v_{n_3}\mathbf{j}_3. \tag{4.23}$$

It is easily seen that the basis vectors $\mathbf{j}_i$ are linear dependent[5] since $\sum_i \mathbf{j}_i = \mathbf{0}$. The linear dependency of the basis vectors results in a linear dependency of the velocity components v_{n_i} which are defined by projection of $\mathbf{v}_h$ onto the respective basis vector $\mathbf{j}_i$:

$$v_{n_1} + v_{n_2} + v_{n_3} = \mathbf{v}_h \cdot (\mathbf{j}_1 + \mathbf{j}_2 + \mathbf{j}_3) = 0. \tag{4.24}$$

[5]Note that the linear dependency holds for representations of any arbitrary vector.

A similar constraint holds for the gradient components of any arbitrary scalar ψ:

$$\frac{\partial \psi}{\partial x_1} + \frac{\partial \psi}{\partial x_2} + \frac{\partial \psi}{\partial x_3} = 0. \tag{4.25}$$

The above given laws in continuous space must also be satisfied by their discretized counterparts. Even though Gassmann (2011) remarks that the constraint for the staggered normal wind components v_{n_i} does not have to be fulfilled at the edge midpoints, she states that the discrete analog to Equation 4.24 has to be met after applying an averaging operation:

$$\widetilde{v_{n_1}}^1 + \widetilde{v_{n_2}}^2 + \widetilde{v_{n_3}}^3 = 0. \tag{4.26}$$

Following Thuburn (2008), the tilde averaging operator is defined by

$$\widetilde{v_{n_1}}^1 = \frac{1}{3}\left(\overline{v_{n_1}}^1 + 2\overline{\overline{v_{n_1}}^2}^3\right), \tag{4.27}$$

where $\overline{(\cdot)}^i$ denotes an arithmetic average between two adjacent values in x_i-direction.

Together with the definition of this averaging operator, Equation 4.26 can be translated to a constraint for the horizontal divergence of the six triangles sharing a vertex (and a constraint for the relative vorticity on its dual hexagonal C-grid). Whenever this constraint is violated, a checkerboard pattern occurs with alternating signs in the divergence of adjacent upper-tip and lower-tip triangles.

A direct consequence is that all the terms involved in the prognostic momentum equation also have to obey the given laws. Unfortunately, this principle is not realizable with C-staggering on a triangular grid. More specifically, as shown in Gassmann (2011), the edge-normal gradient of the Exner pressure (see Eq. 4.3) cannot be constrained without employing an effective D-grid staggering. However, staggered D-grids are known to suffer from a poor representation of the group velocity during geostrophic adjustment (Schoenstadt, 1980) and are therefore generally avoided in atmospheric modelling. It is also worth to mention that averaging of the divergence terms in ICON's prognostic equation system (see Sec. 4.1) only veils the checkerboard pattern.

However, the operational anisotropic fourth-order divergence damping (hereinafter OP4DD) has proven to be an efficient numerical filter so that computational modes are considered to be well controlled in ICON. This can be readily seen from the results of various dynamical core tests such as the Jablonowski-Williamson or the Schaer mountain test (Zaengl et al., 2015) or from real case applications (e.g. Crueger et al., 2018). Nowadays, the operational ICON model at DWD belongs to the worlds' leading global NWP models (see Fig. 14-18 in Haiden et al., 2019).

Due to the incompatibility of the anisotropic divergence damping with local mass sources and sinks (see Sec. 4.3.3), the central task is to construct a numerical filter achieving the following properties besides the compatibility with HYMACS:

i) Efficient mitigation of the checkerboard pattern in the divergence field and

ii) comparable behaviour of the dynamical core with the alternative filter compared to the well-tested operational configuration in benchmark tests.

An intuitive modification of the operational numerical filter in light of the previous discussion is the omission of the vertical divergence term from the fourth-order divergence damping (cf. Eq. 4.12):

$$F'_{div,4o}(\mathbf{v}_h) = -f'_{d,4o}\overline{A_c}^2 \nabla_n \left[div \left\{ \nabla_n (D_h) \right\} \right]. \tag{4.28}$$

Note that a distinction between the coefficient $f_{d,4o}$ of the OP4DD-operator acting on the 3D divergence and the revised one, $f'_{d,4o}$, is made since they can be chosen differently from each other.

It can be expected that the revised numerical filter given by Equation 4.28 still provides efficient control on the checkerboard mode since its actual requirement stems from the horizontal grid geometry. This filter method is thereby well established in dynamical cores of other atmospheric models. For instance, the Community Atmosphere Model 5 (CAM 5; Lauritzen et al., 2012) and the GFDL Finite-Volume Cubed-Sphere Dynamical Core (FV3; see Lin et al., 2017; Ullrich et al., 2017) make use of a fourth-order divergence damping acting on D_h. The latter is implemented within the operational Global Forecast System (GFS) at the US' National Weather Service (NWS) since the 12$^{\text{th}}$ June 2019. Nonetheless, omitting the vertical divergence may result into damping effects on gravity wave modes. Skamarock and Klemp (1992) argue that gravity waves are almost non-divergent which motivates the inclusion of the full 3D-divergence in the numerical filter. Considering the scale-selective property of a relative high order filter, especially short gravity waves (relative to grid-scale) might be affected due to the application of Equation 4.28.

According to the results of the COSMO reference simulation (see above), the application of a second-order, *isotropic* divergence damping is an appealing candidate. Technically, this means that the corresponding damping $F_{div,2o}(\mathbf{v})$ does not only enter ICON's prognostic equation for v_n, but also the w-equation:

$$F_{div,2o}(\mathbf{v}) = F^{v_n}_{div,2o}(\mathbf{v}) + F^{w}_{div,2o}(\mathbf{v}) = f_{d,2o}\overline{A_c} \left\{ \nabla_n \left(D_h + \frac{\partial w}{\partial z} \right) + \frac{\partial}{\partial z} \left(D_h + \frac{\partial w}{\partial z} \right) \right\}. \tag{4.29}$$

The first summand in the bracket corresponding to $F^{v_n}_{div,2o}(\mathbf{v})$ enters the horizontal momentum equation like the fourth-order divergence damping terms (cf. Eq. 4.3). However, the second summand equating to $F^{w}_{div,2o}(\mathbf{v})$ has to be included into the implicit scheme used for solving the vertical wind equation in ICON (cf. Eq. 4.4) since the vertical derivative of w pertains a term related to the vertical propagation of sound waves. A description of the extended implicit vertical wind solver in ICON is given in Appendix A.3.

While the neutral impact on gravity waves is a clear advantage of this filter technique, its effect on the inherent checkerboard pattern is expected to be limited due to the weaker scale selectivity of a lower-ordered scheme (see, e.g., Whitehead et al., 2011). Thus, the isotropic, second-order divergence damping is not tested as a stand-alone filter in this study, but rather combined with the revised fourth-order divergence damping mentioned above (named NEWCDD subsequently):

$$F_{d2,new} = F'_{div,4o}(\mathbf{v}_h) + F_{div,2o}(\mathbf{v}). \tag{4.30}$$

Thus, the main objective of $F_{div,2o}$ is to allow for a slightly reduced strength of the anisotropic fourth-order divergence damping acting on D_h, while retaining a high efficiency in removing checkerboard noise. This is considered beneficial due to the potentially degrading impact on gravity waves mentioned above.

Instead of divergence damping, hyper-diffusion is another common technique to reduce undesired computational modes. However, when such an approach is pursued, the application of the diffusion operator[6] should not only be applied at every physical time step Δt_{phy}, but has to be integrated into the dynamical core. This means that $F_{d2}(\mathbf{v})$ is dropped from $F_d(\mathbf{v})$ in Equation 4.9, while

$$F_{diff}(\mathbf{v}_h) = -k_4 \tilde{\nabla}^2 \left\{ \tilde{\nabla}^2 (v_n) \right\} \tag{4.31}$$

then operates at every dynamical time step Δt_{dyn}. As seen subsequently, different discretizations of the Laplacian are possible to yield efficient diffusion operators.

The first one is similar to Equation 4.11, but applies a modified computation in edge-normal direction. Since the distance between the neighbouring vertices in normal direction is quite large compared to the distance in tangential direction ($\sqrt{3} l_e$ compared to $\tan(\pi/6) l_e$), a more localized Laplace operator can be considered appealing with a symmetric discretization in both horizontal directions. By placing $v_{n,3/4}$ at the cell centers instead of the adjacent vertices in normal direction, the discretized Laplace operator $\tilde{\nabla}^2$ becomes

$$\tilde{\nabla}^2 (v_n) = \frac{v_{n,2} - v_{n,1} - 2v_n}{d_{tv}^2} + \frac{v_{n,4\star} - v_{n,3\star} - 2v_n}{d_{nv}'^2}. \tag{4.32}$$

Here, $v_{n,3\star/4\star}$ denote the normal wind vector components at the cell center positions whose distance reduces now to $d'_{nv} = \tan(\pi/6) l_e$.

It is noted that the computational costs increase substantially with such an approach since the related RBF vector reconstruction needs to be performed at each dynamical core time step. On top of that, an additional vector reconstruction is required due to placing $v_{n,3\star/4\star}$ at the cell centers. Despite the high computational burden, this method (hereinafter NEWDIFF) is tested in this study.

Another approach is rooted back to the development phase of ICON's hydrostatic dynamical core (Wan, 2009) where an identity for the vector Laplacian is exploited:

$$\begin{aligned} \nabla^2 \mathbf{v}_h &= \nabla(\nabla \times \mathbf{v}_h) - \nabla \times (\nabla \times \mathbf{v}_h) \\ \overset{\text{discretization}}{\Rightarrow} \quad \tilde{\nabla}^2 (v_n) &= \nabla_n (D_h) - \nabla_t (\zeta). \end{aligned} \tag{4.33}$$

The *curl* operator used for discretizing the relative vorticity $\zeta = \mathbf{i}_3 \cdot \nabla \times \mathbf{v}_h = curl(\mathbf{v}_h)$ is calculated with the help of the Stokes theorem placing this quantity on the triangles' vertices. Its tangential derivative $\nabla_t \zeta$ is then discretized as a centered difference along the edge between two adjacent vertices. The usefulness of this hyper-diffusion approach (named OLDDIFF subsequently) by applying Equation 4.33 twice (cf. Eq. 4.11) was discussed in detail by Wan (2009) in context of a truncation error analysis on a planar, triangular grid. Despite the non-convergence of

[6] Note that diffusion is used as a synonym for *numerical* diffusion in the following if not stated differently.

the discretized fourth-order diffusion operator against the analytical counterpart, the leading error of the discrete Laplace operator given by

$$\begin{aligned}\tilde{\nabla}^2\left\{\tilde{\nabla}^2(v_n)\right\} =& \nabla_n\left[div\left\{\nabla_n(D_h)\right\}\right] - \nabla_t\left[curl\left\{\nabla_n(D_h)\right\}\right] \\ &+ \nabla_n\left[div\left\{\nabla_t(\zeta)\right\}\right] - \nabla_t\left[curl\left\{\nabla_t(\zeta)\right\}\right]\end{aligned} \tag{4.34}$$

is found to reduce efficiently checkerboard noise. It is noteworthy that the first term in Equation 4.34 corresponds to the (horizontal) fourth-order divergence damping term (cf. Eq. 4.12 and 4.28). Besides, as seen from Equation 2.48 in Wan (2009), this term results into a term mitigating for the checkerboard noise steming from the deficiencies of vector representations on a triangular grid with C-staggering.

In the following sections, the presented filters for mitigating the checkerboard problem are tested and compared in the Jablonowski-Williamson test cases and in the mass lifting experiment. Table 4.2 provides further details on the different filter configurations in the dynamical core of ICON.

While appropriate values for $f_{d,4o}$ and analogously $f'_{d,4o}$ can be deduced from Zaengl et al. (2015), the parameter values for the diffusion operators require some further explanations. In Wan et al. (2013), a small „e-folding time to timestep"-ratio was applied ($\tau_{v_n} = 1$) which was well founded by a truncation error analysis of the unaveraged divergence terms occurring in the equation system of their hydrostatic dynamical core. Although the small value of τ_{v_n} (meaning strong diffusivity) proves to ensure numerical stability, it was argued that the diffusivity in the model might be too strong.

Within this study, higher values for τ_{v_n} are sufficient, since the divergence terms of the mass and energy fluxes are averaged in the ICON's dynamical core. Although this does not solve the checkerboard problem, its effects are alleviated by avoiding the direct emergence of $2\Delta x$-noise in the mass and Exner pressure field.

Finally, it is noted that all configuration parameters for the numerical filters are determined empirically. While idealized experiments may help to ascertain their value range, the exact values remain rather uncertain. Thus, the listed parameters should not be understood as fixed values. They have rather been chosen to obtain optimal results in the following two sections or to allow for explicit comparison purposes. For instance, τ_{v_n} for the diffusion operators were set to yield similar results compared to the NEWCDD configuration in the mass lifting experiments on the Torus gird (see Sec. 4.6), while the resulting performance on a spherical grid is of particular interest for comparison in the next section.

4.5 Repeating the Jablonowski-Williamson test cases with ICON

The deterministic test cases Jablonowski and Williamson (2006a) have been widely employed in recent years and can therefore be considered as a benchmark test for dynamical cores. For instance, they were part of the Dynamical Core Model Intercomparison Project (DCMIP) (see Ullrich et al., 2017) and were performed repeatedly during the development phase of ICON's dynamical core as well (Wan,

Table 4.2: Overview of the different filter configurations in ICON's dynamical core including their acronyms.

Acronym	Filter configuration
OP4DD	operational anisotropic fourth-order divergence damping with $f_{d,4o} = 0.004$ (see Eq. 4.12)
NEWCDD	combined anisotropic fourth-order and isotropic second-order divergence damping with $f'_{d,4o} = 0.0017$ and $f_{d,2o} = 0.002$ (see Eq. 4.30)
OLDDIFF	hyper-diffusion (see Eq. 4.10) using the Laplace discretization of Equation 4.33 with $\tau_{v_n} = 13.0$
NEWDIFF	hyper-diffusion (see Eq. 4.10) using the Laplace discretization of Equation 4.32 with $\tau_{v_n} = 20.0$

2009; Wan et al., 2013; Zaengl et al., 2015). Since the experimental set-up is designed to reveal potential discretization deficiencies on the sphere, the Jablonowski-Williamson (JW) test cases are redone here to check the different numerical filter methods outlined in the previous section. The effects of orography and physical forcing are excluded, thus the integrity check of HYMACS is split off at this stage.

The initial global atmospheric state in the JW test cases is in hydrostatic and geostrophic balance with a near-surface meridional temperature gradient of 80 K between the poles and the equator (see Jablonowski and Williamson, 2006b, for a detailed description). Thus, as long as no initial disturbance is superimposed, the balanced state should be preserved. In practise, the maintenance of the initial atmospheric state is challenging for global models with irregular grid structures. Discretization errors easily break up the zonally symmetric, geostrophic equilibrium which are then prone to induce the development of Rossby waves due to the strong baroclinity.

The ability of the model to mitigate numerical discretization errors can therefore be accessed by measuring the time until the balanced state gets broken. This is tested with the first part of the JW test cases, the *steady-state* test.

The second part, the *baroclinic wave* test, ensures that the numerical filters still allow for the onset of baroclinic development processes. The imposed Gaussian-shaped initial wind perturbation in the Northern Hemisphere grows slowly at the beginning, but results into a rapid cyclogenesis and the development of a baroclinic wave train after 7 to 10 days. Although the process cannot be described analytically as the initial state, this test also reveals potential (resolution dependant) phase speed errors.

4.5.1 The steady-state test

A convenient way to access the degradation of the balanced state is to measure the l_2-error of the surface pressure $p_{sfc}(t)$ with respect to its initial value $p_{sfc}(t_0) = 1000\,\mathrm{hPa}$. The respective l_2-error is given by

$$l_2(p_{sfc}(t,t_0)) = \left\{ \frac{1}{4\pi} \int_{-\frac{\pi}{2}}^{\frac{\pi}{2}} \int_0^{2\pi} \left(p_{sfc}(t) - p_{sfc}(t_0)\right)^2 \cos(\varphi) \mathrm{d}\lambda \mathrm{d}\varphi \right\}^{1/2} \tag{4.35}$$

and thus quantifies the averaged root-squared surface pressure deviation over the sphere, where λ and φ denote the longitude and latitude, respectively. Following Lauritzen et al. (2010), the initial state is considered to be broken when $l_2(p_{sfc}(t, t_0))$ exceeds a value of 0.5 hPa[7].

Figure 4.6 illustrates the time series of the l_2-error of p_{sfc} for the different numerical filter configurations listed in Table 4.2. It is seen that the numerical filters based on divergence damping clearly outperform against the diffusional filters. The balanced initial state is maintained for more than 16 days with the OP4DD- and NEWCDD-configurations, while the l_2-error starts to grow exponentially much earlier with the OLDDIFF- and NEWDIFF-operators. The high-frequent, but small oscillations in the stable phase can be attributed to gravity waves which arise from inaccuracies of the initial atmospheric state in the model. While an exact specification is possible for hydrostatic models, an iterative technique is required for non-hydrostatic models with a height-based vertical coordinate (Jablonowski and Williamson, 2006a).

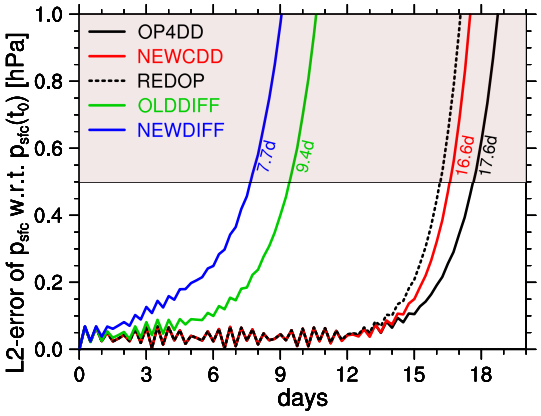

Figure 4.6: Time series of the l_2-error of surface pressure for different numerical filter configurations used in ICON's dynamical core in the JW steady-state test. The lead time when the initial state is considered to be broken ($l_2(p_{sfc}(t, t_0)) > 0.5$ hPa) is given for each filter configuration listed in Table 4.2. The dashed black curve illustrates $l_2(p_{sfc}(t, t_0))$ for the REDOP experiment where the initial state gets broken after 16.1 days. Redrawn from Langguth et al. (2020).

The reason for the much better performance of the divergence damping filters can be explained as follows: As seen in Section 4.4, the problem of representing the horizontal wind vector on a triangular C-grid translates itself into a checkerboard pattern of the divergence field. Thus, the effectiveness of the divergence damping operator appears quite intuitive. Indeed, it has also been shown by the truncation error analysis in Wan (2009) that the divergence damping operator corresponding to the first term in Equation 4.34 of the OLDDIFF-operator tends to compensate the discretization error on a planar triangular grid. By contrast, the mitigation effect is just a by-product in the full OLDDIFF-operator. Even though a somewhat weaker diffusion coefficient k_4 can be chosen in ICON's non-hydrostatic dynamical core, where the divergence terms in the continuity equation and in the first

[7] As pointed out in Lauritzen et al. (2010) the threshold is somehow arbitrarily defined. However, the conclusions are robust for a broad range of values between 0.3 hPa and 8 hPa.

law of thermodynamics are averaged over a four cell-stencil, the central problem mentioned by Wan et al. (2013) remains: The strength of the diffusion must be chosen relatively strong to control reliably the checkerboard pattern.

On top of that, the terms in Equation 4.34 that do not contribute to outweighing the $2\Delta x$-noise introduce additional discretization errors with distorted grid cells on the sphere. In the steady-state JW tests, this is noticed by disturbances developing most likely near the edges of the native icosahedron (not shown), where cell distortion remains strongest despite the spring dynamics optimization Tomita et al. (2002). The discretization of the Laplacian in the NEWDIFF-operator does not explicitly comprise a correction term and therefore even performs worse.

In summary, the fourth-order divergence damping term acting on D_h can be considered as a specialized filter whose major contribution to mitigating the checkerboard noise can be verified in the steady-state test. The temporarily reduced maintenance of the balanced initial state with the NEWCDD-operator can be attributed to the the smaller divergence camping coefficient $f'_{d,4o}$. Performing a sensitivity test of the operational divergence damping acting on the *full* 3D-divergence with the same damping coefficient (REDOP), i.e. $f_{d,4o} = 0.0017$ instead of $f_{d,4o} = 0.004$, leads to a further reduction by about 12 hours compared to the NEWCDD configuration. Thus, the isotropic, second-order divergence contributes less effectively to the removal of the checkerboard noise, but its application pays off due its neutral effect on gravity waves. The NEWCDD configuration therefore can be understood as a compromise between reducing efficiently computational noise and damping gravity waves, where $F_{div,2o}(\mathbf{v})$ puts some extra weight on the former (desired) effect.

4.5.2 The baroclinic wave test

The merit of the NEWCDD-operator compared to the two diffusional operators, OLDDIFF and NEWDIFF, is further confirmed by the baroclinic wave test. Figure 4.7 illustrates the sea level pressure and the 850 hPa relative vorticity on the northern hemisphere after 9 days (a-d) and 11 days (e-h) from the experiments with the OP4DD and NEWCDD configuration, respectively.

After 9 days, the initial perturbation has triggered a well-defined baroclinic wave train. The rightmost cyclone has already undergone a rapid intensification phase, while two further cyclones are present further west. Besides, another cyclogenesis due to the downstream mechanism becomes visible near (50°N, 100°W). The sea level pressure difference between the NEWCDD- and OP4DD-simulation $|\Delta p_{sfc}|$ is smaller than 0.5 hPa everywhere and the vorticity structures keep on resembling each other.

Two days later, both simulations are still hard to distinguish although small areas with $|\Delta p_{sfc}| > 0.5$ hPa arise within the baroclinic wave train. However, $|\Delta p_{sfc}|$ still seldomly exceeds a value of 1 hPa. There are only two systematical differences detectable, one along the cold front of the mature low at (52°N, 125°W) and the other south of the western cyclone near (49°N, 168°W). Both features are related to frontal waves which are slightly displaced. Besides, the eastern frontal wave is a bit stronger (about 2.5 hPa) with the OP4DD-configuration.

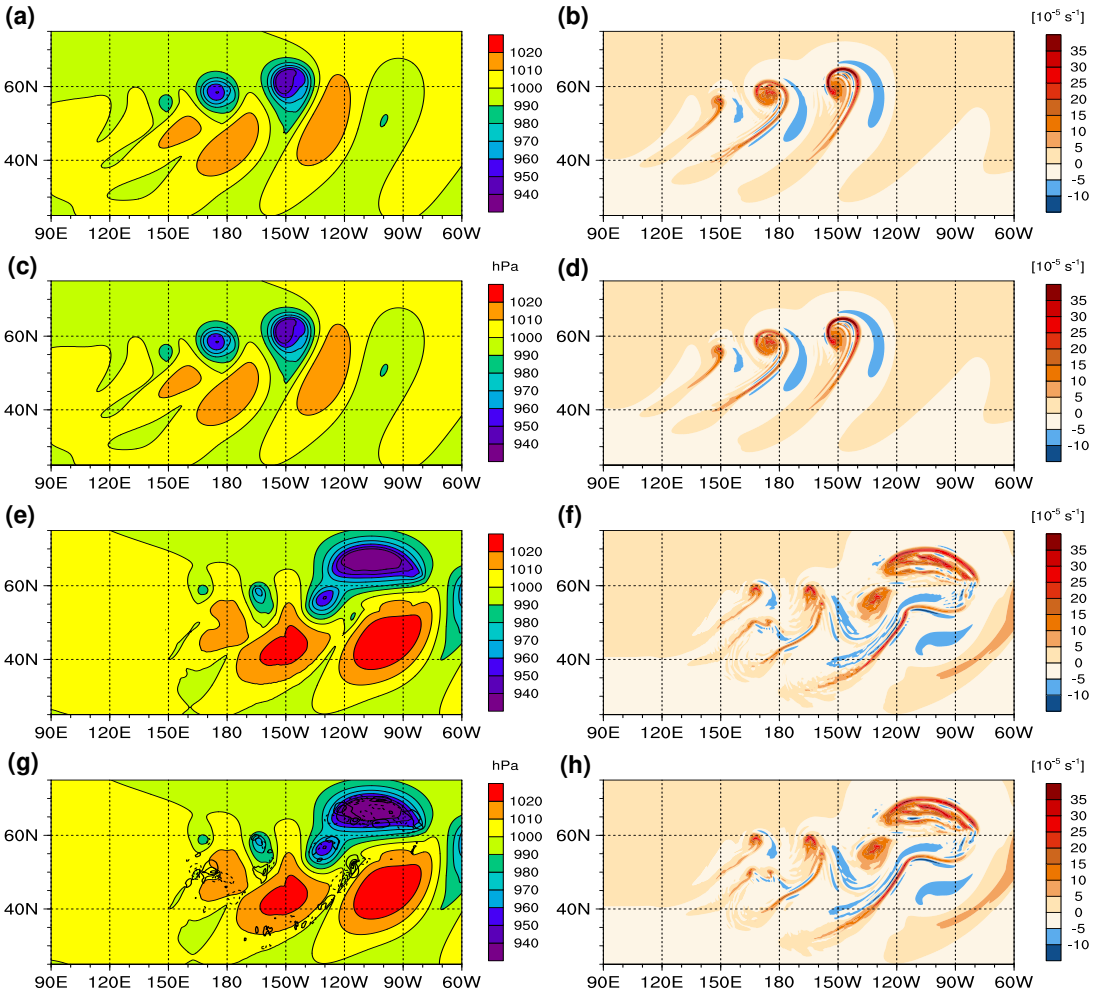

Figure 4.7: (a, c, e, g) Surface pressure and (b, d, f, h) relative vorticity at 850 hPa (both color shading) after (a–d) 9 days and (e–h) 11 days. The results with the OP4DD-configuration are displayed in (a, b) and (e, f). The results with the NEWCDD-configuration are shown in (c, d) and (g, h) along with the surface pressure difference relative to the OP4DD-simulation (black contours every 0.5 hPa). Dashed (solid) contour lines are used for negative (positive) differences, i.e. surface pressure is lower (higher) than in the reference simulation. From Langguth et al. (2020).

Nevertheless, the simulations only diverge slowly from each other and keep on resembling for a longer time. Redefining the l_2-error in Equation 4.35 for the NEWCDD-simulation with respect to the OP4DD-simulation, the globally averaged sea level pressure difference remains below 1 hPa until day 15 (not shown). By contrast, the simulations using the OLDDIFF and NEWDIFF filter configurations diverge much stronger and quicker from the operational one. As can be seen from Figure 4.8, $|\Delta p_{sfc}|$ is already much larger than 0.5 hPa after 9 days for large areas within the baroclinic wave train. The dipole structure close to the center of the second cyclone is indicative for a displacement. Analogously, differences with respect to the OPCDD-configuration in terms of the 850 hPa-vorticity structures are apparent for the eastern low. Additionally, wavenumber-five disturbances start to show up apart from the baroclinic wave train. As pointed out in Zaengl et al. (2015), this indicates an increased grid imprinting on the simulation.

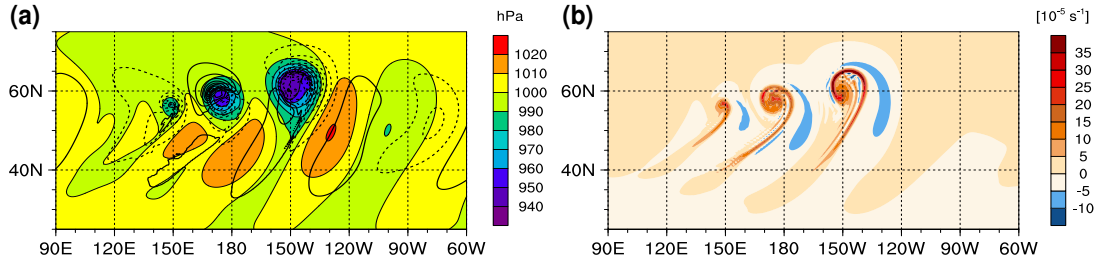

Figure 4.8: As Figure 4.7(c,d), but for the ICON simulation with the OLDDIFF-configuration.

Putting all together, it is stated that the diffusion filters are clearly inferior to the OP4DD- and the NEWCDD- configurations. Hence, no further elaboration on the OLDDIFF- and NEWDIFF-configurations is undertaken subsequently.

4.5.3 Convergence of the solution

Another important aspect of the JW test cases is to access the sensitivity of the results against changes in the horizontal resolution.

In terms of the steady state test, the maintenance of the geostrophic balanced state generally becomes shorter (longer) for decreasing (increasing) horizontal resolution due to the dependency of the discretization error on the grid spacing. For the operational filter configuration of ICON's dynamical core, the initial state is maintained about 2-2.5 days longer with each bisection step in the grid generation procedure reducing the grid spacing from 160 km (R02B04-grid) to 20 km (R02B07-grid) (see Fig. 2 in Zaengl et al., 2015). With the revised NEWCDD configuration, this behaviour is generally reproduced as shown in Figure 4.9. However, starting with a marginally better performance at low resolution (R02B04 and R02B05), the increase in duration of maintaining the balanced state gets somehow weaker at higher resolutions. While lacking an intuitive explanation, the practical relevance of this behaviour is probably limited.

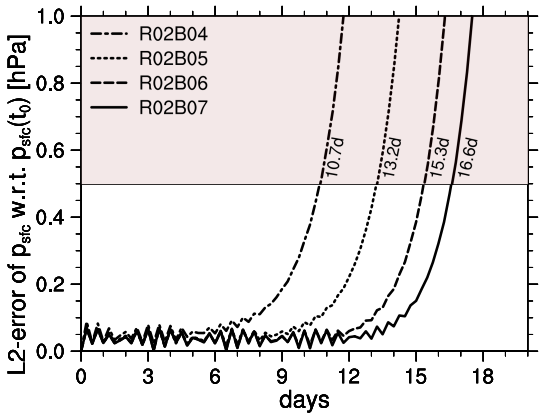

Figure 4.9: As Figure 4.6, but only using the NEWCDD-configuration at different grid resolutions. The JW-tests comprise a R02B04- ($\Delta x_{ICON} \approx 160$ km), a R02B05- ($\Delta x_{ICON} \approx 80$ km), a R02B06- ($\Delta x_{ICON} \approx 40$ km) and a R02B07-grid ($\Delta x_{ICON} \approx 20$ km).

For the baroclinic wave test, a resolution-depending difference between the NEWCDD- and OP4DD-configuration cannot be diagnosed at least for a considerable time period over which the baroclinic wave train evolves. In analogy to the R02B07-simulation, the sea level pressure differences are minor for the lower resolution runs after 9 days when cyclogenetic processes are already quite advanced (Fig. 4.10). There are only small areas north of the middle and eastern cyclone in the R02B04-simulation where $|\Delta p_{sfc}|$ slightly exceeds 0.5 hPa (see Fig. 4.10e). Anyway, this low-resolution simulation also suffers from a noticeable phase lag of the middle and left cyclone compared to the other simulations. This is an undesired, but shared property of the NEWCDD- and the OP4DD-simulation. Using the phase error metric which minimizes the l_2-error with respect to the R02B07-simulation via zonal shifting following Jablonowski and Williamson (2006a), a phase lag of 5° is analyzed for both simulations. Thus, the revised divergence damping does not lead to a performance degradation in this regard.

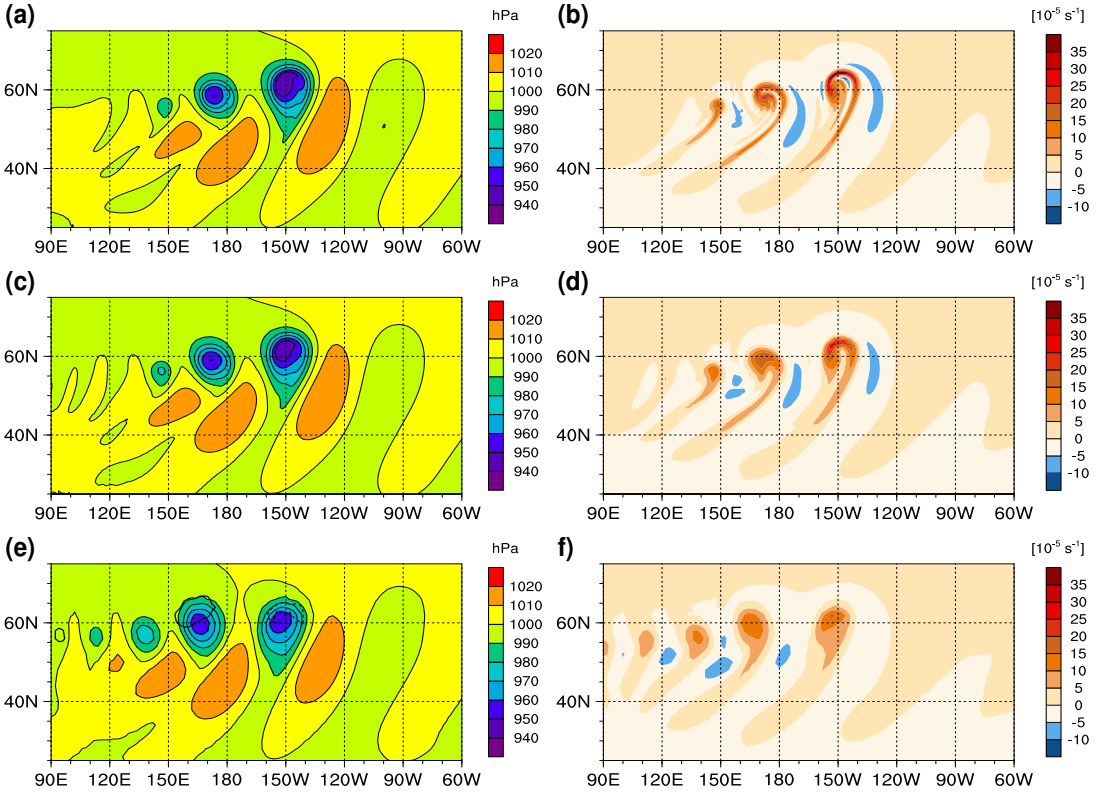

Figure 4.10: As Figure 4.7, but for simulations with the NEWCDD-configuration at different spatial resolutions. The used model grids are R02B06 (a, b), R02B05 (c, d) and R02B04 (e, f) which correspond to grid spacings of 40, 80 and 160 km, respectively.

Apart from that, the coarsening 850 hPa-vorticity structures with larger grid spacing are visually indistinguishable for the operational and the revised filter configuration. Thus, it can be concluded that the NEWCDD-configuration constitutes a proper alternative to the OP4DD-configuration while being compatible with the net mass transfer introduced by HYMACS. The latter property will be demonstrated in the following section in the scope of the mass lifting experiment with varying set-ups.

4.6 Mass lifting experiments with a revised numerical filter

After finding and approving the adopted variant of the divergence damping in the JBW test cases, the NEWCDD configuration is tested within the scope of the mass lifting experiment in the upcoming section. In addition to the *standard* mass lifting test as described in Section 4.3, variations of the experimental setup are conducted in order to investigate the compatibility of the revised numerical filter with HYMACS. In light of the triangular grid and the nature of divergence damping, special attention is directed on the emission of gravity waves and the occurrence of checkerboard noise.

4.6.1 The standard test

Results with ICON's revised filter configuration

As can be seen from Figure 4.11, the NEWCDD-configuration removes the severe flow distortion which was diagnosed with the operational filter configuration (cf. Fig. 4.5). The dynamical response to the net mass transfer with HYMACS is now very similar to the COSMO reference simulation (cf. Fig. 4.4). Thus, the grid-scale gravity waves after initiating (terminating) the mass transfer are present as well as the continuous divergent (convergent) flow pattern around the forcing layers.

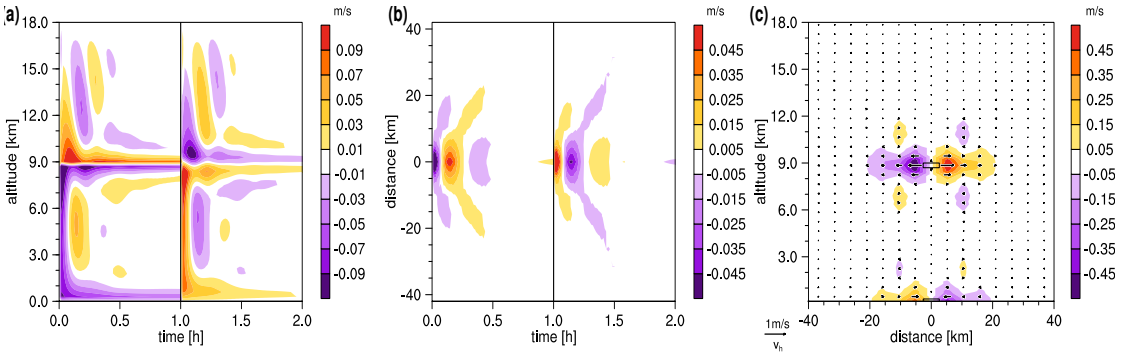

Figure 4.11: As Figure 4.4, but for results of the mass lifting experiment (standard test) obtained with ICON using the NEWCDD-configuration. From Langguth et al. (2020).

Although being small, closer inspection of the NEWCDD simulation also reveals some differences compared to the COSMO reference simulation which deserve further consideration.

At first, a weak cross-circulation can be seen around the entrainment and detrainment layer in the ICON simulation. As opposed to the pronounced divergence around the mass source, the flow pattern becomes slightly convergent about 2000 m above and below the organized detrainment layer (see Fig. 4.11c). An analogous flow pattern with reversed sign is visible above the mass sink. This cross-circulation pattern is also present in the COSMO simulation, but its amplitude is somehow weaker so that it gets concealed with the chosen contour levels. However, sensitivity tests reveal a sensitivity to the strength of the diffusion on horizontal wind in

the COSMO model. A similar strength of the circulation pattern can be attained by reducing the diffusivity (not shown) which suggests that the diagnosed difference crucially depends on details of the numerical filter configuration. Besides, the cross-circulation is also obtained in the analytical study of Shutts (1994) who examined the response to mass forcing in a non-rotational, unsheared flow (see their Fig. 2). Hence, the cross-circulation is considered to be a real feature of the dynamical flow response.

Secondly, the vertical wind oscillation is a bit weaker with NEWCDD in ICON compared to the COSMO reference simulation. This is most pronounced between the entrainment and detrainment layer where the interference of vertically propagating gravity waves leads to local maximum in z-direction (compare Fig. 4.4a and Fig. 4.11a). About 10 min after switching on the mass transfer, $w \approx 0.075\,\mathrm{m/s}$ is reached in COSMO, whereas a maximum of $0.052\,\mathrm{m/s}$ is obtained with ICON.

The amplitude of the vertical wind oscillation depends not only on the strength of the vertical wind diffusion, but also on the configuration of the divergence damping. Since the damping coefficient $f'_{d,4o}$ was argued to damp gravity waves in Section 4.4, reducing its value is expected to yield a larger agreement between both models. However, this comes at the price of less efficient damping of the inherent checkerboard noise in ICON. While this potential issue is addressed quantitatively subsequently, it is noted that the vertical wind signal in the vicinity of the convective grid column is only marginally smaller with ICON. Thus, it is hypothesized that the presented divergence damping configuration of NEWCDD still largely retains gravity waves.

Diagnosis of checkerboard noise

With kinetic energy spectra being fundamental in theoretical studies of geophysical flows and in turbulence theory, they can also be used for evaluating the mass lifting experiments with focus on numerical noise. Even though the kinetic energy spectrum is not expected to follow a well defined shape such as the $k^{-5/3}$ power-law observable for real atmospheric motions at mesoscale (Nastrom et al., 1984), a comparison between the simulations with the COSMO and the ICON model is appealing in the given context. This is related to the fact that the vector representation on a quadrilateral grid is not overspecified so that the COSMO model does not inherit checkerboard noise from the grid geometry. Thus, the checkerboard noise in the ICON model might be identified by a bump near the shortest resolvable wavelength $\lambda = 2\Delta x'_{ICON}$ where $\Delta x'_{ICON}$ corresponds to the effective, spectral grid spacing.

On COSMO's quadrilateral grid, the one-dimensional wavenumber spectra of horizontal kinetic energy from the staggered zonal and meridional wind components is straightforward (see Errico, 1985; Bierdel et al., 2012, for details). Owing to the underlying triangular mesh, interpolation onto a quadrilateral grid is required for ICON as a preliminary step. Additionally, an *a priori* estimation of the above mentioned spectral resolution Δx_{ICON}, especially with regard to the focus on the small-scale checkerboard noise, is mandatory. Following the discussion in

the appendix of Dipankar et al. (2015),

$$\Delta x'_{ICON} = 0.87 l_e \tag{4.36}$$

is applied where l_e denotes the edge length of the triangles. The finer cell-area based grid spacing which reads

$$\Delta x_{ICON} = (3^{1/4} l_e)/2 \approx 0.66 \Delta x'_{ICON} \tag{4.37}$$

on the planar triangular grid is not well suited. The resulting degree of freedom per grid cell would be reduced in this case which in turn leads to alias effects near the Nyquist limit. The effective grid spacing $\Delta x'_{ICON}$ from Equation 4.36 is thereby slightly larger than an estimate where the degree of freedom during the transition from the triangular to a quadrilateral grid is held constant. According to Dipankar et al. (2015), the increase in $\Delta x'_{ICON}$ accounts for interpolation errors.

Since the dynamical flow is forced by the net mass transfer, it is natural to anchor the regular target grid at the circumcenter of the convective grid column. The wind vector components in Cartesian coordinates are reconstructed with the help of a RBF vector reconstruction using a nine-point stencil with a Gaussian kernel following Rípodas et al. (2009). Due to the decreasing density with height, the evolving flow pattern is strongest at the detrainment layer. The flow pattern is also pronounced in the adjacent layers so that the energy spectra are obtained by averaging over three model layers in the following.

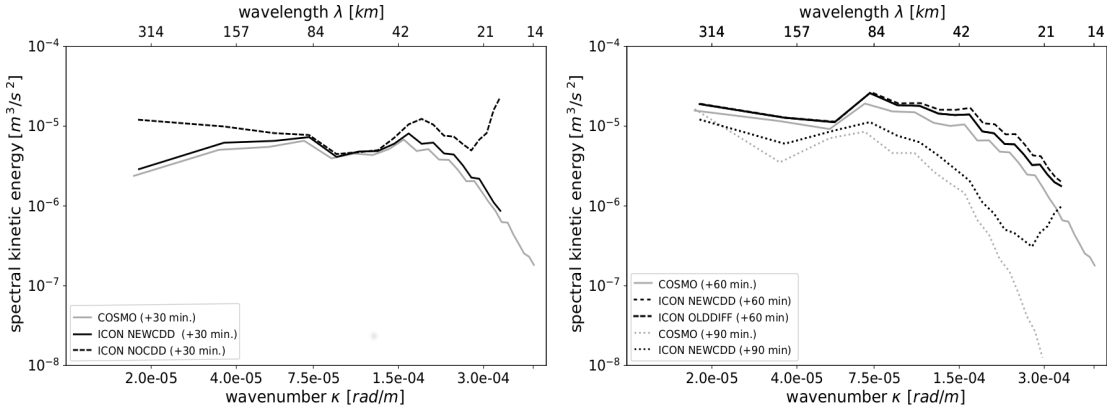

Figure 4.12: Kinetic energy spectra at different times in the standard mass lifting experiment obtained with ICON (black curves) and COSMO (gray curve). (a) Spectra after 30 min of continued mass transfer. The solid curves represent the NEWCDD-configuration and the COSMO reference simulation, respectively. The dashed curve shows the spectrum for a ICON simulation without divergence damping. (b) Spectra at the end of the forcing phase (solid curves) and 30 min after terminating the mass transfer (dotted curves). The dashed curve shows the spectrum using the OLDDIFF-operator after 60 min. The finer spectral resolution of the COSMO simulations is due to the quardilateral grid. Redrawn from Langguth et al. (2020).

Figure 4.12a shows the obtained kinetic energy spectra after 30 min of continued forcing in the COSMO simulation and in the ICON simulation with the NEWCDD-configuration. The shape of both spectra is practically identical and differences are small for all wavenumbers. The maximum of spectral kinetic energy

at $\lambda \approx 40\,\text{km}$ shows that the divergent wind pattern extends over several grid boxes as can be confirmed visually from Figure 4.4c and Figure 4.11c, respectively. The strong decrease of spectral kinetic energy at shorter wavelengths indicates that the numerical filter in the present ICON-configuration efficiently suppresses checkerboard noise. Its smoothing effect can be readily seen from the spectrum of a control experiment with deactivated divergence damping (NOCDD). Ther, a clear bump near the shortest resolvable wavelength $\lambda = 2\Delta x'_{ICON} \approx 18\,\text{km}$ demonstrates that the dynamical response is polluted with numerical noise.

The similarity between the energy spectra from the COSMO and ICON simulations persists qualitatively until the end of the forcing phase, that is after 60 min of continued mass transfer with HYMACS (see the solid curves in Fig. 4.12b). While the maximum of the spectral kinetic energy gets upscaled to larger wavelengths, it still falls off quickly near the shortest resolvable waves. It is therefore confirmed that the NEWCDD-configuration keeps on controlling the inherent checkerboard noise in ICON, even though a weak kink becomes visible. Note that this kink is also visible in the simulation using the OLDDIFF-configuration (dotted line in Fig. 4.12b).

However, the differences between the COSMO and the ICON simulation start to grow with deactivated forcing (Fig. 4.12b). After another period of emitted gravity waves due to the abrupt stop of the mass transfer, the induced flow pattern around the convective grid column starts to fade away. The transition to a new equilibrium with an atmosphere at rest is largely controlled by the numerical filters which dissipate kinetic energy chiefly near the smallest resolvable spatial scales. This can be readily seen from the kinetic energy spectrum of the COSMO simulation 30 min after switching off the mass transfer. While the kinetic energy on large scales ($\lambda \gtrsim \mathcal{O}(10^2\,\text{km})$) has only seen a small decrease, the spectral energy has already been reduced by several orders near the $2\Delta x_{COS}$-limit (see the light gray dotted line in Fig. 4.12b). The decrease in spectral energy in the ICON simulation is similar up to a wavelength of $4\Delta x'_{ICON}$, whereas a clear bump becomes visible near the shortest resolvable scales in ICON. Thus, the checkerboard noise becomes noticeable in the dissipation phase implying a stronger grid imprinting.

The signature of the bump thereby depends on the strength of the second-order and fourth-order divergence damping. As seen in experiments where $f_{d,2o}$ and $f'_{d,4o}$ are varied, the tail of the energy spectrum is sensitive to the strength of the fourth-order divergence damping, while the spectral energy at wavelengths $8\Delta x'_{ICON} \lesssim \lambda \lesssim 4\Delta x'_{ICON}$ mainly depends on the second-order divergence damping (not shown). This observation agrees well with other studies investigating the effect of divergence damping and its order-dependent, scale selective nature (e.g. Skamarock, 2011; Whitehead et al., 2011). Again, it is emphasized that a stronger anisotropic fourth-order divergence damping of course removes the inherent checkerboard noise more efficiently, but also increases the damping of internal gravity waves. The isotropic divergence damping acts less efficiently near the shortest resolvable waves, but can be argued to prevent upscaling of numerical noise.

4.6.2 Further mass lifting experiments

To further investigate the noise suppression capability of the NEWCDD-configuration, the experimental setup of the mass lifting test is modified subsequently. These additional experiments give insight into the dynamical flow response under various situations and therefore serve as a tool to demonstrate that a proper integrity of HYMACS in the new hosting model is achieved.

In addition to varying the atmospheric stratification and the grid spacing in the upcoming experiments, a simple temporal evolution of the idealized convective cell is imposed following the test strategy proposed in Kuell et al. (2007). Instead of an abrupt (de-)activation of the mass transfer, the mass flux and the height of the detrainment layer undergo a linear increase (decrease) over the 10 min. This has a minor impact on the stationary flow pattern, but mainly affects the gravity wave emission. The gradual increase of mass flux weakens the amplitude of the vertical wind oscillation as also pointed out by Chagnon and Bannon (2005a), while the vertical growth of the cell restrengthens the gravity wave signal. Even though the cell aging effect is not implemented in the current HYMACS version coupled to ICON (see Sec. 3.2), the imitation of a convective life cycle is adopted in the following for comparison purposes with Kuell et al. (2007).

Varying the atmospheric background stratification

From theoretical studies, it is known that the properties of gravity waves depend on the atmospheric background stratification which can be described in terms of the Brunt-Väisälä frequency N. It can be shown that the frequency of the associated oscillation in a fluid with constant atmospheric stratification is proportional to N, whereas their amplitude is proportional to its inverse $1/N$ (see, e.g., Bretherton and Smolarkiewicz, 1989; Holton and Hakim, 2013).

In the setup of the mass lifting experiment rather the lapse rate of the background atmosphere Γ than N is held constant, although both quantities are related to each other by

$$N^2 = \frac{g}{\theta}\frac{\partial\theta}{\partial z} = g\left(-\frac{1}{T}\Gamma - \frac{R_d}{c_{pd}}\frac{\partial \ln p}{\partial z}\right). \tag{4.38}$$

Nevertheless, it is expected that the frequency of the vertical wind oscillation becomes smaller while the amplitude gets larger with increasing lapse rate Γ (smaller N) and vice versa. Besides, the results can again be compared to the results obtained with the COSMO model as shown in Kuell et al. (2007).

The simulation results obtained with a lapse rate of $\Gamma = 4\,\mathrm{K/km}$ and $\Gamma = 8\,\mathrm{K/km}$ are consistent with the expectation (see Fig. 4.13). The half-life period of the vertical wind oscillation gets increased from 11 min to 14 min for the less stable stratification corresponding to an increase of about 25 %. This increase in life cycle time agrees well with the results using the COSMO model as reported in Kuell et al. (2007).

While the vertical wind signal is stronger in the simulation with $\Gamma = 8\,\mathrm{K/km}$, the horizontal divergence pattern gets strengthened with $\Gamma = 4\,\mathrm{K/km}$. The partitioning from vertical to horizontal divergence also implies a dependence of the

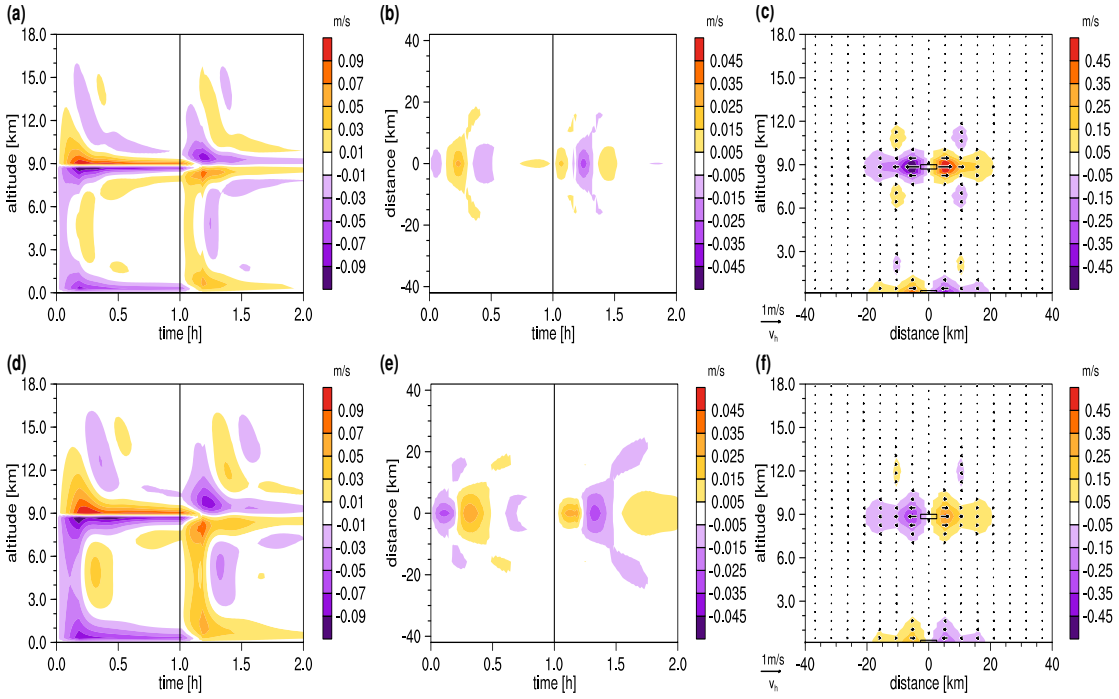

Figure 4.13: As Figure 4.11, but for mass lifting experiments with varying atmospheric stratification and temporal evolution of the mass transfer. (a-c) for Γ = 4 K/km and (d-f) for Γ = 8 K/km. From Langguth et al. (2020).

checkerboard noise on the atmospheric stratification. As can be seen from Figure 4.14, the kink in the kinetic energy spectrum practically becomes invisible in the simulation with a less stable background stratification. By contrast, a small checkerboard signature becomes already visible in a more stable atmosphere after 30 min.

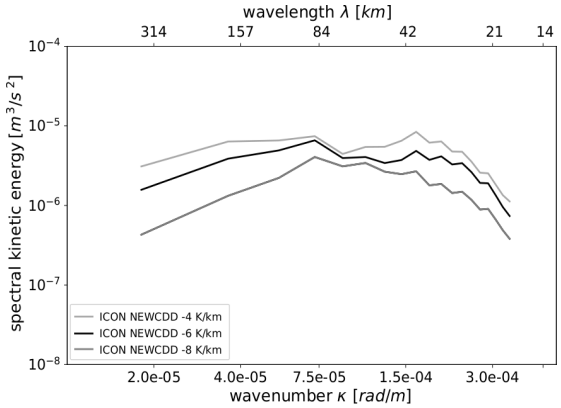

Figure 4.14: As Figure 4.12a, but for varying stratification of the background atmosphere with the NEWCDD-configuration. From Langguth et al. (2020).

Before this result is further discussed in the closing section of this chapter, another important aspect of the dynamical flow response is investigated subsequently.

Independence of the dynamical response from the grid spacing

Since HYMACS should be applicable for model simulations across the mesoscale, its dynamical flow response should not crucially depend on the grid spacing of the hosting model given that the forcing is equivalent. For this purpose, Kuell et al. (2007) performed an experiment with a quadratic 56×56 km cluster of idealized convective columns with varying grid spacings. In order to conduct an analogous experiment, an equilateral cluster is chosen in ICON whose edge length of 84 km yields the same cluster area as in the COSMO model. This cluster then consists of 4 convective columns in the simulation with the coarsest model grid. Three further simulations with finer grid spacings are obtained with the application of successive bisection steps. Since the cluster area as well as the total mass flux is held constant in all simulations, the cluster consists of 4, 16, 64 and 256 grid cells with an edge length l_E of 42 km, 21 km, 10.5 km and 5.25 km (Δx_{ICON} of 28 km, 14 km, 7 km and 3.5 km), respectively.

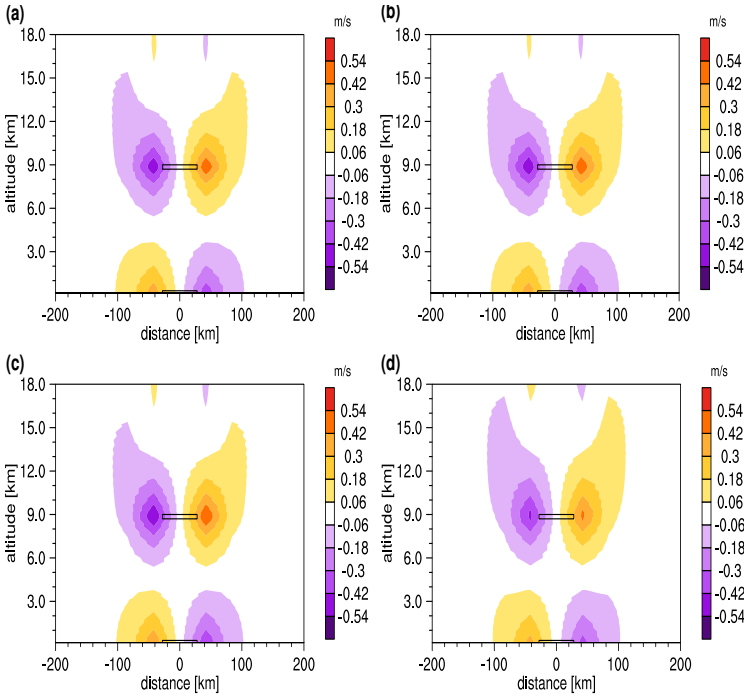

Figure 4.15: Vertical cross-section of the radial wind component through a convective cluster. For comparison, the wind is averaged onto a grid with an edge length of 84 km, while the underlying native grid lengths are (a) l_E = 5.25 km, (b) l_E = 10.5 km, (c) l_E = 21 km and (d) l_E = 42 km, respectively. From Langguth et al. (2020).

Apart from small-scale structures of the highly resolved simulations (not shown), the divergent flow patterns look similar for all simulations after 30 min of mass forcing. To demonstrate this similarity, Figure 4.15 shows a cross-section of the radial wind through the circumcenter of the cluster after coarsening onto a common triangular grid with an edge length of 84 km. The differences are generally minor compared to the overall amplitude of the wind although the flow pattern looks a bit smoother for the simulation with the coarsest grid spacing. This finding again agrees well with the results from the COSMO model (Kuell et al., 2007). Thus, the desired independence from the grid spacing is largely confirmed.

4.7 Intermediate summary and discussion

In the preceding sections of this chapter, it has been demonstrated that the coupling of HYMACS into the ICON model has to be done with care. Due to the subgrid-scale net mass transfer with the hybrid convection parametrization schemes (CPS) not only the physics-dynamics coupling differs from other existing parametrization schemes, but also subtle requirements on the numerical filtering in the dynamical core are imposed. Since the mass forcing induces a divergent flow pattern in all spatial directions, anisotropic divergence damping based on the full 3D divergence leads to severe flow distortion. Such a filter technique is therefore considered to be inapplicable with HYMACS.

Unfortunately, the operational filter in ICON relies on such an approach so that an alternative method has to be found. First, this alternative has to be compatible with the local mass sources and sinks implying that any dependency of the damping term for horizontal momentum on the *vertical* divergence must be avoided as long as no equivalent damping term is imposed on the vertical wind. Second, the filter must efficiently suppress computational modes on a planar, triangular grid, also for slightly distorted spherical grids.

Various idealized tests suggest that the NEWCDD-configuration serves these purposes. By combining the fourth-order divergence damping based on horizontal divergence with an isotropic, second-order divergence damping, the grid imprint is minimized as demonstrated in the Jablonowski-Williamson test cases on the sphere. Any tested filter configuration based on diffusion is inferior since the mitigation of the checkerboard pattern is just a by-product. The NEWCDD-configuration is found to suppress efficiently checkerboard noise under various situations when subgrid net mass transfer occurs with HYMACS. Given that the fourth-order divergence damping is carefully calibrated, gravity waves as a response to the mass forcing are also retained.

However, with the damping coefficients used throughout the experiments in this chapter (see Tab. 4.2), two situations have been identified where a stronger signature of checkerboard noise becomes noticeable; these are the dissipation phase subsequent to the continued mass lifting (Fig. 4.12b) and lingered forcing in an unconditionally stable background atmosphere with a lapse rate of $\Gamma = 4\,\mathrm{K/km}$ (Fig. 4.14).

The first situation is considered to be rather academic. In real case applications with full physics coupling, it is very unlikely that neither small-scale nor large-scale forcing are present when convection has taken place. Thus, the developing upturn in the energy spectrum is expected to be of minor relevance even though it will be rather concealed in a system with more kinetic energy on all scales.

By contrast, the latter case may also become noticeable in real case applications. While the atmosphere is conditionally unstable by definition between the level of free convection (LFC) and level of neutral buoyancy (LNB), stably stratified conditions are present near the cloud top level (CTL). A typical example is deep convection topped close to the tropopause which is not unusual in the summery midlatitudes (Liu and Liu, 2016). However, it is also noted that the assumption of vanishing enthalpy tendencies in the organized detrainment layer is not realistic,

since the updraft air is colder than the environment above the LNB.

While retaining the idealized framework of the mass lifting experiments, the COLDUP experiment is designed to provide further access to the potential emergence of checkerboard noise near the CTL (Langguth et al., 2020). In this experimental set up, a transition zone where the lapse rate gradually decreases from $\Gamma = 8\,\mathrm{K/km}$ to $\Gamma = 4\,\mathrm{K/km}$ is placed right below the forced detrainment layer. The detrained air at CTL is then assumed to be colder than the environment by 2 K. Additionally, organized entrainment at mid-level layers is imposed as motivated by mass flux profiles in Kuell et al. (2007) (see their Fig. 6) and Kain and Fritsch (1990) (see their Fig. 5).

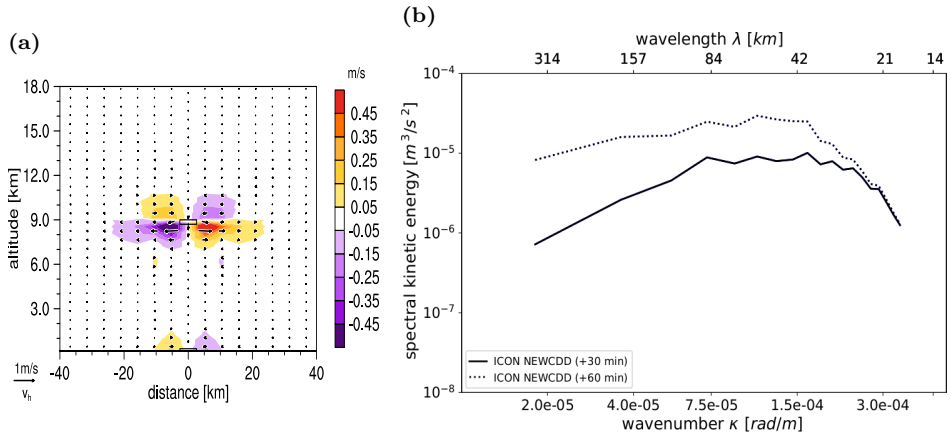

Figure 4.16: Diagnosis of the dynamical flow response in the COLDUP experiment. (a) Cross-section of the grid-scale flow through the convective grid column analogous to Figure 4.5. (b) Kinetic energy spectra after 30 min (solid curve) and 60 min (dotted curve) of mass forcing.

The dynamical flow pattern after 30 min and the kinetic energy spectrum at the end of the forcing phase (after 60 min) is illustrated in Figure 4.16. Due to the negative buoyancy of the entrained air with respect to the environment, grid-scale subsidence is induced. The horizontal outflow then takes place at lower levels so that the strongest flow pattern is induced at model layers 28-30 in this case. In these layers, the atmospheric stratification is reduced compared to the detrainment layer above. Thus, the kink in the energy spectrum is still absent after 60 minutes of lingered forcing indicating that the above mentioned signature of checkerboard noise is again less relevant in more realistic applications.

It can be argued that the statement also holds for cloud tops which really reach or even cross the tropopause[8] since the entrained air then becomes even colder with respect to the environment. Besides, the spreading of the organized detrainment flux in the cloud model of HYMACS (see Sec. 3.3) is expected to lessen the proneness to relevant checkerboard noise.

Finally, it should be emphasized that the mentioned divergence damping coefficients $f'_{d,4o}$ and $f_{d,2o}$ of the NEWCDD- configuration are understood as a first guideline. Especially, for simulations with full physics forcing and in the presence of real topography, higher values are probably suitable in order to suppress reliably checkerboard noise. However, albeit being the important regulating skew for

[8]The tropopause is commonly defined by elevated layers with $\Gamma \leq 2\,\mathrm{K/km}$.

removing checkerboard noise, the fourth-order divergence damping based on horizontal divergence should be increased carefully. With substantially higher values than presented, say $f'_{d4,o} > 0.0025$, checkerboard noise is quite strongly controlled, but gravity waves get damped noticeably as well.

5 Test series with ICON-HYMACS

In order to access the performance of HYMACS coupled to the ICON model in real case applications, a continuous series of model simulations over a three-monthly period from May until July 2017 was performed. This is the first time that HYMACS is evaluated systematically in a quasi-operational framework. Previous studies by Kuell and Bott (2008, 2009, 2011, 2014, 2019) with HYMACS coupled to the COnsortium for Small-scale Modeling (COSMO) model indicate potential improvements compared to classical convection parametrization schemes (CPS) in representing precipitation in terms of the spatial patterns, coupling with the grid-scale flow and the diurnal cycle. However, their studies comprise only a small number of case studies which has been selected by focusing on rainy days.

The studies by Ong et al. (2017) and Malardel and Bechtold (2019) who implemented a hybrid version of the Kain-Fritsch and the Bechtold-Tiedtke scheme, respectively, also either focused on idealized simulations or performed single case studies. Thus, it still has not been verified if the above mentioned advantages of HYMACS against classical CPS constitute a systematic feature. This test series is therefore considered to bridge the gap between experimental and profound evidence that simulations at gray-zone resolutions benefit from the hybrid approach.

The remainder of this chapter is organized as follows: Section 5.1 deals with the experimental design and gives an overview on the model configuration used for the simulations of the test series. In addition to outlining the numerical representation of convection with different CPS in ICON, details on the model domain, the configuration of the dynamical core and the set-up of the model's physics package are described. Section 5.2 then presents some detail on the observational data set against which the simulations is evaluated, before synoptic and climatological aspects of the investigated time period are given in Section 5.3. After outlining a proper strategy to evaluate precipitation in NWP models (see Sec. 5.4), the simulations with the hybrid scheme are analyzed statistically in Section 5.5. The evaluation also comprises a systematic comparison between the ICON simulations with HYMACS and the those with the operational Bechtold-Tiedtke scheme. Finally, a summary is provided in Section 5.6. Thereby, the elaborated systematic characteristics of both schemes are further explored and reasoned from a physical-dynamical point of view.

5.1 Model configuration and experimental design

In the following, the evaluation focuses on two branches of simulations that only differ in terms of the used CPS from each other. The branch of the reference simulations makes use of the operational Bechtold-Tiedtke scheme and will be

abbreviated by *ICON-BT* throughout this chapter. The branch of the target simulations applying HYMACS is denoted by *ICON-HYM* hereinafter.

Like in the idealized experiments described of the previous chapter, ICON version 2.3.0. equipped with HYMACS is used to perform the simulations of the test series. This model version was operational at DWD from 06/06/2018 until 16/07/2018 and apart from the required modifications due to our chosen experimental set-up described below, the model was set up as close as possible to the operational configuration[1].

Following the case studies performed in Kuell and Bott (2009, 2011, 2019), we choose Central Europe as the target domain for verification. During its development in the COSMO model over the last decade, HYMACS has been tuned for this region while it has neither been tested in regions with a considerably different convective regime such as the tropics nor at global scale. In order to obtain some basic similarities with previous applications of HYMACS, ICON's limited area mode (ICON-LAM) is used in this study. In contrast to the operational model set-up with a two-way coupled regional R03B08-nest ($\Delta x_{ICON,nest} \approx 6.5\,\text{km}$) over Europe (ICON-EUnest) as part of the global model domain on a R03B07-grid (ICON-global; $\Delta x_{ICON,glob} \approx 13\,\text{km}$), the simulations are driven by externally supplied boundary data. However, the limited-area grid used here has been generated by bisecting the operationally applied global R03B07-grid so that the model domain coincides with the ICON-EUnest in terms of grid spacing (i.e. $\Delta x_{ICON,LAM} = \Delta x_{ICON,nest} \approx 6.5\,\text{km}$) and grid box location.

Figure 5.1 depicts the model domain in comparison with the (operational) ICON-EUnest. With an area of 2300x1800 km in zonal and meridional direction, respectively, the simulation domain is indeed smaller than ICON-EUnest, but it is considered to be large enough to allow for a development of mesoscale flow patterns over its central parts. The model simulations start at 00 UTC on each consecutive day in the period of the test series and comprise an integration time of 48 hours.

Along the lateral boundaries, the modelled atmospheric state is relaxed towards the prescribed boundary data which are supplied hourly from the initialized analysis product of ICON-EUnest. The horizontal width of the *nudging zone* comprises eight cell rows and relaxation is applied as forcing terms for the model's prognostic variables v_n, θ_v, ρ and q^v following the technique proposed by Davies (1976, 1983). The outermost four cell rows constitute the *lateral boundary zone* where the atmospheric state is completely prescribed from the boundary data.

In vertical direction, 60 levels with a minimum depth of 20 m near the surface and a maximum depth of 400 m in the lower stratosphere are used following the operational grid configuration of the ICON-EUnest. In order to avoid spurious reflection of vertically propagating waves, a Rayleigh sponge layer is applied starting at a height of 14.5 km. Thus, the vertical wind is damped towards zero over the uppermost 8 km following the method proposed by Klemp et al. (2008) whereby damping increases with height to realize a zero-flux condition at model top. The

[1] Changes to the operational forecasting system with ICON at ICON are documented on https://www.dwd.de/DE/fachnutzer/forschung_lehre/numerische_wettervorhersage/nwv_aenderungen/_functions/DownloadBox_modellaenderungen/nwv_aenderungen_icon_gesamt.html?nn=16102&lsbId=479218.

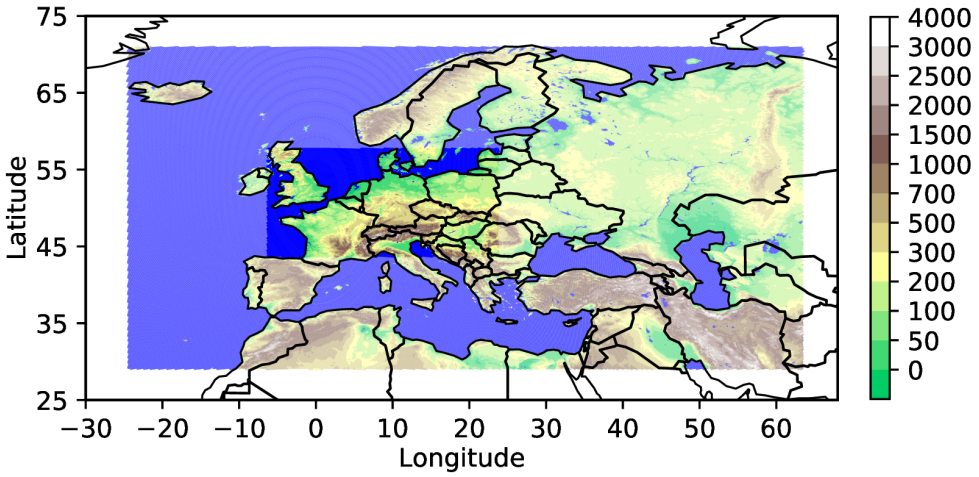

Figure 5.1: Topographic height of the surface in the operational ICON-EUnest and the ICON-LAM model domain. The model domain of ICON-LAM as used in this study is highlighted.

height of the Rayleigh sponge layer is placed well above the tropopause to avoid damping of relevant flow features near the cloud tops of very deep convective cells. However, it can be located at lower altitudes compared to the recommendation given in Kuell et al. (2007) since the mass conservation violation mentioned therein does not arise in a modeling system with an explicit formulation of the continuity equation (see Sec. 4.1).

Following the results of Chapter 4, a notable, but necessary difference compared to the operational model configuration pertains the divergence damping. Here, we rely on the new combined divergence damping (NEWCDD)-configuration with slightly increased damping coefficients of $f_{d,2o} = 0.0025$ and $f'_{d,4o} = 0.0022$ (cf. Tab. 4.2). This was found empirically to suppress checkerboard noise and to yield best results in real-world model with full physical forcing. Note, that the alternative divergence damping is also applied in the reference simulations with the Bechtold-Tiedtke scheme to ensure that any differences to ICON-HYM can be attributed to the choice of the CPS. The configuration of the numerical diffusion follows again the operational set-up, where an e-folding time to time step ratio of $\tau_w = 16.0$ is used for the vertical wind (see Eq. 4.4). For horizontal momentum and temperature diffusion, $\tau_{v_n} = \tau_T = 24.0$ are chosen (see Eq. 4.3 and 4.6), whereas the latter is combined with a Smagorinsky diffusion equipped with a scaling factor of $f_s = 0.025$ (see Eq. 4.10).

Apart from the usage of HYMACS for representing convection, the configuration of the ICON's NWP physics package is again inherited from the operational set-up. In particular, this includes the parametrization of radiative processes with the Rapid Radiative Transfer Model (Mlawer et al., 1997; Barker et al., 2003), a five categorical single-moment scheme to model bulk microphysical processes on grid-scale (Seifert, 2008; Doms et al., 2011) and a 2^{nd}-order TKE-based turbulence scheme (Raschendorfer, 2001) for describing turbulence fluxes in the troposphere (TURBDIFF) and surface-to-atmosphere exchanges (TURBTRAN). Additionally, a diagnostic cloud cover scheme developed by Koehler et al. at DWD (Prill et al.,

2019) is used as well as the Lott and Miller scheme (Lott and Miller, 1997) to account for subgrid-scale ororaphic drag.

The configuration of all the above mentioned physical parametrization is unchanged with respect to the ICON-EUnest. This means that no further tuning of disposal parameters is undertaken with HYMACS to optimize the model's performance. Note, that especially the configuration of the turbulence scheme is known to interact strongly with the CPS (see, e.g., Zampieri et al., 2005; Flaounas et al., 2011) which was optimized with the Bechtold-Tiedtke scheme in ICON.

The only differences in the configuration of the physical parametrization pertain the non-orographic gravity wave drag (Orr et al., 2010) and the usage of the land-soil model TERRA (Schrodin and Heise, 2002; Heise et al., 2006).

The former scheme is deactivated since the effect of the parametrized non-orographically forced gravity waves is most relevant in the stratosphere and mesopause, where only the former is partially included in the model domain extending up to a height of 22.5 km. In addition, a Rayleigh sponge layer is applied in the lower stratosphere (see above) so that stratospheric dynamics are not supposed to be represented explicitly in the limited area domain. Large-scale effects of the stratosphere-troposphere coupling are considered to be of minor relevance for the lead time of our simulations and are furthermore incorporated implicitly by the lateral boundary conditions of the relative small model domain (see above).

While the operational land-soil model TERRA makes use of a tile approach with up to four different surface types within a single grid cell, only the dominant land surface type is regarded in the simulations at hand for pragmatic reasons. Even though a tiled approach allows for an improved calculation of cell-averaged surface fluxes when the subgrid land surface type is highly variable, it is not likely that the untiled approach crucially distorts the comparison between ICON-HYM and ICON-BT. However it is noted that potential improvements in triggering (deep) convection may be possible using the tiled approach in conjunction with both CPS.

A final note pertains the configuration of the Bechtold-Tiedtke scheme. Although the implemented scheme constitutes a spin-off of the CPS used operationally in the IFS model (see Sec. 2.5), there exists a remarkable difference in the configuration of the closure for deep convection in the ICON version at hand. The correction technique towards nonequilibrium convection (see Eq. 2.42) is only applied in the tropics (for $25°N < \varphi < 25°S$) in ICON version 2.3.0. While this approach is beneficial for representing the diurnal cycle of precipitation (Bechtold et al., 2014b), its application in midlatitudes turned out to degrade the overall performance of this ICON version in operational applications (Guenther Zaengl (ICON), personal communication, 09/05/2020). The associated consequences will be further discussed in the last chapter of this thesis.

5.2 Observational data - The RADKLIM dataset

To evaluate model simulations, a high-quality observational product is required whose spatio-temporal properties match the properties of the model data. Point measurements at station sites are problematic for evaluating modelled precipitation since especially convective precipitation occupies high variance on spatial scales

with $\mathcal{O}(10^2\text{-}10^3\,\mathrm{m})$. Since these scales are not captured on grid-scale with mesoscale models, representativeness errors are induced (e.g. Lochbihler et al., 2017).

By contrast, precipitation quantities derived from radar observations are more suitable for the two following reasons. First, instead of observing precipitation at a specific location, weather radars can detect precipitation patterns over a larger radial domain which extends up to a distance of 150 km from the radar station site. Second, the precipitation intensity derived from a backscattered microwave signal reflects the properties of a larger atmospheric volume such as the gridded data of a numerical model.

However, radar data also suffer from systematic observation errors such as noise, clutter and beam-blocking (see, e.g., Wagner et al., 2018). Therefore, a sophisticated calibration procedure is mandatory to retrieve a high-quality observation product allowing for quantitative evaluation. Following Rossa et al. (2008), it is advisable to deploy such a product for verifying precipitation forecasts.

The „RADar KLIMatologie“ (engl.: Radar climatology) (RADKLIM) dataset provided by DWD is considered to be a product fulfilling the above mentioned requirement (Winterrath et al., 2017). It provides precipitation rates at a temporal resolution of 5 minutes (YW product) as well as hourly precipitation amounts (RW product) obtained from the German radar network. The radar network covers all parts of Germany and also includes some areas of the neighbouring countries providing continuous observational data since 1st January 2001.

The RADKLIM dataset is based on the RADar OnLine AdjustmeNt (RADOLAN) procedure which processes the reflectively data obtained by 17 ground-based C-Band radar stations of the German radar network to quantitative precipitation products. This procedure went operational in June 2006 and constitutes a synthesis between radar and rain gauge observations based on a weighted adjustment difference and factor method (Bartels et al., 2004). Several correction algorithms are applied to the raw data such as the elimination of clutter pixels due to backscattered signals of non-meteorological targets (e.g. insects, birds or solid objects), compensation of orographic shading effects and smoothing with gradient filters. The correction procedure has been continuously refined over the last years resulting in steady data quality enhancement, but also in an inconsistent dataset.

In order to arrive at a consistent dataset, the data from the German radar network back to the year 2001 were reanalyzed using a consistent data procedure. Climatological processing algorithms are involved in this procedure which comprise improved detection and correction of clutter and spoke artefacts as well as a correction approach accounting for signal reduction with increasing distance and altitude (Winterrath et al., 2017). It is noted, that such techniques are based on longer time series which are therefore barely feasible in an online approach such as the RADOLAN procedure. The study by Kreklow et al. (2020) confirms the benefits of the sophisticated reanalysis procedure, pointing out that the RADKLIM dataset shows up with much less artefacts in the precipitation product than the operational RADOLAN dataset. Despite a persisting negative bias in the precipitation totals which can be diagnosed from comparison with independent rain gauge observations, the RADKLIM data is considered to serve as a reliable dataset for evaluation.

Due to the considerably higher spatial resolution of the RADKLIM data on a polar stereographic grid with a grid spacing of 1 km, aggregation onto ICON's coarser triangular grid is mandatory for verification purposes. The aggregation is performed with the help of the Climate Data Operators (CDO) software (Schulzweida, 2019) which offers a first order conservative remapping method provided by YAC's (Yet Another Coupler) interpolation stack (Hanke et al., 2016). In contrast to simplified interpolation methods such as bi-linear interpolation this ensures that the area-integrated precipitation amount remains (approximately) unchanged after aggregation on the coarser target grid.

A final note pertains the validity timestamp of the precipitation products. The hourly product of the RADKLIM dataset as well as its RADOLAN counterpart, both called RW, are not valid at every full hour, but at minute 50. Thus, there is a time shift between the hourly precipitation product from the radar dataset with respect to the (typical) model output being valid at every full hour. While this time shift may be ignored for long accumulation periods, e.g. for monthly precipitation amounts, this is not true for evaluation on a subdaily time scale. Thus, we make use of the YW product which is available every 5 minutes and accumulate the precipitation rates to hourly amounts in this study. Note that the YW product is *quasi-adjusted* on the RW product reasoning such a procedure.

On spatial scales, the aggregated and remapped YW product is limited to the domain of the RW product as depicted in Figure 5.2. This confines the data more or less to the German territory and is motivated by the fact that edge regions of the observational domain are excluded where the beam height reaches several kilometers (see Fig. 1 in Pejcic et al., 2020). Besides, temporary failure of individual radar station may be compensated due to overlapping observation radii.

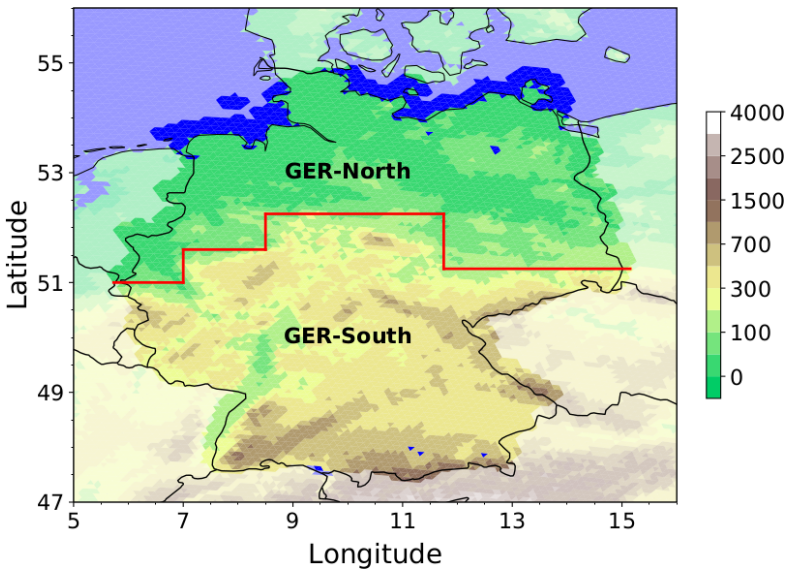

Figure 5.2: Sub-domain of the ICON-LAM model domain for which verification against RADKLIM observations is performed. The topographic height of the surface from the model is plotted with the verification domain highlighted. The red line separates the two subregions GER-North and GER-South that are introduced later in the evaluation.

5.3 Synoptic and climatological classification

An overview on the climatological classification of the months May to July 2017 is provided by Figure 5.3 which illustrates monthly averages and deviations with respect to the climatological reference period 1961-1990 in terms of precipitation, temperature and sunshine duration. In addition to this overview, further insight is provided in the following complemented by an analysis of the synoptic-scale circulation patterns, both reasoning the choice of the test period in this thesis.

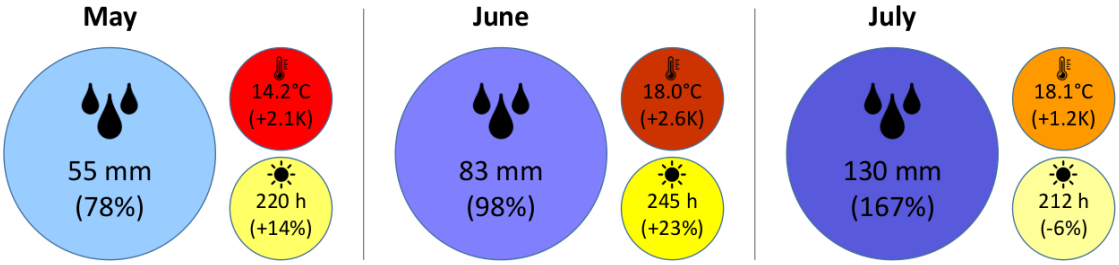

Figure 5.3: Overview on the monthly precipitation, temperature and sunshine duration with deviations relative to the climatological reference period 1961-1990 for May (left), June (center), July (right) 2017. Data source: DWD

The month May 2017 was fairly dry compared to the climatological reference period. Based on around 2000 station sites of the German observational network operated by DWD, averaged precipitation summed up to 55 mm which is about 20 % below the climatological mean (72 mm). However, large regional differences in terms of monthly precipitation are present (see Fig. 5.4a). Within a nearly 200 km broad, meridional zone from the Hamburg region to Northern Bavarian, monthly precipitation accumulated to 60-100 mm, while near the Alps and some parts of Baden-Wuerttemberg and Hesse registered more than 100 mm precipitation with local maxima exceeding 200 mm. By contrast, large parts of Eastern and North-western Germany generally recorded low monthly precipitation amounts, barely getting more than 40 mm rain. The dominance of convective precipitation in the latter regions can readily be seen from a high spatial variance in the monthly rainfall amount.

On a sub-monthly scale, four distinct rainy periods can be identified. The first period lasted until the end of the first decade and was dominated by a pronounced trough which cut off over Central Europe at the turn of the month. Downstream of an evolving ridge over the Eastern Atlantic, continuous rain along an occlusion front initially affected mainly Southern Germany and lead to 20-50 mm precipitation within the first two days of May 2017 in wide parts of Bavaria and eastern Baden-Wuerttemberg. The following days, showery weather triggered by cold air at high altitudes was observed over all parts of Germany, before cyclogenetic processes due to another cut-off low over Southwestern Europe again affected predominately Southern Germany.

The second rainy period between the 11th and 15th May was caused by several short wave troughs at the eastern flank of a broad low west of Great Britain. Cold air at high altitudes again triggered deep convection including some organization due to dynamic forcing associated with the travelling short wave troughs.

The last two periods had a clear summery character since warm and moist air originating from the Mediterranean region was involved. Large-scale lifting of such air masses in front of a sharp trough over Western Europe induced the development of a mesoscale convective system in the afternoon of the 19th May over Thuringia which also leads to heavy rain in the broad, meridional zone from the Hamburg region to Northern Bavarian mentioned above. Thunderstorms were also observed in Bavaria, while more continuous rain affected large parts of Western Germany. Strong deep convection with a smaller degree of organization was observed over the last days of May when a trough extending to the Iberian Peninsula induced advection of an unstable, summery air mass. Apart from these two rainy periods, the second half of May 2017 was dominated by a longer period with sunny and summery weather, thus resulting in a positive deviation of temperature and sunshine duration (+2.1 K and +14 %, respectively).

Warm conditions also persist throughout June whose averaged 2m-temperature of 18.0°C (2.6 K against the reference period 1961-1990) resulted in the fourth warmest June in Germany since 1881 when routine observations started. An extended period of anticyclonic circulation pattern over Central Europe accompanied by above-average temperature was present in the middle of the month. Nevertheless, except from Western Germany, 60-100 mm rain was observed over many regions which places this month close to the climatological mean in terms of precipitation (Fig. 5.4b). Above-average precipitation amounts exceeding 150 mm in some regions were again recorded near the Alps as well as in the north-eastern parts of Germany.

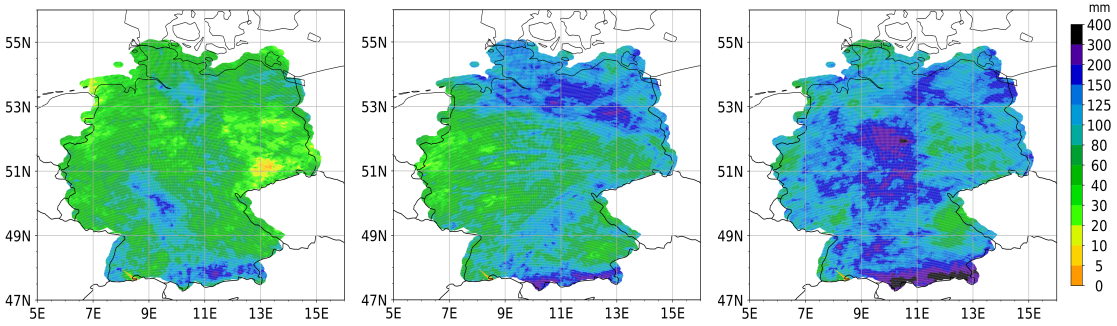

Figure 5.4: Accumulated monthly precipitation of May (left), June (center) and July (right) 2017 based on the RW product of the RADKLIM dataset.

The monthly rain pattern can be mainly attributed to two rainy periods at the beginning and by the end of the month. In the first decade, a broad long-wave trough extended southwards over the Eastern Atlantic and induced frequent cyclogenesis along its frontal zone. The travelling lows induced several air mass changes over Central Europe which lead to frontal and convective precipitation. The most rainy day in this period was the 3rd June when a low-level short wave formed over Germany in a moist and warm air mass affected by large scale lifting. Within a broad zone which extended from Southwestern Germany up to Brandenburg 20-40 mm rain in 24 hours was recorded at many station sites, while convective systems travelling from the Alpine region induced heavy rain over Bavaria with up to 105 mm/24h near Bayreuth.

Starting from the 27th June, the second rainy period was initiated by a strong trough which was established over Southwestern Europe. On its eastern flank, regions with synoptic-scale lifting induced the development of surface lows with large scale rain areas, but also deep convection within an unstable, moist air mass. Especially, the low which formed in the lee of the Eastern Alps in the night to the 29th June and moved to the north afterwards was accompanied by long lasting, intensive rain over Northeastern Germany. In the region between Hamburg and Berlin 50-100 mm rain was recorded in 24 hours with local extremes of up to 196.9 mm/24h at the airport Berlin-Tegel. Apart from these two periods, strong convective rain events were observed on the 15th and 22nd June when short-wave troughs passed over Northern Germany.

The last month of the test series, July 2017, brought above-average precipitation amounts to nearly all parts of Germany (Fig. 5.4c). Especially during the second half of the month, cyclonic circulation patterns persisted over Central Europe accompanied by prevalent strong deep convection and continuous rain. Averaged over all station sites of DWD's national observation network, 130 mm precipitation was registered throughout this month which corresponds to an excess over the climatological mean (78 mm) by more than 60 %. Despite the rainy weather, above-average temperatures with respect to the reference period 1961-1990 were recorded (+1.2 K), where the southern parts show up with a stronger positive deviation than Northern Germany (e.g. +0.7 K for Lower Saxony, but +1.5 K in Bavaria). The monthly sunshine duration was close to average with a tendency to above-average cloudiness over the low mountain range of Central Germany.

Again focusing on a sub-monthly, one can identify two rainy periods similar to the previous month June. However, it is noted that the periods showed up with a longer duration and are associated with stronger precipitation events compared to the previous month.

The first rainy period starts in the second half of the first decade. After a few days where a surface anticyclone dominated Germany except from the most northern part, the frontal zone of the polar jet was located over Northern Europe. South of this zonally oriented polar jet along which rather shallow disturbances travel eastwards, moist and warm air gets slowly advected from the Mediterranean. Through interaction of weak synoptic disturbances with a moist air mass, more or less organized deep convection has been observed for several days of Central and Southern Germany. A short-wave trough located over Great Britain pushed this air mass further north around the 10th July before moving across Northern Germany, thus inducing showers and thunderstorms over all Central Europe.

The third decade was then dominated by a cut-off low which formed on 19th July near Ireland and then approaches slowly, but steadily Central Europe. On the eastern flank of the cut-off low, several squall-lines developed and moved over Germany with local heavy rain events (e.g. 42 mm/h in Berlin Tegel on 22nd July, 16 CEST). The convective weather pattern persisted until the cut-off low was located right over Germany around the 25th July. Strong large-scale lifting then led to continuous and partially intensive rain over all Germany with main focus on the Central Germany. Up to 300 mm rain were recorded within 72 hours in the Harz region marking a major precipitation event. The last days of July were

then affected by a new trough complex located to the west inducing again frequent thunderstorms over Central Europe.

In summary, the chosen period consists of three months with varying hydrological characteristics from rather dry to wet conditions. All typical kinds of precipitation ranging from frontal rain over organized deep convection to scattered air mass convection were observed in the test period. Thus, the test period is considered to comprise all precipitation phenomena that are common for a summery period over Central Europe. Even though this period does not cover a complete summer season, but includes the late spring month May, it was decided to exclude August 2017 since this month was wetter than average similar to July. Besides, it is noted that May 2017 was dominated by summery weather resulting in a monthly averaged temperature of 14.2°C which is fairly close to the monthly average of June in the reference period 1961-1990 (15.4°C).

5.4 On the verification of precipitation forecasts

In addition to developing physical parametrization schemes and dynamical cores of NWP models, forecast evaluation is crucial for accessing and monitoring their performance. More elaborated statistical methods to score weather predictions has supported the continuous achievements in numerical modeling over the last decades (see, e.g., Bauer et al., 2015) and therefore, verification is nowadays considered to be a prerequisite in the field of model development (Wilks, 2011). In the following subsections, an outline on the basics of forecast verification is presented complemented by an overview on evaluation techniques for precipitation forecasts used in this study.

5.4.1 Basics of forecast verification

Since the atmosphere constitutes a high dimensional, non-linear system and since various model parameters are inherently uncertain (e.g. Lorenz, 1965), verification is regarded as a comparison between two stochastic systems. Formally, this means that two random variables become subject to the verification, that are the model forecast $M = \{(m, f_M(m)); m \in \mathbb{P}\}$ and the observation $O = \{(o, f_O(o)); o \in \mathbb{Q}\}$. Here, m and o represent a set of model forecast and observation realisations, $f_M(m)$ and $f_O(o)$ denote the respective probability density function (PDF), while $\mathbb{P}$ and $\mathbb{Q}$ constitute the corresponding sample spaces. Following the framework of Murphy and Winkler (1987), the *joint* random variable $\mathbf{X} = (M, O)$ is of particular interest for verification which can be further formalized as

$$\mathbf{X} = \{((m, o), f_{\mathbf{X}}(m, o)); (m, o) \in \mathbb{P} \times \mathbb{Q}\}. \tag{5.1}$$

Thus, the joint distribution $f_{\mathbf{X}}(m, o)$ describes the association between the forecasts and the observations. The degree of correspondence between both can then be quantified using so-called score functions $S(m, o)$ which assign a single value A_s to the forecast system at hand.

If a forecasting system is compared against a reference forecasting system, its *skill* is of particular interest (Wilks, 2011). Defining skill as the relative improvement over the reference, the corresponding two scores A_s and A_{ref} are combined to a *skill score* A_{skill} with the help of

$$A_{skill} = \frac{A_s - A_{s,ref}}{A_{s,per} - A_{s,ref}}. \tag{5.2}$$

Here, A_{per} represents the best possible score which would be reached by an hypothetically perfect forecasting system. In case of $A_s = A_{s,per}$, A_{skill} would attain its maximum value $A_{skill} = 1$, while $A_{skill} = 0$ holds when both systems show up with the same performance. However, in case that the competing forecasting system is superior (inferior) to its reference, positive (negative) values of A_{skill} are obtained. It is noted that this holds for positively (larger values of A_s are better) and negatively (smaller values of A_s are better) oriented scores.

While forecast verification can be undertaken for continuous quantities x, it is also common to turn these quantities into categorical events by applying specific thresholds t_x. In the simplest case, the verification then deals with categorical forecasts of dichotomous events so that the sample space of the observations S_O and of the observations S_O reduce to:

$$\begin{aligned} M &= \left\{ m \in S_M = \{(m_0, \overline{m_0})\}, \{p(m_0), 1 - p(m_0)\} \right\}, \\ O &= \left\{ o \in S_O = \{(o_0, \overline{o_0})\}, \{p(o_0), 1 - p(o_0)\} \right\}. \end{aligned} \tag{5.3}$$

Here, the probabilities for the event occurrence $p(m_0)$ and $p(o_0)$ are sufficient to describe the statistics of the forecasts and the observations individually. Their complements, denoted by bars in Equation 5.3, are easily obtained by subtracting $p(m_0)$ and $p(o_0)$ from 1, respectively. Introducing the binary event indicators $I_{m,x}$ and $I_{o,x}$ for the model forecasts and the observations

$$I_{m,x} = \begin{cases} 1 & \text{if } x_m \geq t_x, \\ 0 & \text{else,} \end{cases} \quad , \qquad I_{o,x} = \begin{cases} 1 & \text{if } x_o \geq t_x, \\ 0 & \text{else,} \end{cases} \tag{5.4}$$

the multinomial joint random variable $\mathbf{X}$ is then written as:

$$\mathbf{X} = \{((m,o), p(m,o)); (m,o) = (I_{m,x}, I_{o,x}) \in \{(1,1),(1,0),(0,1),(0,0)\}\}. \tag{5.5}$$

With only four possible outcomes, the joint distribution can be conveniently summarized in classical 2x2 contingency tables. Each cell of the relative 2x2 contingency table in Table 5.1 represents the maximum likelihood estimator for the probability of the j^{th} category p_j. The maximum likelihood estimator can be obtained by dividing the number of forecast-observation pairs of the respective category Φ_j with the total number of realizations N. Then, $p_1 = p(m_0, o_0)$ corresponds to the relative occurrence of hits, $p_2 = p(m_0, \overline{o_0})$ is related to false alarms, while $p_3 = p(\overline{m_0}, o_0)$ and $p_4(\overline{m_0}, \overline{o_0})$ refer to misses and correct rejections, respectively. The marginal probabilities for the event occurrence $p(m_0)$ and $p(o_0)$ as well as their complements are also displayed in the last column and last row of the 2x2 contingency table, respectively.

		Observation		
		o_0	$\overline{o_0}$	
Fore-	m_0	$p_1 = \Phi_1/N$	$p_2 = \Phi_2/N$	$p(m_0) = p_1 + p_2$
cast	$\overline{m_0}$	$p_3 = \Phi_3/N$	$p_4 = \Phi_4/N$	$p(\overline{m_0}) = p_3 + p_4$
		$p(o_0) = p_1 + p_3$	$p(\overline{o_0}) = p_2 + p_4$	$\sum_i p_i = 1$

Table 5.1: The classical, relative 2x2 contingency table where the inner elements constitute the joint probability of all four outcomes for dichotomous events. The equation for each joint probability is the maximum likelihood estimator for the respective category. The lower row and the most-right column denote the marginal probabilities of the observation and the forecast, respectively.

Based on the simple contingency table, several scalar attributes and scores can be formulated to access the quality of model forecasts. Additionally, scores for higher dimensional contingency tables (see, e.g., Rodwell et al., 2010) as well as scores for verifying forecasts of continuous variables have been developed so that a great plethora of different forecast verification measures exists. While their properties and their application in geoscience have gained a lot of attention in the literature (see, e.g., Wilks, 2011; Jolliffe and Stephenson, 2012, for comprehensive overviews), we now turn to the specific problem of evaluating precipitation forecasts.

5.4.2 Techniques to evaluate precipitation forecasts

The nature of precipitation processes and the related statistical properties complicate the verification of (quantitative) precipitation forecasts (e.g. Gilleland et al., 2009; Rodwell et al., 2010).

Subsequently, the basic issues and pitfalls are examined. Since theses challenges hold for categorical as well as for continuous precipitation forecasts, both prediction types are subject to the discussion. The aim is to provide reasoning on the evaluation strategy that is chosen for evaluating the test series at hand. However, for a comprehensive description on the verification problem of precipitation, the references presented herein should be consulted.

One issue in the context of scoring precipitation forecasts can be related to the highly non-Gaussian shape of the PDF of precipitation accumulations. In Germany, for instance, no precipitation or negligible precipitation amounts on a sub-daily time scale clearly dominate the spectrum. In terms of three-hourly precipitation P_{3h}, more than 80 % of the periods are dry (i.e. $P_{3h} < 0.1\,\mathrm{mm/3h}$), while weak precipitation amounts with $P_{3h} < 1\,\mathrm{mm/3h}$ still comprise roughly 10 % of the observations (Wahl et al., 2017). Even though the PDF continues to drop quickly for higher accumulation amounts, it still exhibits a fairly long *tail*. Thus, the underlying PDF is commonly best described by a right-skewed Gamma function (Wilks, 2011; Martinez-Villalobos and Neelin, 2019).

The effect of the non-Gaussian nature of accumulated precipitation can easily be accessed in terms of classical metrics for continuous variables. Widely applied verification metrics in this context are the *Mean Absolute Error* (MAE) as well

as the *Mean Squared Error* (MSE)

$$MAE = \frac{1}{N}\sum_{i=1}^{N}|m_i - o_i|, \quad MSE = \frac{1}{N}\sum_{i=1}^{N}(m_i - o_i)^2, \tag{5.6 a,b}$$

where N denotes the number of forecast-observation pairs (Murphy, 1988).

Especially the MSE is sensitive to large errors, since differences between observation and prediction are squared. Large values are easily obtained in the presence of strong precipitation events (e.g. $P_{3h} > 10\,\mathrm{mm/3h}$) in both, the simulations and the observations. Although these events are rare, the corresponding contributions may become dominant in terms of the continuous error metric. Consequently, a model that does not produce any strong precipitation amounts may be honoured compared to another model which produces such amounts, but fails to exactly match these events in space and time (see below). Contrarily, erroneous forecasts of weak precipitation events during dry periods only contribute slightly to the MAE and MSE.

To adopt to the statistical characteristics of precipitation accumulations, Ward and Folland (1991) propose to evaluate the error in the probability space as opposed to the measurement space. The *Linear Error in Probability Space* ($LEPS$)

$$LEPS\,(m, o) = \frac{1}{N}\sum_{i=1}^{N}|F_O(m_i) - F_O(o_i)| \tag{5.7}$$

constitutes the mean error in terms of the cumulative density function (CDF) of the observations F_O (cf. Eq. 5.6a) which is related to the corresponding PDF by differentiation

$$f_O(x) = \frac{dF_O(x)}{dx}.$$

Using the $LEPS$, deviations between observed and modelled precipitation amounts are weighted according to the slope of the observed PDF. Thus, errors in predicting weak precipitation amounts as well as mismatches in capturing dry periods become more relevant, whereas deviations at the tail of the PDF only contribute slightly to the error metric. A model that produces no large precipitation amounts is not honoured anymore and gets penalized when it operates inaccurately on the left tail of the PDF as opposed to the MAE and MSE.

Together with the generic expression in Equation 5.2, a skill score of the $LEPS$ can be constructed. With $LEPS_{per} = 0$, $LEPS_{skill}$ reads

$$LEPS_{skill} = 1 - \frac{LEPS\,(m^1, o)}{LEPS\,(m^2, o)}, \tag{5.8}$$

which can be used to directly compare the performance of two competing forecasting systems m^1 and m^2 such as ICON-HYM and ICON-BT.

In analogy to verifying continuous precipitation amounts, the evaluation of precipitation events with the help of the 2x2 contingency table is commonly adopted to the statistical nature of precipitation. This is also related to the attempt to score forecasts with a single scalar, even though the dimensionality of this categorical forecast problem is three. The aim of the summarizing score function is to

focus on *relevant* properties of the forecast-observation pairs which are then used for comparison purposes between different forecast products.

However, sorting out the relevant properties of categorical precipitation forecasts is a somehow ambiguous process so that different (skill) scores are typically applied. The Heidke Skill Score and the Equitable Threat Score are widely used methods that both try to account for correct forecasts (hits or/and correct rejections) by chance. Note that especially random forecasts of dry events (e.g. $P_{3h} < 0.1\,\mathrm{mm/3h}$) may attain seemingly good scoring results if yes and no forecasts are equally credited (cf. Example 7.1 in Wilks, 2011).

In addition to the statistical characteristics of precipitation, the complex and chaotic nature of precipitation processes complicates the forecast verification. Indeed, point-to-point verification is considered to be an unsuitable approach at convective gray-zone resolutions for two reasons (see also Rossa et al., 2008, for a discussion).

First, the spatial resolution of the NWP model is still too coarse to explicitly resolve individual convective cells. The required necessity for parametrization (see Sec. 2.3) involves naturally some degree of uncertainty so that it cannot be expected that such a modeling approach yields a perfect match in space and time between forecasts and observations.

Second, errors on mesoscale grow significantly quicker than errors on larger scales (e.g. Lorenz, 1969). Even if the larger-scale atmospheric state is well captured, scoring model simulations at mesoscale are prone to large errors when point-to-point comparisons to the observations are performed (Mass et al., 2002). This is related to the fact that small spatial (and/or temporal) displacements of precipitation patterns get penalized twice, once for missing their correct location and once for placing them at a location where they are not supposed to be. In the verification community, this is commonly described as the *double penalty problem*.

Thus, it is common practise to relax the requirement for exact matching on spatio-temporal scale. The so-called *fuzzy verification* framework with the basic assumption that a forecast is still useful despite some displacement (Ebert, 2009) is well established in this context. The degree of displacement is controlled by defining a local neighbourhood which can be a circular (squared) region with radius r_s (edge length l_s) surrounding the location of interest. Temporal neighborhoods can be defined and added as well, e.g. a time window of three hours for hourly precipitation amounts. Since the appropriate (spatial and/or temporal) scale s is unknown, the neighborhood size may be allowed to vary. By doing so, valuable information on the forecast quality on different scales is obtained.

For precipitation, several different fuzzy techniques have been introduced (see Ebert, 2008, for a review). One of the most intuitive approaches comprises a simple upscaling technique where the observations and forecasts are averaged to coarser scales. On this coarser scale, continuous and categorical scores can then be applied for verification (e.g. Yates et al., 2006). To serve its purpose, the neighborhood scale must at least exceed the effective model resolution (typically 6-8 Δx) to avoid accounting for random displacements. Hence, a neighborhood scale of 50 – 100 km is regarded as a reasonable choice for contemporary atmospheric models with $\Delta x \lesssim 10\,\mathrm{km}$.

In Theis et al. (2005), the fuzzy verification method was extended to take up a probabilistic interpretation by estimating the probability of a predicted event within the predefined neighborhood. This is done by first converting the gridded continuous precipitation amounts to a field of binary events based on an user-defined threshold (see Eq. 5.4). The respective threshold t_P can thereby be varied such as the spatio-temporal scale s. The corresponding forecast probability $\langle p(m_0)\rangle_s$ is then estimated by the fraction of event grid boxes within the local neighbourhood, that is

$$\langle p(m_0)\rangle_s = \frac{1}{n}\sum_{j=1}^{n}\left(I_{m,x}\right)_j . \tag{5.9}$$

Here, $\langle\cdot\rangle_s$ indicates the neighbourhood region which comprises n grid boxes covered by the radius r or the edge length l on a spatial scale.

The probabilistic interpretation enables the application of common probabilistic scores such as the Brier Score (BS) or its subvariant, the Fractions Brier Score (FBS).
The BS is a proper scoring rule (Broecker, 2009) that is analogous to the MSE, but operates on the squared difference between the forecast probability and the discrete event:

$$BS = \frac{1}{N}\sum_{i=1}^{N}\left[\left(\langle p(m_0)\rangle_s\right)_i - \left(I_{o,x}\right)_i\right]^2 . \tag{5.10}$$

This approach was applied in the study of Theis et al. (2005) to generate a probabilistic *pseudo-ensemble* from deterministic precipitation forecasts.

The study of Roberts and Lean (2008) modified the probabilistic point of view by replacing the discrete observation at grid point i with the observed fraction of events in the neighborhood. Combining the resulting FBS given by

$$FBS = \frac{1}{N}\sum_{i=1}^{N}\left[\left(\left\langle p(m_0)\right\rangle_s\right)_i - \left(\left\langle p(o_0)\right\rangle_s\right)_i\right]^2 \tag{5.11}$$

with the highest attainable Fractional Skill Score value FBS_{worst}, the Fractional Skill Score (FSS) is obtained:

$$FSS = 1 - \frac{FBS}{FBS_{worst}} \tag{5.12}$$

$$\text{with} \qquad FBS_{worst} = \frac{1}{N}\sum_{i=1}^{N}\left(\left\langle p(m_0)\right\rangle_s\right)_i^2 + \left(\left\langle p(o_0)\right\rangle_s\right)_i^2 . \tag{5.13}$$

The FSS has some convenient properties which ease its interpretation as stated in Roberts (2008), Roberts and Lean (2008), and Skok and Roberts (2016):

i) A value of $FSS = 0$ indicates a complete mismatch between forecast and observation given the neighborhood scale s. This value is always obtained when either no events are predicted while some occur or vice versa.

ii) With increasing neighborhood size the obtained FSS-value becomes larger and asymptotes to 1 in case of an unbiased forecast.

iii) A random forecast with $\langle p(m_0)\rangle_{s=0} = f_o$ yields $FSS = f_0$ in case of a single-pixel neighborhood ($s = 0$). Here, f_o denotes the fractional area coverage of observed precipitation events and thus, the FSS increases with the areal coverage of events in the target domain.

iv) A forecast can be considered useful when it attains a higher FSS than a random forecast on a neighborhood domain consisting of $n = 1/f_o$ grid points. As shown in Skok and Roberts (2016), the corresponding threshold FSS_{useful} is given by

$$FSS \geq FSS_{useful} = 0.5 + \frac{f_o}{2}\left(\frac{1}{2 - f_o}\right) \tag{5.14}$$

provided that the model forecast is unbiased.

Due to its intuitive interpretation, the FSS has become one of the standard metrics for precipitation verification.

Besides, other techniques than the fuzzy verification framework have been developed. Among others, these comprise object-based techniques which aim to identify and compare precipitation features from the forecast and the observation field as well as scale decomposition methods. Recent examples in this context are the displacement-amplitude score introduced by Keil and Craig (2009) or verification techniques based on shift-invariant wavelet-transformations (see, e.g., Buschow and Friederichs, 2020, 2021). However, the subsequent evaluation relies on standard verification techniques as introduced above.

While the joint distribution of forecasts and observations is of particular interest in forecast verification, investigation of the marginal distribution provides additional useful insight. This is due to the fact that the joint distribution can be factorized into a conditional and marginal distribution following Murphy and Winkler (1987).
In context of the task at hand, histograms of precipitation rates as well as the predicted diurnal cycle of area-averaged precipitation amounts and intensities are commonly compared against observations (see, e.g. Lean et al., 2008; Bechtold et al., 2014b; Wahl et al., 2017). This allows us to distill shifts in the diurnal cycle and systematic deficiencies in modeling the PDF of precipitation.

To measure the latter quantitatively, the integrated quadratic distance IQD can be applied (Thorarinsdottir et al., 2013) as a proper divergence function. With

$$IQD(F_{P,o}, F_{P,m}) = \int_{-\infty}^{\infty} (F_{P,o}(x) - F_{P,m}(x))^2 \,\mathrm{d}x, \tag{5.15}$$

this scoring rule is negatively oriented similar to the MSE. The lower the value of IQD, the higher is the similarity between the modelled and observed PDF of accumulated precipitation amounts.

From a categorical forecasting point of view, the systematic bias b of predicted precipitation events is also of particular interest. The systematic, or unconditioned bias, is related to the (relative) 2x2 contingency table introduced in Table 5.1 and evaluates the quotient between the probability of observed and modelled events:

$$b = \frac{p(m_0)}{p(o_0)} = \frac{p_1 + p_2}{p_3 + p_4}. \tag{5.16}$$

While the optimal value of b is 1, $b > 1$ means that a model tends to produce too many precipitation events. Contrarily, underestimating these events yields $b < 1$.

It is noted that the analysis of the marginal distribution of precipitation must also be conducted in consideration of the double penalty problem. Thus, the spatio-temporal scale has to be chosen large enough when the mentioned tools are applied.

5.5 Evaluation of the simulation test series

Following the previous discussion, a careful assessment of the strengths and weaknesses of the model simulations as presented in Section 5.1 is performed. The aim is to reveal potential added value when HYMACS instead of the conventional Bechtold-Tiedtke scheme is used to represent deep convection at gray-zone resolutions. Likewise, drawbacks of the hybrid CPS can be worked out.

Although the model simulations differ with respect to the applied convection scheme, the atmospheric state is the same at initialization time. Thus, it cannot be expected that larger systematic differences already develop during the first integration hours. Spin-up effects resulting from the differing CPS of the driving model may also degrade the performance of ICON-HYM with respect to the reference simulations during the initial time period. Since the initialization of the model simulations takes place at 00 UTC (02 CEST) and spin-up effects are noticeable for at least 6 hours after initialization (e.g. Zhao and Zhang, 2018), considerable parts of the diurnal cycle on the first simulation day should not be used for quantitative comparison. Therefore, the subsequent evaluation focuses on the second simulation day which starts 22 hours after initialization and ends at forecast hour 46.

Apart from the pitfalls of the first simulation hours, this time window has the advantage that mesoscale structures originating from convective processes during the first day may affect the evaluation period. Since those convective mesoscale structure have to be largely captured by the respective CPS in a free forecast, differences between both schemes at hand are enhanced while the atmospheric state at coarser spatial scales remains close to each other (cf. Fig. 1.3 in Sec. 1.1).

The subsequent evaluation is structured as follows: At first, monthly precipitation patterns accumulated from the second simulation day are analyzed and compared qualitatively against radar observations. This gives some initial insight into the dependency of the simulated precipitation from the convection parametrization including its mesoscale effects on the atmospheric dynamics.

A detailed frequency analysis of daily and hourly precipitation then sheds light on the statistical properties of precipitation in the summer season at hand. The simulated and observed marginal distributions of precipitation sums are analyzed with the help of histograms and the differences between both are scored by applying the IQD-function (see Eq. 5.15). Thus, a first quantitative assessment of the systematic strengths and deficiencies of the respective CPS is undertaken.

The subsequent investigation of the diurnal cycle provides further insight with focus on the sub-daily variations. Area-averaged hourly precipitation rates as well as precipitation intensities are evaluated along with subdaily variations in the

underlying PDF of precipitation events in terms of the IQD. Simultaneously, a regional distinction in the evaluation procedure is established.

The last two subsections deal with the analysis of the joint distribution of (re-) forecasts and observations. Starting on a coarse spatial scale by evaluating the area-integrated precipitation amounts over Northern and Southern Germany, the problem of *double penalty* is circumvented. The performance of the two forecasting systems ICON-HYM and ICON-BT is then accessed in terms of the $LEPS$ skill score given by Equation 5.8.

Afterwards, the evaluation of the model simulations in terms of the Fractions Skill Score (FSS) gives access to the model performance at varying spatial scales (see Eq. 5.13). It is worth noting that the FSS is calculated on ICON's native triangular grid. Besides, the neighborhood scale is not expressed in terms of the number of grid squares like in Roberts and Lean (2008), but defined by a neighborhood radius r_s. The radius is thereby chosen to be a multiple of the grid spacing Δx_{ICON}. An example with $r_s = 2\Delta x_{ICON}$ is illustrated in Figure 5.5.

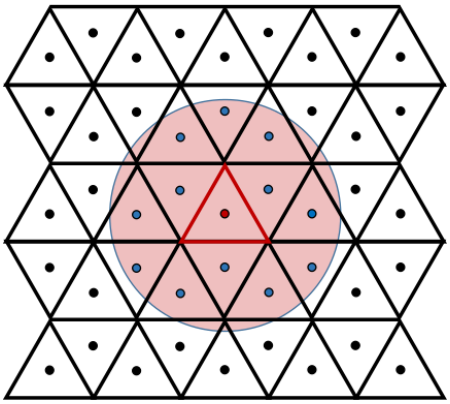

Figure 5.5: Exemplary neighborhood around a grid point on a planar triangular grid with $r_s = 2\Delta x_{ICON}$. The center of the neighborhood coincides with the circumcenter of the triangle highlighted in red. The circumcenters of the triangular cells inside the neighborhood are marked in blue.

Although a profound number of daily (re-)forecasts is evaluated in this study ($N_0 = 92$), sampling uncertainty has to be taken into account. This is especially true when scores are calculated to judge if one forecasting system outperforms the other.

A common method to quantify the sampling uncertainty is based on the non-parametric bootstrapping technique which repeatedly resamples the underlying data with replacement to generate permuted score values (see, e.g., Efron and Tibshirani, 1994; Lahiri, 2013, for comprehensive overviews). However, the simulations during the test series are autocorrelated so that the so-called non-overlapping block bootstrapping procedure is applied in this thesis. Instead of resampling from individual data points in the collection of simulations, the test period is subdivided into continuous blocks of length L_B that are used for resampling.

The block length L_B thereby has to chosen with care to produce reliable uncertainty estimates. In general, it depends on the degree of autocorrelation of the underlying data (Wilks, 1997). For precipitation verification in the midlatitudes, L_B is typically set to the approximate length of a synoptic period which is in the

order of one week (e.g Wahl, 2015). Specifically, L_B is set to seven days for daily and to five days for subdaily precipitation amounts in this study which translates to 13 and 18 different blocks over the test period, respectively. Based on these blocks, 1000 bootstraps are performed from which the 90 % confidence interval is estimated in the subsequent evaluation.

For estimating the uncertainty of the FSS, the block bootstrapping is combined with a spatial bootstrapping technique. Similar to the blocks, the triangular cells in the neighborhood are resampled (with replacement) when iterating over all grid boxes of the verification domain. This approach results in 1000 additional permuted FSS-values for each realization.

5.5.1 Monthly precipitation

The evaluation of the ICON simulations with HYMACS and the Bechtold-Tiedtke scheme starts with a qualitative assessment on the modelled monthly precipitation within the test period.

Figure 5.6 illustrates the differences between the modelled and observed monthly precipitation from May to July 2017 for ICON-HYM (left column) and ICON-BT (center column). As mentioned above, the (hourly) precipitation is accumulated over the second simulation day of all model runs within the respective months. The observed accumulated precipitation (OBS) are based on the YW product of the RADKLIM dataset and are presented in the rightmost column.

Despite the rather long accumulation time, it cannot be expected that precipitation patterns close to the meso-γ scale are adequately captured by the model simulations. Especially in regions where convection dominates the monthly precipitation pattern, e.g. in Thuringia and Rhineland-Palatinate in May (Fig. 5.6a), the double-penalty problem becomes obvious. In these regions, strongly varying differences between observed and simulated monthly precipitation are due to small displacement errors and should not be overemphasized.

However, deficiencies on larger-scales can be identified as well. For instance, the high monthly precipitation amounts between Hamburg and Berlin are largely underestimated with ICON-HYM and ICON-BT in June (Fig. 5.6b). This indicates that the cyclone leading to intensive continuous rain over Northeastern Germany by the end of June (see Sec. 5.3) was not accurately captured by the ICON simulations in general. Another example pertains the large (under-)overestimation of precipitation in (Central) Eastern Germany in July (Fig. 5.6c) which can be attributed to the cut-off low around 25$^{\text{th}}$ July. Due to evaluating the second simulation day, mesoscale flow structures depending on the differing representation of (deep) convection also become present in the monthly precipitation pattern of the model simulations. Thus, there does not only exist considerable differences between the observation and the simulations, but also between the competing simulations. One of this remarkable difference can be seen in the difference plots for May where ICON-BT underestimates strongly the monthly precipitation near and south off Hamburg. The simulations with HYMACS show a much less systematic difference pattern in this region. This indicates that the convective mesoscale systems affecting parts of Central Germany by end of the second decade are better

represented with the hybrid CPS.

While there are also examples where ICON-BT performs better than ICON-HYM (e.g. over North Rhine-Westphalia in July), the difference patterns at smaller scales appear to be more organized with HYMACS. In regions with a dominant contribution of convection to the monthly precipitation amount, *shower streets* can be identified as aligned areas with alternating sign in the precipitation difference. Such features are natural to high-resolution simulations and indicate a pronounced coupling of the simulated convective precipitation pattern to the environmental dynamics. Although increasing the differences in a point-to-point evaluation as a manifestation of the double penalty problem, this is considered to be a beneficial feature of HYMACS.

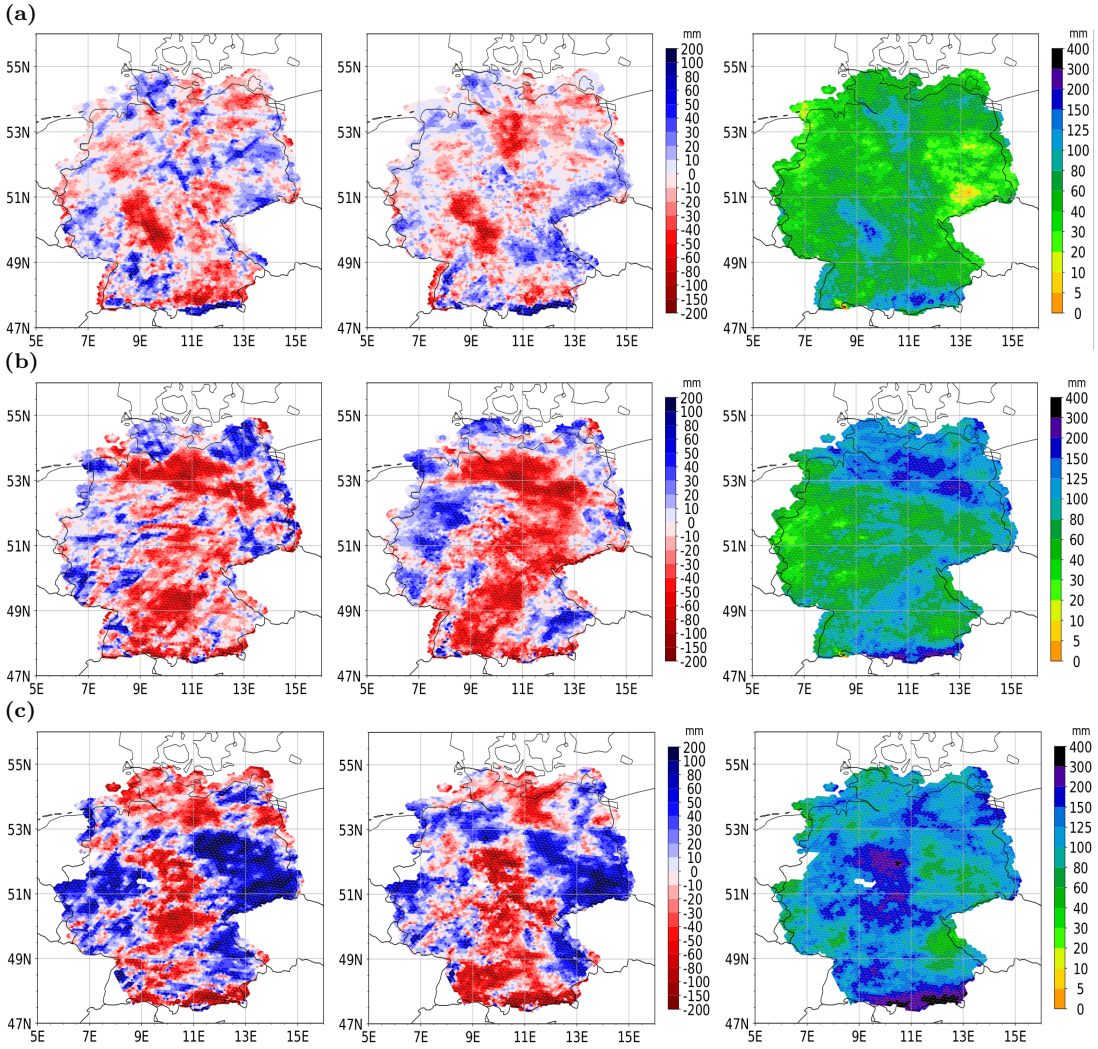

Figure 5.6: Differences of modelled monthly precipitation (left column: ICON-HYM - OBS, center column: ICON-BT - OBS) on the second simulation day compared to the RADKLIM observations for (a) May, (b) June and (c) July. The OBS is derived from the YW product and was remapped onto ICON's native grid. The accumulation periods coincide with model simulation times, i.e. the 1st May is excluded from the monthly precipitation in May 2017. The regions with missing data close to the western border are due to radar failures at the station sites Essen and Freiburg leading to a temporal data coverage of less than 95 % in July 2017.

5.5.2 Frequency analysis of hourly and daily precipitation

Now, we turn our attention to the marginal distribution of precipitation in the test period by analyzing the frequency of precipitation events on a daily and hourly scale.

The green bars in Figure 5.7 show the observed relative frequency for different classes of daily precipitation over all Germany. Nearly half of the observations (48.31 %) belong to the category *dry day* which is defined for 24 h precipitation amounts P_{24h} below 0.1 mm in this study. Weak rain days (0.1 mm/24h $\leq P_{24h} <$ 2 mm/24h) constitute the dominant class for *wet days*, while the frequency quickly decreases for higher precipitation amounts. The classes belonging to moderately rainy days (5 mm/24h $\leq P_{24h} <$ 30 mm/24h) occur at a frequency in the order of 1-10 %, whereas higher daily precipitation amounts are rare. Note that the decrease in the frequency for higher precipitation accumulations is stretched in Figure 5.7 due to the increasing class size. In fact, the frequency distribution corresponds to a right-skewed Gamma distribution which is common for precipitation data (see Sec. 5.4.2).

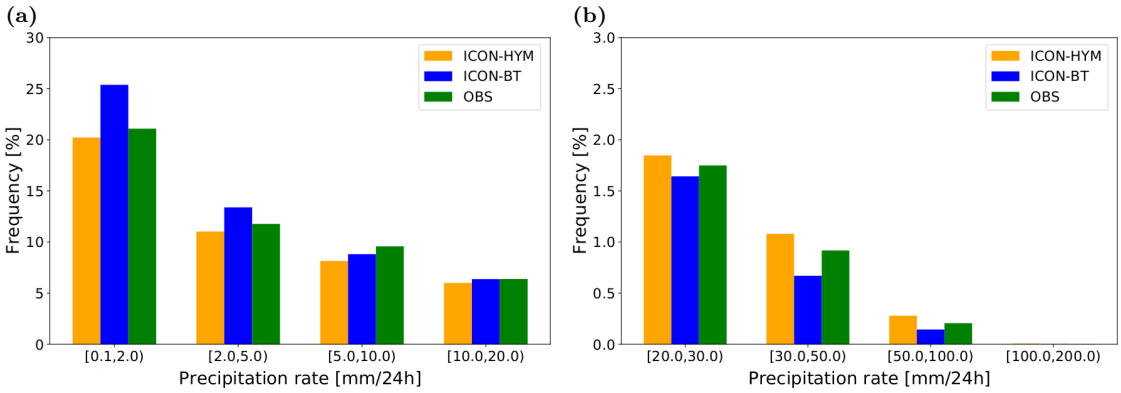

Figure 5.7: Relative frequency distribution of daily precipitation for all months of the test series May-July. The model data is evaluated on the second simulation day and only where corresponding radar observations (remapped onto ICON's triangular grid) are available.

The model simulations with HYMACS capture the frequency distribution quite well, although the occurrence of dry days is slightly overestimated (51.38 %). This slight overestimation can mainly be attributed to lower than observed frequencies for the weak and moderate precipitation classes. However, stronger daily precipitation events (with $P_{24h} >$ 30 mm/24h) tend to occur too often with HYMACS.

By contrast, the simulations with the operational Bechtold-Tiedtke scheme show up with a high tendency for weakly rainy days. Nearly 40 % of the events belong to the respective classes (0.1 mm/24h $\leq P_{24h} <$ 2 mm/24h and 2 mm/24h $\leq P_{24h} <$ 5 mm/24h) which is considerably more than observed. Strong precipitation events are however even rarer than in the observations, but cannot outweigh the overestimation of weak precipitation events. Thus, contrary to HYMACS, the chance for dry days is reduced compared to the observations.

Quantifying the similarity between the frequencies of observed and simulated daily precipitation amounts with the help of the IQD metric (see Eq. 5.15) confirms that the PDF of daily precipitation is better captured with ICON-HYM.

With $IQD = 0.0282\,\text{mm/24h}(+0.0360/-0.0081\,\text{mm/24h})$, ICON-BT attains a considerably higher value than the competing simulations with HYMACS whose evaluation yields $IQD = 0.0052\,\text{mm/24h}(+0.0043/-0.0037\,\text{mm/24h})$. Albeit the relatively large 90 % confidence interval indicating uncertainty due to the moderate sample size, the better representation of the marginal distribution of daily precipitation can be traced back to a better representation of weak precipitation events with ICON-HYM compared to ICON-BT. Yet, also the PDF of daily precipitation with HYMACS is still significantly different from the observed one since the 99 % significance level yields $IQD \sim \mathcal{O}(10^{-4})$ which is one order smaller than the obtained IQD with ICON-HYM.

Analysis of the monthly relative frequency distribution of daily precipitation events reveals that the tendency of the operational Bechtold-Tiedtke scheme to produce too much light precipitation is most pronounced for May 2017. While the radar observations as well as the simulations with HYMACS show up with a frequency of dry days close to 60 % (58.20 % in OBS and 59.28 % in ICON-HYM), ICON-BT simulates many weak precipitation events with an outstanding maximum in the weakest precipitation class of this month (see Fig. 5.8a).

Contrarily, the proneness of HYMACS for strong precipitation events can be attributed to the wettest month of the test series, July 2017 (see Fig. 5.8b). Especially, daily precipitation in the class 30-50 mm/24h occur much more frequently in this month than in the observations (nearly 2 % compared to around 1.3 %). However, the differences in the strong daily precipitation classes are rather small with some tendency towards underestimation in May and June, manifesting the general likeliness to more dry days in the simulations with HYMACS.

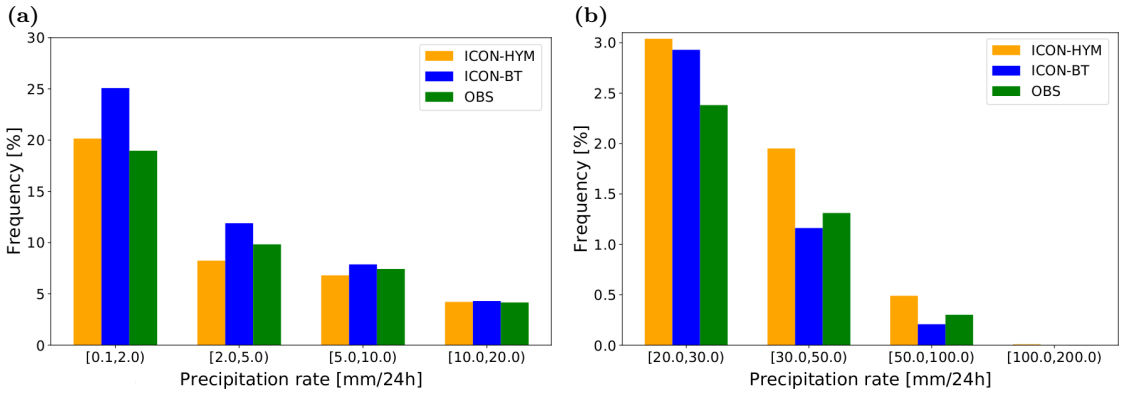

Figure 5.8: Clipped relative frequency distributions of daily precipitation for the months May (a) and July (b). While for May precipitation classes with $P_{24h} < 20\,\text{mm/24h}$ are displayed, the classes with daily precipitation amounts exceeding 20 mm are shown for July.

To further analyze the characteristics of accumulated precipitation amounts in the model simulations and in the observations, the frequency analysis is conducted for hourly precipitation P_{1h} in the following. The respective frequencies of different precipitation classes for the period May-July are displayed in Figure 5.9. The characteristic property of the ICON-BT to produce too many weak precipitation events is again obvious, whereas the frequencies for the precipitation classes with $P_{1h} < 2\,\text{mm/h}$ only differ slightly between ICON-HYM and OBS. No precipitation

events, again classified as events with $P_{1h} < 0.1\,\mathrm{mm/h}$, occur in roughly 90 % of the cases in the observation and in the simulations with HYMACS, whereas ICON-BT underestimates these events by nearly 4 %. This result is analogous to the analysis of daily precipitation and indicates that the systematic overestimation of weak precipitation can be directly linked to short-lived convective precipitation events with the Bechtold-Tiedtke scheme.

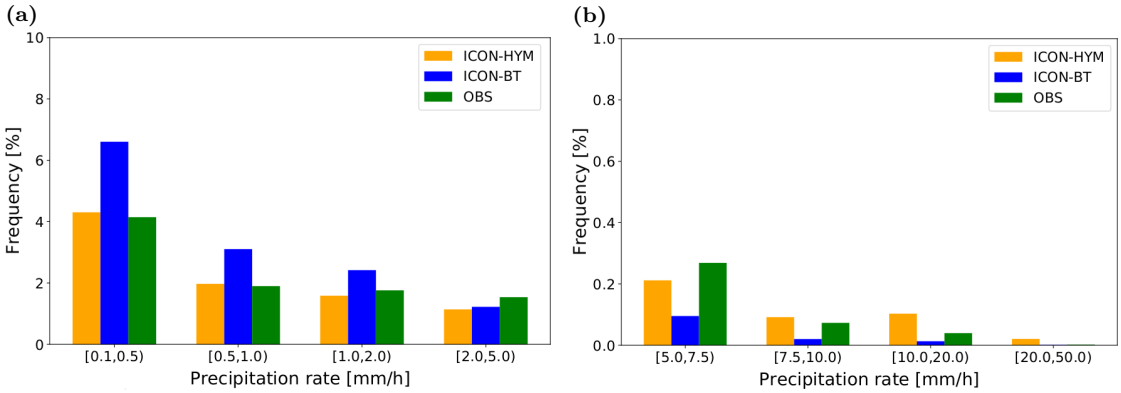

Figure 5.9: As Figure 5.7, but for hourly precipitation.

The simulations of ICON-BT also underestimate clearly moderate and strong precipitation events, while ICON-HYM now shows up with a notable overestimation of events with $P_{1h} \geq 10\,\mathrm{mm/h}$. The latter seems to outweigh the slight underestimation of hourly precipitation rates between 2 mm/h and 7.5 mm/h with HYMACS. Apart from a varying amplitude of the respective frequency classes, the described characteristic of hourly precipitation can be diagnosed for all three months separately (not shown).

The IQD for all hourly precipitation events confirms quantitatively that the simulated probability distribution with ICON-HYM is closer to the the observed one. With the hybrid CPS, ICON only attains a value of IQD = 0.0011 mm/1h(+0.0056/ -0.0002 mm/1h), whereas ICON-BT shows up with a significant higher value of IQD = 0.0112 mm/1h(+0.0056/-0.0084 mm/1h). Thus, the relative difference in IQD between both model configurations is on average larger for hourly precipitation than for daily precipitation. This confirms that changing the model's CPS mainly affects short-term precipitation events since these are naturally linked to convection.

Putting the results of the frequency analysis together, a first hypothesis can be made on the underlying dynamic-physical reasons. The tendency of the Bechtold-Tiedtke scheme to produce too many precipitation events along with an underestimation of their intensity may indicate that convective instability is released too early. Opposed to that, the modest overestimation of strong precipitation events aligned with producing too less moderate precipitation events with HYMACS may be explained by a too strong convective suppression during noon. A more detailed analysis of the diurnal cycle of precipitation is therefore conducted next.

5.5.3 Diurnal cycle of precipitation

The daily cycle of precipitation is evaluated in terms of the hourly precipitation amounts as well as the intensity of precipitation events that are both averaged in space and time. The former includes *no-rain* events, whereas events with $P_{1h} < 0.1\,\mathrm{mm/h}$ are filtered out for the intensity. However, due to occasional maintenance of some radar stations, some areas have observational gaps during the test period (see also Fig. 5.4). In order to avoid contributions from areas with frequently missing observations, grid points with less than 95 % data coverage for a specific daytime are disregarded.

Analysis for all Germany

Figure 5.10 illustrates the daily cycle of averaged hourly precipitation accumulations over Germany. The observations from May to July show a clear diurnal cycle in mean precipitation (black curve in Fig. 5.10a). During the first half of the day, the precipitation activity is reduced and reaches a weak minimum at local noon[2]. From 11 CEST onward, the averaged precipitation rate starts to increase with steepest slope in the early afternoon and reaches its maximum between 17 and 20 CEST. In the evening hours and during the first half of the night, the precipitation activity again drops towards the baseline activity of the morning hours.

The overall shape of the mean diurnal cycle of precipitation is reproduced quite well with ICON-HYM (red curve in Fig. 5.10a). Until early noon, there are only minor differences in the averaged precipitation activity. However, the midday minimum is somehow stronger compared to the observation due to a stronger decline in mean precipitation between 8 and 12 CEST. The increase during the afternoon hours is slightly delayed and results in an overestimation of the maximum precipitation activity shifted by 1-2 hours towards the evening. A steeper than observed decline in averaged precipitation follows for the last hours of the day.

The differences compared to the observations are considerably larger with ICON-BT (blue curve in Fig. 5.10a). The precipitation activity increases between midnight and the morning hours and then remains at higher level close to 0.13 mm/h. Albeit being weak in the observations, a midday minimum is absent in the simulations with the operational Bechtold-Tiedtke scheme and the daily maximum of mean precipitation occurs too early by at least two hours. Thus, while the precipitation activity keeps on being high during the early evening in the observations, the mean precipitation already drops quite quickly with ICON-BT before it reaches its daily minimum at around 22 CEST.

The daily cycle in the precipitation intensity is less pronounced, but resembles the temporal course of mean precipitation in general (black curve in Fig. 5.10b). Between morning and noon, the median of the precipitation intensity is close to 1.1 mm/h and then increases towards 1.3 mm/h in the evening hours. The increase in intensity is less continuous than the increase in the overall mean precipitation rate and its maximum is also slightly shifted to the late evening, while the decrease continues throughout the night and early morning hours. As can be seen from the

[2]Monthly evaluation of the mean precipitation reveals that the midday minimum is clearly visible in July, but absent in the two remaining months.

shaded area illustrating the interquartile range, the spatial variability is large in the observations and points out to considerable regional dependencies of the rainfall intensity (see below).

In analogy to the mean precipitation rate, ICON-HYM reproduces the general shape of the daily cycle, but overestimates its amplitude (red curve in Fig. 5.10b). The minimum median intensity drops to 0.9 mm/h at local noon, while the maximum reaches up to 1.35 mm/h at 21 CEST. The subsequent decrease at night is therefore also steeper than in the observations.

However, the differences are even larger in terms of the intensity with ICON-BT compared to the mean precipitation (blue curve in Fig. 5.10b). A phase shift of about 10 hours is analyzed with a maximum at the end of the night/early morning and a minimum during the evening hours. In addition to the strong phase shift, the precipitation intensity and its spatial variability are considerably smaller compared to the observations. Thus, the tendency of the Bechtold-Tiedtke scheme to produce too frequent, but too weak precipitation events can be diagnosed over all day times. This characteristic feature is also reflected in the frequency bias b which is always greater than 1 with ICON-BT and even exceeds a value of 1.5 around noon between 10 and 15 CEST. All in all, the diurnal cycle of precipitation is therefore poorly represented with the classical CPS in the test series at hand.

Contrarily, the frequency bias of ICON-HYM is generally much closer to 1 showing that the hybrid CPS is better calibrated. Nonetheless, systematic weaknesses can be identified for HYMACS as well. While b remains close to 1 at noon, a noticeable underestimation ($b < 1$) builds up in the afternoon hours. Due to the convectively driven daily cycle of precipitation, this indicates that convective cells are likely to be suppressed at this day times with HYMACS. The consequence of this behaviour has already been noted above, that is a delayed diurnal and slightly stronger maximum in mean precipitation and intensity. Likewise, the higher 25th percentile of precipitation intensity in the evening hours can be reasoned.

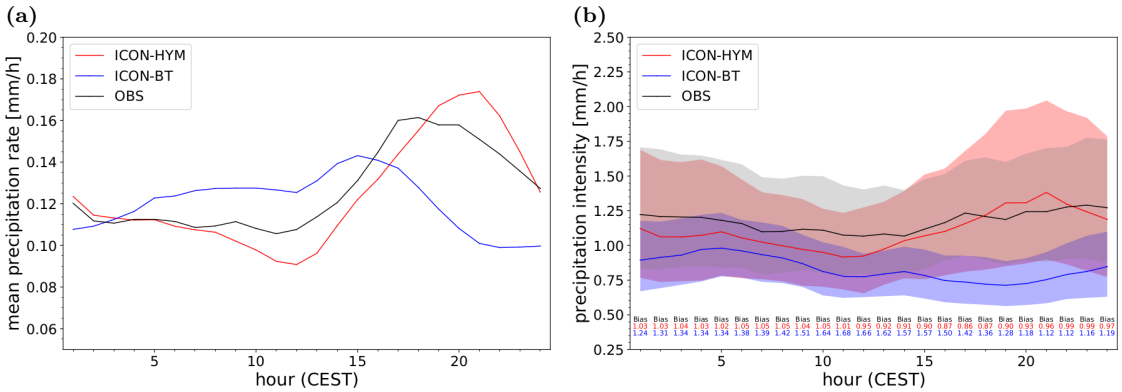

Figure 5.10: (a) Diurnal cycle of mean precipitation and (b) precipitation intensity for all Germany between May and July 2017. The latter is calculated from events with $P_{1h} \geq 0.1$ mm/h (right). The shaded areas in (b) show the interquartile range of spatial variability for the precipitation intensity. For mean precipitation, the variability is omitted for illustration purposes. Besides, hourly values of the frequency bias are given in (b) for ICON-HYM (red) and ICON-BT (blue).

Regional differences in diurnal cycle

So far, the evaluation has been performed collectively for all Germany. However, the topographical and climatological characteristics of Germany are diverse. The North German Lowlands occupy a maritime character in its western part, whereas Central and Southern Germany are dominated by low mountain range areas bordered by the Alps to the south. Since mountains play a crucial role for precipitation patterns in general ranging from orographic (stratiform) precipitation to triggering of deep convection (e.g. Fuhrer and Schaer, 2005; Wulfmeyer et al., 2008; Kirshbaum et al., 2018), spatial separation of the investigation area enables a more detailed analysis.

In the following, the investigation area is separated along the northern edge of the low mountain range to serve this purpose. The border between both regions is illustrated by the red line in Figure 5.2 separating the region GER-North with typically less than 100 - 150 m elevation in the north from an elevated and often highly diverse topographical region GER-South to the south[3].

As indicated by the black curves in Figure 5.11(a,b), the observed diurnal cycle of mean precipitation for GER-North and GER-South differ quite remarkably from each other: While the precipitation activity reaches its daily minimum during the second half of the night and then increases continuously until the evening in GER-North, a midday minimum in mean precipitation is clearly visible for GER-South. Besides, the daily maximum occurs already in the late afternoon/early evening while nightly rain remains at a moderate level until early morning in GER-South.

The diurnal cycle of precipitation intensity also differ for both regions as revealed by the black curves in Figure 5.11(c-d). Such as the mean precipitation rate, the intensity is weakest in Southern Germany between morning and noon and then increases during the afternoon hours. However, the intensity remains high and even keeps on slightly increasing in the late evening and at night, indicating that the area of precipitation reduces after sunset. For GER-North, the peak in intensity coincides roughly with the peak of mean precipitation. However, it is noted that the prior increase mainly occurs in the afternoon hours, indicating that the increase in mean precipitation between morning and noon is realized by an increase in the precipitating area.

The ICON-simulations with the two different CPS also reveal different regional characteristics: Apart from the delay for the daily maximum of precipitation, ICON-HYM captures the diurnal cycle in mean and intensity reasonably well for GER-South (red curves in Fig. 5.11(a,c)). The moderate underestimation in mean precipitation between midnight and noon can be attributed to an underestimation of the intensity since the frequency bias is close to 1. In the afternoon hours, this underestimation can rather be traced back to a negative frequency bias which also tends to outweigh the slightly too strong precipitation intensity in the evening.

With ICON-BT, the differences in the diurnal cycle compared to the observations are large for mean precipitation and intensity over GER-South (blue curves in Fig. 5.11(a,c)). Between the morning and the afternoon, the mean precipitation

[3] GER-North covers around 45 % (3942 grid points) of the complete German region (9018 grid points).

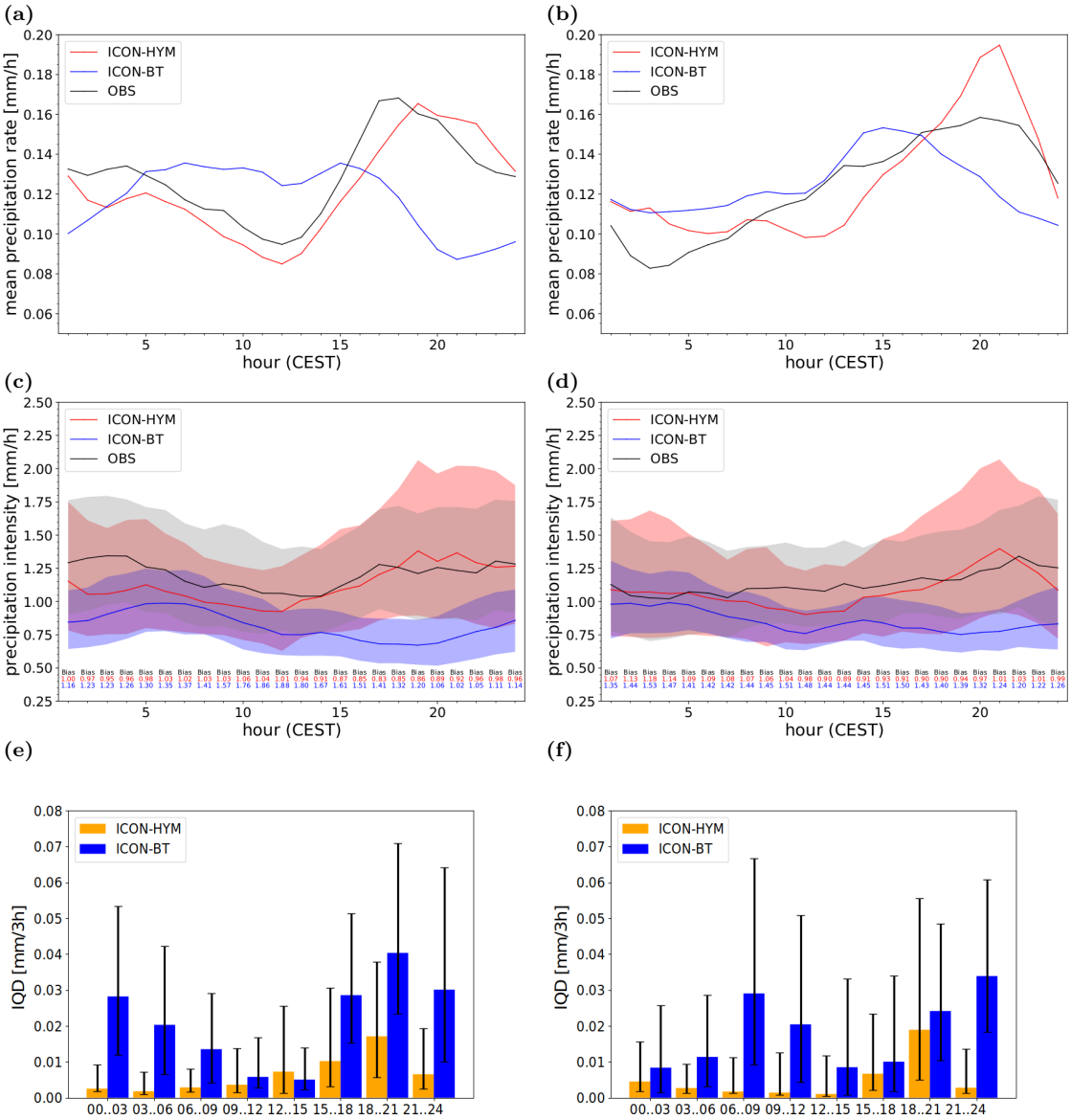

Figure 5.11: Diurnal cycle of precipitation in South (left column) and North (right column) Germany. (a,b) Mean precipitation analogous to Figure 5.10a. (c,d) Precipitation intensity analogous to Figure 5.10b. (e,f) Integrated quadratic distance (IQD) for 3h precipitation amounts. The vertical bar illustrates the 95 % confidence interval estimated via block bootstrapping. The 99 % significance level attains values of $\mathcal{O}(10^{-4}\text{-}10^{-5})$ and is therefore omitted.

is relatively high and only shows up with a very weak midday minimum. The intensity, which is strongly underestimated for the whole day, decreases during this period, thus indicating that the Bechtold-Tiedtke scheme produces too many precipitation events. Consequently, a large frequency bias up to $b = 1.88$ is reached during noon. In the afternoon and early evening, mean precipitation again drops too early which can be attributed to a strong decrease in the precipitation area. Even though the frequency bias approaches 1 in the evening, the intensity of precipitation events keeps on being severely underestimated. Likewise, the spatial variability is much smaller than in the observations.

A closer look on the diurnal cycle of precipitation intensity can be obtained by repeating the IQD-analysis (see Sec. 5.5.2) on a sub-daily scale. The IQD-values of ICON-HYM and ICON-BT for 3h accumulations of precipitation P_{3h} in GER-South are displayed in Figure 5.11e. Generally, the similarity between the observed and simulated frequency of P_{3h} is higher with ICON-HYM compared to ICON-BT. This is especially true in the late evening as well as between midnight and the morning hours when ICON-HYM attains $IQD << 0.01\,\mathrm{mm/3h}$. However, the PDF is also better captured when HYMACS underestimates the frequency of precipitation events and tends to overestimate between 15 and 21 CEST. Thus, the negative bias and the tendency towards too strong precipitation events of ICON-HYM in this period are still less severe than the strong underestimation of precipitation intensity with ICON-BT in this period.

Interestingly, both CPS yield similar values of the IQD between 9 and 15 CEST. Around noon, the similarity between the observed and modelled PDF of P_{3h} already starts to decrease with ICON-HYM. Simultaneously, the IQD with the Bechtold-Tiedtke scheme reaches its daily minimum since the underestimation in precipitation intensity is moderate in this period despite the strong frequency bias. Nevertheless, the analysis confirms that the marginal distribution of precipitation is consistently better captured with HYMACS for practically all daytimes in GER-South.

The diurnal cycle of precipitation is generally also better represented with ICON-HYM over the flat region of Northern Germany (Fig. 5.11(b,d)). The precipitation intensities fit again much better with the observations and also the daily maximum in precipitation activity in the evening is reproduced apart from a slight temporal delay.

However, the regional analysis also reveals some weaknesses with the hybrid scheme. In addition to the tendency of producing too strong precipitation events in the evening (note again the high values for the 25th percentile), the hourly area-averaged precipitation is clearly overestimated around the daily precipitation peak. Besides, there is a local minimum around noon that is not covered by the observations. Indeed, the shape of the area-averaged hourly precipitation even fits better for ICON-BT in this period although the following peak occurs again too early. Thus, HYMACS outperforms ICON-BT to a lesser extent in terms of the diurnal cycle of precipitation in GER-North. With the Bechtold-Tiedtke schemes, the precipitation intensity and the amplitude of diurnal cycle are still generally underestimated, but ICON-HYM now also overestimates noticeably the latter one.

In terms of the IQD for three hourly precipitation (Fig. 5.11f), smaller differences with respect to the observation are again consistently obtained with the hybrid CPS over the course of the day. While ICON-HYM still outperforms ICON-BT around noon in GER-North, the gap between both model configurations shrinks in the evening hours. This is consistent with the result obtained above in the sense that the strong overestimation of the diurnal peak in precipitation with HYMACS outweighs the systematic feature of too frequent and too weak precipitation events with the Bechtold Tiedtke scheme.

All in all, the regional analysis provides further details on the characteristics of the diurnal cycle of precipitation with both CPS at hand. A positive frequency

bias, a too early peak in the diurnal cycle of precipitation and a systematic underestimation of the precipitation intensity are consistently found for both regions with ICON-BT. ICON-HYM performs generally better than the operational CPS, but exhibits a regional dependency. While the diurnal cycle of precipitation is only slightly shifted towards the evening over the mountainous parts of Germany, larger discrepancies are found in the lowlands of Northern Germany. There, a local minimum around midday followed by an overestimated precipitation peak in the evening hours further indicates that the convective suppression over noon is too strong with HYMACS. As a consequence, more near-surface instability can accumulate which is then released towards the end of the day by more intensive than observed convection.

Since the latter feature is partly concealed by the analysis for all Germany, the regions GER-North and GER-South will be investigated separately in the subsequent evaluation focusing on the joint distribution of simulation and observation.

5.5.4 Verification of area-integrated precipitation forecasts

The verification of area-integrated precipitation forecasts for the regions GER-South and GER-North is evaluated in terms of the Linear Error in Probability Space (see Eq. 5.7). Both subdomains are considered to be large enough so that spatial integration in the respective region is sufficient to relax the double penalty problem.

The required cumulative probability distribution from the observations CDF_o is thereby estimated from the full available RADKLIM data set for each month of the test series. Despite the rather short time series providing 19 years of precipitation data (2001-2019), this data set is considered to represent the statistical nature of precipitation apart from extreme events (Winterrath et al., 2019) with sufficient accuracy. Note that extreme events do not substantially affect the shape of the CDF since these events are rare by definition.

For comparison between the two competing model configurations ICON-HYM and ICON-BT, Figure 5.12 illustrates the $LEPS$ skill score (see Eq. 5.8) for daily precipitation and for 3h precipitation as a function of daytime for the mountainous region GER-South. The line in the boxplots represents the unpermuted $LEPS_{skill}$ of the precipitation forecasts. The sample uncertainty estimated via 5-day block bootstrapping is illustrated by the box and whiskers which denote the interquartile and interdecile range from 1000 bootstrapping steps.

While ICON-HYM outperforms ICON-BT in terms of daily precipitation accumulations, the situation is less clear on a sub-daily time scale. Over night and in the morning hours, the skill of the simulations with HYMACS tends to be positive, even though sampling uncertainty is quite large.

However, despite the clear overestimation of 3h precipitation with ICON-BT and the smaller deviations in temporally averaged precipitation of ICON-HYM with respect to the observations (cf. Fig. 5.11a), $LEPS_{skill}$ is already smaller than zero at early noon (between 09 and 12 CEST). By evaluating each month of the test series separately, it is seen that the poorer performance of HYMACS is caused by a too pronounced decline of precipitation during midday in June (not shown).

Thus, the change in sign of skill might be attributed to the too strong convective inhibition with HYMACS in this daytime period mentioned earlier.

Around 15 CEST, the area-integrated precipitation with ICON-BT reaches its daily maximum while the increase in precipitation activity still lags behind ICON-HYM. The skill of HYMACS remains slightly negative ($LEPS_{skill} \approx -0.05$) until the strong underestimation of P_{3h} with the Bechtold-Tiedtke scheme becomes effective in the evening hours. For the last six hours of the day, ICON-HYM significantly outperforms ICON-BT ($LEPS_{skill} \approx 0.19$). As indicated by the smaller sample uncertainty range, this signal is robust for the test period at hand.

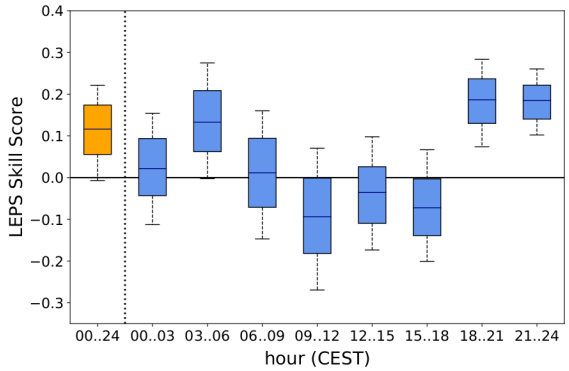

Figure 5.12: *LEPS* skill score for area-integrated precipitation in GER-South taking the forecasts with the Bechtold-Tiedtke scheme as a reference. The leftmost column illustrates $LEPS_{skill}$ of daily precipitation, whereas the rest accounts for three hourly precipitation evaluated on different daytimes. The horizontal line in the boxes indicates the unpermuted $LEPS_{skill}$ over the whole test period, whereas the box and whiskers illustrate the interquartile and interdecile range of the sampling uncertainty estimated via 5-day block bootstrapping with 1000 bootstrapping steps.

By contrast, ICON-HYM only outperforms ICON-BT between 21 and 24 CEST in the second half of the day in Northern Germany (Fig. 5.13). Before this small time window, $LEPS_{skill}$ is significantly negative which can be attributed to strong overestimation of the daily maximum and a delayed increase in the area-integrated precipitation during the afternoon with the hybrid CPS. Aggregated over a large domain, this effect overcompensates the too early drop in precipitation activity with ICON-BT as diagnosed previously.

Interestingly, ICON-BT shows up with a comparatively high *LEPS* compared to ICON-HYM at early noon (between 09 and 12 CEST) for GER-North when the modelled averaged precipitation rate is fairly close to the observed one. Detailed analysis reveals that this feature can be related to days when Northern Germany was located between a trough over southern Scandinavia and a high pressure system to the southwest (e.g 23$^{\text{rd}}$-26$^{\text{th}}$ May and 10$^{\text{th}}$-15$^{\text{th}}$ June). At these times, cold air masses are advected at low levels which then lead to boundary layer instability due to solar heating. While this causes only shallow convection in the observations, the Bechtold-Tiedtke scheme tends to produce weak rain showers in these situations. Thus, ICON-HYM then outperforms ICON-BT despite the unobserved drop in the area-averaged precipitation rate.

During night and in the morning, ICON-BT has some tendency to perform slightly better than ICON-HYM. However, due to the sampling uncertainty, the

differences are rather minor. Lastly, despite the variable skill of HYMACS on a sub-daily scale in GER-North, its capability to predict daily precipitation is again noticeably better compared to ICON-BT.

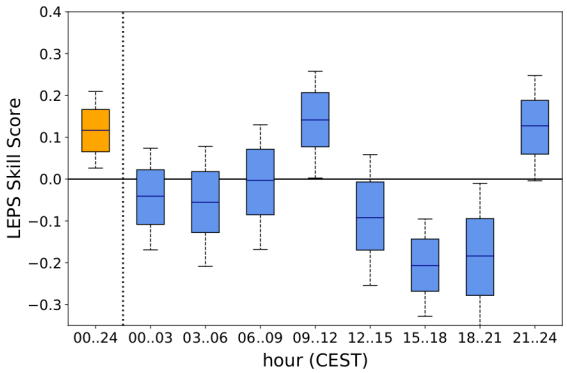

Figure 5.13: As Figure 5.12, but for the region GER-North.

All in all, the validation results in both regions for the area-integrated precipitation scored with the $LEPS$ skill score are aligned with the previously obtained results. Especially, in the (late) evening hours, ICON-HYM outperforms ICON-BT due to the systematic underestimation of precipitation activity with the classical CPS. However, the weakness of HYMACS to produce too less precipitation at midday and in the afternoon is emphasized with the $LEPS$-analysis. Even when the averaged precipitation rate is close to the observations as for ICON-HYM between 15 and 18 CEST in GER-North, the explicit pairing of forecasts and observations reveals stronger deficiencies compared to ICON-BT. This further points out to the hypothesis that a too strong convective suppression might be a systematic property with HYMACS.

Nonetheless, upscaling the precipitation forecasts on large domains such as GER-North and GER-South largely conceals spatial patterns on mesoscale. The subsequent evaluation therefore focuses on further evaluating both model configurations on finer spatial scales by using the Fractions Skill Score as a scale-dependant verification technique.

5.5.5 Verification of spatial precipitation patterns

Figure 5.14 illustrates the averaged Fractions Skill Score (see Eq. 5.13) of hourly precipitation rates for the region GER-South with ICON-HYM. The x-axis corresponds to the radius defining the neighborhood size r_s which varies between 13 km ($r_s = 2\Delta x_{ICON}$) and 104 km ($r_s = 16\Delta x_{ICON}$)[4]. The y-axis corresponds to the daytime so that the diurnal cycle of the FSS across various spatial scales can be analyzed. Different hourly precipitation thresholds $t_{P,1h}$ of 0.1 mm/h, 0.5 mm/h, 1 mm/h, 2 mm/h, 5 mm/h and 10 mm/h have been chosen to define the binary events (cf. Eq. 5.4). While the lower thresholds typically include stratiform precipitation events, higher thresholds can be used to focus on convective precipitation.

[4]The FSS is calculated for each simulation over a range of neighborhood scale with a stride length of 13 km = $2\Delta x_{ICON}$.

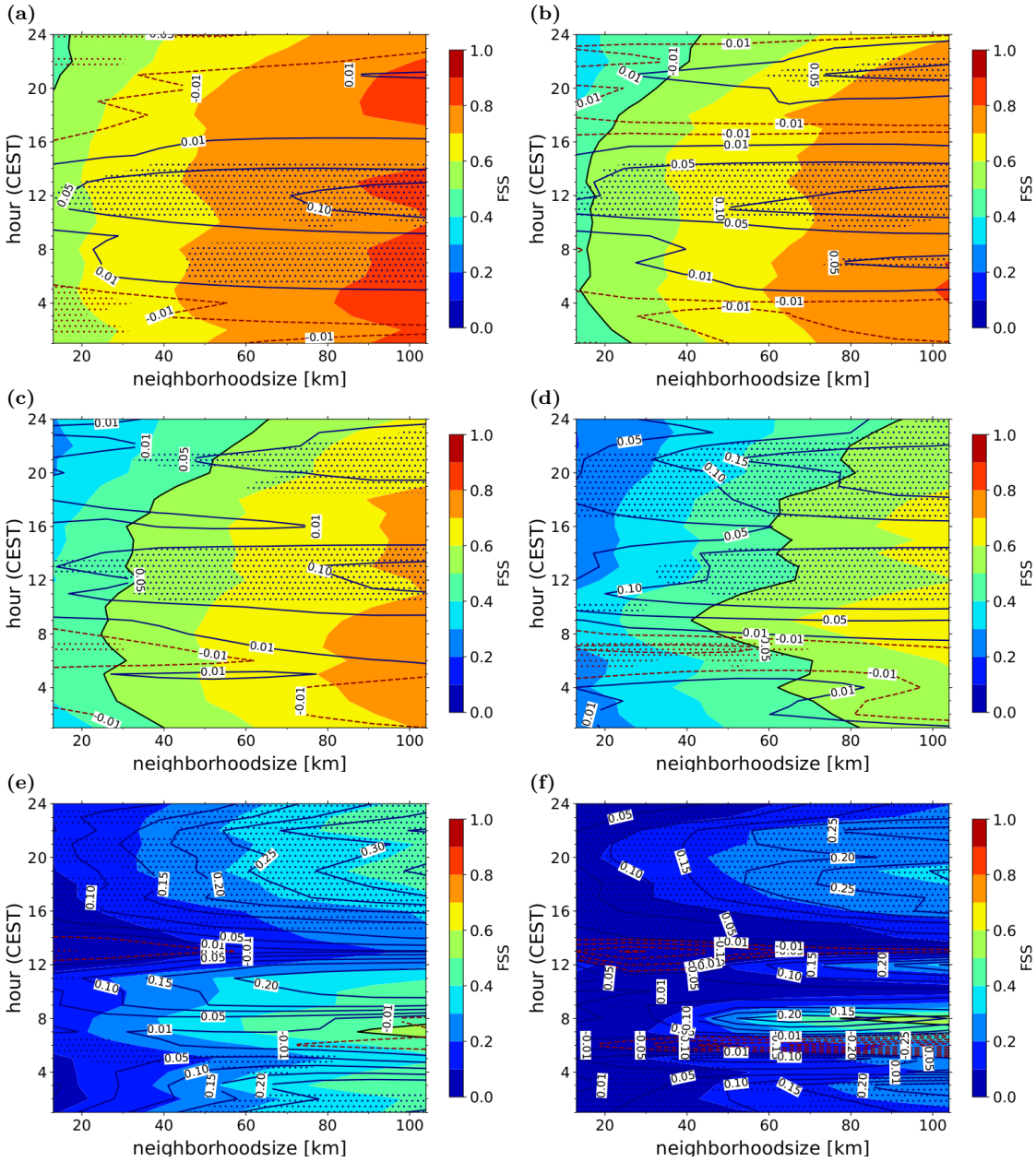

Figure 5.14: Temporally averaged FSS from ICON-HYM simulations (color shading) for different neighborhood scales (x-axis) and over daytime (y-axis) obtained for GER-South. Different absolute thresholds for defining the binary events are applied, that are (a) $t_{P,1h}$ = 0.1 mm/h, (b) $t_{P,1h}$ = 0.5 mm/h, (c) $t_{P,1h}$ = 1 mm/h, (d) $t_{P,1h}$ = 2 mm/h, (e) $t_{P,1h}$ = 5 mm/h and (f) $t_{P,1h}$ = 10 mm/h. Solid (dotted) contour lines denote that the FSS with ICON-HYM is higher (lower) than with ICON-BT. Hatched areas with dots highlight spatio-temporal scales where the sign of the difference is robust within a 90 % confidence interval. The confidence interval was estimated by combining local bootstrapping with 5-day block bootstrapping.

For small threshold values ($t_{P,1h} \leq 0.5$ mm/h), FSS-values of about 0.5 are already obtained for small neighborhood scales with $r_s < 50$ km (see Fig. 5.14a,b). Thus, ICON-HYM is capable to serve *useful* forecasts for precipitation events close to ICON's effective spatial model resolution which was found at about $6\,\Delta x_{ICON} \simeq$

39 km in Zaengl et al. (2015). For increasing neighborhood radii, the skill for predicting weak precipitation events continuously grows reaching values of 0.7 to 0.8 for the largest analyzed neighborhood sizes. While the skill remains nearly constant on the second simulation day until the late afternoon, a drop in forecast quality becomes apparent in the evening hours.

The additionally plotted solid and dashed contour lines in blue and red denote the FSS-difference between ICON-HYM and ICON-BT. Solid lines denote positive differences indicating that the simulations with HYMACS has more skill on average than the simulations with the Bechtold-Tiedtke scheme, whereas dashed lines represent the opposite case. The hatched area highlights spatio-temporal scales where the sign of the FSS-difference is robust over a 90 % confidence interval.

It is seen that differences are mostly minor on small spatial scales for weak precipitation events in Southern Germany (see Fig. 5.14a,b) with some indication of superiority of ICON-BT between midnight and early morning as well as before midnight. Over noon, ICON-HYM tends to outperform. On larger spatial scales, the FSS-differences show a relative gain of skill for ICON-HYM. Especially over noon, ICON-HYM clearly outperforms ICON-BT, while better results are also obtained in the morning hours and for $t_{P,1h} = 0.5\,\mathrm{mm/h}$ in the evening hours. This pattern can be largely attributed to the previously analyzed systematic biases in the simulations with the Bechtold-Tiedtke scheme. These are an overestimation of weak precipitation events at local noon and an underestimation when the diurnal cycle of precipitation reaches its maximum.

The latter characteristic feature becomes more evident for higher precipitation thresholds, which more and more exclude stratiform precipitation events. While the forecast skill degrades quite quickly (Fig. 5.14c-e), the FSS remains significantly larger with the hybrid CPS in the evening hours, but also at night. Although ICON-HYM attains FSS-value slightly below 0.5 for $t_{P,1h} = 5\,\mathrm{mm/h}$ and, strictly speaking, fails to provide a useful forecast at a neighborhood scale with $r_s \approx 100\,\mathrm{km}$, it performs much better than ICON-BT.

Precipitation events with $P_{1h} \gtrsim 10\,\mathrm{mm/h}$ are very rare and are barely captured by none of the ICON simulations at all (see Fig. 5.14f). Nevertheless, some skill is obtained by ICON-HYM in the early morning where such strong precipitation events is most likely linked to mesoscale convective systems that persisted throughout the night. However, the relevance of the results based on such a threshold should not be over-interpreted. In addition to the scarcity of these events which is manifested in a large sampling uncertainty (not shown), it is also likely that the averaged displacement error approaches the scale of the domain size. As pointed out by Skok and Roberts (2016), this spatial error must not dominate to allow for a meaningful assessment on the forecast quality in terms of the FSS.

The mean Fractions Skill Score for GER-North with ICON-HYM is displayed in Figure 5.15. In general, the results are comparable to GER-South. For weak precipitation ($t_{P,1h} \leq 1\,\mathrm{mm/h}$), the FSS-differences between ICON-HYM and ICON-BT are minor for most parts of the day (see Fig. 5.15a-c). Stronger, positive differences between local noon and afternoon with some robustness between 13 and 16 CEST can again be attributed to the strong overestimation of weak precipitation events with ICON-BT. While the diurnal cycle of precipitation already

peaks too early with the Bechtold-Tiedtke scheme, the simulations with HYMACS clearly overestimate the maximum in the evening hours. Consequently, the differences in FSS range between slight negative and weakly positive values towards the end of the day.

The most notable benefit from the hybrid scheme is obtained for $2\,\text{mm/h} \leq t_{P,1h} \leq 5\,\text{mm/h}$ in the morning hours and in the early afternoon. While the forecast of events with a minimum precipitation rate of 2 mm/h is still useful with ICON-BT in the morning hours (albeit the FSS is clearly smaller), only forecasts with the hybrid scheme are useful at neighborhood scales $r_s < 100\,\text{km}$ in the early afternoon (see Fig. 5.15d). For $t_{P,1h} = 5\,\text{mm/h}$ (Fig. 5.15e), HYMACS exclusively provides useful forecasts in the morning, in the afternoon and in the late evening. For higher thresholds, the FSS-value again tracks low for most daytimes in all ICON simulations.

As argued in Roberts (2008), using absolute thresholds for performing the FSS-calculation involve the models' biases. This is also seen in the results presented above: ICON-HYM outperforms ICON-BT at these times when the conventional CPS produces too many weak precipitation events (especially in the afternoon) and when stronger precipitation events are targeted in general.

To remove the bias effect and to focus exclusively on the spatial accuracy, thresholds can be defined based on percentiles. In the following, four different percentiles are used for the evaluation, that are the 90th, the 95th, the 97.5th and the 99th percentile, respectively. It is noted that lower percentile values are possible in principle, but reduce significantly the number of simulation dates that can be used for evaluation. For instance, only 18-23 out of 91 days in the test period show up with 85 th percentiles that are non-zero in the observations of the region GER-South between 01 and 15 CEST. Besides, the analysis is rather focused on localized, convective precipitation events with higher percentiles since they correspond to higher absolute threshold values.

The bias-corrected mean FSS-values for GER-South based on the four different percentiles are illustrated in Figure 5.16. For the 90th percentile, the precipitation forecasts become useful at a neighborhood scale of $r_s \simeq 40\,\text{km}$ (Figure 5.16a). Apart from the first five hours of the second simulation day, the FSS-differences between ICON-HYM and ICON-BT are mostly small and the sign of the FSS-difference is seldom robust over a 90 % confidence interval. Thus, the performance of both models in capturing widespread precipitation events (at minimum 10 % of the target domain are covered with precipitation for the 90th percentile) is comparable. The widespread character with the 90th percentile threshold is also reflected in the corresponding averaged absolute threshold which vary between 0.83 mm/h (03 CEST) and 1.17 mm/h (18 CEST).

Interestingly, larger positive FSS-differences are obtained between midnight and the early morning hours of the second simulation day. With HYMACS, the FSS is up to 0.05 higher than with the Bechtold-Tiedtke scheme, especially on neighborhood scales of $50\,\text{km} \leq r_s \leq 100\,\text{km}$. Closer inspection of the results indicate that this signal can be attributed to slightly improved representation of weak to modest nightly rain events with some convective character as a remedy of the previous day.

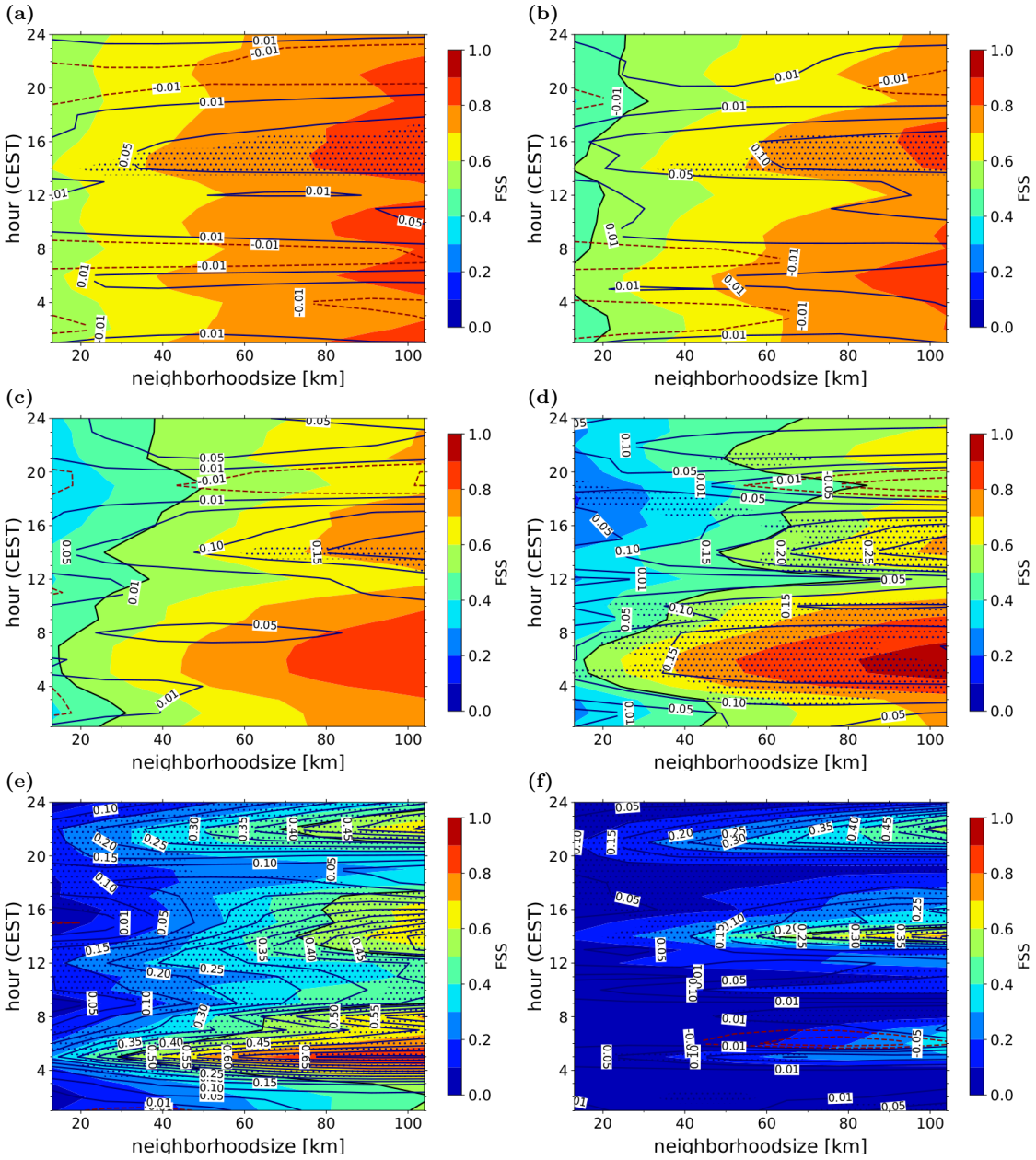

Figure 5.15: As Figure 5.14, but for region GER-North.

Starting with the results from the 95th percentile (Fig. 5.16b,c), some improvement in the spatial precipitation pattern is attained with ICON-HYM in the late afternoon and in the morning hours. With corresponding absolute thresholds between 1.23 mm/h (13 CEST) and 1.70 mm/h (19 CEST) for the 95 th percentile and 1.60 mm/h (11 CEST) and 2.62 mm/h (19 CEST) for the 97.5th percentile, the evaluation focuses more and more on localized, convective precipitation. Thus, not only the bias of convective precipitation is removed at this daytime, but also the spatial patterns tends to be better captured compared to ICON-BT even though the FSS-differences are not always robust.

From early noon until early afternoon, but also in the late evening, the FSS-differences vary around zero indicating that ICON-HYM does not yield an im-

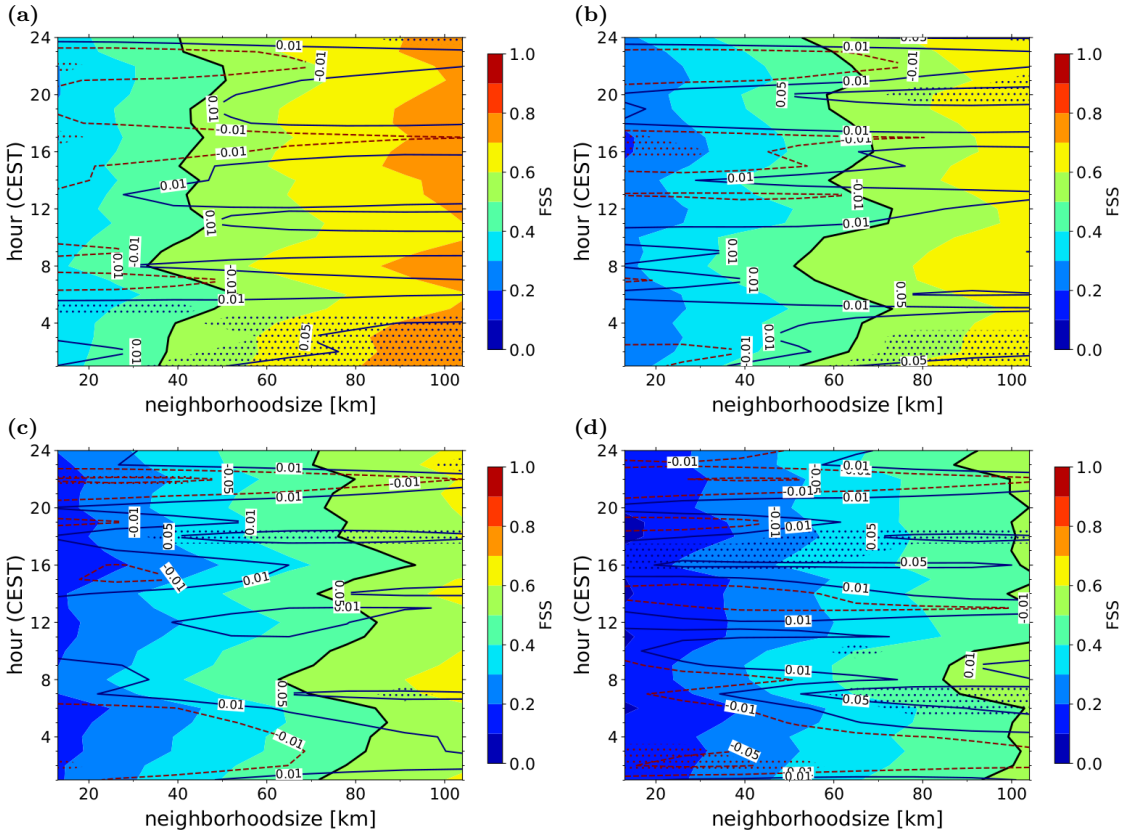

Figure 5.16: As Figure 5.14, but for bias-corrected FSS-analysis. Thresholding is based on different percentiles, that are (a) the 90th percentile, (b) the 95th percentile, (c) the 97.5th percentile, and (d) the 99th percentile.

provement. The aforementioned relative gain of HYMACS in the late evening for higher absolute thresholds can therefore be completely attributed to the systematic underestimation of stronger precipitation events with the Bechtold-Tiedtke scheme.

Based on the 99th percentile (see Fig. 5.16), whose corresponding absolute values vary between 2.04 mm/h (11 CEST) and 3.84 mm/h (18 CEST) on average, ICON-HYM continues to occasionally outperform on neighborhood scales larger than $r_s > 50\,km$. The slightly negative FSS-differences on smaller scales are of minor relevance, since the low FSS-values are indicative for unskilled predictions for localized precipitation events at these scales in general. The neighborhood scale boundary for useful predictions is indeed located around $r_s \simeq 100$ km.

Furthermore, the frequency bias of ICON-BT starts to reach and exceed a value of 2 for these events. Thus, the obtained results must be considered with care since the strong underprediction in ICON-BT begins to dominate at all spatial scales hampering an exclusive investigation and comparison of spatial precipitation patterns (Roberts, 2008).

The ability of the ICON simulations to represent precipitation patterns for different neighborhood scales in Northern Germany is summarized in Figure 5.17.

For the 90th percentile with associated observed absolute threshold values between 0.52 mm/h (02 CEST) and 1.02 mm/h (21 CEST), skilful predictions can again be obtained on spatial scales with $r_s \geq 40$ km (Fig. 5.17a). For most of the

day, differences between both simulations are small with some tendency of ICON-BT to yield better results in the early morning and around midday. Although this signal is not robust within a 90 % confidence interval, this shows that the above mentioned superiority of ICON-HYM based on absolute thresholds between 13 and 16 CEST is attributed to the strong bias with the Bechtold-Tiedtke scheme. In addition to the general tendency to produce too many weak precipitation events, the diurnal cycle of precipitation attains its maximum at this time in ICON-BT.

Larger and more robust positive FSS-differences are obtained for the evening hours (from around 19 CEST onwards). Despite the too intense and delayed maximum of daily precipitation, the spatial precipitation patterns are better captured at this period with ICON-HYM. This feature also persists for higher percentiles for the 95th and 97.5th percentile (Fig. 5.17b,c), while the results obtained for the 99th percentile (Fig. 5.17d) has to be interpreted again with care (see above).

Together with the results obtained for the region GER-South, it is concluded that HYMACS at least slightly improves the representation of precipitation patterns and fosters ICON's capability to produce *useful* precipitation forecasts when convection dominates. The shift of the performance gain with HYMACS towards the afternoon for the southern parts of the Germany can be reasoned with the earlier precipitation peak of the diurnal cycle in this region (compare Fig. 5.11a,b). At earlier daytimes, convection is less dominant and hence, the FSS-differences are either insignificant or rather unstructured (apart from the early morning hours for region GER-South).

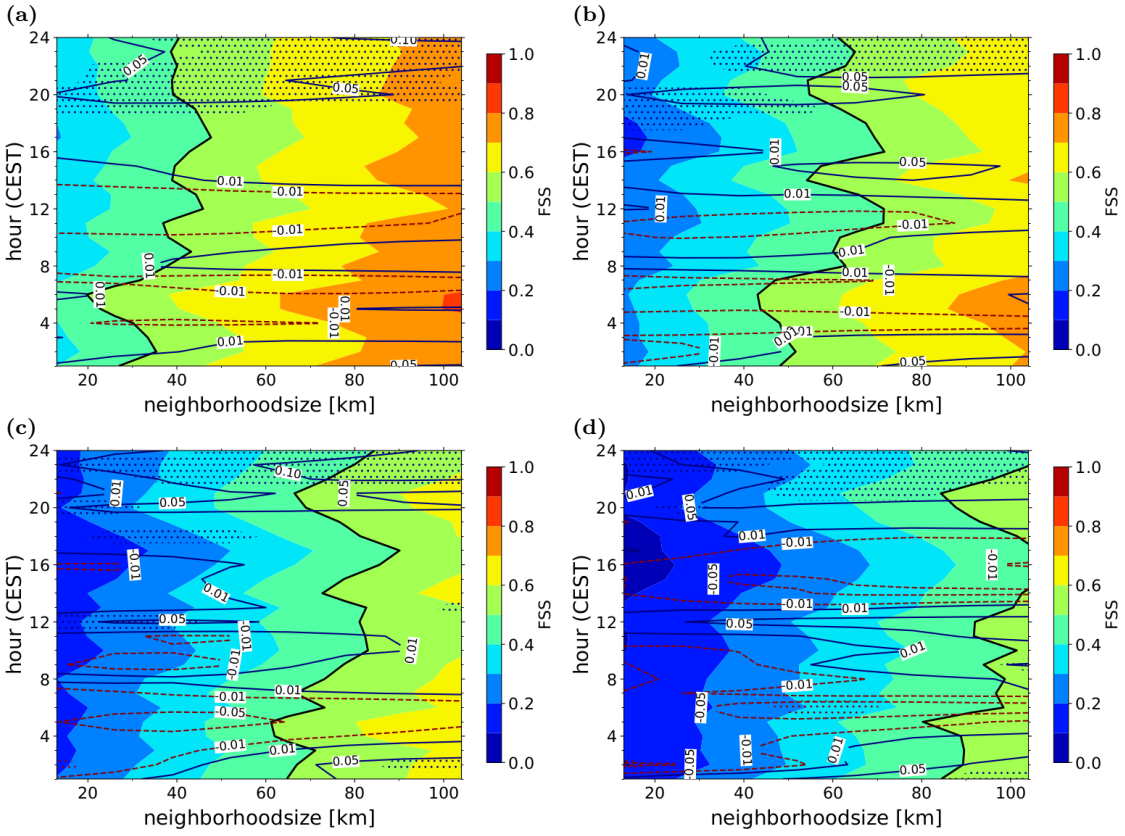

Figure 5.17: As Figure 5.16, but for region GER-North.

5.6 Understanding and discussing the results

The preceding evaluation and comparison of the simulations with HYMACS and the Bechtold-Tiedtke scheme has revealed several benefits of the hybrid approach compared to the classical CPS. Namely, these comprise a more realistic PDF of daily and hourly precipitation amounts, a better representation of the diurnal cycle of precipitation and improvements in capturing precipitation patterns. Besides, the strong overestimation of precipitation events gets removed with HYMACS in ICON.

However, the systematical evaluation also uncovered that the simulations with HYMACS tend to suppress convection too effectively from noon to the afternoon. As opposed to ICON-BT, a slight underestimation of precipitation events is diagnosed in this period with HYMACS followed by a delayed diurnal peak in precipitation activity in the evening. This weakness is most pronounced in the Lowlands of Northern Germany, where ICON-BT clearly outperforms ICON-HYM between 12 and 21 CEST in terms of area-aggregated precipitation amounts.

In the following, further analysis is therefore conducted to understand the behaviour of both schemes. Since the above mentioned deficiency of ICON-HYM is strongest in Northern Germany, the investigation focuses on this region.

Investigating the diurnal cycle of precipitation with parametrized deep convection

Due to the dominance of convection on the diurnal cycle of summery precipitation, it is natural to examine $CAPE$ as a quantity measuring the amount of buoyant energy which can be released by deep convection. Even though $CAPE$ itself does not correlate well with precipitation rates as argued in Barkiđija and Fuchs (2013), it allows us to access how HYMACS and the Bechtold-Tiedtke scheme act on the convective instability of PBL air over the course of the day. To lessen the dominance of the near-surface air directly affected by enthalpy input due to solar irradiation, mean-layer $CAPE$ ($CAPE\text{-}ML$) is evaluated. For the computation of $CAPE\text{-}ML$, a parcel is formed by mixing air from the first 50 hPa above the surface before Equation 2.8 is applied.

The diurnal cycle of $CAPE\text{-}ML$ in GER-North is illustrated in Figure 5.18. Until the morning hours, the differences between ICON-HYM and ICON-BT are minor. From about 9 CEST onward, $CAPE\text{-}ML$ begins to diverge between both model configurations when solar irradiation starts to destabilize the PBL. While the curve has a parabolic shape with a maximum of about 135 J/kg at 17 CEST in the simulations with HYMACS, the growth of $CAPE\text{-}ML$ is clearly flatter over noon in ICON-BT. The daily maximum only reaches a value of 95 J/kg and is shifted towards the evening. Additionally, the spatial variability of $CAPE\text{-}ML$ is considerably smaller until the afternoon hours. Both indicates that destabilization is extensively outweighed by convective processes when solar forcing is strongest.

During the evening, the differences are quickly reduced showing that the higher level of convective instability is efficiently removed in the simulations with ICON-HYM. Together with the distinct pick in precipitation in the evening hours, the adjustment is likely to be realized via deep convection.

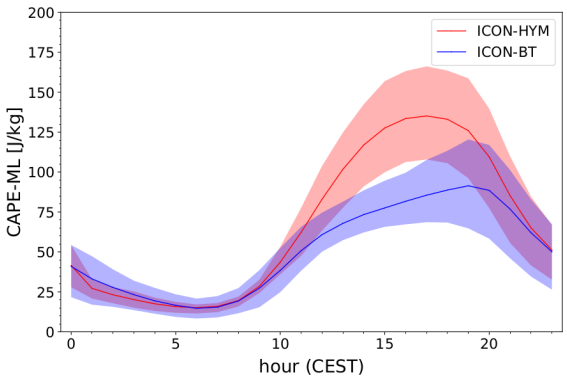

Figure 5.18: Diurnal cycle of averaged mean-layer $CAPE$ in Northern Germany in all simulations of the test series with ICON-HYM and ICON-BT. The solid line indicates the median of $CAPE\text{-}ML$ over the domain, whereas the shaded areas illustrate the interquartile range of the spatial variability.

The considerably differing diurnal cycle can be linked to the activity of the respective operating parametrization schemes. The diurnal cycle of convective cells in the region of interest is shown in Figure 5.19. Lightly shaded bars denote the number of all convective cells while bold bars are used to illustrate the occurrence of deep convective cells.

It is seen that the total number of convective cells follows the diurnal cycle of solar radiation apart from a small temporal shift towards the afternoon. While the shape of the corresponding diurnal cycle is similar, the number of parametrized convective cells with ICON-BT is twice as high as with ICON-HYM (note the different scales of the y-axis in Fig. 5.19). Thus, ventilation of the heated PBL occurs more widespread with the Bechtold-Tiedtke scheme while more convective clouds also induce a cooling effect due to reduced solar irradiation.

However, shallow convection is not necessarily the key driver in reducing atmospheric instability since higher tropospheric layers remain more or less unaffected (cf. Sec. 2.1). This circumstance is explicitly reflected in the Bechtold-Tiedtke scheme, where shallow convection is not handled with a $CAPE$-based closure assumption contrarily to penetrative convection (see Sec. 2.5). Thus, the further increase with ICON-BT compared to ICON-HYM in the number of deep convective cells and the notable temporal shift in its diurnal cycle is of high relevance.

With the Bechtold-Tiedtke scheme, the number of deep (precipitating) convective cells is about four times higher and the activity increases continuously from the morning hours until 15 CEST. By contrast, the number of these cells remains low until noon with HYMACS and peaks later in the evening. The reduced growth of convective instability in ICON-BT is therefore largely attributable to parametrized deep convection developing earlier and much more widespread.

The more widespread occurrence of deep convection cells also explains the reduced spatial variability in $CAPE\text{-}ML$ mentioned above. The spatial variability gets just increased lately in the early evening hours when the activity of deep convection already starts to drop. Thereby, the diurnal reduction of solar heating is outweighed leading to the delayed, but still weak daily maximum of $CAPE\text{-}ML$ at 19-20 CEST with ICON-BT.

The rather flat diurnal cycle of $CAPE$ as well as the too early peak in precip-

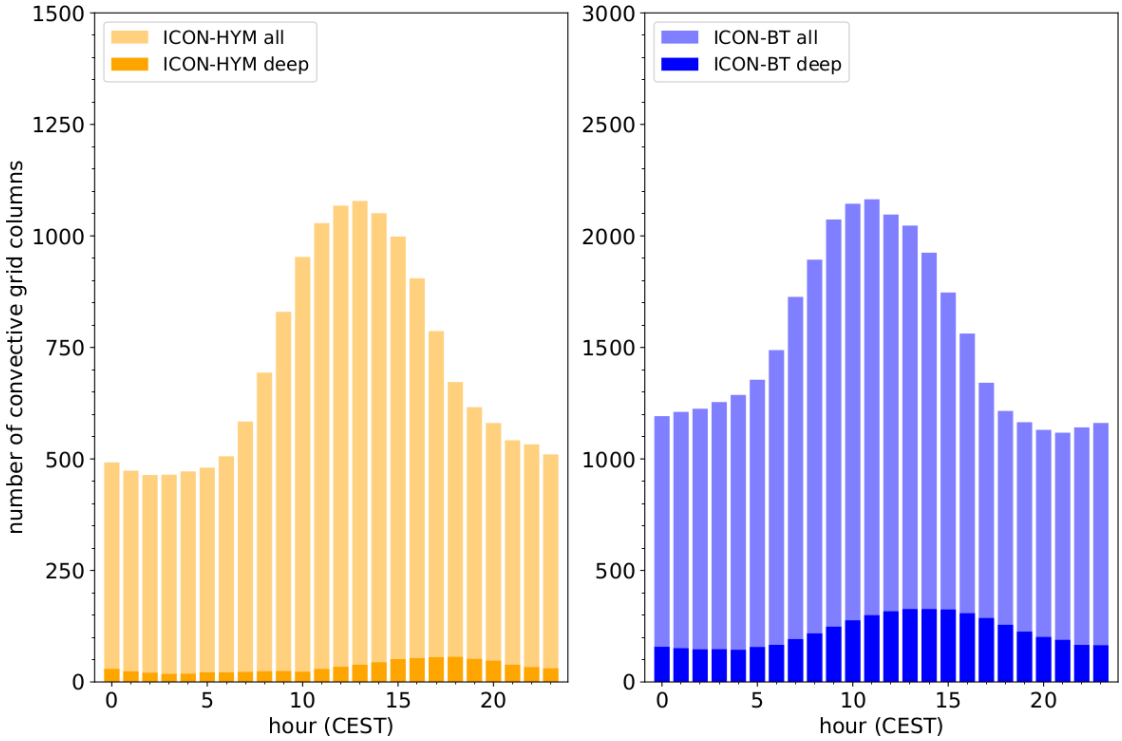

Figure 5.19: Diurnal cycle of the number of parametrized convective grid columns with (a) the HYMACS and (b) the Bechtold-Tiedtke scheme in Northern Germany for all simulations of the test series. The lightly shaded bars comprise all convective columns while bold bars denote deep convective columns only.

itation activity have already been recognized in earlier studies and motivated the introduction of the modified $CAPE$ closure to represent nonequilibrium convection (see Sec. 2.5 and Bechtold et al. (2014b)). However, the revised closure was not applied operationally in ICON version 2.3.0 used for the simulations in this test series. Therefore, strong convective adjustment already takes place with the Bechtold-Tiedtke scheme once the atmospheric conditions start to favor penetrative convection. It can therefore be expected that an activation of the modified $CAPE$ closure yields an improvement in the representation of the diurnal cycle of precipitation with the classical CPS. It is noted that this change in the operational ICON model was carried out with model version 2.3.2 in late summer 2018. Thus, newer model versions probably show up with an improved representation of the diurnal cycle of precipitation.

Yet, the opposing characteristics of HYMACS in ICON deserve further explanations. Due to the special feature of the hybrid scheme to allow for a net mass transfer, a more detailed investigation of the diurnal cycle of the parametrized and grid-scale mass fluxes is appealing.

Figure 5.20 shows the domain-averaged *net* vertical mass fluxes at level 43 in Northern Germany. In the lowlands of GER-North this corresponds to an approximated height of 2000 m above surface placing the level of interest close to the top of a well-mixed convective PBL.

While the amplitude of the vertical mass fluxes is small with the Bechtold-Tiedtke scheme since the convective overturning is closed locally by definition, the

simulations with HYMACS have a pronounced diurnal cycle. Until the morning, grid-scale mass fluxes are minor and the aggregated convective mass flux with HYMACS is similar to the total mass flux in ICON-BT. However, with increasing convective activity, the parametrized upward transport grows and reaches its maximum in the late afternoon hours. Until 15 CEST, the vertical mass transport with HYMACS is clearly dominated by shallow convection, whereas deep convective clouds constitutes for 20 % of the convective mass transport. The parametrized upward transport by shallow convection is thereby largely balanced by grid-scale subsidence so that the net vertical mass flux tends to be smaller than in the simulation with the Bechtold-Tiedtke scheme. Note that there is a local temporal minimum at 15 CEST, where the parametrized upward mass flux is completely balanced by grid-scale subsidence.

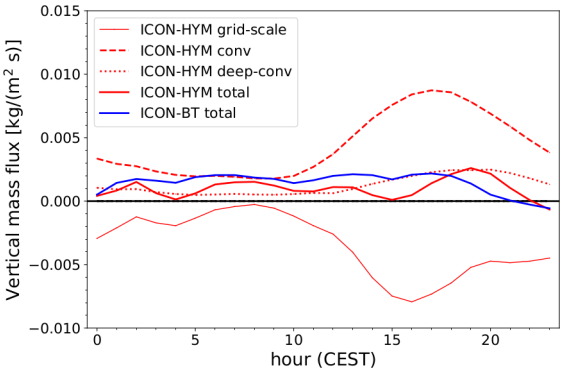

Figure 5.20: Diurnal cycle of area-integrated vertical mass fluxes in GER-North for all simulations in the test series. The mass flux is evaluated at model level 43 which is placed about 2000 m above surface. Positive (negative) values denote an upward (downward) mass transport.

The strong grid-scale subsidence close to the top of the PBL in the afternoon hours implies divergence at near-surface levels due to continuity. Since deep convection at these daytimes is mostly surface-based and since the engulfment of heated air below cloud base is crucially linked to grid-scale convergence with HYMACS (see Eq. 3.30), shallow convection effectively suppresses the development of stronger convective activity until the afternoon. While this process is considered to be partly realistic, it can be hypothesized that the strength of the stabilization process is overestimated. The missing adjustment through deep convection allows the PBL air to continue heating and therefore results in a further increase of $CAPE$ until afternoon (cf. Fig. 5.18).

Towards evening, the activity of deep convection grows and reaches its maximum around 20 CEST. The maximum in the total convective mass transports precedes the maximum of the mass transport by deep convection showing that the dominance of shallow convection diminishes in the afternoon. Simultaneously, there is also a noticeable decrease in the mass flux due to grid-scale subsidence. Closer inspection reveals that the reduced grid-scale mass flux directed downwards can be attributed to local, intense upward fluxes on grid-scale (not shown). In other words, the convective instability gets partly removed via explicitly resolved processes.

To a certain degree, this effect is desirable at convective gray-zone resolutions. However, due to the analyzed overestimation in the amplitude of the diurnal cycle of precipitation, it is expected that the transfer of convective processes onto grid-scale is also too strong.

The better performance of ICON-HYM in Southern Germany also fits into the line of arguments: While shallow convection still induces grid-scale divergence near surface thereby suppressing penetrative convection, its effect gets outweighed due to the presence of heterogeneous topography. Local thermally induced wind systems such as mountain-valley circulations come along with local convergences which help to trigger deep convection (see e.g Kirshbaum et al., 2018). Thus, the strength of the diurnal maximum of precipitation activity can still be captured reasonably with HYMACS. Nevertheless, the overestimated minimum around noon and the moderate shift of the maximum of precipitation activity towards the evening indicate that the above mentioned process is present in this region as well.

Is parametrization of deep convection still rewarding at $\Delta x_{ICON} = 6.5\,\mathrm{km}$?

In order to complete the comparison on the performance of a classical and a hybrid CPS at gray-zone resolutions, a third branch of simulations has been conducted in this thesis. Albeit a grid spacing of $\Delta x_{ICON} = 6.5\,\mathrm{km}$ is unequivocally too coarse for a proper representation of deep convection, several studies point out benefits in the reproducing precipitation statistics when the parametrization of penetrative convection is deactivated (see, e.g., Marsham et al., 2013; Argüeso et al., 2020; Ou et al., 2020). To probe this behaviour, a reduced version of the Bechtold-Tiedtke scheme has been tested as well.

In the respective model configuration, abbreviated by ICON-$\mathrm{BT}_{\mathrm{shallow}}$ in the following, parametrization is turned off when the depth of the parametrized convective clouds exceeds 130 hPa. Thus, penetrative convection can only be released on grid-scale. In addition to the this ad-hoc switch, turbulent and organized entrainment rates along the parametrized plume are enhanced compared to ICON-BT.

In terms of the marginal distribution of hourly and daily precipitation, the simulations with ICON-$\mathrm{BT}_{\mathrm{shallow}}$ share many similarities with ICON-HYM. The relative frequency distribution of hourly precipitation is shown in Figure 5.21. It is seen that the overestimation of weak precipitation events is removed while more strong precipitation events are produced. Thus, the underlying PDF is better represented with unparametrized deep convection close to the lower edge of gray-zone resolutions.

However, weaknesses of the simulations with HYMACS diagnosed above tend to be reinforced with ICON-$\mathrm{BT}_{\mathrm{shallow}}$, especially in the mountainous region GER-South. There, the diurnal peak in precipitation is strongly delayed and occurs just before midnight while another peak is visible in the morning hours (see Fig. 5.22a). By contrast, the precipitation activity is clearly underestimated over daytime which is also manifested in a pronounced negative frequency bias in the afternoon ($b \approx 0.7$). Likewise, a tendency towards stronger than observed precipitation events in the evening and over night is simulated (see Fig. 5.22b).

Due to these weaknesses, ICON-HYM mostly outperforms ICON-$\mathrm{BT}_{\mathrm{shallow}}$ in

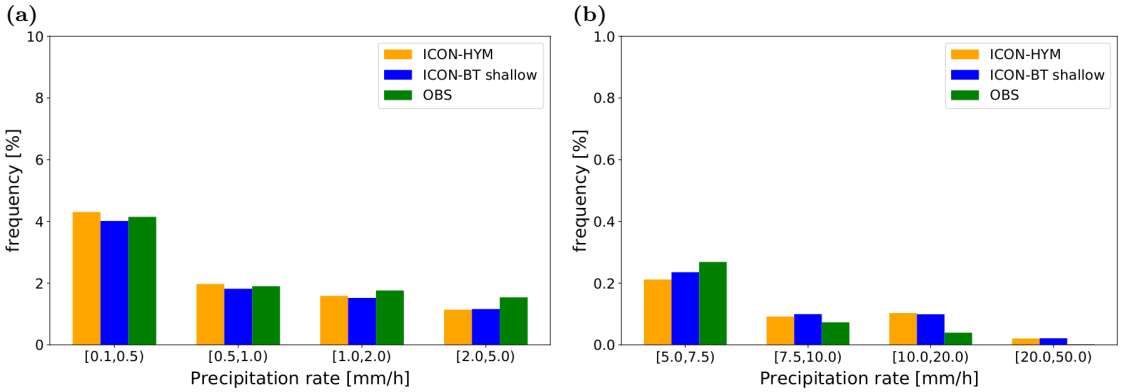

Figure 5.21: Relative frequency distribution of hourly precipitation for all Germany. In contrast to Figure 5.9, the frequency distribution for the simulations with the reduced Bechtold-Tiedtke scheme (ICON-BT$_{\text{shallow}}$) is displayed (blue bars).

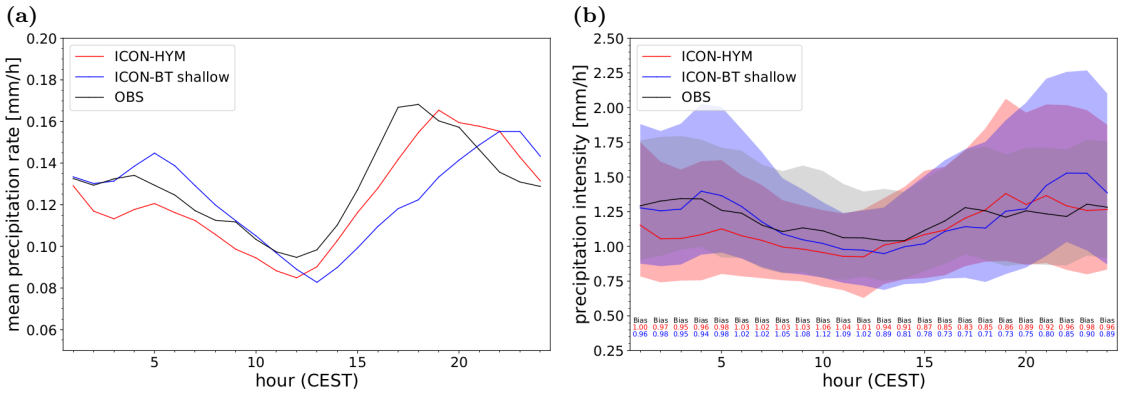

Figure 5.22: Diurnal cycle of mean precipitation (a) and of precipitation intensity (b) for GER-South. In contrast to Figure 5.11(c,d), the blue line (values) shows the results for ICON-BT$_{\text{shallow}}$.

terms of the area-integrated precipitation in the GER-South. Apart from a time period around local noon, $LEPS_{skill}$ is positive and indicates a significant improvement for the second half of the day (Fig. 5.23). Thus, the simulations with a hybrid CPS yield the best results for the mountainous region in this test period.

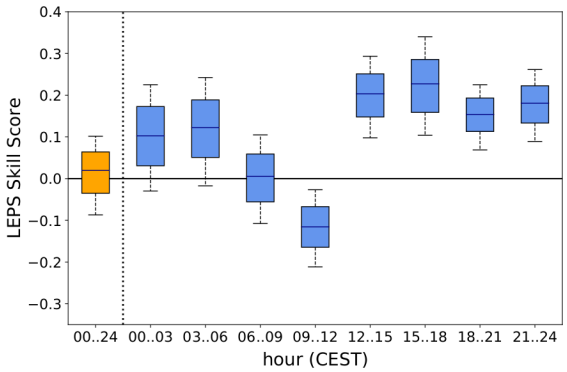

Figure 5.23: *LEPS* skill score for area-integrated precipitation for GER-South analogous to Figure 5.12, but taking the forecasts with ICON-BT$_{\text{shallow}}$ as a reference.

In the Lowlands of Northern Germany, the benefits from the hybrid approach largely vanish. The diurnal cycles of precipitation resemble each other with a

smaller overestimation of the evening peak while the negative frequency is still slightly stronger with ICON-BT$_{\text{shallow}}$ (not shown). In terms of the area-integrated precipitation, $LEPS_{skill}$ strongly varies over the day with advantages for the reduced classical scheme from midnight to morning and in the late afternoon. Similar to the comparison with the full Bechtold-Tiedtke scheme, ICON-HYM outperforms around noon and in the late evening while daily precipitation is significantly better predicted (not shown).

In terms of the spatial precipitation patterns, the results from the bias-corrected Fractions Skill Score analysis indicate a similar level of forecast quality with ICON-HYM and ICON-BT$_{\text{shallow}}$ for both regions. Daytimes and scales with significant FSS-differences are usually sparse for all analyzed percentiles. For localized precipitation, e.g., the 97.5 th percentile (Fig. 5.24), slight benefits for the hybrid approach are revealed in the early afternoon and in the morning in GER-North while the reduced Bechtold-Tiedtke scheme tends to outperform over the first hours of the second simulation day in GER-South.

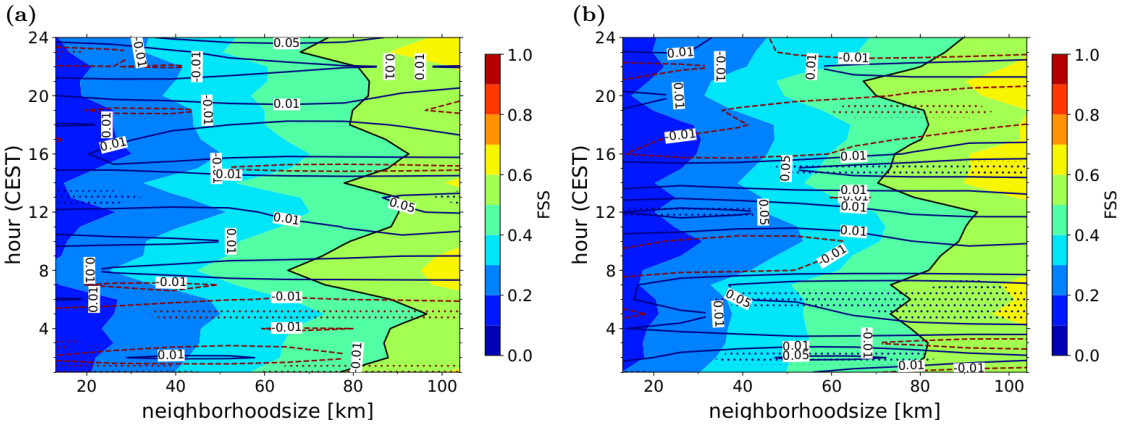

Figure 5.24: Contour plots of the averaged FSS with thresholding based on the 97.5 th percentile from ICON-HYM simulations at different neighborhood scales (x-axis) and over daytime (y-axis) for GER-South (a) and GER-North (b). The solid and dotted lines denote the relative difference with respect to the simulations with the reduced Bechtold-Tiedtke scheme. Analogous to Figure 5.14–5.17, the hatched areas denote spatio-temporal scales where the sign of difference is robust within a 90 % confidence interval.

Despite the small differences, this is a remarkable result. Since the representation of the spatial precipitation pattern at mesoscale can be related to the coupling with the environmental flow, the comparable performance in terms of the FSS indicates that the simulations with HYMACS attain a similar coupling as the simulations with *explicit* deep convection.

6 Conclusion and outlook

6.1 Summary and discussion

Due to the ever increasing computational power, the spatio-temporal resolution of contemporary NWP and climate models has become finer and finer over the last decades. With a grid spacing in the range of 2-10 km in operational model applications, these models have entered the gray-zone of deep convection where the separation between (explicit) grid-scale and (parametrized) subgrid-scale dynamics becomes blurry. To improve the representation of convection at gray-zone resolutions, the hybrid convection parametrization scheme HYMACS has been developed starting from the study of Kuell et al. (2007). In this thesis, this scheme was implemented successfully and tested extensively into the modeling framework of ICON, the current operational model of the Deutscher Wetterdienst (engl.: German Weather Service) (DWD).

After introducing the nature of moist convection, the study reviewed the classical and the hybrid approach for its parametrization and presents recent challenges in this domain (see Ch. 2 and Sec. 3.1). While the classical approach relies on the Reynolds averaging procedure in a quasi-Boussinesq flow, the hybrid ansatz relies on principles of fluid volumes with a decomposition of the barycentric velocity. The resulting separation between grid-scale and subgrid-scale motions breaks up the conventional assumption that the parametrized convective motion constitutes a locally closed system with respect to mass. Thus, the allowed net mass transfer constitutes an outstanding feature of the hybrid approach which is expected to yield a more realistic representation of convection when the transition between explicit and parametrized convective dynamics becomes blurry.

A detailed description of HYMACS as a realization of the hybrid approach followed the survey on representing convection in numerical models (Sec. 3.2). Thereby, the cloud model, the trigger function and the closure assumption of HYMACS were compared with the Bechtold-Tiedtke scheme, the operational convection parametrization schemes (CPS) in ICON. Besides, updates to the scheme which have been integrated during this study were documented (Sec. 3.3).

Afterwards, the ICON model and the coupling of HYMACS was described in Chapter 4. While the physics-dynamics coupling shares similarities with the coupling of a conventional CPS, the following key aspects have to be considered:

i) With a net mass transport, the physics-dynamics coupling can neither be performed at constant density nor at constant pressure. The mass forcing does not only affect the tendencies in HYMACS, but also enters the transformation of these tendencies to the prognostic variables of the hosting model.

ii) The mass forcing must also be considered to warrant moisture tracer consistency when a reduced calling frequency is exploited for the transport scheme.

iii) The vertical divergence should not be used to numerically filter the horizontal momentum as long as no equivalent term is applied to the vertical wind.

Especially the last aspect attained a lot of attention in this thesis since the numerical filter leads to a severe distortion of the grid-scale dynamical flow response in ICON (see Fig. 4.5). After a careful re-investigation on the requirement for numerical filters on triangular grids, a revised configuration was proposed in this study (Sec. 4.4). The revised filter combines an isotropic second-order divergence damping with an anisotropic fourth-order divergence damping where the anisotropic part only accounts for the horizontal velocity field as opposed to the operational filter. The proposed filter can be viewed as a compromise that aims to maximize the desired mitigation of numerical noise while the effect on physical modes, namely the gravity waves, is minimized.

The suitability of the revised numerical filter was then tested in the Jablonowski-Williamson benchmark test cases and in the mass lifting experiments (see Secs. 4.5–4.6). It was found that the suppression of computational modes was efficient and thus, the revised filter approach applied when HYMACS was coupled with ICON.

In Chapter 5 of this thesis, ICON-HYMACS was then tested systematically in real case applications by conducting a series of re-forecasts between Mai and July 2017. The test series comprised 92 simulations where HYMACS competes against the operational Bechtold-Tiedtke scheme at gray-zone resolution ($\Delta x_{ICON} \simeq 6.5\,\mathrm{km}$) in a limited area application of ICON over Central Europe.
A statistical evaluation revealed the following merits with HYMACS (cf. Sec. 5.5):

i) The marginal distribution of daily and hourly precipitation amounts is better represented. Particularly, the overestimation of weak precipitation events is largely removed compared to the operational Bechtold-Tiedtke scheme.

ii) The diurnal cycle of mean precipitation is better captured. The too early onset at noon during summertime does not occur and also the diurnal cycle in precipitation intensity is better represented.

iii) The simulated spatial precipitation patterns also become slightly improved as revealed by a bias-corrected FSS-analysis. This is especially true when convection dominates, e.g. in the afternoon and evening.

Since other physical parametrizations than convection in ICON are tuned with the Bechtold-Tiedtke scheme rather than with HYMACS, this is a notable result.

Besides, parametrizing deep convection with the hybrid scheme was still beneficial compared to an explicit treatment at gray-zone resolutions (Sec. 5.6).

6.2 Shortcomings with HYMACS and steps for improvement

Despite the above mentioned merits, the statistical evaluation also uncovered that HYMACS tends to suppress convection too effectively during the afternoon. This

was particularly noticed for Northern Germany where a delayed and overestimated diurnal precipitation maximum is diagnosed.

The physical reasoning for this behaviour have been traced back to the net mass transport due to shallow convection (Sec. 5.6). During noon, this parametrized mass transport induces compensational subsidence on grid-scale close to the top of the planetary boundary layer (PBL) which leads to divergence near the surface. Since horizontal mass flux convergence is used to constrain the updraft mass flux at cloud base, convection which roots in the lower parts of the PBL gets effectively suppressed. A non-observable minimum around noon and a delayed increase in mean precipitation in the afternoon are a manifestation of this process. Thus, HYMACS tends to favor situations which resemble a *loaded gun*, that is a continued fueling of $CAPE$ over the day which then gets released quickly in the evening. Besides, the scheme becomes tied to the *self-induced* dynamics.

Due to the difficult-to-control feedback between grid-scale flow and subgrid-scale convection, other CPS have rather refrained from using closure assumptions based on explicit dynamics over the last two decades (e.g., Bechtold et al., 2008; Yano et al., 2013). Instead, it is nowadays more common to relate the convective intensity to quantities depending on the atmospheric instability such as $CAPE$ or the cloud work function as proposed by the quasi-equilibrium framework (Arakawa and Schubert, 1974). While this framework has also its shortcomings in the presence of strongly varying PBL forcing on small spatio-temporal scales over land, Bechtold et al. (2014b) has previously suggested a modification of the CAPE-closure in the Bechtold-Tiedtke scheme to accommodate for nonequilibrium convection.

Indeed, the requirement for the latter has also been noticed in this study. With a deactivated modification of the CAPE-closure in the Bechtold-Tiedtke scheme in ICON version 2.3.0, the diurnal maximum of precipitation is simulated too early at noon. However, in ICON version 2.3.1 ICON, the adaption for nonequlibrium convection was implemented successfully after some adjustments [1] have been applied to the scheme (Guenther Zaengl (DWD), personal communication, 09/05/2020). While this update is expected to reduce the gap between the ICON simulations with HYMACS and the Bechtold-Tiedtke scheme, a similar closure assumption for deep convection is appealing for the hybrid scheme.

Likewise, the closure assumption for shallow convection in HYMACS can be altered to depend on the thermodynamical forcing in the PBL. Again, the Bechtold-Tiedtke scheme serves as a good example for such an approach.

In analogy to the revision of the closure assumptions for different types of convection, the formulation of the updraft mixing rates with the environment is another relevant target for future updates of HYMACS. Instead of applying constant (turbulent) mixing rates for shallow and deep convection, observational and modeling studies with large-eddy simulations suggest a dependency on the cloud radii and the ambient relative humidity (e.g. Simpson and Wiggert, 1969; Stratton and Stirling, 2012). While the smaller shallow convective clouds are typically subject to stronger lateral mixing compared to deep convection, the dependency on

[1] These adjustments comprise a capping of negative $PCAPE_{PBL}$-values (cf. Eq. 2.42) to impede too intense convection in the late afternoon and a reduced modification in the presence of small $PCAPE$-values.

the environmental humidity is still subject to research studies (e.g. Stratton and Stirling, 2012; De Rooy et al., 2013). However, it is well recognized that the mid-tropospheric moisture availability plays a crucial role in controlling the convective cloud-top height (e.g. Derbyshire et al., 2004; Zhang and Klein, 2010). Imitating the various dependencies of lateral mixing as well as accounting for other non-local effects is of increasing relevance in contemporary CPS (Arakawa, 2004) and thus is of particular interest in the future development of HYMACS in ICON.

Indeed, HYMACS has already been equipped with a scheme to account for non-local effects of convection in the study of Kuell and Bott (2011). A cell aging and transport mechanism lead to a decrease in turbulent mixing and a higher precipitation efficiency at mature cloud stages (see Sec. 3.2). The concept thereby agrees with observations as presented, for instance, in Stratton and Stirling (2012). Additionally, a gust front trigger eases the initialization of convection downstream of existing cells and thus imitates cell propagation and secondary triggering (see Sec. 3.2.2). Several studies indicate that these processes are increasingly important at convective gray-zone resolutions (e.g. Rio et al., 2013; Torri et al., 2015). However, the cell aging effect and the gust front trigger have been developed for quadrilateral grids. An adaption for ICON's triangular grid is still pending, and thence constitutes an important step in the future development of HYMACS in the new hosting model.

Enhancing the scale adaptivity of the scheme in future developments of HYMACS also deserves further consideration in the multi-scale modelling framework of ICON. In recent years, the smooth transition from parametrized towards explicit representation of deep convection with the help of the unified parametrization framework developed by Arakawa and Wu (2013) has attained a lot of attention as discussed briefly in Section 2.4. Their approach to scale the parametrized convective transport based on an estimate of the cloud fraction σ_c is based on relaxing the small-area approximation which allows equating the environmental value of the quantity ψ with its grid-scale value. Since this simplification is also applied with the hybrid approach (cf. Eq. 3.11), an analogous scaling of the convective transports with HYMACS is a proper mean to enhance its scale-adaptivity as well.

While different approaches to estimate σ_c have been tested successfully over the recent years in other CPS (see, e.g., Han et al., 2017; Kwon and Hong, 2017; Jeworrek et al., 2019) and could therefore be transferred to HYMACS, the orchestration with other physical parametrization schemes is also of increasing interest at gray-zone resolutions (cf. Sec. 2.4). The lack of consistency between the simple parametrization of cloud and precipitation formation in CPS compared to contemporary cloud microphysics schemes and the parallel handling of mixing processes in the PBL with the turbulence and the CPS are vibrant challenges that must be tackled (see, e.g., Arakawa, 2004; Wu and Arakawa, 2014).

Although some limitations and issues still remain with HYMACS, this work laid the foundation to allow progress with the hybrid approach in the multi-scale modeling framework of ICON. Together with the on-going developments in the modeling community (see, e.g., Rio et al., 2019, for a recent review), it is expected that future advancements of HYMACS can contribute to reduce the representation problem of moist convection in numerical models of the atmosphere.

Appendices

A Details on the coupling of HYMACS with ICON

The implementation of the HYMACS into the modeling framework of ICON imposed some technical challenges. While some of these has already been mentioned in Chapter 4, the following sections provide some more details on certain aspects.

In the first section, the (partially) implicit convective Exner pressure tendency (see Eq. 4.22) is derived which is used to couple HYMACS into ICON. Its implementation is considered to enhance the numerical stability, particularly in the presence of strong parametrized mass transports. Additionally, the usage of a mass flux limiter in HYMACS is detailed.

The second section elaborates on the proper handling of the convective mass sources in conjunction with the tracer transport scheme of ICON. The technical details on this turned out to be crucial since an incorrect coupling proved to induce severe buoyancy disturbances which used to spoil the grid-scale dynamics in the development phase of this thesis. However, a comprehensive outline is required to understand the rationale behind the chosen approach and thus, it was decided to add this section to the appendix.

The third and last section is dedicated to some details on ICON's dynamical core. After outlining the predictor-corrector scheme which is used to integrate the model equations in time, an in-detail description of the implicit vertical wind solver follows. In this thesis, the solver was extended to include a second-order (isotropic) divergence damping term (cf. Eq. 4.29). In addition to damping vertically propagating sound waves, this filter helps to suppress checkerboard noise without affecting the gravity waves triggered by a subgrid-scale mass transport.

A.1 Implicit Exner pressure tendency with HYMACS in ICON

With increasing vertical resolution of the grid, the numerical stability of the model integration may be imperiled by tendencies from physical parametrization schemes realizing strong subgrid-scale transports in vertical direction. This is in particular true for the convection parametrization scheme which frequently overturn substantial amounts of air via intensive, parametrized updraft mass fluxes.

In the Bechtold-Tiedtke scheme, the numerical integration is stabilized with the help of a *partially* implicit convective tendency for the generic quantity ψ (see Bechtold et al., 2008; ECMWF, 2017; Beljaars et al., 2018). Ignoring the presence of downdrafts for convenience, the convective tendency (cf. Eq. 2.19) in pressure

coordinates can be discretized by

$$\frac{\psi_k^{n+1} - \psi_k^n}{\Delta t} = \frac{g}{\Delta p}\left[(m_u\psi_u)_{k+1/2} - (m_u\psi_u)_{k-1/2} - (m_u)_{k+1/2}\psi_k - (m_u)_{k-1/2}\psi_{k-1}\right] + (S_{\psi,u})_k, \tag{A.1}$$

where an upwind difference scheme is applied for the subsidence terms (the last two terms in the bracket). While these terms involve the grid-scale values of ψ from the hosting model, the updraft quantity ψ_u, the mass flux M_u and the internal sources $S_{\psi,u}$ are provided by the cloud model of the Bechtold-Tiedtke scheme in the IFS model (see Eqs. 2.25–2.28).

Of particular interest for the numerical stability is now the Courant-Friedrichs-Lewy (CFL) criterion which reads

$$m_u < \frac{\Delta p}{g\Delta t}. \tag{A.2}$$

As shown in Beljaars et al. (2018), the accordingly chosen mass flux limiter would reduce noticeably the updraft mass flux in operational applications of the Bechtold-Tiedtke scheme (see their Figure 8).

In order to relax the numerical constraint from the CFL criterion, Bechtold et al. (2008) propose to evaluate the grid-scale ψ-terms on the RHS of Equation A.1 at the provisionally updated time-level $\tilde{n}^\star$. Rearranging the term then yields a simple bi-linear equation system for $\psi_k^{\tilde{n}^\star}$ and $\psi_{k-1}^{\tilde{n}^\star}$ which can be solved in a straightforward manner. The provisionally updated values of $\psi_k^{\tilde{n}^\star}$ are finally evaluated to obtain the convective tendency:

$$\left(\frac{\partial\psi_k}{\partial t}\right)_{conv} = \frac{\psi_k^{\tilde{n}^\star} - \psi_k^n}{\Delta t}. \tag{A.3}$$

Although ψ_u itself depends on ψ and thus does not yield a fully implicit form of the convective tendency, it was found to allow for a less strict CFL limit as formulated by Equation A.2. Indeed, a relaxation factor of 3 has been introduced in the Bechtold-Tiedtke scheme which still warrants numerical stability during integration.

Unfortunately, an analogous approach for all quantities subject to the parametrization scheme is not feasible with HYMACS. This is due to the fact that the subsidence term is absent with the hybrid approach. However, the transformation equation for the convective Exner pressure tendency in ICON allows us to deploy a partially implicit formulation as well:

The convective π-tendency marks the starting point which is repeated from Equation 4.21 for convenience:

$$\left.\frac{\partial\pi}{\partial t}\right|_{conv} = \frac{R_d}{c_{vd}}\pi\left(\frac{1}{1+\alpha}\left.\frac{\partial\alpha}{\partial t}\right|_{conv} + \frac{1}{\rho}\left.\frac{\partial\rho}{\partial t}\right|_{conv} + \frac{1}{h}\left.\frac{\partial h}{\partial t}\right|_{conv}\right). \tag{A.4}$$

While all tendencies from the cloud model of HYMACS are involved in the transformation, the associated grid-scale quantities also appear as pre-factors including the Exner-pressure π. Using the Euler forward scheme to discretize the convective

tendency and evaluating the grid-scale variables at the provisional time-level $\tilde{n}^\star$ then yields for the convectively updated Exner pressure $\pi_k^{\tilde{n}^\star}$:

$$\pi^{\tilde{n}^\star} = \frac{c_{vd}\pi^n}{-R_d\Delta t\left[\frac{1}{1+\alpha^{\tilde{n}^\star}}\frac{\partial\alpha}{\partial t}\Big|_{conv} + \frac{1}{\rho^{\tilde{n}^\star}}\frac{\partial\rho}{\partial t}\Big|_{conv} + \frac{1}{h^{\tilde{n}^\star}}\frac{\partial h}{\partial t}\Big|_{conv}\right]}. \tag{A.5}$$

Here, the updated values of the grid-scale quantities on the RHS are directly deduced from the convective tendencies with

$$\begin{aligned} \alpha^{\tilde{n}^\star} &= \alpha^n + \Delta t\frac{\partial\alpha}{\partial t}\Big|_{conv}, \quad \rho^{\tilde{n}^\star} = \rho^n + \Delta t\frac{\partial\rho}{\partial t}\Big|_{conv}, \\ h^{\tilde{n}^\star} &= h^n + \Delta t\frac{\partial h}{\partial t}\Big|_{conv} = c_{pd}T^n + \Delta t\frac{\partial h}{\partial t}\Big|_{conv}. \end{aligned} \tag{A.6}$$

Application of Equation A.3 finally gives the discretized convective Exner pressure tendencies that is used for coupling HYMACS with ICON (see also Eq. 4.22):

$$\begin{aligned} \frac{\partial\pi}{\partial t}\Big|_{conv} &= \frac{A_\pi^\star}{A_\pi}\pi^n \\ \text{with} \quad A_\pi &= c_{vd} - R_d\Delta t_{dyn}\left(\frac{1}{h^{\tilde{n}^\star}}\frac{\partial h}{\partial t} + \frac{1}{1+\alpha^{\tilde{n}^\star}}\frac{\partial\alpha}{\partial t}\Big|_{conv} + \frac{1}{\rho^{\tilde{n}^\star}}\frac{\partial\rho}{\partial t}\Big|_{conv}\right) \\ \text{and} \quad A_\pi^\star &= \frac{c_{vd} - A_\pi}{\Delta t_{dyn}}. \end{aligned} \tag{A.7}$$

This partly implicit approach is thereby combined with an empirically determined limiter for the maximal organized entrainment rate

$$\epsilon_{org,max} = 1.5M_{u,0}\frac{\Delta z}{1000} \qquad \text{with} \quad M_{u,0} = \frac{\Delta p_{src}}{g}\frac{A}{\tau_{HYM}}. \tag{A.8}$$

Here, $M_{u,0}$ corresponds to the approximated mass flux of a standard convective cell that overturns the air mass in a source layer of depth $\Delta p_{src} = 60\,\text{hPa}$ within one hour (i.e. $\tau_{HYM} = 3600\,\text{s}$).

Applying both approaches was found to warrant numerical stability in the ICON simulations provided that the mass flux does not exceed its CFL-based maximum value by a factor 3 like in the Bechtold-Tiedtke scheme.

A.2 Convective mass sources in the moisture transport scheme of ICON

As mentioned at the end of Section 4.2, care must be taken when coupling HYMACS into ICON in conjunction with the (moisture) tracer transport scheme. Subsequently, a more detailed description on the handling of subgrid net mass fluxes is provided which largely follows the documentation given by Reinert (2020).

The tracer mass continuity equation constitutes the starting point which can be rewritten based on Equation 4.7 as

$$\frac{\partial}{\partial t}(\rho q^k) + \nabla\cdot(\rho q^k\mathbf{v}) = \rho\frac{\partial q^k}{\partial t}\Big|_{force} + q^k\frac{\partial\rho}{\partial t}\Big|_{force}. \tag{A.9}$$

Here, the terms due to subgrid-scale transport processes $F_s(q^k)$ and phase changes have been collocated in a generic forcing tendency

$$S(\rho q^k)\big|_{force} \equiv \left.\frac{\partial(\rho q^k)}{\partial t}\right|_{force}, \tag{A.10}$$

which has been split up with the help of the product rule.
It is noted that HYMACS provides tendencies in both, the density ρ and the specific moisture content q^k. This contrasts to other physical parameterization schemes in ICON which only provide tendencies for the latter due to the isochoric physics-dynamics coupling.

However, local mass sources and sinks also need to be taken into account when the so-called incremental analysis update (IAU) is applied during initialization. In this case, the grid-scale density ρ as well as other prognostic model variables are pulled towards the analyzed state over a given time window where the model is started from a *first guess* atmospheric state (see Prill et al., 2020, for a detailed description on the IAU technique).

From Equation A.9, the continuity equation for moist air can be recovered by summing up over all moisture species and the specific mass of dry air q^d. While there is no prognostic equation for q^d, the continuity equation of moist air is solved explicitly in ICON. The corresponding Equation 4.17 is repeated here and reads

$$\frac{\partial \rho}{\partial t} + \nabla \cdot (\rho \mathbf{v}) = \left.\frac{\partial \rho}{\partial t}\right|_{conv} + S(\rho)\big|_{IAU}, \tag{A.11}$$

where the incremental analysis update on the density $S(\rho)\big|_{IAU}$ is now added to the convective density tendency on the RHS.

An important property of Equation A.9 and A.11 is that an initially uniform spatial distribution of an arbitrary tracer species remains unchanged in the absence of source and sink terms for q^k. It is desirably that this property, known as *consistency with continuity* (CWC), also holds in discretized form within atmospheric models. This is especially true when the virtual moisture increment α is explicitly taken into account in the model's first law of thermodynamics as it is done with the prognostic Exner pressure in ICON. In this case, violation of CWC may induce spurious buoyancy effects which may even jeopardize the numerical stability of the model. Thus, a careful orchestration of the temporal integration in the dynamical core and with the tracer transport scheme is mandatory both are performed separately.

The numerical integration of the tracer mass continuity equation is performed with a so-called *flux-form semi-Lagrangian* scheme with a finite volume discretization in ICON. This means that the value of q^k defined at the circumcenter is interpreted as the average value over the grid cell's volume $\Delta V_i = A_i \Delta z_i$ rather than a grid point value. Changes in the grid cell's content of the moisture species q^k due to advection are computed by fluxes over the rigid cell walls for which trajectory calculations are performed.

As shown in more detail in Reinert (2020), the temporally discretized form of Equation A.9 can be written schematically as:

$$\overline{\rho q^k}^{n+1} = \overline{\rho q^k}^{n} + \Delta t_{phy} \left(\mathcal{H}(\overline{q^k}^{z,n^\star}) + \mathcal{V}(\overline{q^k}^{h,n^\star}) + \overline{S}(\rho q^k)\big|_{force} \right). \tag{A.12}$$

Here, the overbar indicates the aforementioned average of the cell volume. The change in the cell content of the moisture species q^k between time level n and $n+1$ is then determined by the (averaged) in-box source term $\overline{S}(\rho q^k)\big|_{phy}$ as well the horizontal and vertical flux divergences of q^k denoted by the transport operators $\mathcal{H}(\overline{q^k}^{z,n^\star})$ and $\mathcal{V}(\overline{q^k}^{h,n^\star})$, respectively. It is worth mentioning that these operators only act on the line integral of the tracer q^k at intermediate time steps $n^\star$ along the faces of the triangular grid box where $\overline{(\cdot)}^h$ and $\overline{(\cdot)}^z$ denote averages on the lateral and upper/lower faces. The involved mass fluxes are thereby provided by the dynamical core. While references to the technique of the advection operators can be found in Prill et al. (2020) and Reinert (2020), we proceed with the temporal integration method:

A fractional step approach is used for solving Equation A.12 which means that the three updating terms are computed sequentially. Besides, the temporal integration is performed with the physical time step $\Delta t_{phy} = 5\Delta t_{dyn}$. Provided that the mass fluxes over the cell faces are tracked in the dynamical core, the computational burden of the (moisture) tracer transport problem is reduced significantly. This is possible since fast sound and gravity wave modes are irrelevant for the transport process and since the atmospheric moisture content can be neglected above the lower levels of the stratosphere where grid-scale wind velocities close to the speed of sound may occur.

However, the fractional step approach introduces some arbitrariness in the ordering of the update terms in Equation A.12. This results into a *splitting error* which reduces the accuracy of the time integration to $\mathcal{O}(\Delta t)$ when a fixed ordering such as

$$\overline{\rho q^k}^{n^\star} = \overline{\rho q^k}^{n} + \Delta t_{phy}\mathcal{V}(\overline{q^k}^{h,n}), \tag{A.13}$$

$$\overline{\rho q^k}^{n^{\star\star}} = \overline{\rho q^k}^{n^\star} + \Delta t_{phy}\mathcal{H}(\overline{q^k}^{z,n^\star}), \tag{A.14}$$

$$\overline{\rho q^k}^{n+1} = \overline{\rho q^k}^{n^{\star\star}} + \Delta t_{phy}\overline{S}(\rho q^k)\big|_{force} \tag{A.15}$$

is used.

Higher orders of accuracy for the temporal integration can be obtained by permuting the sequence order of the $\mathcal{H}$ and $\mathcal{V}$ transport operators as well as the source term $\overline{S}(\rho q^k)\big|_{phy}$ on consecutive time steps. This approach is oftentimes referred as a poor-man *Strang splitting*, where only the order of the transport operators are reversed between even and odd time steps in ICON.

Another complication with the fractional step approach is related to the requirement for calculating the mass fraction q^k at intermediate time steps for the transport operators $\mathcal{H}$ and $\mathcal{V}$. Since only the grid averaged moisture content $\overline{\rho q^k}^{n'}$ with $n' \in \{n^\star, n^{\star\star}\}$ is known from the integration procedure, a proper grid-scale density value must be chosen for conversion. As shown in Section 4.3 of Reinert (2020), choosing ρ^n or ρ^{n+1} which are directly available from ICON's dynamical core breaks the CWC property mentioned above. Thus, following the method of Easter (1993), the continuity equation of moist air (Eq. A.11) must be performed along with the sequence splitting. Thereby, the subgrid mass source terms from the

IAU technique and from the newly coupled hybrid convection scheme HYMACS require further consideration to maintain the consistency with continuity.

In ICON, the following computation chain is implemented, where special attention should be paid on the occurrence of the source terms of ρ:

1. Compute an intermediate density $\overline{\rho}^{n^\star}$ already updated by $S(\rho)\big|_{IAU}$ and $\partial\rho/\partial t\big|_{conv}$ to correct $\overline{\rho q^k}^n$

$$\begin{aligned} \overline{\rho}^{n^\star} &= \overline{\rho}^n + \Delta t_{phy}\left(\overline{S}(\rho)\big|_{IAU} + \left.\frac{\partial\rho}{\partial t}\right|_{conv}\right) \\ \overline{\rho q^k}^n &\approx \overline{\rho}^{n^\star}\,\overline{q^k}^n. \end{aligned} \tag{A.16}$$

2. Perform the horizontal and vertical transport of the (moisture) species in reversed order for consecutive time steps and update the air mass consistently, starting with the values from step 1

$$\begin{aligned} \overline{\rho q^k}^{n^\star} &= \overline{\rho q^k}^n + \Delta t_{phy}\begin{cases}\mathcal{V}(\overline{q^k}^n) & \text{even time step}\\ \mathcal{H}(\overline{q^k}^n) & \text{odd time step}\end{cases} \\ \overline{\rho}^{n^{\star\star}} &= \begin{cases}\overline{\rho}^{n^\star} + \Delta t_{phy}\mathcal{V}(1) & \text{even time step}\\ \overline{\rho}^{n+1} - \Delta t_{phy}\mathcal{V}(1) & \text{odd time step}\end{cases} \\ \overline{q^k}^{n^\star} &= \frac{\overline{\rho q^k}^{n^\star}}{\overline{\rho}^{n^{\star\star}}} \\ \overline{\rho q^k}^{n^{\star\star}} &= \overline{\rho q^k}^{n^\star} + \Delta t_{phy}\begin{cases}\mathcal{H}(\overline{q^k}^{n^\star}) & \text{even time step}\\ \mathcal{V}(\overline{q^k}^{n^\star}) & \text{odd time step.}\end{cases} \end{aligned} \tag{A.17}$$

3. Perform the final update by adding the subgrid source/sink terms. Also subtract the density effect which has been used to update $\overline{\rho q^k}^n$ in step 1 to avoid double counting:

$$\begin{aligned} \overline{\rho q^k}^{n+1} &= \overline{\rho q^k}^{n^{\star\star}} + \Delta t\left\{S(\rho q^k)\big|_{force} - \overline{q^k}^n\,\Delta t_{phy}\left(\overline{S}(\rho)\big|_{IAU} + \left.\frac{\partial\rho}{\partial t}\right|_{conv}\right)\right\} \\ \overline{q^k}^{n+1} &= \frac{\overline{\rho q^k}^{n+1}}{\rho^{n+1}}. \end{aligned} \tag{A.18}$$

By going to all steps, it is easy to verify that an initially uniform distribution of q^k remains uniform unless subgrid sources or sinks of q^k are involved. The CWC property is therefore maintained as desired.

In the context of coupling properly HYMACS with the transport scheme in ICON, two details are highlighted: First, such as the incremental analysis update $\overline{S}(\rho)\big|_{IAU}$, the convective density tendency has to be passed to the transport scheme[1]. Second, the convective tendencies of q^k *must* involve a correction to the net mass transfer. This is already ensured in HYMACS by using Equation 3.13.

[1]This is done in ICON's dynamics-tracer-physics interface routine `mo_nh_dtp_interface.f90`.

A.3 Implicit vertical wind solver with isotropic divergence damping

Before we dive into the details of the implicit vertical wind solver of ICON, an outline on the time integration procedure is provided. This outline is mandatory in order to understand the meaning of different terms appearing in the vertical wind solver which was complemented by an isotropic divergence damping term in this thesis. However, for the sake of brevity, the explanation on the ICON's time integration is limited to the most relevant aspects. A more comprehensive description can be obtained from Prill et al. (2020).

The predictor-corrector scheme

The motivation to deploy the so-called iterative predictor-corrector scheme is that it allows for a higher accuracy than the simple Euler forward scheme without introducing the implicity of a trapezodial scheme. While the former is only of first order accuracy, the latter attains a second order accuracy.

Describing the evolution of the atmospheric state $\mathbf{X}$ generically with a first-order differential equation system of the form

$$\frac{d}{dt}\mathbf{X}(\mathbf{r},t) = F(\mathbf{X}(\mathbf{r},t)), \tag{A.19}$$

where $\mathbf{r}$ denotes the location vector and F is an arbitrary forcing function, the predictor-corrector scheme applies the two following steps to propagate the atmospheric state $\mathbf{X}$ from time-level t^n to t^{n+1}:

For the predictor step, F is evaluated at the current time-level t^n in order to retrieve an *intermediate* solution for the atmospheric state $\mathbf{X}(\mathbf{r}, t^{n+1\star})$. This intermediate solution is used in the second step, the corrector step, to refine the estimate on F. Linear temporal interpolation is applied for the refined estimate which is then used to predict the final state $\mathbf{X}(\mathbf{r}, t^{n+1})$.

Mathematically, these both steps can be sketched by:

$$\text{Predictor step}: \quad \mathbf{X}(\mathbf{r}, t^{n+1\star}) = \mathbf{X}(\mathbf{r}, t^n) + \Delta t F(\mathbf{X}(\mathbf{r}, t^n)), \tag{A.20}$$

$$\text{Corrector step}: \quad \mathbf{X}(\mathbf{r}, t^{n+1}) = \mathbf{X}(\mathbf{r}, t^n) + \Delta t \left\{F(\mathbf{X}(\mathbf{r}, t^n)), F(\mathbf{X}(\mathbf{r}, t^{n+1\star}))\right\}_\alpha . \tag{A.21}$$

Here, the temporal averaging operator $\{\cdot\}$ has been introduced which reads

$$\left\{f(t^n), f(t^{n+1})\right\}_\alpha = \alpha f(t^n) + (1-\alpha) f(t^{n+1}) \qquad \text{with } \alpha \in [0,1]. \tag{A.22}$$

Depending on the parameter α which should not be confused with the virtual moisture increment in this section, different imitations of the classical Euler schemes can be realized. For $\alpha = 1$, the predictor-corrector scheme imitates the Euler backward scheme which is also termed the Matsuno scheme then (Matsuno, 1966). The Heun's method (Heun et al., 1900) is applied when $\alpha = 0.5$ is set to imitate the trapezodial scheme.

The temporally discretized ICON equations

For the temporal integration of ICON's equation system, two different temporal averaging operators α_1 and α_2 for horizontal momentum in terms of v_n and for the thermodynamic quantities π and θ_v are applied. Additionally, terms related to vertically propagating sound waves are treated implicitly. These comprise vertical derivatives of the vertical wind w and the Exner pressure perturbation π' whose degree of implicitness is controlled by the parameter η which is defined analogously to Equation A.22. The perturbation term π' is thereby given by the residual of the *full* Exner pressure π with respect to a hydrostatic reference state π_0.

Using the predictor-corrector scheme in conjunction with an implicit handling of terms subject to fast modes in vertical direction, the Equations 4.3–4.6 can be discretized temporally as follows:

Predictor step:

$$\frac{v_n^{n+1\star} - v_n^n}{\Delta t_{dyn}} = -\operatorname{adv}\left(v_n^{\hat{n}}\right) - c_{pd}\theta_v^n \frac{\partial \pi'^{\tilde{n}}}{\partial n} + F(v_n^n), \tag{A.23}$$

$$\frac{w^{n+1\star} - w^n}{\Delta t_{dyn}} = -\operatorname{adv}\left(w_n^{\hat{n}}\right) - c_{pd}\theta_v'^n \frac{d\pi_0}{dz} - c_{pd}\theta_v^n \frac{\partial}{\partial z}\left\{\pi'^n, \pi'^{n+1\star}\right\}_\eta, \tag{A.24}$$

$$\frac{\rho^{n+1\star} - \rho^n}{\Delta t_{dyn}} = -\nabla_h \cdot \left(\mathbf{v}_h^{n+1\star}\rho^n\right) - \frac{\partial}{\partial z}\left[\left\{w^n, w^{n+1\star}\right\}_\eta \rho^n\right] - \left.\frac{\partial \rho}{\partial t}\right|_{conv}^n, \tag{A.25}$$

$$\begin{aligned}\frac{\pi^{n+1\star} - \pi^n}{\Delta t_{dyn}} = &-\frac{R_d}{c_{vd}}\left(\frac{\pi^n}{\rho^n\theta_v^n}\right)\left[\nabla_h \cdot \left(\mathbf{v}_h^{n+1\star}\rho^n\theta_v^n\right) + \frac{\partial}{\partial z}\left[\left\{w^{n+1\star}, w^n\right\}_\eta \rho^n\theta_v^n\right]\right] \\ &+ Q_{\pi,dia}^n,\end{aligned} \tag{A.26}$$

Corrector step:

$$\begin{aligned}\frac{v_n^{n+1} - v_n^n}{\Delta t_{dyn}} = &-\left\{\operatorname{adv}\left(v_n^n\right), \operatorname{adv}\left(v_n^{n+1\star}\right)\right\}_{\alpha_1} \\ &c_{pd}\theta_v^n \frac{\partial \pi'^{\tilde{n}}}{\partial n} + F\left(v_n^n\right) \\ &- F'_{div,4o}\left(\mathbf{v}_h^{n+1\star}\right) + F_{div,2o}^{v_n}\left(\mathbf{v}^{n+1\star}\right),\end{aligned} \tag{A.27}$$

$$\begin{aligned}\frac{w^{n+1} - w^n}{\Delta t_{dyn}} = &-\left\{\operatorname{adv}\left(w^n\right), \operatorname{adv}\left(w^{n+1\star}\right)\right\}_{\alpha_1} - c_{pd}\left\{\theta_v'^n, \theta_v'^{n+1\star}\right\}_{\alpha_2}\frac{d\pi_0}{dz} \\ &- c_{pd}\left\{\theta_v^n, \theta_v^{n+1\star}\right\}_{\alpha_2}\frac{\partial}{\partial z}\left\{\pi'^n, \pi'^{n+1}\right\}_\eta \\ &+ \left\{F_{div,2o}^w\left(\mathbf{v}^{n+1\star}\right), F_{div,2o}^w\left(\mathbf{v}^{n+1}\right)\right\}_\eta,\end{aligned} \tag{A.28}$$

$$\frac{\rho^{n+1} - \rho^n}{\Delta t_{dyn}} = -\nabla_h \cdot \left(\mathbf{v}_h^{n+1}\rho^n\right) - \frac{\partial}{\partial z}\left[\left\{w^{n+1}, w^n\right\}_\eta, \left\{\rho^n, \rho^{n+1\star}\right\}_{\alpha_2}\right] - \left.\frac{\partial \rho}{\partial t}\right|_{conv}^n, \tag{A.29}$$

$$\frac{\pi^{n+1}-\pi^n}{\Delta t_{dyn}} = -\frac{R_d}{c_{vd}}\left(\frac{\pi^n}{\rho^n\theta_v^n}\right)\Bigg[\nabla_h\cdot\left(\mathbf{v}_h^{n+1}\rho^n\theta_v^n\right) + \frac{\partial}{\partial z}\left[\left\{w^n, w^{n+1}\right\}_\eta \left\{\rho^n, \rho^{n+1\star}\right\}_{\alpha_2}\left\{\theta_v^n, \theta_v^{n+1\star}\right\}_{\alpha_2}\right]\Bigg] + Q_{\pi,dia}^n. \tag{A.30}$$

Here, ICON's model equations are written down in the expanded version with the additional terms due to the coupling with HYMACS (cf. Eq. 4.17 and Eq. 4.30).

The above mentioned temporal averaging operators α_1 and α_2 default to 0.65 and 0.4. Both values have been found to improve the numerical stability in dynamical core tests (Zaengl et al., 2015).

Technically, the integration of the model equations starts with the computation of the new (intermediate) values of horizontal momentum $v_n^{n+1\star}$ and v_n^{n+1}, respectively. This also involves the advection term for horizontal momentum which reads

$$\mathrm{adv}(v_n^n) = \frac{\partial K_h^n}{\partial n} + (\zeta^n + f)v_t^n + w^n\frac{\partial w_n^n}{\partial z}.$$

The edge-normal horizontal wind velocity component is then used to calculate the horizontal flux divergencies in the continuity equation and in ICON's first law of thermodynamics. Additionally, the advection term for vertical momentum $\mathrm{adv}(w^n) = \mathbf{v}_h^n\cdot\nabla_h w^n + w^n\frac{\partial w^n}{\partial z}$ can be computed explicitly. For the remaining terms, the implicit vertical wind solver is used which is outlined below.

For enhancing the numerical stability of the time integration and for the sake of computational efficiency, a few modifications are established in the integration scheme (Eqs. A.23–A.30).

First, the horizontal and vertical momentum advection terms in the predictor step (see Eqs. A.23–A.24) are reused from the preceding corrector step as denoted by $\hat{n}$. This has the advantage that the advection terms must only be computed once per time step. The first dynamical time step after application of the fast physics update remains an exception due the accompanied momentum update by the fast physical processes.

Second, the horizontal pressure gradient is evaluated in terms of an extrapolated Exner pressure at the predictor and the corrector step. The extrapolation involves time level $n-1$ and n and reads

$$\pi'^{\hat{n}} = (1+\gamma)\pi'^{n} - \gamma\pi'^{n-1},$$

where $\gamma = \frac{1}{3}$ is used as the default. By doing so, horizontally propagating sound waves are damped efficiently as demonstrated by the sound-wave–gravity-wave described in Baldauf et al. (2014).

Of particular interest for the stability of the numerical integration are also the divergence damping terms applied in the corrector step. While the operational configuration only involves an anisotropic fourth-order divergence damping in the prognostic equation for v_n (cf. Eq. 4.12), the revised configuration proposed in this study (cf. Eq. 4.28) also includes second-order divergence damping in the prognostic equation for w (see Section 4.4 for a discussion on the rationale). This introduces a damping term in Equation A.37 where D denotes the three-dimensional divergence, that is $D = D_h + \partial w/\partial z$. These terms also become subject of the implicit vertical wind solver.

The implicit w-solver with isotropic divergence damping

Before the computations of the continuity equation of moist air and the first law of thermodynamics can be finalized, an updated value for the vertical wind w is required. However, this update also depends on the (vertical gradient of the) Exner pressure π at the new time-level so that an implicit solution becomes mandatory. The motivation for the horizontally explicit, vertically implicit (HeVi) integration scheme is related to the presence of accoustic modes which would otherwise constrain the allowable time step Δt_{dyn} in the dynamical core to small values.

In case of ICON, the mutual dependency of w and π can be removed by inserting the first law of thermodynamics into the prognostic equation for the vertical wind. This step yields a linear equation system for w at the new time level which can be solved in a straightforward manner.

In the following, this procedure is demonstrated explicitly for the predictor step. The spatially discretized of Equation A.24 and Equation A.26 can be written after some rearrangements as

$$w_{k+1/2}^{n+1\star} = Z_{w,k+1/2}^{exp,(n,n\star)} - \Delta t_{dyn} c_{pd} \theta_{v,k+1/2}^{n} \eta \frac{\pi_k'^{n+1\star} - \pi_{k+1}'^{n+1\star}}{\Delta z_{k+1/2}}, \tag{A.31}$$

$$\begin{aligned} \pi_k'^{n+1\star} =& Z_{\pi,k}^{exp,(n,n+1\star)} \\ & - \Delta t_{dyn} \frac{R_d}{c_{vd}} \left(\frac{\pi^n}{\rho^n \theta_v^n} \right)_k \eta \frac{\left(w^{n+1\star} \rho^n \theta_v^n\right)_{k-1/2} - \left(w^{n+1\star} \rho^n \theta_v^n\right)_{k+1/2}}{\Delta z_k}. \end{aligned} \tag{A.32}$$

Here, $\Delta z_k = z_{k-1/2} - z_{k+1/2}$ denotes the k^{th} full-layer thickness bounded by the half-levels $k-1/2$ and $k+1/2$, respectively. Likewise, $\Delta z_{k+1/2} = z_k - z_{k+1}$ is the thickness of the layer between the two full-levels k and $k+1$. Note that a top-down ordering of the vertical levels is applied in ICON.

For convenience, a shorthand notation for the explicit terms of the vertical wind $Z_{w,k+1/2}^{exp,(n,\hat{n})}$ and Exner pressure $Z_{\pi,k}^{exp,(n,n+1\star)}$ have been introduced. Both terms are given by

$$\begin{aligned} Z_{w,k+1/2}^{exp,(n,n\star)} =& w_k^n - \Delta t_{dyn} \Bigg[\mathrm{adv}(w_{k+1/2}^{n\star}) + c_{pd} \theta_{v,k+1/2}'^{n} \left. \frac{d\pi_0}{dz} \right|_{k+1/2} \\ & + c_{pd} \theta_{v,k+1/2}^{n} (1-\eta) \frac{\pi_k'^{n} - \pi_{k+1}'^{n}}{\Delta z_{k+1/2}} \Bigg], \end{aligned} \tag{A.33}$$

$$\begin{aligned} Z_{\pi,k}^{exp,(n,n+1\star)} =& \pi_k^n - \Delta t_{dyn} \frac{R_d}{c_{vd}} \left(\frac{\pi^n}{\rho^n \theta_v^n} \right)_k \Bigg[\nabla_h \cdot \left(\mathbf{v}_h^{n+1\star} \rho^n \theta_v^n \right)_k \\ & + (1-\eta) \frac{\left(w^n \rho^n \theta_v^n\right)_{k-1/2} - \left(w^n \rho^n \theta_v^n\right)_{k+1/2}}{\Delta z_k} \Bigg] + \Delta t_{dyn} Q_k^n, \end{aligned} \tag{A.34}$$

where ρ and θ_v at the half-levels are computed with an upwind-biased reconstruction based on the Miura scheme (Miura, 2007).

The nominator of the implicit term on the RHS of Equation A.31 is then obtained with the help of Equation A.32 which allows us to separate the new values for the vertical wind on the three half-levels $k-1/2$, $k+1/2$ and $k+3/2$ from purely

explicit terms. After a couple of algebraic steps, one obtains

$$\begin{aligned}
&- w^{n+1\star}_{k-1/2}\left[\Delta t_{dyn}\frac{c_{pd}\theta^n_{v,k+1/2}}{\Delta z_{k+1/2}}\eta\Delta t_{dyn}\frac{R_d}{c_{vd}}\frac{\eta\Lambda^n_k}{\Delta z_k}\left(\rho^n\theta^n_v\right)_{k-1/2}\right]\\
&+ w^{n+1\star}_{k+1/2}\left[1+\Delta t_{dyn}\frac{c_{pd}\theta^n_{v,k+1/2}}{\Delta z_{k+1/2}}\eta\Delta t_{dyn}\frac{R_d}{c_{vd}}\left(\rho^n\theta^n_v\right)_{k-1/2}\eta\left(\frac{\Lambda^n_k}{\Delta z_k}+\frac{\Lambda^n_{k+1}}{\Delta z_{k+1}}\right)\right]\\
&- w^{n+1\star}_{k+3/2}\left[\Delta t_{dyn}\frac{c_{pd}\theta^n_{v,k+1/2}}{\Delta z_{k+1/2}}\eta\Delta t_{dyn}\frac{R_d}{c_{vd}}\frac{\eta\Lambda^n_{k+1}}{\Delta z_{k+1}}\left(\rho^n\theta^n_v\right)_{k+3/2}\right]\\
=&Z^{exp,(n,n\star)}_{w,k+1/2}-\Delta t_{dyn}\frac{c_{pd}\theta^n_{v,k+1/2}}{\Delta z_{k+1/2}}\eta\left(Z^{exp,(n,n+1\star)}_{\pi,k}-Z^{exp,(n,n+1\star)}_{\pi,k+1}\right),
\end{aligned}\tag{A.35}$$

where the short-cut notation

$$\Lambda^n_k=\frac{\pi^n_k}{\rho^n_k\theta^n_{v,k}}\tag{A.36}$$

was introduced.
Equation A.35 forms a linear equation system which can be written in matrix form $\underline{\mathbf{A}}\mathbf{x}=\mathbf{b}$. The first and the third line of Equation A.35 constitute the sub-diagonal entries of $\underline{\mathbf{A}}$, whereas the second row constitutes the main diagonal. This trigonal equation system can be solved sequentially with the so-called *Thomas algorithm* (see, e.g., Datta, 2010) provided that boundary conditions for the vertical wind at the top and the bottom half-level are prescribed. In ICON, the surface and the top of the modelled atmosphere are considered to be impermeable, i.e. $w^n_{ke+1/2}=w^n_{1/2}=0$. For nested domains, the vertical wind at the upper boundary is obtained from the vertical wind on the parent grid.

Since no numerical filtering is applied in the predictor step, no changes are required with the revised filter configuration introduced in this thesis. However, the isotropic divergence damping term enters the vertical wind equation in the corrector step. Discretizing Equation A.28 like A.31 then yields

$$\begin{aligned}
w^{n+1}_{k+1/2}=&Z^{exp,(n,n+1\star)}_{w,k+1/2}-\Delta t_{dyn}c_{pd}\left\{\theta^n_{v,k+1/2},\theta^{n+1\star}_{v,k+1/2}\right\}_{\alpha_2}\eta\frac{\pi'^{n+1}_k-\pi'^{n+1}_{k+1}}{\Delta z_{k+1/2}}\\
&+f_{2d,o}\overline{A}_c\Delta t_{dyn}\frac{1}{\Delta z_{k+1/2}}\left\{D^{n+1\star}_k,D^{n+1}_k\right\}_\eta,
\end{aligned}\tag{A.37}$$

where $Z^{exp,(n,n+1\star)}_{w,k+1/2}$ is defined in analogy to Equation A.33 except that the dependency on time-level $n\star$ (the preceding corrector step) is replaced by time-level $n+1\star$ due to the temporal averaging operator $\{\cdot\}_{\alpha_2}$. The last term in Equation A.37 involves the full three-dimensional divergence whose discretized form reads

$$D^n_k=div(\mathbf{v}_h)^k_n+\frac{w^n_{k-1/2}-w^n_{k+1/2}}{\Delta z_k},\tag{A.38}$$

with $div(\mathbf{v}_h)$ defined in Equation 4.13.

Proceeding in analogy to the corrector step described above, one obtains additional terms involving *unknown* w-terms at time-level $n+1$ as well as explicit

terms of w and v_n at time levels n and $n+1$, respectively. As can be verified by simple algebraic steps, the additional terms Σ are

$$\begin{aligned}\Sigma = &\frac{f_d}{\Delta t_{dyn}}\overline{A}_c\Bigg[(1-\eta)\frac{D_k^{n+1\star}-D_{k+1}^{n+1\star}}{\Delta z_{k+1/2}}+\eta\frac{div(\mathbf{v}_h)_k^{n+1\star}-div(\mathbf{v}_h)_{k+1}^{n+1\star}}{\Delta z_{k+1/2}}\\ &+\eta\frac{1}{\Delta z_{k+1/2}}\left(\frac{w_{k-1/2}^{n+1}-w_{k+1/2}^{n+1}}{\Delta z_k}+\frac{w_{k+1/2}^{n+1}-w_{k+3/2}^{n+1}}{\Delta z_{k+1}}\right)\Bigg],\end{aligned} \tag{A.39}$$

where the explicit terms are placed in the first row while the implicit terms are present in the second row.

Thus, the basic procedure of the vertical wind solver remains unchanged, but additional terms have to be taken into account when the second-order isotropic divergence damping is applied in the dynamical core.

List of abbreviations

BOMEX Barbados Oceano-graphic and Meteorological Experiment

CAM5 Community Atmosphere Model 5

CDF cumulative density function

CDO Climate Data Operators

COLDUP experiment with cold updraft detrainment

COSMO COnsortium for Small-scale Modeling

CPS convection parametrization schemes

CTL cloud top level

DCMIP Dynamical Core Model Intercomparison Project

DWD Deutscher Wetterdienst (engl.: German Weather Service)

ECMWF European Centre for Medium-Range Forecasts

FV3 GFDL Finite-Volume Cubed-Sphere Dynamical Core

GATE GARP Atlantic Tropical Experiment

GER-North Northern Germany used for precipitation forecast verification (see Figure 5.2)

GER-South Southern Germany for precipitation forecast verification (see Figure 5.2)

GFS Global Forecast System

HYMACS HYbrid MAss flux Convection Scheme

ICON ICOsahedral Non-hydrostatic

ICON-BT ICON model with the Bechtold-Tiedtke scheme

ICON-BT$_{\text{shallow}}$ As ICON-BT without parametrizing deep convection

ICON-EUnest ICON-nest over Europe

ICON-global global ICON model

ICON-HYM ICON with HYMACS

ICON-LAM ICON's limited area mode

IFS Integrated Forecasting System

JW Jablonowski-Williamson

LCL lifting condensation level

LES large-eddy simulations

LFC level of free convection

LFS level of free sinking

LHS left hand side

LNB level of neutral buoyancy

MCS mesoscale convective system

MJO Madden-Julian oscillation

MODIS Moderate Resolution Imaging Spectroradiometer

MPI-M Max Planck Institute for Meteorology

NASA National Aeronautics and Space Administration

NEWCDD new combined divergence damping

NEWDIFF hyper-diffusion with new discretization of the Laplace operator

NWP numerical weather prediction

NWS National Weather Service

OBS observed accumulated precipitation

OLDDIFF hyper-diffusion with old discretization of the Laplace operator

OP4DD operational anisotropic fourth-order divergence damping

PBL planetary boundary layer

PDF probability density function

RADKLIM „RADar KLIMatologie“ (engl.: Radar climatology)

RADOLAN RADar OnLine AdjustmeNt

RBF radial basic function

REDOP reduced operational anisotropic fourth-order divergence damping

RHS right hand side

RW rain gauge adjusted hourly precipitation amount

SLEVE Smooth LEvel VErtical

TERRA land-soil model for soil-vegetation-atmosphere-transfer

TURBDIFF prognostic TKE turbulence scheme

TURBTRAN surface-to-atmosphere transfer scheme

WRF Weather Research and Forecasting

YAC Yet Another Coupler

YW quasi-adjusted 5 minutes precipitation rate

List of symbols

A	arbitrary horizontal area
A_s	score value
A_c	horizontal area of a triangular grid cell
A_g	horizontal area of a grid box
$A_\pi, A^\star_\pi$	auxiliary quantities for implicit convective Exner pressure tendency
A_{skill}	skill score
BS	Brier Score
B	buoyancy acceleration
$CAPE$	convective available potential energy
$CAPE$	convective available potential energy
CIN	convective inhibition
CIN_{crit}	critical CIN value for pretrigger condition
$CIN_{u,subcl}$	subcloud layer CIN
D_{cl}	convective cloud depth
$D^{deep}_{cl,min}$	minimum cloud depth for deep convection
Δp_{cl}	convective cloud depth in pressure units
Δp_{sfc}	difference in surface air pressure with respect to some reference
D_h	horizontal divergence
D^{org}_u	organized, area-integrated updraft detrainment rate
D^{turb}_u, D^{turb}_d	turbulent, area-integrated detrainment rate of the updraft and downdraft
D_u, D_d	area-integrated updraft and downdraft detrainment rate
$D_{u\to d}, E_{u\to d}$	up-to-downdraft detrainment and entrainment rates
E^{org}_u	organized, area-integrated updraft entrainment rate
E^{turb}_u, E^{turb}_d	turbulent, area-integrated entrainment rate of the updraft and downdraft
E_u, E_d	area-integrated updraft and downdraft entrainment rate
FBS	Fractional Brier Score
FSS	Fractions Skill Score
$\mathbf{F}, F_n$	generic flux vector and its normal component
F_{d1}, F_{d2}	sub-components of numerical filter F_d
$F_{d2,new}$	combined divergence damping operator
F_d	numerical filter in the prognostic equation for v_n
F_{diff}	fourth-order background diffusion operator
$F_{div,2o}$	isotropic second-order divergence damping operator
$F_{div,4o}, F'_{div,4o}$	anisotropic fourth-order divergence damping operator acting on $\mathbf{v}$ and $\mathbf{v}_h$
F_O	cumulative density function of observed random variable X
$\mathbf{F}_\psi$	non-convective flux of ψ
$F_s(\Psi)$	subgrid-scale tendency of Ψ
F_{smag}	Smagorinsky diffusion operator
$F_{u\to d}$	fallout of precipitable hydrometeors from the updraft
$G^{l\to i}_u$	freezing rate in the updraft
$G^{(l,i)\to(r,s)}_u$	conversion rate of cloud condensate to precipitation in the updraft
IQD	integrated quadratic distance
I^k	source/sinks of the k$^{\text{th}}$ moisture species due to phase changes
$I_{o,x}, I_{m,x}$	observed and modelled event indicator
$\mathbf{J}_c$	convective mass flux vector
$\mathbf{J}^\psi_c$	convective flux of ψ
K_h	horizontal kinetic energy
K_u, K_d	kinetic energy of updraft air and downdraft air
L_B	block length
$LEPS$	linear error in probability space
L_R	baroclinic Rossby radius of deformation
L	horizontal length scale of atmospheric processes
L_v, L_f	latent heat of evaporation and fusion
MAE	Mean Absolute Error

O, M	set of observations and forecasts
MSE	Mean Squared Error
M_u, M_d	area-integrated mass fluxes of the up- and downdraft regions
N	Brunt-Väisälä frequency
N_m	moist Brunt-Väisälä frequency
N_{slow}	number of parametrized slow-physics processes
$PCAPE$	density-weighted convective available potential energy
$PCAPE_{PBL}$	reference value of $PCAPE$ for relaxation corrected for boundary layer forcing
$PCAPE_{ref}$	reference value of $PCAPE$ for relaxation
$\mathbb{Q}, \mathbb{P}$	sample spaces of observations and forecasts
P_{nh}	threshold for accumulated precipitation amount over n hours
Ψ	conserved quantity
Q_1	apparent heat source
Q_2	apparent moisture sink
Q_R	radiative heating rate
$Q_{dia,h}$	diabatic heating effect on the enthalpy
$Q_{\pi,dia}$	diabatic heating effect on the Exner pressure
RH	relative humidity
RH_d	relative humidity in the downdraft
S_O, S_M	dichotomous sample spaces of categorical observations and forecasts
S_ψ	internal source of ψ
$S_{\psi,c}$	source term of the convective part
T_0	temperature parameter for TKE-trigger
R_d	gas constant for dry air
T_f	freezing temperature
$T_{f\to l}$	upper bound for ice in downdraft condensate
$T^\star$	temperature scale
$T^{\star\star}$	temperature scaling parameter for TKE trigger
T_u	updraft temperature
T_v	virtual temperature
T_v^{prcl}, T_v^{env}	virtual temperature of air parcel and its environment
$\overline{T_v}, T_v'$	virtual temperature of the basic state and its perturbation
$T_{v,u}, T_{v,d}$	virtual temperature of updraft and downdraft air
V_t	terminal velocity of precipitable hydrometeors in the updraft
$\mathbf{X}$	joint set of observations and forecasts
b	bias
γ_{GF}	cold pool velocity
c^v	condensation rate
c_m	momentum source coefficient
c_p, c_{pd}	specific heat capacity of (dry) air at constant pressure
c_{pr}	auto-conversion coefficient in the updraft
c_u^v	updraft condensation rate
c_v, c_{vd}	specific heat capacity of (dry) air at constant density
$\frac{\partial}{\partial n}$	horizontal derivative in edge-normal direction
d_{tv}, d_{nv}	distance in tangential and normal direction for discrete Laplace operator
d_u, e_u	detrainment and entrainment rate of the updraft
$d_{u,org}$	organized detrainment rate
e^v	evaporation rate
e_d^v	downdraft evaporation rate
$d_u^\star, e_u^\star$	enhanced detrainment and entrainment rates for updraft momentum
$f_O(o), f_M(m)$	PDF of observations and forecasts
f	Coriolis frequency
$f_{d,4o}, f'_{d,4o}$	coefficient for fourth-order divergence damping acting on $\mathbf{v}$ and $\mathbf{v}_h$
$f_{d,2o}$	coefficient for second-order divergence damping acting on $\mathbf{v}$
f_o	fractional area coverage of observed events
$f_o^{u,l}$	orientation factor of upper- or lower-tip triangular cell
f_t	reduction factor for buoyancy acceleration in turbulent updrafts
g	terrestrial gravity acceleration
h	enthalpy
h_m	moist static energy
h_{il}	liquid water static energy
$h_{m,u}$	moist static energy of updraft air
$\mathbf{i}_i$	i^{th} component of the Cartesian basis vector
$\mathbf{j}_i$	i^{th} component of the triangular basis vector

k_4	coefficient of fourth-order background diffusion operator for v_n
k	vertical level index
ke	total number of vertical layers
k_b	number of bisection steps
k_D	scaling parameter for minimum cloud depth for deep convection
k_{FC}	scaling parameter for the Fritsch-Chappell trigger
l_2	l2-error
l_e	length of triangular edge
m^1, m^2	realizations of model 1 and model 2
m_c, m_e	convective and environmental mass flux per unit area
o_i, m_i	individual pair of observation and forecast
o, m	realizations of observations and forecasts
$m^\star$	normalized convective mass flux
m_u, m_d	updraft and downdraft mass flux
$n, \tilde{n}^\star$	time-level and intermediate time-level after convective updates
n_c, n_e, n_v	number of cells, edges and vertices (triangular grid)
n_r	number of root division steps
o_0, m_0	observed and modeled dichotomous events
$\overline{o_0}, \overline{m_0}$	observed and modeled dichotomous non-events
$p(o_0), p(m_0)$	probability of the event occurrence in the observations and forecasts
p	air pressure
p_{00}	reference air pressure
p_0	pressure at departure level
$\overline{p}, p'$	(hydrostatic) air pressure of the basic state and its perturbation
p_j	probability of the j^{th} category in the 2x2 contingency table
p_{sfc}	surface air pressure
p_{src}	depth of convective source layer in pressure units
q^i	specific content of ice
q^i_u, q^i_d	specific content of ice of updraft and downdraft air
q^k	specific content of the k^{th} moisture species
q^l	specific content of liquid water
q^l_{crit}	critical cloud water content in the updraft
q^l_u, q^l_d	specific content of liquid water of updraft and downdraft air
q^r	specific content of rain
q^r_u, q^r_d	specific content of rain of updraft and downdraft air
q^s	specific content of snow
q^s_u, q^s_d	specific content of snow of updraft and downdraft air
q^v	specific water vapor content
$\overline{q^v}, q^{v\prime}$	specific moisture content of the basic state and its perturbation
q^v_{sat}	saturation specific water vapor content
q^v_u, q^v_d	specific moisture content of updraft and downdraft air
n	number of grid boxes in neighborhood region
r_s, l_s	radius and edge length of neighborhood region
r^{org}_u	detrained fraction of updraft mass flux
R_v	gas constant of water vapor
$r_{v,s}$	saturation mixing ratio of water
s	dry static energy
s_c, s_e	ensemble-average of dry static energy in convective clouds and its ambient average
w_c, w_e	ensemble-average of vertical velocity in convective clouds and its ambient average
s_i	dry static energy of an individual convective cloud
w_i	vertical velocity of an individual convective cloud
t	time
t_x	threshold for continuous quantities
$\overline{u}_{PBL}$	vertically averaged wind speed in the planetary boundary layer
$\mathbf{v}_b$	barycentric velocity vector
$\mathbf{v}_c, \mathbf{v}_e$	convective and environmental velocity vector
$\tilde{\mathbf{v}}_c$	relative convective velocity vector
$\mathbf{v}_h$	horizontal wind vector
$\mathbf{v}_{h,\Gamma}$	velocity vector at the interface between convective and environmental part
$\widehat{\mathbf{v}_b}, \mathbf{v}''$	density weighted-average velocity vector and its perturbation

$\mathbf{v}_{h,u}$	horizontal velocity vector of updraft air
$v_{n,i\star}$	reconstructed normal wind vector component at cell center position
v_n, v_t	horizontal normal and tangential velocity component relative to cell edge
w_0	reference vertical velocity for the Fritsch-Chappell trigger
w	vertical velocity
$\overline{w}_u^D$	averaged updraft velocity over the convective cloud
$w_{u,0}, w_{d,0}$	start vertical velocity in the updraft and downdraft computation
w_u	vertical velocity of updraft air
x_i	i$^{\text{th}}$-direction in trivariate coordinate system
z	height (position in vertical direction)
z_0	height of departure level
$\Delta T_{v,u}^{FC}$	Fritsch-Chappell temperature increment
$\Delta T_{v,u}^{GF}$	gust front trigger temperature increment
$\Delta T_{v,u}^{TKE}$	TKE trigger temperature increment
Δp	model layer depth in pressure units
Δq_u^{pr}	change per layer in specific content of precipitable hydrometeors in updraft
Δt	time step
$\Delta t_{dyn}, \Delta t_{phy}, \Delta t_{tr}$	dynamical, physical and tracer advection time step
Δx_{cos}	grid spacing of COSMO model
Δx_{ICON}	grid spacing on ICON's triangular grid
$\Delta x'_{ICON}$	effective, spectral grid spacing of ICON
Δz	model layer depth in height coordinates
Γ	lapse rate
α	virtual moisture increment
β	dilution factor in turbulent updrafts
β_d	drag coefficient
$\delta_1^{shal}, \delta_1^{deep}$	base fractional detrainment rate for shallow and deep convection
δ, ϵ	fractional detrainment and entrainment rate
Δx	grid spacing in an atmospheric model
$\epsilon_1^{shal}, \epsilon_1^{deep}$	base fractional entrainment rate for shallow and deep convection
γ	virtual mass coefficient
γ_{GF}	scaling factor for the gust front trigger
κ	wavenumber
λ	wavelength
λ_u	link factor of the initial downdraft mass flux to the updraft mass flux at cloud base
$\mu_u^{turb}, \mu_d^{turb}$	turbulent mixing parameter of the up- and downdraft
$\mu_{u\to d}$	up- to downdraft transfer coefficient
$\nabla^2, \tilde{\nabla}^2$	discretized Laplace operators
∇_n, ∇_t	discretized gradient in normal and tangential direction
ω	generalized vertical velocity in pressure coordinates
$\overline{\omega}, \omega'$	generalized vertical velocity in pressure coordinates of the basic state and its perturbation
Φ_j	counts of the j^{th} category in the 2x2 contingency table
π	Exner pressure
ψ	arbitrary (specific) quantity
$\widehat{\psi}, \psi''$	density weighted-average of ψ and its perturbation
ψ_u, ψ_d	specific content of Ψ within the parametrized up- and downdrafts
ρ	density of moist air
$\overline{\rho}, \rho'$	density of the basic state and its perturbation
ρ_c, ρ_e	partial density of the convective and the environmental volume part
σ_c	fractional coverage of an ensemble of convective clouds
σ_k^{conv}	mass sinks due to parametrized convective precipitation
σ_i	fractional coverage of an individual convective cloud
τ_c	convective time scale
τ_{PBL}	characteristic time scale of the planetary boundary layer
τ_x	e-folding time to time step ratio for diffusion operator on physical quantity x
θ	potential temperature
θ_e	equivalent potential temperature
θ_v	virtual potential temperature
φ	latitude
ζ	relative vorticity

Bibliography

Ahn, M.-S., D. Kim, Y.-G. Ham, and S. Park (2020). "Role of Maritime Continent land convection on the mean state and MJO propagation". In: *Journal of Climate* 33.5, pp. 1659–1675. DOI: 10.1175/JCLI-D-19-0342.1.

Anthes, R. A. (1977). "A cumulus parameterization scheme utilizing a one-dimensional cloud model". In: *Monthly Weather Review* 105.3, pp. 270–286. DOI: 10.1175/1520-0493(1977)105%3C0270:ACPSUA%3E2.0.CO;2.

Arakawa, A. and J.-H. Jung (2011). "Multiscale modeling of the moist-convective atmosphere—A review". In: *Atmospheric research* 102.3, pp. 263–285. DOI: 10.1016/j.atmosres.2011.08.009.

Arakawa, A., J.-H. Jung, and C.-M. Wu (2011). "Toward unification of the multiscale modeling of the atmosphere". In: *Atmospheric Chemistry and Physics* 11.8, pp. 3731–3742. DOI: 10.5194/acp-11-3731-2011.

Arakawa, A. (2004). "The cumulus parameterization problem: Past, present, and future". In: *Journal of Climate* 17.13, pp. 2493–2525. DOI: 10.1175/1520-0442(2004)017%3C2493:RATCPP%3E2.0.CO;2.

Arakawa, A., J.-H. Jung, and C.-M. Wu (2016). "Multiscale modeling of the moist-convective atmosphere". In: *Meteorological monographs* 56, pp. 16–1. DOI: 10.1175/AMSMONOGRAPHS-D-15-0014.1.

Arakawa, A. and W. H. Schubert (1974). "Interaction of a cumulus cloud ensemble with the large-scale environment, Part I". In: *Journal of Atmospheric Sciences* 31.3, pp. 674–701. DOI: 10.1175/1520-0469(1974)031%3C0674:IOACCE%3E2.0.CO;2.

Arakawa, A. and C.-M. Wu (2013). "A unified representation of deep moist convection in numerical modeling of the atmosphere. Part I". In: *Journal of the Atmospheric Sciences* 70.7, pp. 1977–1992. DOI: 10.1175/JAS-D-12-0330.1.

Argüeso, D., R. Romero, and V. Homar (2020). "Precipitation features of the Maritime Continent in parameterized and explicit convection models". In: *Journal of Climate* 33.6, pp. 2449–2466. DOI: 10.1175/JCLI-D-19-0416.1.

Baldauf, M., A. Seifert, J. Foerstner, D. Majewski, and M. Raschendorfer (2011). "Operational convective-scale numerical weather prediction with the COSMO model: description and sensitivities". In: *Monthly Weather Review* 139, pp. 3887–3905. DOI: 10.1175/MWR-D-10-05013.1.

Baldauf, M. (2010). "Linear stability analysis of Runge–Kutta-based partial time-splitting schemes for the Euler equations". In: *Monthly Weather Review* 138.12, pp. 4475–4496. DOI: 10.1175/2010MWR3355.1.

– (2013). *A new fast-waves solver for the Runge-Kutta dynamical core*. Tech. rep. Offenbach, Germany: Deutscher Wetterdienst. DOI: 10.5676/DWDpub/nwv/cosmo-tr2.

Baldauf, M., D. Reinert, and G. Zaengl (2014). "An analytical solution for linear gravity and sound waves on the sphere as a test for compressible, non-hydrostatic numerical models". In: *Quarterly Journal of the Royal Meteorological Society* 140.683, pp. 1974–1985. DOI: 10.1002/qj.2277.

Barker, H. W., G. Stephens, P. Partain, J. Bergman, B. Bonnel, K. Campana, E. E. Clothiaux, S. Clough, S. Cusack, J. Delamere, et al. (2003). "Assessing 1D atmospheric solar radiative transfer models: Interpretation and handling of unresolved clouds". In: *Journal of Climate* 16.16, pp. 2676–2699. DOI: 10.1175/1520-0442(2003)016%3C2676:ADASRT%3E2.0.CO;2.

Barkiđija, S. and Ž. Fuchs (2013). "Precipitation correlation between convective available potential energy, convective inhibition and saturation fraction in middle latitudes". In: *Atmospheric research* 124, pp. 170–180. DOI: 10.1016/j.atmosres.2012.12.010.

Bartels, H., E. Weigl, T. Reich, P. Lang, A. Wagner, O. Kohler, N. Gerlach, et al. (2004). "Projekt RADOLAN–Routineverfahren zur Online-Aneichung der Radarniederschlagsdaten mit Hilfe von automatischen Bodenniederschlagsstationen (Ombrometer)". In: *Deutscher Wetterdienst, Hydrometeorologie* 5. URL: https://www.dwd.de/DE/leistungen/radolan/radolan_info/abschlussbericht_pdf.

Barthold, F. E. and D. A. Kristovich (2011). "Observations of the cross-lake cloud and snow evolution in a lake-effect snow event". In: *Monthly weather review* 139.8, pp. 2386–2398. DOI: 10.1175/MWR-D-10-05001.1.

Bauer, P., A. Thorpe, and G. Brunet (2015). "The quiet revolution of numerical weather prediction". In: *Nature* 525.7567, pp. 47–55. DOI: 10.1038/nature14956.

Bechtold, P., E. Bazile, F. Guichard, P. Mascart, and E. Richard (2001). "A mass-flux convection scheme for regional and global models". In: *Quarterly Journal of the Royal Meteorological Society* 127.573, pp. 869–886. DOI: 10.1002/qj.49712757309.

Bechtold, P., J.-P. Chaboureau, A. Beljaars, A. Betts, M. Koehler, M. Miller, and J.-L. Redelsperger (2004). "The simulation of the diurnal cycle of convective precipitation over land in a global model". In: *Quarterly Journal of the Royal Meteorological Society: A journal of the atmospheric sciences, applied meteorology and physical oceanography* 130.604, pp. 3119–3137. DOI: 10.1256/qj.03.103.

Bechtold, P. (2017). *Atmospheric moist convection*. URL: https://www.ecmwf.int/node/16953.

Bechtold, P., R. Forbes, I. Sandu, S. Lang, and M. Ahlgrimm (2020). "A major moist physics upgrade for the IFS". In: vol. 164, pp. 24–32. DOI: 10.21957/3gt59vx1pb.

Bechtold, P., M. Koehler, T. Jung, F. Doblas-Reyes, M. Leutbecher, M. J. Rodwell, F. Vitart, and G. Balsamo (2008). "Advances in simulating atmospheric variability with the ECMWF model: From synoptic to decadal time-scales". In: *Quarterly Journal of the Royal Meteorological Society: A journal of the atmospheric sciences, applied meteorology and physical oceanography* 134.634, pp. 1337–1351. DOI: 10.1002/qj.289.

Bechtold, P., I. Sandu, D. Klocke, N. Semane, M. Ahlgrimm, A. Beljaars, R. Forbes, and M. Rodwell (July 2014a). "The role of shallow convection in ECMWF's

Integrated Forecasting System". In: 725, p. 27. DOI: 10.21957/heba1qwem. URL: https://www.ecmwf.int/node/8016.

Bechtold, P., N. Semane, P. Lopez, J.-P. Chaboureau, A. Beljaars, and N. Bormann (2014b). "Representing equilibrium and nonequilibrium convection in large-scale models". In: *Journal of the Atmospheric Sciences* 71.2, pp. 734–753. DOI: 10.1175/JAS-D-13-0163.1.

Beljaars, A., G. Balsamo, P. Bechtold, A. Bozzo, R. Forbes, R. J. Hogan, M. Koehler, J.-J. Morcrette, A. M. Tompkins, P. Viterbo, et al. (2018). "The numerics of physical parametrization in the ECMWF model". In: *Frontiers in Earth Science* 6, p. 137. DOI: 10.3389/feart.2018.00137.

Bellenger, H., K. Yoneyama, M. Katsumata, T. Nishizawa, K. Yasunaga, and R. Shirooka (2015). "Observation of moisture tendencies related to shallow convection". In: *Journal of the Atmospheric Sciences* 72.2, pp. 641–659. DOI: 10.1175/JAS-D-14-0042.1.

Bengtsson, L., M. Steinheimer, P. Bechtold, and J.-F. Geleyn (2013). "A stochastic parametrization for deep convection using cellular automata". In: *Quarterly Journal of the Royal Meteorological Society* 139.675, pp. 1533–1543. DOI: 10.1002/qj.2108.

Betts, A. (1973). "Non-precipitating cumulus convection and its parameterization". In: *Quarterly Journal of the Royal Meteorological Society* 99.419, pp. 178–196. DOI: 10.1002/qj.49709941915.

Betts, A. K. (1986). "A new convective adjustment scheme. Part I: Observational and theoretical basis". In: *Quarterly Journal of the Royal Meteorological Society* 112.473, pp. 677–691. DOI: 10.1002/qj.49711247307.

Bierdel, L., T. Selz, and G. Craig (2017). "Theoretical aspects of upscale error growth through the mesoscales: An analytical model". In: *Quarterly Journal of the Royal Meteorological Society* 143.709, pp. 3048–3059. DOI: 10.1002/qj.3160.

Bierdel, L., P. Friedrichs, and S. Bentzien (2012). "Spatial kinetic energy spectra in the convection-permitting limited-area NWP model COSMO-DE". In: *Meteorologische Zeitschrift* 21.3, pp. 245–258. DOI: 10.1127/0941-2948/2012/0319.

Birch, C. E., M. J. Roberts, L. Garcia-Carreras, D. Ackerley, M. J. Reeder, A. P. Lock, and R. Schiemann (2015). "Sea-breeze dynamics and convection initiation: The influence of convective parameterization in weather and climate model biases". In: *Journal of Climate* 28.20, pp. 8093–8108. DOI: 10.1175/JCLI-D-14-00850.1.

Bollmeyer, C., J. Keller, C. Ohlwein, S. Wahl, S. Crewell, P. Friederichs, A. Hense, J. Keune, S. Kneifel, I. Pscheidt, et al. (2015). "Towards a high-resolution regional reanalysis for the European CORDEX domain". In: *Quarterly Journal of the Royal Meteorological Society* 141.686, pp. 1–15. DOI: 10.1002/qj.2486.

Boutle, I., J. Eyre, and A. Lock (2014). "Seamless stratocumulus simulation across the turbulent gray zone". In: *Monthly Weather Review* 142.4, pp. 1655–1668. DOI: 10.1175/MWR-D-13-00229.1.

Bretherton, C. S., P. N. Blossey, and M. Khairoutdinov (2005). "An energy-balance analysis of deep convective self-aggregation above uniform SST". In: *Journal of the atmospheric sciences* 62.12, pp. 4273–4292. DOI: 10.1175/JAS3614.1.

Bretherton, C. S. and P. K. Smolarkiewicz (1989). "Gravity waves, compensating subsidence and detrainment around cumulus clouds". In: *Journal of Atmospheric Sciences* 46.6, pp. 740–759. DOI: 10.1175/1520-0469(1989)046%3C0740:GWCSAD%3E2.0.CO;2.

Brockhaus, P., D. Luthi, and C. Schar (2008). "Aspects of the diurnal cycle in a regional climate model". In: *Meteorologische Zeitschrift* 17.4, pp. 433–444. DOI: 10.1127/0941-2948/2008/0316.

Broecker, J. (2009). "Reliability, sufficiency, and the decomposition of proper scores". In: *Quarterly Journal of the Royal Meteorological Society: A journal of the atmospheric sciences, applied meteorology and physical oceanography* 135.643, pp. 1512–1519. DOI: 10.1002/qj.456.

Bryan, G. H., J. C. Wyngaard, and J. M. Fritsch (2003). "Resolution requirements for the simulation of deep moist convection". In: *Monthly Weather Review* 131, pp. 2394–2416. DOI: 10.1175/1520-0493(2003)131%3C2394:RRFTSO%3E2.0.CO;2.

Buschow, S. and P. Friederichs (2020). "Using wavelets to verify the scale structure of precipitation forecasts". In: *Advances in Statistical Climatology, Meteorology and Oceanography* 6.1, pp. 13–30. DOI: 10.5194/ascmo-6-13-2020.

– (2021). "SAD: Verifying the scale, anisotropy and direction of precipitation forecasts". In: *Quarterly Journal of the Royal Meteorological Society* 147.735, pp. 1150–1169. DOI: 10.1002/qj.3964.

Buschow, S., J. Pidstrigach, and P. Friederichs (2019). "Assessment of wavelet-based spatial verification by means of a stochastic precipitation model (wv_verif v0. 1.0)". In: *Geoscientific Model Development* 12.8, pp. 3401–3418. DOI: 10.5194/gmd-12-3401-2019.

Chaboureau, J.-P., F. Guichard, J.-L. Redelsperger, and J.-P. Lafore (2004). "The role of stability and moisture in the diurnal cycle of convection over land". In: *Quarterly Journal of the Royal Meteorological Society: A journal of the atmospheric sciences, applied meteorology and physical oceanography* 130.604, pp. 3105–3117. DOI: 10.1256/qj.03.132.

Chagnon, J. M. and P. R. Bannon (2005a). "Adjustment to injections of mass, momentum, and heat in a compressible atmosphere". In: *Journal of the atmospheric sciences* 62.8, pp. 2749–2769. DOI: 10.1175/JAS3503.1.

– (2005b). "Wave response during hydrostatic and geostrophic adjustment. Part I: Transient dynamics". In: *Journal of the atmospheric sciences* 62.5, pp. 1311–1329. DOI: 10.1175/JAS3283.1.

Ciesielski, P. E., W. H. Schubert, and R. H. Johnson (1999). "Large-scale heat and moisture budgets over the ASTEX region". In: *Journal of the atmospheric sciences* 56.18, pp. 3241–3261. DOI: 10.1175/1520-0469(1999)056%3C3241:LSHAMB%3E2.0.CO;2.

Cohen, A. E., S. M. Cavallo, M. C. Coniglio, and H. E. Brooks (2015). "A review of planetary boundary layer parameterization schemes and their sensitivity in simulating southeastern US cold season severe weather environments". In: *Weather and forecasting* 30.3, pp. 591–612. DOI: 10.1175/WAF-D-14-00105.1.

Crueger, T., M. A. Giorgetta, R. Brokopf, M. Esch, S. Fiedler, C. Hohenegger, L. Kornblueh, T. Mauritsen, C. Nam, A.-K. Naumann, et al. (2018). "ICON-A, the

atmosphere component of the ICON earth system model: II. Model Evaluation". In: *Journal of Advances in Modeling Earth Systems* 10.7, pp. 1638–1662. DOI: 10.1029/2017MS001233.

Dai, A. (2006). "Precipitation characteristics in eighteen coupled climate models". In: *Journal of climate* 19.18, pp. 4605–4630. DOI: 10.1175/JCLI3884.1.

Dai, A., X. Lin, and K.-L. Hsu (2007). "The frequency, intensity, and diurnal cycle of precipitation in surface and satellite observations over low-and mid-latitudes". In: *Climate dynamics* 29.7-8, pp. 727–744. DOI: 10.1007/s00382-007-0260-y.

Danilov, S. (2010). "On utility of triangular C-grid type discretization for numerical modeling of large-scale ocean flows". In: *Ocean Dynamics* 60.6, pp. 1361–1369. DOI: 10.1007/s10236-010-0339-6.

Datta, B. N. (2010). *Numerical linear algebra and applications*. Vol. 116. Siam. ISBN: 978-0-89871-685-6.

Davies, H. C. (1983). "Limitations of some common lateral boundary schemes used in regional NWP models". In: *Monthly Weather Review* 111.5, pp. 1002–1012. DOI: 10.1175/1520-0493(1983)111%3C1002:LOSCLB%3E2.0.CO;2.

– (1976). "A lateral boundary formulation for multi-level prediction models". In: *Quarterly Journal of the Royal Meteorological Society* 102.432, pp. 405–418. DOI: 10.1002/qj.49710243210.

De Rooy, W. C., P. Bechtold, K. Froehlich, C. Hohenegger, H. Jonker, D. Mironov, A. Pier Siebesma, J. Teixeira, and J.-I. Yano (2013). "Entrainment and detrainment in cumulus convection: An overview". In: *Quarterly Journal of the Royal Meteorological Society* 139.670, pp. 1–19. DOI: 10.1002/qj.1959.

Del Genio, A. D., W. Kovari, M.-S. Yao, and J. Jonas (2005). "Cumulus microphysics and climate sensitivity". In: *Journal of climate* 18.13, pp. 2376–2387. DOI: 10.1175/JCLI3413.1.

Deng, A. and D. Stauffer (2006). "On improving 4-km mesoscale model simulations". In: *Journal of applied meteorology and climatology* 45.3, pp. 361–381. DOI: 10.1175/JAM2341.1.

Derbyshire, S., I. Beau, P. Bechtold, J.-Y. Grandpeix, J.-M. Piriou, J.-L. Redelsperger, and P. Soares (2004). "Sensitivity of moist convection to environmental humidity". In: *Quarterly Journal of the Royal Meteorological Society: A journal of the atmospheric sciences, applied meteorology and physical oceanography* 130.604, pp. 3055–3079. DOI: 10.1256/qj.03.130.

Derbyshire, S., A. Maidens, S. Milton, R. Stratton, and M. Willett (2011). "Adaptive detrainment in a convective parametrization". In: *Quarterly Journal of the Royal Meteorological Society* 137.660, pp. 1856–1871. DOI: 10.1002/qj.875.

Dipankar, A., B. Stevens, R. Heinze, C. Moseley, G. Zaengl, M. Giorgetta, and S. Brdar (2015). "Large eddy simulation using the general circulation model ICON". In: *Journal of Advances in Modeling Earth Systems* 7, pp. 963–986. DOI: 10.1002/2015MS000431.

Doms, G. and M. Baldauf (2015). *A description of the nonhydrostatic regional model LM. Part I: Dynamics and Numerics*. (also available at www.cosmo-model.org). Consortium for small scale modelling. Deutscher Wetterdienst. Offenbach, Germany.

Doms, G. et al. (2011). *A description of the Nonhydrostatic COSMO model. Part II: Physical Parameterization*. (also available at www.cosmo-model.org). Consortium for small scale modelling. Deutscher Wetterdienst. Offenbach, Germany.

Donner, L. J. and V. T. Phillips (2003). "Boundary layer control on convective available potential energy: Implications for cumulus parameterization". In: *Journal of Geophysical Research: Atmospheres* 108.D22. DOI: 10.1029/2003JD003773.

Donner, L. J., C. J. Seman, R. S. Hemler, and S. Fan (2001). "A cumulus parameterization including mass fluxes, convective vertical velocities, and mesoscale effects: Thermodynamic and hydrological aspects in a general circulation model". In: *Journal of climate* 14.16, pp. 3444–3463. DOI: 10.1175/1520-0442(2001)014%3C3444:ACPIMF%3E2.0.CO;2.

Doswell III, C. A., H. E. Brooks, and R. A. Maddox (1996). "Flash flood forecasting: An ingredients-based methodology". In: *Weather and Forecasting* 11.4, pp. 560–581. DOI: 10.1175/1520-0434(1996)011%3C0560:FFFAIB%3E2.0.CO;2.

Durran, D. R. and J. B. Klemp (1982). "On the effects of moisture on the Brunt-Väisälä frequency". In: *Journal of Atmospheric Sciences* 39.10, pp. 2152–2158. DOI: 10.1175/1520-0469(1982)039%3C2152:OTEOMO%3E2.0.CO;2.

Easter, R. C. (1993). "Two modified versions of Bott's positive-definite numerical advection scheme". In: *Monthly Weather Review* 121.1, pp. 297–304. DOI: 10.1175/1520-0493(1993)121%3C0297:TMVOBP%3E2.0.CO;2.

Ebert, E. E. (2008). "Fuzzy verification of high-resolution gridded forecasts: a review and proposed framework". In: *Meteorological Applications: A journal of forecasting, practical applications, training techniques and modelling* 15.1, pp. 51–64. DOI: 10.1002/met.25.

– (2009). "Neighborhood verification: A strategy for rewarding close forecasts". In: *Weather and Forecasting* 24.6, pp. 1498–1510. DOI: 10.1175/2009WAF2222251.1.

ECMWF (2017). "Part IV: Physical processes". In: *IFS Documentation CY43R3*. IFS Documentation 4. ECMWF. URL: https://www.ecmwf.int/node/17736.

Efron, B. and R. J. Tibshirani (1994). *An introduction to the bootstrap*. CRC press. ISBN: 9780412042317. DOI: 10.1201/9780429246593.

Emanuel, K. A., J. David Neelin, and C. S. Bretherton (1994). "On large-scale circulations in convecting atmospheres". In: *Quarterly Journal of the Royal Meteorological Society* 120.519, pp. 1111–1143. DOI: 10.1002/qj.49712051902.

Errico, R. M. (1985). "Spectra computed from a limited area grid". In: *Monthly Weather Review* 113.9, pp. 1554–1562. DOI: 10.1175/1520-0493(1985)113%3C1554:SCFALA%3E2.0.CO;2.

Flaounas, E., S. Bastin, and S. Janicot (2011). "Regional climate modelling of the 2006 West African monsoon: sensitivity to convection and planetary boundary layer parameterisation using WRF". In: *Climate Dynamics* 36.5-6, pp. 1083–1105. DOI: 10.1016/j.atmosres.2016.12.009.

Folkins, I., T. Mitovski, and J. Pierce (2014). "A simple way to improve the diurnal cycle in convective rainfall over land in climate models". In: *Journal of Geophysical Research: Atmospheres* 119.5, pp. 2113–2130. DOI: 10.1002/2013JD020149.

Fowler, L. D. and D. A. Randall (2002). "Interactions between cloud microphysics and cumulus convection in a general circulation model". In: *Journal of the atmospheric sciences* 59.21, pp. 3074–3098. DOI: 10.1175/1520-0469(2002)059%3C3074:IBCMAC%3E2.0.CO;2.

Fowler, L. D., W. C. Skamarock, G. A. Grell, S. R. Freitas, and M. G. Duda (2016). "Analyzing the Grell–Freitas convection scheme from hydrostatic to nonhydrostatic scales within a global model". In: *Monthly Weather Review* 144.6, pp. 2285–2306. DOI: 10.1175/MWR-D-15-0311.1.

Fritsch, J. and C. Chappell (1980). "Numerical prediction of convectively driven mesoscale pressure systems. Part I: Convective parameterization". In: *Journal of the Atmospheric Sciences* 37.8, pp. 1722–1733. DOI: 10.1175/1520-0469(1980)037%3C1722:NPOCDM%3E2.0.CO;2.

Fuhrer, O. and C. Schaer (2005). "Embedded cellular convection in moist flow past topography". In: *Journal of the Atmospheric Sciences* 62.8, pp. 2810–2828. DOI: 10.1175/JAS3512.1.

Gassmann, A. (2011). "Inspection of hexagonal and triangular C-grid discretizations of the shallow water equations". In: *Journal of Computational Physics* 230, pp. 2706–2721. DOI: 10.1016/j.jcp.2011.01.014.

– (2013). "A global hexagonal C-grid non-hydrostatic dynamical core (ICON-IAP) designed for energetic consistency". In: *Quarterly Journal of the Royal Meteorological Society* 139.670, pp. 152–175. DOI: 10.1002/qj.1960.

Gassmann, A. and H.-J. Herzog (2007). "A consistent time-split numerical scheme applied to the nonhydrostatic compressible equations". In: *Monthly Weather Review* 135, pp. 20–36. DOI: 10.1175/MWR3275.1.

– (2008). "Towards a consistent numerical compressible non-hydrostatic model using generalized Hamiltonian tools". In: *Quarterly Journal of the Royal Meteorological Society* 134, pp. 1597–1613. DOI: 10.1002/qj.297.

Gassmann, A. (2018). "Discretization of generalized Coriolis and friction terms on the deformed hexagonal C-grid". In: *Quarterly Journal of the Royal Meteorological Society* 144.716, pp. 2038–2053. DOI: 10.1002/qj.3294.

Gerard, L. and J.-F. Geleyn (2005). "Evolution of a subgrid deep convection parametrization in a limited-area model with increasing resolution". In: *Quarterly Journal of the Royal Meteorological Society: A journal of the atmospheric sciences, applied meteorology and physical oceanography* 131.610, pp. 2293–2312. DOI: 10.1256/qj.04.72.

Gill, A. (1981). "Homogeneous intrusions in a rotating stratified fluid". In: *Journal of Fluid Mechanics* 103, pp. 275–295. DOI: 10.1017/S0022112081001341.

Gilleland, E., D. Ahijevych, B. G. Brown, B. Casati, and E. E. Ebert (2009). "Intercomparison of spatial forecast verification methods". In: *Weather and forecasting* 24.5, pp. 1416–1430. DOI: 10.1175/2009WAF2222269.1.

Giorgetta, M. A., R. Brokopf, T. Crueger, M. Esch, S. Fiedler, J. Helmert, C. Hohenegger, L. Kornblueh, M. Koehler, E. Manzini, et al. (2018). "ICON-A, the atmosphere component of the ICON Earth System Model: I. Model description". In: *Journal of Advances in Modeling Earth Systems* 10.7, pp. 1613–1637. DOI: 10.1029/2017MS001242.

Grandpeix, J.-Y. and J.-P. Lafore (2010). "A density current parameterization coupled with Emanuel's convection scheme. Part I: The models". In: *Journal of the Atmospheric Sciences* 67.4, pp. 881–897. DOI: 10.1175/2009JAS3044.1.

Gray, M. (1999). "An investigation into convectively generated potential-vorticity anomalies using a mass-forcing model". In: *Quarterly Journal of the Royal Meteorological Society* 125.557, pp. 1589–1605. DOI: 10.1002/qj.49712555706.

Gray, M., G. Shutts, and G. Craig (1998). "The role of mass transfer in describing the dynamics of mesoscale convective systems". In: *Quarterly Journal of the Royal Meteorological Society* 124.548, pp. 1183–1207. DOI: 10.1002/qj.49712454808.

Gregory, D., R. Kershaw, and P. Inness (1997). "Parametrization of momentum transport by convection. II: Tests in single-column and general circulation models". In: *Quarterly Journal of the Royal Meteorological Society* 123.541, pp. 1153–1183. DOI: 10.1002/qj.49712354103.

Gregory, D., J.-J. Morcrette, C. Jakob, A. Beljaars, and T. Stockdale (2000). "Revision of convection, radiation and cloud schemes in the ECMWF Integrated Forecasting System". In: *Quarterly Journal of the Royal Meteorological Society* 126.566, pp. 1685–1710. DOI: 10.1002/qj.49712656607.

Grell, G. A., S. R. Freitas, et al. (2014). "A scale and aerosol aware stochastic convective parameterization for weather and air quality modeling". In: *Atmos. Chem. Phys* 14.10, pp. 5233–5250. DOI: 10.5194/acpd-13-23845-2013.

Gross, M., H. Wan, P. J. Rasch, P. M. Caldwell, D. L. Williamson, D. Klocke, C. Jablonowski, D. R. Thatcher, N. Wood, M. Cullen, et al. (2016). "Recent progress and review of issues related to Physics Dynamics Coupling in geophysical models". In: *arXiv e-prints*, arXiv–1605. URL: https://arxiv.org/abs/1605.06480.

– (2018). "Physics–dynamics coupling in weather, climate, and Earth system models: Challenges and recent progress". In: *Monthly Weather Review* 146.11, pp. 3505–3544. DOI: 10.1175/MWR-D-17-0345.1.

Hagemann, S., K. Arpe, and E. Roeckner (2006). "Evaluation of the hydrological cycle in the ECHAM5 model". In: *Journal of climate* 19.16, pp. 3810–3827. DOI: 10.1175/JCLI3831.1.

Haiden, T., M. Janousek, F. Vitart, L. Ferranti, and F. Prates (2019). "Evaluation of ECMWF forecasts, including the 2019 upgrade". In: DOI: 10.21957/MLVAPKKE. URL: https://www.ecmwf.int/node/19277 (visited on 04/24/2020).

Han, J., W. Wang, Y. C. Kwon, S.-Y. Hong, V. Tallapragada, and F. Yang (2017). "Updates in the NCEP GFS cumulus convection schemes with scale and aerosol awareness". In: *Weather and Forecasting* 32.5, pp. 2005–2017. DOI: 10.1175/WAF-D-17-0046.1.

Han, J.-Y. and S.-Y. Hong (2018). "Precipitation forecast experiments using the Weather Research and Forecasting (WRF) Model at gray-zone resolutions". In: *Weather and Forecasting* 33.6, pp. 1605–1616. DOI: 10.1175/WAF-D-18-0026.1.

Han, J.-Y., S.-Y. Hong, and Y. C. Kwon (2020). "The performance of a revised simplified Arakawa–Schubert (SAS) convection scheme in the medium-range forecasts of the Korean Integrated Model (KIM)". In: *Weather and Forecasting* 35.3, pp. 1113–1128. DOI: 10.1175/WAF-D-19-0219.1.

Hanke, M., R. Redler, T. Holfeld, and M. Yastremsky (2016). "YAC 1.2. 0: new aspects for coupling software in Earth system modelling". In: *Geoscientific Model Development* 9, pp. 2755–2769. DOI: 10.5194/gmd-9-2755-2016.

Heise, E., B. Ritter, and E. Schrodin (2006). *Operational implementation of the multilayer soil model TERRA*. Tech. rep.

Hesselberg, T. (1926). "Die Gesetze der ausgeglichenen atmosphärischen Bewegungen". In: *Beitr. Phys. Atmos* 12, pp. 141–160.

Heun, K. et al. (1900). "Neue Methoden zur approximativen Integration der Differentialgleichungen einer unabhängigen Veränderlichen". In: *Z. Math. Phys* 45, pp. 23–38.

Heus, T., G. Van Dijk, H. J. Jonker, and H. E. Van den Akker (2008). "Mixing in shallow cumulus clouds studied by Lagrangian particle tracking". In: *Journal of the Atmospheric Sciences* 65.8, pp. 2581–2597. DOI: 10.1175/2008JAS2572.1.

Holland, J. Z. (1970). "Preliminary report on the BOMEX sea-air interaction program". In: *Bulletin of the American Meteorological Society* 51.9, pp. 809–821. DOI: 10.1175/1520-0477(1970)051%3C0809:PROTBS%3E2.0.CO;2.

Holloway, C., S. Woolnough, and G. Lister (2012). "Precipitation distributions for explicit versus parametrized convection in a large-domain high-resolution tropical case study". In: *Quarterly Journal of the Royal Meteorological Society* 138.668, pp. 1692–1708. DOI: 10.1002/qj.1903.

Holloway, C. E., J. C. Petch, R. J. Beare, P. Bechtold, G. C. Craig, S. H. Derbyshire, L. J. Donner, P. R. Field, S. L. Gray, J. H. Marsham, et al. (2014). *Understanding and representing atmospheric convection across scales: Recommendations from the meeting held at Dartington Hall, Devon, UK, 28–30 January 2013*. DOI: 10.1002/asl2.508.

Holton, J. R. and G. J. Hakim (2013). *An Introduction to Dynamic Meteorology*. Vol. 88. Academic Press. ISBN: 978-0123848666.

Homeyer, C. R. and K. P. Bowman (n.d.). "A 22-year Evaluation of Convection Reaching the Stratosphere over the United States". In: *Journal of Geophysical Research: Atmospheres* (), e2021JD034808. DOI: 10.1029/2021JD034808.

Hong, S.-Y. and J. Dudhia (2012). "Next-generation numerical weather prediction: Bridging parameterization, explicit clouds, and large eddies". In: *Bulletin of the American Meteorological Society* 93.1, ES6–ES9. DOI: 10.1175/2011BAMS3224.1.

Horinouchi, T., S. Pawson, K. Shibata, U. Langematz, E. Manzini, M. A. Giorgetta, F. Sassi, R. Wilson, K. Hamilton, J. De Grandpre, et al. (2003). "Tropical cumulus convection and upward-propagating waves in middle-atmospheric GCMs". In: *Journal of the Atmospheric Sciences* 60.22, pp. 2765–2782. DOI: 10.1175/1520-0469(2003)060%3C2765:TCCAUW%3E2.0.CO;2.

Houze Jr, R. A. (2004). "Mesoscale convective systems". In: *Reviews of Geophysics* 42.4. DOI: 10.1029/2004RG000150.

– (2010). "Clouds in tropical cyclones". In: *Monthly Weather Review* 138.2, pp. 293–344. DOI: 10.1175/2009MWR2989.1.

– (2014). *Cloud dynamics*. Academic press. ISBN: 9780123742667.

Jablonowski, C. and D. L. Williamson (2006a). "A baroclinic instability test case for atmospheric model dynamical cores". In: *Quarterly Journal of the Royal Meteorological Society* 132.621C, pp. 2943–2975. DOI: 10.1256/qj.06.12.

– (2006b). "A baroclinic wave test case for dynamical cores of general circulation models: Model intercomparisons". In: *National Center for Atmospheric Research NCAR Tech. Note NCAR/TN-4691STR*. DOI: 10.5065/D6765C86.

Jakob, C. and A. P. Siebesma (2003). "A new subcloud model for mass-flux convection schemes: Influence on triggering, updraft properties, and model climate". In: *Monthly weather review* 131.11, pp. 2765–2778. DOI: 10.1175/1520-0493(2003)131%3C2765:ANSMFM%3E2.0.CO;2.

Jeworrek, J., G. West, and R. Stull (2019). "Evaluation of cumulus and microphysics parameterizations in WRF across the convective gray zone". In: *Weather and Forecasting* 34.4, pp. 1097–1115. DOI: 10.1175/WAF-D-18-0178.1.

Johnson, R. H., T. M. Rickenbach, S. A. Rutledge, P. E. Ciesielski, and W. H. Schubert (1999). "Trimodal characteristics of tropical convection". In: *Journal of climate* 12.8, pp. 2397–2418. DOI: 10.1175/1520-0442(1999)012%3C2397:TCOTC%3E2.0.CO;2.

Jolliffe, I. T. and D. B. Stephenson (2012). *Forecast verification: a practitioner's guide in atmospheric science*. John Wiley & Sons. ISBN: 9780470660713. DOI: 10.1002/9781119960003.

Kain, J. S. (2004). "The Kain–Fritsch convective parameterization: an update". In: *Journal of applied meteorology* 43.1, pp. 170–181. DOI: 10.1175/1520-0450(2004)043%3C0170:TKCPAU%3E2.0.CO;2.

Kain, J. S. and J. M. Fritsch (1990). "A one-dimensional entraining/detraining plume model and its application in convective parameterization". In: *Journal of Atmospheric Sciences* 47.23, pp. 2784–2802. DOI: 10.1175/1520-0469(1990)047%3C2784:AODEPM%3E2.0.CO;2.

– (1993). "Convective parameterization for mesoscale models: The Kain-Fritsch scheme". In: *The representation of cumulus convection in numerical models*. Springer, pp. 165–170. DOI: 10.1007/978-1-935704-13-3_16.

Kain, J. S., S. J. Weiss, D. R. Bright, M. E. Baldwin, J. J. Levit, G. W. Carbin, C. S. Schwartz, M. L. Weisman, K. K. Droegemeier, D. B. Weber, et al. (2008). "Some practical considerations regarding horizontal resolution in the first generation of operational convection-allowing NWP". In: *Weather and Forecasting* 23.5, pp. 931–952. DOI: 10.1175/WAF2007106.1.

Keane, R. J., G. C. Craig, C. Keil, and G. Zaengl (2014). "The Plant–Craig stochastic convection scheme in ICON and its scale adaptivity". In: *Journal of the Atmospheric Sciences* 71.9, pp. 3404–3415. DOI: 10.1175/JAS-D-13-0331.1.

Keil, C. and G. C. Craig (2009). "A displacement and amplitude score employing an optical flow technique". In: *Weather and Forecasting* 24.5, pp. 1297–1308. DOI: 10.1175/2009WAF2222247.1.

Kirshbaum, D. J., B. Adler, N. Kalthoff, C. Barthlott, and S. Serafin (2018). "Moist orographic convection: Physical mechanisms and links to surface-exchange processes". In: *Atmosphere* 9.3, p. 80. DOI: 10.3390/atmos9030080.

Klemp, J., J. Dudhia, and A. Hassiotis (2008). "An upper gravity-wave absorbing layer for NWP applications". In: *Monthly Weather Review* 136.10, pp. 3987–4004. DOI: 10.1175/2008MWR2596.1.

Kreklow, J., B. Tetzlaff, B. Burkhard, and G. Kuhnt (2020). "Radar-Based Precipitation Climatology in Germany—Developments, Uncertainties and Potentials". In: *Atmosphere* 11.2, p. 217. DOI: 10.3390/atmos11020217.

Kuell, V. and A. Bott (2008). "A hybrid convection scheme for use in nonhydrostatic numerical weather prediction models". In: *Meteorologische Zeitschrift* 17, pp. 775–783. DOI: 10.1127/0941-2948/2008/0342.

– (2009). "Application of the hybrid convection parameterization scheme HYMACS to different meteorological situations". In: *Atmospheric Research* 94, pp. 743–753. DOI: 10.1016/j.atmosres.2009.04.002.

– (2011). "Simulation of non-local effects of convection with the hybrid mass flux convection scheme HYMACS". In: *Meteorologische Zeitschrift* 20, pp. 227–241. DOI: 10.1127/0941-2948/2011/0212.

– (2014). "Stochastic parameterization of cloud processes". In: *Atmospheric Research* 143, pp. 176–197. DOI: 10.1016/j.atmosres.2014.01.027.

– (2019). "A physical subgrid-scale information exchange (PSIE) system for parametrization schemes in numerical weather prediction models". In: *Quarterly Journal of the Royal Meteorological Society* 145.719, pp. 767–783. DOI: 10.1002/qj.3464.

Kuell, V., A. Gassmann, and A. Bott (2007). "Towards a new hybrid cumulus parameterisation scheme for use in nonhydrostatic weather prediction models". In: *Quarterly Journal of the Royal Meteorological Society* 133, pp. 479–490. DOI: 10.1002/qj.28.

Kuo, H. and W. Raymond (1980). "A quasi-one-dimensional cumulus cloud model and parameterization of cumulus heating and mixing effects". In: *Monthly Weather Review* 108.7, pp. 991–1009. DOI: 10.1175/1520-0493(1980)108%3C0991:AQODCC%3E2.0.CO;2.

Kwon, Y. C. and S.-Y. Hong (2017). "A mass-flux cumulus parameterization scheme across gray-zone resolutions". In: *Monthly Weather Review* 145.2, pp. 583–598. DOI: 10.1175/MWR-D-16-0034.1.

Lahiri, S. N. (2013). *Resampling methods for dependent data*. Springer Science & Business Media. ISBN: 978-1-4757-3803-2. DOI: 10.1007/978-1-4757-3803-2.

Lang, S., W. Tao, J. Simpson, and B. Ferrier (2003). "Modeling of convective–stratiform precipitation processes: Sensitivity to partitioning methods". In: *Journal of Applied Meteorology* 42.4, pp. 505–527. DOI: 10.1175/1520-0450(2003)042%3C0505:MOCSPP%3E2.0.CO;2.

Langguth, M., V. Kuell, and A. Bott (2020). "Implementing the HYbrid MAss flux Convection Scheme (HYMACS) in ICON-First idealized tests and adaptions to the dynamical core for local mass sources". In: *Quarterly Journal of the Royal Meteorological Society* 146.731, pp. 2689–2716. DOI: 10.1002/qj.3812.

Lauritzen, P. H., C. Jablonowski, M. A. Taylor, and R. D. Nair (2010). "Rotated versions of the Jablonowski steady-state and baroclinic wave test cases: A dynamical core intercomparison". In: *Journal of Advances in Modeling Earth Systems* 2.4. DOI: 10.3894/JAMES.2010.2.15.

Lauritzen, P. H., A. A. Mirin, J. Truesdale, K. Raeder, J. L. Anderson, J. Bacmeister, and R. B. Neale (2012). "Implementation of new diffusion/filtering operators in the CAM-FV dynamical core". In: *The International Journal of High Performance Computing Applications* 26.1, pp. 63–73. DOI: 10.1177%2F1094342011410088.

Lean, H. W., P. A. Clark, M. Dixon, N. M. Roberts, A. Fitch, R. Forbes, and C. Halliwell (2008). "Characteristics of high-resolution versions of the Met Office Unified Model for forecasting convection over the United Kingdom". In: *Monthly Weather Review* 136.9, pp. 3408–3424. DOI: 10.1175/2008MWR2332.1.

Leuenberger, D., M. Koller, O. Fuhrer, and C. Schaer (2010). "A generalization of the SLEVE vertical coordinate". In: *Monthly Weather Review* 138.9, pp. 3683–3689. DOI: 10.1175/2010MWR3307.1.

Lin, S.-J., W. Putman, L. Harris, and the FV3-team (2017). *FV3 - The GFDL finite-volume cubed-sphere dynamical core*. Tech. rep. NWS/NCEP/EMC.

Liu, C. and M. W. Moncrieff (2007). "Sensitivity of cloud-resolving simulations of warm-season convection to cloud microphysics parameterizations". In: *Monthly weather review* 135.8, pp. 2854–2868. DOI: 10.1175/MWR3437.1.

Liu, N. and C. Liu (2016). "Global distribution of deep convection reaching tropopause in 1 year GPM observations". In: *Journal of Geophysical Research: Atmospheres* 121.8, pp. 3824–3842. DOI: 10.1002/2015JD024430.

Lochbihler, K., G. Lenderink, and A. P. Siebesma (2017). "The spatial extent of rainfall events and its relation to precipitation scaling". In: *Geophysical Research Letters* 44.16, pp. 8629–8636. DOI: 10.1002/2017GL074857.

Lorenz, E. N. (1965). "A study of the predictability of a 28-variable atmospheric model". In: *Tellus* 17.3, pp. 321–333. DOI: 10.3402/tellusa.v17i3.9076.

– (1969). "The predictability of a flow which possesses many scales of motion". In: *Tellus* 21.3, pp. 289–307. DOI: 10.3402/tellusa.v21i3.10086.

Lott, F. and M. J. Miller (1997). "A new subgrid-scale orographic drag parametrization: Its formulation and testing". In: *Quarterly Journal of the Royal Meteorological Society* 123.537, pp. 101–127. DOI: 10.1002/qj.49712353704.

Maddox, R. A. (1983). "Large-scale meteorological conditions associated with midlatitude, mesoscale convective complexes". In: *Monthly Weather Review* 111.7, pp. 1475–1493. DOI: 10.1175/1520-0493(1983)111%3C1475:LSMCAW%3E2.0.CO;2.

Malardel, S. and P. Bechtold (2019). "The coupling of deep convection with the resolved flow via the divergence of mass flux in the IFS". In: *Quarterly Journal of the Royal Meteorological Society* 145.722, pp. 1832–1845. DOI: 10.1002/qj.3528.

Malardel, S. and N. P. Wedi (2016). "How does subgrid-scale parametrization influence nonlinear spectral energy fluxes in global NWP models?" In: *Journal of Geophysical Research: Atmospheres* 121.10, pp. 5395–5410. DOI: 10.1002/2015JD023970.

Mapes, B. E. (1997). "Equilibrium vs. activation control of large-scale variations of tropical deep convection". In: *The physics and parameterization of moist atmospheric convection*. Springer, pp. 321–358. DOI: 10.1007/978-94-015-8828-7_13.

Markowski, P. and Y. Richardson (2011). *Mesoscale meteorology in midlatitudes*. Vol. 2. John Wiley & Sons. DOI: 10.1002/9780470682104.

Marsham, J. H., N. S. Dixon, L. Garcia-Carreras, G. M. Lister, D. J. Parker, P. Knippertz, and C. E. Birch (2013). "The role of moist convection in the West African monsoon system: Insights from continental-scale convection-permitting simulations". In: *Geophysical Research Letters* 40.9, pp. 1843–1849. DOI: 10.1002/grl.50347.

Martinez-Villalobos, C. and J. D. Neelin (2019). "Why do precipitation intensities tend to follow gamma distributions?" In: *Journal of the Atmospheric Sciences* 76.11, pp. 3611–3631. DOI: 10.1175/JAS-D-18-0343.1.

Mass, C. F., D. Ovens, K. Westrick, and B. A. Colle (2002). "Does increasing horizontal resolution produce more skillful forecasts?: The Results of Two Years of real-Time Numerical Weather Prediction over the Pacific Northwest". In: *Bulletin of the American Meteorological Society* 83.3, pp. 407–430. DOI: 10.1175/1520-0477(2002)083%3C0407:DIHRPM%3E2.3.CO;2.

Matsuno, T. (1966). "Numerical integrations of the primitive equations by a simulated backward difference method". In: *Journal of the Meteorological Society of Japan. Ser. II* 44.1, pp. 76–84. DOI: 10.2151/jmsj1965.44.1_76.

Miura, H. (2007). "An upwind-biased conservative advection scheme for spherical hexagonal–pentagonal grids". In: *Monthly weather review* 135.12, pp. 4038–4044. DOI: 10.1175/2007MWR2101.1.

Miyakawa, T., M. Satoh, H. Miura, H. Tomita, H. Yashiro, A. T. Noda, Y. Yamada, C. Kodama, M. Kimoto, and K. Yoneyama (2014). "Madden–Julian Oscillation prediction skill of a new-generation global model demonstrated using a supercomputer". In: *Nature communications* 5.1, pp. 1–6. DOI: 10.1038/ncomms4769.

Mlawer, E. J., S. J. Taubman, P. D. Brown, M. J. Iacono, and S. A. Clough (1997). "Radiative transfer for inhomogeneous atmospheres: RRTM, a validated correlated-k model for the longwave". In: *Journal of Geophysical Research: Atmospheres* 102.D14, pp. 16663–16682. DOI: 10.1029/97JD00237.

Morrison, H. and A. Gettelman (2008). "A new two-moment bulk stratiform cloud microphysics scheme in the Community Atmosphere Model, version 3 (CAM3). Part I: Description and numerical tests". In: *Journal of Climate* 21.15, pp. 3642–3659. DOI: 10.1175/2008JCLI2105.1.

Murphy, A. H. (1988). "Skill scores based on the mean square error and their relationships to the correlation coefficient". In: *Monthly weather review* 116.12, pp. 2417–2424. DOI: 10.1175/1520-0493(1988)116%3C2417:SSBOTM%3E2.0.CO;2.

Murphy, A. H. and R. L. Winkler (1987). "A general framework for forecast verification". In: *Monthly weather review* 115.7, pp. 1330–1338. DOI: 10.1175/1520-0493(1987)115%3C1330:AGFFFV%3E2.0.CO;2.

Nastrom, G., K. S. Gage, and W. Jasperson (1984). "Kinetic energy spectrum of large-and mesoscale atmospheric processes". In: *Nature* 310.5972, pp. 36–38. DOI: 10.1038/310036a0.

Nitta, T. and S. Esbensen (1974). "Heat and moisture budget analyses using BOMEX data". In: *Monthly Weather Review* 102.1, pp. 17–28. DOI: 10.1175/1520-0493(1974)102%3C0017:HAMBAU%3E2.0.CO;2.

Niziol, T. A., W. R. Snyder, and J. S. Waldstreicher (1995). "Winter weather forecasting throughout the eastern United States. Part IV: Lake effect snow". In: *Weather and Forecasting* 10.1, pp. 61–77. DOI: 10.1175/1520-0434(1995)010%3C0061:WWFTTE%3E2.0.CO;2.

Ogura, Y. and H.-R. Cho (1973). "Diagnostic determination of cumulus cloud populations from observed large-scale variables". In: *Journal of the Atmospheric Sciences* 30.7, pp. 1276–1286. DOI: 10.1175/1520-0469(1973)030%3C1276:DDOCCP%3E2.0.CO;2.

Ong, H., C.-M. Wu, and H.-C. Kuo (2017). "Effects of artificial local compensation of convective mass flux in the cumulus parameterization". In: *Journal of Advances in Modeling Earth Systems* 9.4, pp. 1811–1827. DOI: 10.1002/2017MS000926.

Orlanski, I. (1975). "A rational subdivision of scales for atmospheric processes". In: *Bulletin of the American Meteorological Society*, pp. 527–530. DOI: 10.1175/1520-0477-56.5.527.

Orr, A., P. Bechtold, J. Scinocca, M. Ern, and M. Janiskova (2010). "Improved middle atmosphere climate and forecasts in the ECMWF model through a nonorographic gravity wave drag parameterization". In: *Journal of climate* 23.22, pp. 5905–5926. DOI: 10.1175/2010JCLI3490.1.

Ou, T., D. Chen, X. Chen, C. Lin, K. Yang, H.-W. Lai, and F. Zhang (2020). "Simulation of summer precipitation diurnal cycles over the Tibetan Plateau at the gray-zone grid spacing for cumulus parameterization". In: *Climate Dynamics* 54.7, pp. 3525–3539. DOI: https://link.springer.com/article/10.1007/s00382-020-05181-x.

Paegle, J. (1978). "The transient mass-flow adjustment of heated atmospheric circulations". In: *Journal of Atmospheric Sciences* 35.9, pp. 1678–1688. DOI: 10.1175/1520-0469(1978)035%3C1678:TTMFAO%3E2.0.CO;2.

Park, S. (2014). "A unified convection scheme (UNICON). Part I: Formulation". In: *Journal of Atmospheric Sciences* 71.11, pp. 3902–3930. DOI: 10.1175/JAS-D-13-0233.1.

Pearson, K., G. Lister, C. Birch, R. Allan, R. Hogan, and S. Woolnough (2014). "Modelling the diurnal cycle of tropical convection across the 'grey zone'". In: *Quarterly Journal of the Royal Meteorological Society* 140.679, pp. 491–499. DOI: 10.1002/qj.2145.

Pejcic, V., P. Saavedra Garfias, K. Muehlbauer, S. Troemel, and C. Simmer (2020). "Comparison between precipitation estimates of ground-based weather radar composites and GPM's DPR rainfall product over Germany". In: *Meteorologische Zeitschrift*, pp. 451–466. DOI: 10.1127/metz/2020/1039.

Plant, R. and G. C. Craig (2008). "A stochastic parameterization for deep convection based on equilibrium statistics". In: *Journal of the Atmospheric Sciences* 65.1, pp. 87–105. DOI: 10.1175/2007JAS2263.1.

Polavarapu, R. and G. Austin (1979). "A review of the GARP Atlantic Tropical Experiment (GATE)". In: *Atmosphere-Ocean* 17.1, pp. 1–13. DOI: 10.1080/07055900.1979.9649047.

Prein, A., A. Gobiet, M. Suklitsch, H. Truhetz, N. Awan, K. Keuler, and G. Georgievski (2013). "Added value of convection permitting seasonal simula-

tions". In: *Climate Dynamics* 41.9-10, pp. 2655–2677. DOI: 10.1007/s00382-013-1744-6.

Prein, A. F., W. Langhans, G. Fosser, A. Ferrone, N. Ban, K. Goergen, M. Keller, M. Toelle, O. Gutjahr, F. Feser, et al. (2015). "A review on regional convection-permitting climate modeling: Demonstrations, prospects, and challenges". In: *Reviews of geophysics* 53.2, pp. 323–361. DOI: 10.1002/2014RG000475.

Prill, F., D. Reinert, D. Rieger, and G. Zaengl (2020). *Working with the ICON model*. Deutscher Wetterdienst. Offenbach, Germany. DOI: 10.5676/DWDpub/nwv/icontutorial2020.

Prill, F., D. Reinert, D. Rieger, G. Zaengl, J. Schroeter, J. Foerstner, S. Werchner, M. Weimer, R. Ruhnke, and B. Vogel (2019). *Working with the ICON model - Pratical exercises for NWP mode and ICON-ART*. Deutscher Wetterdienst. Offenbach, Germany.

Raschendorfer, M. (2001). "The new turbulence parameterization of LM". In: *COSMO newsletter* 1, pp. 89–97.

Rauber, R. M., B. Stevens, H. T. Ochs III, C. Knight, B. Albrecht, A. Blyth, C. Fairall, J. Jensen, S. Lasher-Trapp, O. Mayol-Bracero, et al. (2007). "Rain in shallow cumulus over the ocean: The RICO campaign". In: *Bulletin of the American Meteorological Society* 88.12, pp. 1912–1928. DOI: 10.1175/BAMS-88-12-1912.

Raymond, D., Ž. Fuchs, S. Gjorgjievska, and S. Sessions (2015). "Balanced dynamics and convection in the tropical troposphere". In: *Journal of Advances in Modeling Earth Systems* 7.3, pp. 1093–1116. DOI: 10.1002/2015MS000467.

Raymond, D. J. and M. J. Herman (2011). "Convective quasi-equilibrium reconsidered". In: *Journal of Advances in Modeling Earth Systems* 3.3. DOI: 10.1029/2011MS000079.

Reichstein, M., G. Camps-Valls, B. Stevens, M. Jung, J. Denzler, N. Carvalhais, et al. (2019). "Deep learning and process understanding for data-driven Earth system science". In: *Nature* 566.7743, pp. 195–204. DOI: 10.1038/s41586-019-0912-1.

Reinert, D. (2020). *The tracer transport module Part I: A mass consistent finite volume approach with fractional steps*. Tech. rep. DOI: 10.5676/DWD_pub/nwv/icon_005.

Rio, C., F. Hourdin, J.-Y. Grandpeix, and J.-P. Lafore (2009). "Shifting the diurnal cycle of parameterized deep convection over land". In: *Geophysical Research Letters* 36.7. DOI: 10.1029/2008GL036779.

Rio, C., A. D. Del Genio, and F. Hourdin (2019). "Ongoing breakthroughs in convective parameterization". In: *Current Climate Change Reports* 5.2, pp. 95–111. DOI: 10.1007/s40641-019-00127-w.

Rio, C., J.-Y. Grandpeix, F. Hourdin, F. Guichard, F. Couvreux, J.-P. Lafore, A. Fridlind, A. Mrowiec, R. Roehrig, N. Rochetin, et al. (2013). "Control of deep convection by sub-cloud lifting processes: the ALP closure in the LMDZ5B general circulation model". In: *Climate dynamics* 40.9-10, pp. 2271–2292. DOI: 10.1007/s00382-012-1506-x.

Rípodas, P., A. Gassmann, J. Foerstner, D. Majewski, M. Giorgetta, P. Korn, L. Kornblueh, H. Wan, G. Zaengl, L. Bonaventura, et al. (2009). "Icosahedral Shal-

low Water Model (ICOSWM): results of shallow water test cases and sensitivity to model parameters". In: *Geoscientific Model Development* 2, pp. 231–251. URL: 10.5194/gmd-2-231-2009.

Roberts, N. (2008). "Assessing the spatial and temporal variation in the skill of precipitation forecasts from an NWP model". In: *Meteorological Applications: A journal of forecasting, practical applications, training techniques and modelling* 15.1, pp. 163–169. DOI: 10.1002/met.57.

Roberts, N. M. and H. W. Lean (2008). "Scale-selective verification of rainfall accumulations from high-resolution forecasts of convective events". In: *Monthly Weather Review* 136.1, pp. 78–97. DOI: 10.1175/2007MWR2123.1.

Rodwell, M. J., D. S. Richardson, T. D. Hewson, and T. Haiden (2010). "A new equitable score suitable for verifying precipitation in numerical weather prediction". In: *Quarterly Journal of the Royal Meteorological Society* 136.650, pp. 1344–1363. DOI: 10.1002/qj.656.

Rossa, A., P. Nurmi, and E. Ebert (2008). "Overview of methods for the verification of quantitative precipitation forecasts". In: *Precipitation: Advances in measurement, estimation and prediction*. Springer, pp. 419–452. DOI: 10.1007/978-3-540-77655-0_16.

Rotunno, R. and K. A. Emanuel (1987). "An air–sea interaction theory for tropical cyclones. Part II: Evolutionary study using a nonhydrostatic axisymmetric numerical model". In: *Journal of Atmospheric Sciences* 44.3, pp. 542–561. DOI: 10.1175/1520-0469(1987)044%3C0542:AAITFT%3E2.0.CO;2.

Rotunno, R., J. B. Klemp, and M. L. Weisman (1988). "A theory for strong, long-lived squall lines". In: *Journal of Atmospheric Sciences* 45.3, pp. 463–485. DOI: 10.1175/1520-0469(1988)045%3C0463:ATFSLL%3E2.0.CO;2.

Rysman, J.-F., C. Claud, and J. Delanoë (2016). "Monitoring deep convection and convective overshooting from 60 S to 60 N using MHS: a Cloudsat/CALIPSO-based assessment". In: *IEEE Geoscience and Remote Sensing Letters* 14.2, pp. 159–163. DOI: 10.1109/LGRS.2016.2631725.

Sakradzija, M., A. Seifert, and A. Dipankar (2016). "A stochastic scale-aware parameterization of shallow cumulus convection across the convective gray zone". In: *Journal of Advances in Modeling Earth Systems* 8.2, pp. 786–812. DOI: 10.1002/2016MS000634.

Salzen, K. von, N. A. McFarlane, and M. Lazare (2005). "The role of shallow convection in the water and energy cycles of the atmosphere". In: *Climate dynamics* 25.7-8, pp. 671–688. DOI: 10.1007/s00382-005-0051-2.

Schaeer, C., D. Leuenberger, O. Fuhrer, D. Luethi, and C. Girard (2002). "A new terrain-following vertical coordinate formulation for atmospheric prediction models". In: *Monthly Weather Review* 130.10, pp. 2459–2480. DOI: 10.1175/1520-0493(2002)130%3C2459:ANTFVC%3E2.0.CO;2.

Schlemmer, L. and C. Hohenegger (2014). "The formation of wider and deeper clouds as a result of cold-pool dynamics". In: *Journal of the Atmospheric Sciences* 71.8, pp. 2842–2858. DOI: 10.1175/JAS-D-13-0170.1.

Schoenstadt, A. L. (1980). "A transfer function analysis of numerical schemes used to simulate geostrophic adjustment". In: *Monthly Weather Review* 108.8,

pp. 1248–1259. DOI: 10.1175/1520-0493(1980)108%3C1248:ATFAON%3E2.0.CO;2.

Schrodin, R. and E. Heise (2002). *The multi-layer version of the DWD soil model TERRA-LM*.

Schultz, M., C. Betancourt, B. Gong, F. Kleinert, M. Langguth, L. Leufen, A. Mozaffari, and S. Stadtler (2021). "Can deep learning beat numerical weather prediction?" In: *Philosophical Transactions of the Royal Society A* 379.2194, p. 20200097. DOI: 10.1098/rsta.2020.0097.

Schulzweida, U. (Oct. 2019). *CDO User Guide*. DOI: 10.5281/zenodo.3539275. URL: 10.5281/zenodo.3539275.

Seifert, A. (2008). "A revised cloud microphysical parameterization for COSMO-LME". In: *COSMO Newsletter* 7, pp. 25–28.

Shutts, G. (1994). "The adjustment of a rotating, stratified fluid subject to localized sources of mass". In: *Quarterly Journal of the Royal Meteorological Society* 120.516, pp. 361–386. DOI: 10.1002/qj.49712051607.

– (1995). "An analytical model of the balanced flow created by localized convective mass transfer in a rotating fluid". In: *Dynamics of atmospheres and oceans* 22.1-2, pp. 1–17. DOI: 10.1016/0377-0265(94)00401-H.

Simpson, J. (1971). "On cumulus entrainment and one-dimensional models". In: *Journal of Atmospheric Sciences* 28.3, pp. 449–455. DOI: 10.1175/1520-0469(1971)028%3C0449:OCEAOD%3E2.0.CO;2.

Simpson, J. and V. Wiggert (1969). "Models of precipitating cumulus towers". In: *Monthly Weather Review* 97.7, pp. 471–489. DOI: 10.1175/1520-0493(1969)097%3C0471:MOPCT%3E2.3.CO;2.

Skamarock, W., J. Klemp, et al. (2019). *A description of the advanced research WRF model version 4 (No. NCAR/TN-556+ STR)*. Tech. rep. NCAR/TN-556+ STR. DOI: 10.5065/1dfh-6p97.

Skamarock, W., J. Klemp, J. Dudhia, D. O. Gill, D. M. Barker, W. Wang, and J. G. Powers (2008). *A description of the advanced research WRF version 3. NCAR TN-475+ STR*. Tech. rep. DOI: 10.5065/D68S4MVH.

Skamarock, W. C. (2004). "Evaluating mesoscale NWP models using kinetic energy spectra". In: *Monthly weather review* 132.12, pp. 3019–3032. DOI: 10.1175/MWR2830.1.

Skamarock, W. C. and J. B. Klemp (1992). "The stability of time-split numerical methods for the hydrostatic and the nonhydrostatic elastic equations". In: *Monthly Weather Review* 120.9, pp. 2109–2127. DOI: 10.1175/1520-0493(1992)120%3C2109:TSOTSN%3E2.0.CO;2.

Skamarock, W. C. (2011). "Kinetic energy spectra and model filters". In: *Numerical Techniques for Global Atmospheric Models*. Springer, pp. 495–512. DOI: 10.1007/978-3-642-11640-7_14.

Skok, G. and N. Roberts (2016). "Analysis of fractions skill score properties for random precipitation fields and ECMWF forecasts". In: *Quarterly Journal of the Royal Meteorological Society* 142.700, pp. 2599–2610. DOI: 10.1002/qj.2849.

Song, X. and G. J. Zhang (2011). "Microphysics parameterization for convective clouds in a global climate model: Description and single-column model

tests". In: *Journal of Geophysical Research: Atmospheres* 116.D2. DOI: 10.1029/2010JD014833.

Steinheimer, M., M. Hantel, and P. Bechtold (2008). "Convection in Lorenz's global energy cycle with the ECMWF model". In: *Tellus A: Dynamic Meteorology and Oceanography* 60.5, pp. 1001–1022. DOI: 10.1111/j.1600-0870.2008.00348.x.

Stensrud, D. J. (2009). *Parameterization schemes: keys to understanding numerical weather prediction models*. Cambridge University Press. ISBN: 9780521126762.

Stensrud, D. J. and J. L. Anderson (2001). "Is midlatitude convection an active or a passive player in producing global circulation patterns?" In: *Journal of climate* 14.10, pp. 2222–2237. DOI: 10.1175/1520-0442(2001)014%3C2222:IMCAAO%3E2.0.CO;2.

Stephens, G. L., T. L'Ecuyer, R. Forbes, A. Gettelmen, J.-C. Golaz, A. Bodas-Salcedo, K. Suzuki, P. Gabriel, and J. Haynes (2010). "Dreary state of precipitation in global models". In: *Journal of Geophysical Research: Atmospheres* 115.D24. DOI: 10.1029/2010JD014532.

Stevens, B. (2005). "Atmospheric moist convection". In: *Annual Review Earth Planetary Sciences* 33, pp. 605–643. DOI: 10.1146/annurev.earth.33.092203.122658.

Stratton, R. and A. Stirling (2012). "Improving the diurnal cycle of convection in GCMs". In: *Quarterly Journal of the Royal Meteorological Society* 138.666, pp. 1121–1134. DOI: 10.1002/qj.991.

Suhas, E. and G. J. Zhang (2014). "Evaluation of trigger functions for convective parameterization schemes using observations". In: *Journal of Climate* 27.20, pp. 7647–7666. DOI: 10.1175/JCLI-D-13-00718.1.

Sun, Y. (2017). "Scale Interaction and Mid-latitude Atmospheric Predictability: Impacts of Moist Convection and Gravity Waves". PhD thesis. The Pennsylvania State University. URL: https://ui.adsabs.harvard.edu/abs/2017PhDT.....367S.

Sundqvist, H. (1978). "A parameterization scheme for non-convective condensation including prediction of cloud water content". In: *Quarterly Journal of the Royal Meteorological Society* 104.441, pp. 677–690. DOI: 10.1002/qj.49710444110.

Theis, S., A. Hense, and U. Damrath (2005). "Probabilistic precipitation forecasts from a deterministic model: A pragmatic approach". In: *Meteorological Applications: A journal of forecasting, practical applications, training techniques and modelling* 12.3, pp. 257–268. DOI: 10.1017/S1350482705001763.

Thorarinsdottir, T. L., T. Gneiting, and N. Gissibl (2013). "Using proper divergence functions to evaluate climate models". In: *SIAM/ASA Journal on Uncertainty Quantification* 1.1, pp. 522–534. DOI: 10.1137/130907550.

Thuburn, J. (2008). "Numerical wave propagation on the hexagonal C-grid". In: *Journal of Computational Physics* 227.11, pp. 5836–5858. DOI: 10.1016/j.jcp.2008.02.010.

Thuburn, J., H. Weller, G. K. Vallis, R. J. Beare, and M. Whitall (2018). "A framework for convection and boundary layer parameterization derived from conditional filtering". In: *Journal of the Atmospheric Sciences* 75.3, pp. 965–981. DOI: 10.1175/JAS-D-17-0130.1.

Tiedtke, M. (1989). "A comprehensive mass flux scheme for cumulus parameterization in large-scale models". In: *Monthly weather review* 117.8, pp. 1779–1800. DOI: 10.1175/1520-0493(1989)117%3C1779:ACMFSF%3E2.0.CO;2.

Tomita, H., M. Satoh, and K. Goto (2002). "An optimization of the icosahedral grid modified by spring dynamics". In: *Journal of Computational Physics* 183.1, pp. 307–331. DOI: 10.1006/jcph.2002.7193.

Torri, G., Z. Kuang, and Y. Tian (2015). "Mechanisms for convection triggering by cold pools". In: *Geophysical Research Letters* 42.6, pp. 1943–1950. DOI: 10.1002/2015GL063227.

Tromeur, E. and W. B. Rossow (2010). "Interaction of tropical deep convection with the large-scale circulation in the MJO". In: *Journal of climate* 23.7, pp. 1837–1853. DOI: 10.1175/2009JCLI3240.1.

Ullrich, P. A., C. Jablonowski, J. Kent, P. H. Lauritzen, R. Nair, K. A. Reed, C. M. Zarzycki, D. M. Hall, D. Dazlich, R. Heikes, et al. (2017). "DCMIP2016: A review of non-hydrostatic dynamical core design and intercomparison of participating models". In: *Geoscientific Model Development* 10, pp. 4477–4509. DOI: 10.5194/gmd-10-4477-2017.

Vlček, O. and R. Huth (2009). "Is daily precipitation Gamma-distributed?: Adverse effects of an incorrect use of the Kolmogorov–Smirnov test". In: *Atmospheric Research* 93.4, pp. 759–766. DOI: 10.1016/j.atmosres.2009.03.005.

Wagner, A., D. Heinzeller, S. Wagner, T. Rummler, and H. Kunstmann (2018). "Explicit convection and scale-aware cumulus parameterizations: High-resolution simulations over areas of different topography in Germany". In: *Monthly Weather Review* 146.6, pp. 1925–1944. DOI: 10.1175/MWR-D-17-0238.1.

Wahl, S. (2015). "Uncertainty in mesoscale numerical weather prediction". PhD thesis. Rheinische Friedrich-Wilhelms University of Bonn. URL: http://hdl.handle.net/20.500.11811/6560.

Wahl, S., C. Bollmeyer, S. Crewell, C. Figura, P. Friederichs, A. Hense, J. D. Keller, and C. Ohlwein (2017). "A novel convective-scale regional reanalysis COSMO-REA2: Improving the representation of precipitation". In: *Meteorologische Zeitschrift* 26.4, pp. 345–361. DOI: 10.1127/metz/2017/0824.

Wan, H. et al. (2013). "The ICON-1.2 hydrostatic atmospheric dynamical core on triangular grids, Part I: Formulation and performance of the baseline version". In: *Geoscientific Model Development* 6, pp. 735–763. DOI: 10.5194/gmd-6-735-2013.

Wan, H. (2009). "Developing and testing a hydrostatic atmospheric dynamical core on triangular grids". PhD thesis. Max Plank Institute for Meteorology Hamburg, Germany. DOI: 10.17617/2.993988.

Ward, M. N. and C. K. Folland (1991). "Prediction of seasonal rainfall in the north Nordeste of Brazil using eigenvectors of sea-surface temperature". In: *International Journal of Climatology* 11.7, pp. 711–743. DOI: 10.1002/joc.3370110703.

Weisman, M. L., C. Davis, W. Wang, K. W. Manning, and J. B. Klemp (2008). "Experiences with 0–36-h explicit convective forecasts with the WRF-ARW model". In: *Weather and Forecasting* 23.3, pp. 407–437. DOI: 10.1175/2007WAF2007005.1.

Weller, H., W. McIntyre, and D. Shipley (2020). "Multifluids for Representing Subgrid-Scale Convection". In: *Journal of Advances in Modeling Earth Systems* 12.8, e2019MS001966. DOI: 10.1029/2019MS001966.

Weller, H. and W. A. McIntyre (2019). "Numerical solution of the conditionally averaged equations for representing net mass flux due to convection". In: *Quarterly Journal of the Royal Meteorological Society* 145.721, pp. 1337–1353. DOI: 10.1002/qj.3490.

Whitehead, J. P., C. Jablonowski, R. B. Rood, and P. H. Lauritzen (2011). "A stability analysis of divergence damping on a latitude–longitude grid". In: *Monthly weather review* 139.9, pp. 2976–2993. DOI: 10.1175/2011MWR3607.1.

Wilks, D. S. (1997). "Resampling hypothesis tests for autocorrelated fields". In: *Journal of Climate* 10.1, pp. 65–82. DOI: 10.1175/1520-0442(1997)010%3C0065:RHTFAF%3E2.0.CO;2.

– (2011). *Statistical methods in the atmospheric sciences*. Vol. 100. Academic press. ISBN: 9780123850225.

Winterrath, T., C. Brendel, M. Hafer, T. Junghaenel, A. Klameth, E. Walawender, E. Weigl, and A. Becker (2017). *Erstellung einer radargestützten Niederschlagsklimatologie*. Vol. 251. DOI: 10.17169/refubium-25153.

Winterrath, T., T. Brendel, T. Junghaenel, A. Klameth, K. Lengfeld, E. Walawender, E. Weigl, M. Hafer, and A. Becker (2019). "An overview of the new radar-based precipitation climatology of the Deutscher Wetterdienst–data, methods, products". In: *Rainfall Monitoring, Modelling and Forecasting in Urban Environment. UrbanRain18: 11th International Workshop on Precipitation in Urban Areas. Conference Proceedings*. ETH Zurich, Institute of Environmental Engineering, pp. 132–137. DOI: 10.3929/ethz-b-000347607.

Wolfram, P. J. and O. B. Fringer (2013). "Mitigating horizontal divergence "checkerboard" oscillations on unstructured triangular C-grids for nonlinear hydrostatic and nonhydrostatic flows". In: *Ocean Modelling* 69, pp. 64–78. DOI: 10.1016/j.ocemod.2013.05.007.

Wu, C.-M. and A. Arakawa (2014). "A unified representation of deep moist convection in numerical modeling of the atmosphere. Part II". In: *Journal of the Atmospheric Sciences* 71.6, pp. 2089–2103. DOI: 10.1175/JAS-D-13-0382.1.

Wulfmeyer, V., A. Behrendt, H.-S. Bauer, C. Kottmeier, U. Corsmeier, A. Blyth, G. Craig, U. Schumann, M. Hagen, S. Crewell, et al. (2008). "The Convective and Orographically induced Precipitation Study: A research and development project of the World Weather Research Program for improving quantitative precipitation forecasting in low-mountain regions". In: *Bulletin of the American Meteorological Society* 89.10, pp. 1477–1486. DOI: 10.1175/2008BAMS2367..

Wyngaard, J. C. (2004). "Toward numerical modeling in the "Terra Incognita"". In: *Journal of Atmospheric Sciences* 61.14, pp. 1816–1826. DOI: 10.1175/1520-0469(2004)061%3C1816:TNMITT%3E2.0.CO;2.

Xu, K.-M., R. T. Cederwall, L. J. Donner, W. W. Grabowski, F. Guichard, D. E. Johnson, M. Khairoutdinov, S. K. Krueger, J. C. Petch, D. A. Randall, et al. (2002). "An intercomparison of cloud-resolving models with the atmospheric radiation measurement summer 1997 intensive observation period data". In: *Quarterly Journal of the Royal Meteorological Society: A journal of the atmospheric*

sciences, applied meteorology and physical oceanography 128.580, pp. 593–624. DOI: 10.1256/003590002321042117.

Yanai, M., S. Esbensen, and J.-H. Chu (1973). "Determination of bulk properties of tropical cloud clusters from large-scale heat and moisture budgets". In: *Journal of Atmospheric Sciences* 30.4, pp. 611–627. DOI: 10.1175/1520-0469(1973)030%3C0611:DOBPOT%3E2.0.CO;2.

Yanai, M. and R. H. Johnson (1993). "Impacts of cumulus convection on thermodynamic fields". In: *The representation of cumulus convection in numerical models*. Springer, pp. 39–62. DOI: 10.1007/978-1-935704-13-3_4.

Yano, J.-I., M. Bister, Ž. Fuchs, L. Gerard, V. T. J. Phillips, S. Barkidija, and J.-M. Piriou (2013). "Phenomenology of convection-parameterization closure". In: *Atmospheric Chemistry and Physics* 13.8, pp. 4111–4131. DOI: 10.5194/acp-13-4111-2013. URL: https://acp.copernicus.org/articles/13/4111/2013/.

Yates, E., S. Anquetin, V. Ducrocq, J.-D. Creutin, D. Ricard, and K. Chancibault (2006). "Point and areal validation of forecast precipitation fields". In: *Meteorological Applications: A journal of forecasting, practical applications, training techniques and modelling* 13.1, pp. 1–20. DOI: 10.1017/S1350482705001921.

Zaengl, G., D. Reinert, P. Ripodas, and M. Baldauf (2015). "The ICON (ICOsahedral Non-hydrostatic) modelling framework of DWD and MPI-M: Description of the non-hydrostatic dynamical core". In: *Quarterly Journal of the Royal Meteorological Society* 141.687, pp. 563–579. DOI: 10.1002/qj.2378.

Zampieri, M., P. Malguzzi, and A. Buzzi (2005). "Sensitivity of quantitative precipitation forecasts to boundary layer parameterization: a flash flood case study in the Western Mediterranean". In: *Natural Hazards and Earth System Sciences* 5.4, pp. 603–612. DOI: 10.5194/nhess-5-603-2005.

Zdunkowski, W. and A. Bott (2003). *Dynamics of the Atmosphere: A course in theoretical Meteorology*. Cambridge University Press. ISBN: 978-0521809498.

Zhang, F., N. Bei, R. Rotunno, C. Snyder, and C. C. Epifanio (2007). "Mesoscale predictability of moist baroclinic waves: Convection-permitting experiments and multistage error growth dynamics". In: *Journal of Atmospheric Sciences* 64.10, pp. 3579–3594. DOI: 10.1175/JAS4028.1.

Zhang, G. J. (2002). "Convective quasi-equilibrium in midlatitude continental environment and its effect on convective parameterization". In: *Journal of Geophysical Research: Atmospheres* 107.D14, ACL–12. DOI: 10.1029/2001JD001005.

– (2009). "Effects of entrainment on convective available potential energy and closure assumptions in convection parameterization". In: *Journal of Geophysical Research: Atmospheres* 114.D7. DOI: 10.1029/2008JD010976.

Zhang, Y. and S. A. Klein (2010). "Mechanisms affecting the transition from shallow to deep convection over land: Inferences from observations of the diurnal cycle collected at the ARM Southern Great Plains site". In: *Journal of the Atmospheric Sciences* 67.9, pp. 2943–2959. DOI: 10.1175/2010JAS3366.1.

Zhao, B. and B. Zhang (2018). "Assessing hourly precipitation forecast skill with the fractions skill score". In: *Journal of Meteorological Research* 32.1, pp. 135–145. DOI: 10.1007/s13351-018-7058-1.

Acknowledgements

Around five years of work was needed to put this thesis on paper. Despite all the unexpected obstructions, comprising the preparation of the first own lecture as a young scientist after my Master thesis and working simultaneously in a new, exciting job, I'm incredibly happy to have passed this process. The long way until submission would not have been possible without the support from many kind people. While the list of all people supporting me over the last years is probably too long to be mentioned here, I want to highlight the following contributions:

- Prof. Dr. Andreas Bott for leading the supervision of my PhD project, for all his support, many discussions and advises , also going beyond my research, and for the great time I could spend in his working group.
- Dr. PD Martin Schultz for offering me the chance to start working in a very exciting position at JSC, for continuously sharpen my scientific writing skills and for the great aid in getting my PhD done.
- Dr. Daniel Reinert from DWD for many hours of fruitful and exciting discussions on the ICON model, on HYMACS and on other modelling topics. Without his valuable hints on the ICON model, it would have taken me even more time to get HYMACS work in the new hosting model.
- Dr. Volker Küll for very extensive and exciting discussions on HYMACS and for sharing his great modelling experience.
- Maike Hacker for the very nice colleague time in the working group as the second PhD student. All the discussions, chatting rounds and personal talks motivated and kept my head up.
- Dr. Günther Zängl and Dr. Florian Prill from DWD for their great support with the ICON model. While Günther was always available for answering questions on model developments and its capacities, Florian was the technical expert for running my ICON simulations.
- Dr. Almut Gassmann from IAP Kühlungsborn for her great explanations on the triangular grid geometry and some extremely helpful e-mails.
- Felix Kleinert, Maike Hacker, Scarlet Stadtler, Sonja Kreinberg and Volker Küll for carefully reviewing my thesis to improve the text.
- My former AGB research group at the IfGeo (Meteorological Section) and my current research group ESDE at the JSC for creating a nice working environment and for all the scientific and personal exchange.
- My friends for supporting me emotionally and giving me the possibility to reset my mind.
- My parents and my sister who continuously supported me over my whole life, all the patience and the huge amounts of relaxing moments.
- My better half Sonja Kreinberg who probably supported me the most over all the years and always made me feel home and comfortable irrespective how challenging the work on my PhD project was.

The ICON model is jointly developped by the German Weather Service (DWD) and the Max Planck Institute for Meteorology (MPI-M). All ICON simulations were performed on the HPC system *Cray XC40* at DWD. The development of the COSMO model was also led by DWD, while the simulations were run on the *cluma*-machine at the IfGeo - Meteorological Section. Thanks also go to Marc Mertes, IT-manager, for administrating the systems.

BONNER METEOROLOGISCHE ABHANDLUNGEN

Herausgegeben vom Institut für Geowissenschaften der Universität Bonn, Abteilung Meteorologie, durch Prof. Dr. H. FLOHN (Hefte 1-25), Prof. Dr. M. HANTEL (Hefte 26-35), Prof. Dr. H.-D. SCHILLING (Hefte 36-39), Prof. Dr. H. KRAUS (Hefte 40-49), ab Heft 50 durch Prof. Dr. A. HENSE.

Heft 1-79: siehe `https://www.ifgeo.uni-bonn.de/abteilungen/meteorologie/bibliothek/bonner-meteorologische-abhandlungen-bma`

80-94: open access, verfügbar unter `https://bonndoc.ulb.uni-bonn.de/xmlui/handle/20.500.11811/1627`

Heft 80: ***Tanja Zerenner***: Atmospheric downscaling using multi-objective genetic programming, 2016, [erschienen] 2017, X, 191 S.

Heft 81: ***Sophie Stolzenberger***: On the probabilistic evaluation of decadal and paleoclimate model predictions, 2017, IV, 122 S.

Heft 82: ***Insa Thiele-Eich***: Flooding in Dhaka, Bangladesh, and the challenge of climate change, 2017, V, 158 S.

Heft 83: ***Liselotte Bach***: Towards a probabilistic regional reanalysis for Europe, 2017 [erschienen] 2018, VI, 114 S.

Heft 84: ***Yen-Sen Lu***: Propagation of land surface model uncertainties in terrestrial system states, 2017, [erschienen] 2018, X, 120 S.

Heft 85: ***Rüdiger Hewer***: Stochastic physical models for wind fields and precipitation extremes, 2018, 99 S.

Heft 86: ***Sebastian Knist***: Land-atmosphere interactions in multiscale regional climate change simulations over Europe, 2018, VIII, 147 S.

Heft 87: ***Jessica Keune***: Integrated terrestrial simulations at the continental scale: Impact of groundwater dynamics and human water use on groundwater-to-atmosphere feedbacks during the European heatwave in 2003, 2019, IX, 172 S.

Heft 88: ***Christoph Beekmans***: 3-D Cloud Morphology and Evolution Derived from Hemispheric Stereo Cameras, 2019, [erschienen] 2020, VIII, 118 S.

Heft 89: ***Nils Weitzel***: Climate field reconstructions from pollen and macrofossil syntheses using Bayesian hierarchical models, 2019, [erschienen] 2020, XII, 153 S.

Heft 90: ***Alexander Kelbch***: Investigations to quantify individual exposure to solar ultraviolet erythemal radiation including cloud meteorological impact, 2020, III, 107 S.

Heft 91: ***Mari L. Schmidt***: Improvement of hail detection and nowcasting by synergistic combination of information from polarimetric radar, model predictions, and in-situ observations, 2020, VI, 136 S.

Heft 92: ***Sebastian Brune***: Der Wavelet-basierte Organisationsindex als Maß der konvektiven Organisation über Deutschland und dem tropischen Atlantik, 2021, IV, 121 S.

Heft 93: ***Sebastian Buschow***: Spatial Verification with Wavelets, 2022, V, 195 S.

Heft 94: ***Michael Langguth***: Representation of deep convection at gray-zone resolutions - Implementing and testing the HYbrid MAss flux Convection Scheme (HYMACS) in the ICON model, 2022, VI, 173 S.

Institut für Geowissenschaften
Abteilung Meteorologie
Mathematisch Naturwissenschaftliche Fakultät
Universität Bonn

institut für geowissenschaften
METEOROLOGIE